

# The Hunt for Red Dwarf Binaries and Hot Planets in the WFCAM Transit Survey.



# The Hunt for Red Dwarf Binaries and Hot Planets in the WFCAM Transit Survey.

Proefschrift

ter verkrijging van  
de graad van Doctor aan de Universiteit Leiden,  
op gezag van de Rector Magnificus prof. mr. C.J.J.M. Stolker,  
volgens besluit van het College voor Promoties  
te verdedigen op woensdag 27 maart 2013  
klokke 13.45 uur

door

Sebastiaan Victor Nefs

geboren te Halsteren  
in 1983

Promotiecommissie

Promotoren: Prof. Dr. I. A. G. Snellen  
Prof. Dr. C.W.M. Fridlund

Overige leden: Dr. I. Ribas (IEEC Barcelona, Spain)  
Dr. S.T. Hodgkin (IoA Cambridge, UK)  
Prof. Dr. S.F. Portegies-Zwart  
Prof. Dr. C.U. Keller  
Prof. Dr. H.J.A. Röttgering

## **To Nicole**

*"Yesterday is history,  
Tomorrow is a mystery,  
Today is a gift,  
that's why we call it the Present."*

**Cover image: This artist's impression shows a pair of active red dwarf stars in a binary. This thesis is for a large part devoted to their study. Credit: J. Pinfield, for the RoPACS network.**

# Contents

	Page
<b>Chapter 1. Introduction</b>	<b>1</b>
1.1 M-dwarfs - general characteristics . . . . .	1
1.2 M-dwarfs - why study them? . . . . .	2
1.3 Low-mass binary formation . . . . .	3
1.3.1 Observational constraints . . . . .	3
1.3.2 Fragmentation scenarios . . . . .	4
1.4 Close binaries . . . . .	5
1.4.1 Close versus wide . . . . .	5
1.4.2 Close binary types . . . . .	8
1.4.3 The close binary period distribution . . . . .	8
1.5 The mass-radius relation for M-dwarfs . . . . .	9
1.6 Planets around M-dwarfs . . . . .	10
1.7 WFCAM Transit Survey . . . . .	12
1.8 This thesis . . . . .	13
1.9 Future work . . . . .	13
1.10 Note to Chapter 3 . . . . .	14
<b>Chapter 2. Minimizing follow-up for space-based transit surveys</b>	<b>19</b>
2.1 Introduction . . . . .	20
2.2 Method . . . . .	21
2.2.1 Transit fitting . . . . .	21
2.2.2 Transit parameters . . . . .	21
2.2.3 MCMC . . . . .	22
2.3 Tests on synthetic lightcurves . . . . .	23
2.3.1 Transiting hot Jupiter . . . . .	23
2.3.2 Transiting super-Earth . . . . .	25
2.4 Tests on candidates in the CoRoT IRa01 field . . . . .	26
2.4.1 The data set . . . . .	26
2.4.2 Pre-cleaning of the lightcurves . . . . .	27
2.4.3 Fitting the lightcurves . . . . .	27
2.5 Discussion . . . . .	31
2.6 Conclusions . . . . .	33
<b>Chapter 3. WTS: Masses and Radii of M-dwarf EBs</b>	<b>43</b>
3.1 Introduction . . . . .	44
3.2 The WFCAM Transit Survey . . . . .	46
3.3 Observations and Data Reduction . . . . .	47
3.3.1 UKIRT/WFCAM <i>J</i> -band photometry . . . . .	47

3.3.2	INT/WFC <i>i</i> -band follow-up photometry . . . . .	50
3.3.3	IAC80/CAMELOT <i>g</i> -band follow-up photometry . . . . .	51
3.3.4	WHT low-resolution spectroscopy . . . . .	52
3.3.5	WHT/ISIS intermediate-resolution spectroscopy . . . . .	53
3.4	Identification of M-dwarf Eclipsing Binaries . . . . .	53
3.4.1	The M-dwarf sample . . . . .	53
3.4.2	Eclipse detection . . . . .	57
3.4.3	Candidate selection . . . . .	58
3.5	Low-resolution spectroscopic analysis . . . . .	58
3.5.1	Surface Gravity . . . . .	58
3.5.2	Metallicity . . . . .	58
3.5.3	H $\alpha$ Emission . . . . .	60
3.5.4	Spectral type and effective temperature . . . . .	60
3.6	Light curve analysis . . . . .	61
3.6.1	Error analysis . . . . .	67
3.6.2	Light ratios . . . . .	67
3.6.3	Star spots . . . . .	70
3.7	Radial velocity analysis . . . . .	71
3.8	Absolute dimensions and space velocities . . . . .	72
3.9	Discussion . . . . .	75
3.9.1	The mass-radius diagram . . . . .	75
3.9.2	The mass-T <sub>eff</sub> diagram . . . . .	78
3.9.3	A mass-radius-period relationship? . . . . .	80
3.10	Conclusions . . . . .	83
<b>Chapter 4. Eclipsing M-dwarf binaries in WTS</b>		<b>95</b>
4.1	Introduction . . . . .	96
4.2	Motivation . . . . .	97
4.2.1	The AML timescale argument . . . . .	97
4.2.2	Periods at contact . . . . .	101
4.3	Observations and data reduction . . . . .	102
4.3.1	WTS J band time-series photometry . . . . .	102
4.3.2	INT broad-band photometry . . . . .	103
4.3.3	Low resolution spectroscopy . . . . .	104
4.4	Sample selection . . . . .	104
4.4.1	Variability statistic . . . . .	104
4.4.2	Orbital period determination . . . . .	105
4.4.3	Selection of the final sample . . . . .	106
4.5	Characterisation of the eclipsing binary systems . . . . .	107
4.5.1	Binary classification . . . . .	107
4.5.2	The effective temperature . . . . .	110
4.6	Results & Discussion . . . . .	111
4.6.1	Comparison with previous studies . . . . .	114
4.6.2	The period-colour relation . . . . .	114
4.6.3	Constraints to binary evolution scenarios . . . . .	116

---

4.7	Conclusion . . . . .	117
<b>Chapter 5. Low-mass ratio M-dwarf binary</b>		<b>129</b>
5.1	Introduction . . . . .	130
5.2	Observations & Data Reduction . . . . .	132
5.2.1	WTS J-band time series photometry . . . . .	132
5.2.2	INT i'-band follow-up photometry . . . . .	132
5.2.3	Low resolution spectroscopy . . . . .	135
5.2.4	WHT ISIS optical spectroscopy . . . . .	135
5.2.5	GEMINI/GNIRS infra-red spectroscopy . . . . .	138
5.3	Spectroscopic analysis . . . . .	139
5.3.1	Analysis of the low resolution ISIS spectrum . . . . .	139
5.3.2	Radial velocities . . . . .	141
5.4	Lightcurve modelling . . . . .	143
5.4.1	WFCAM J-band photometry . . . . .	143
5.4.2	INT i'-band photometry . . . . .	147
5.4.3	Stellar Masses and Radii . . . . .	148
5.5	Discussion . . . . .	148
5.5.1	The mass-ratio distribution . . . . .	149
5.5.2	The mass-radius relation for M-dwarfs . . . . .	150
5.5.3	Non-synchronous rotation? . . . . .	154
5.6	Conclusion . . . . .	155
5.7	Acknowledgements . . . . .	156
<b>Nederlandse samenvatting</b>		<b>163</b>
<b>Curriculum Vitae</b>		<b>171</b>
<b>Nawoord</b>		<b>173</b>



---

# Chapter 1

---

## Introduction

The advent of infra-red-sensitive astronomical detectors and arrays has, over the last few decades, led to a revived interest into the fundamental properties of M-dwarf stars. This thesis presents the first results from the Wide Field Camera Transit Survey (WTS), a dedicated and ongoing photometric infra-red survey, that hunts for low-mass binaries and planetary companions around M-dwarfs. The goal of this work is, by investigating M-dwarfs in eclipsing binary systems, to gain a better understanding of how low-mass stars are formed and how they evolve. In this introduction we first describe some of the general characteristics of M-dwarf stars (Section 1.1), followed by a discussion in Section 1.2 on the importance of M-dwarf studies. Section 1.3 introduces possible low-mass binary formation scenarios and potential observational constraints on these theories. In Section 1.4 the importance of close (eclipsing) M-dwarf systems is emphasized in relation to existing theories and simulations of binary formation and evolution. Current discrepancies of fundamental observed M-dwarf properties with evolution models are reviewed in Section 1.5, which pose a challenge to M-dwarf planet characterisation efforts, which are discussed in Section 1.6. The observational data for this thesis, high quality infra-red light curves from the WTS, are detailed in Section 1.7. We end the introduction with a short outline of the various thesis chapters (Section 1.8) and a last section (Section 1.9) on possible future work.

### 1.1 M-dwarfs - general characteristics

M-dwarfs are the smallest hydrogen burning stars that live on the stellar main sequence. They bridge the mass gap between cool deuterium-burning brown dwarfs and solar-like stars, and range in mass from  $0.07\text{-}0.08M_{\odot}$  to  $0.60\text{-}0.65M_{\odot}$  (Baraffe & Chabrier 1996). M-dwarfs are highly abundant throughout our Milky Way, e.g. Henry et al. (2007) find that M-dwarfs represent  $>70\%$  of all stars in number. Of the 77 known stars in 5 parsec (pc) around our Sun<sup>1</sup>, 62.3% are M-dwarfs, 5.2% brown dwarfs and only 2.6% are solar type (spectral class G) stars. The closest M-dwarf is Proxima Centauri, at a distance of only 1.3 pc. Yet, ironically, of all the  $\sim 6000$  stars accessible to the naked eye, none are M-dwarfs. The brightest observed M-dwarf is Lacaille 8760 (AX Microscopii; distance 12.9 pc) at V band magnitude 6.69. This is because M-dwarfs are intrinsically faint, with luminosities ranging from  $\sim 7\%$  to only 0.015% that of the Sun (Baraffe & Chabrier 1996). M-dwarfs are brightest at (infra)red wavelengths explaining why, historically, they were also difficult to access with telescopes.

The observed atmospheric temperatures of M-dwarfs range from  $\sim 2000$  to  $\sim 3900$  K, which is low enough for simple molecules (e.g. Titanium Oxide, TiO and water, H<sub>2</sub>O) to be stable

---

<sup>1</sup>RECONS (REsearch Consortium On Nearby Stars) census of all known objects within 10 pc, 01 January 2012, <http://www.chara.gsu.edu/RECONS/>

and provide significant absorption in the optical and infra-red parts of their spectra. The M-dwarf spectral class (which ranges from M0 to M9) is actually defined by the presence of TiO absorption bands in the spectrum. An important difference between M-dwarfs and solar-type stars is in the structure of their atmospheres. Models indicate that stars with mass less than 35% of the Sun are fully convective, and higher mass M-dwarfs have a radiative core. This core increases in size from  $\sim 50\%$  of  $R_*$  for a  $0.4 M_\odot$  M-dwarf to  $\sim 65\%$  for  $0.6 M_\odot$ , and to  $\sim 70\%$  for a solar type star (Chabrier & Baraffe 1997). Convection occurs because the M-dwarf interior has a high density compared to the temperature and is consequently opaque to radiation. M-dwarfs are very slow hydrogen burners because their core temperature is relatively low ( $< 10^7$  K) and the resulting helium is constantly remixed by the convection. This means that M-dwarfs have a nearly constant luminosity and spectral type while on the main sequence and that no M-dwarf has yet evolved from the main sequence since the Big Bang.

Many M-dwarfs are chromospherically and magnetically active, and this activity manifests itself by flares, ejections of mass and periodic brightness variations caused by rotational modulation of cool surface star spots. In Sun-like stars, with masses between about 0.35 and  $1.3 M_\odot$ , the dynamo that gives rise to this activity (the  $\alpha\Omega$  – dynamo) is believed to be generated at the thin boundary between the convective envelope and radiative core, the *tachocline* (e.g. Parker 1993; Charbonneau & MacGregor 1997; Thompson et al. 2003). Here, magnetic fields are generated by the combined action of differential rotation (the  $\Omega$  effect) and the twisting of field lines by cyclonic convection (the  $\alpha$  effect) (e.g. Parker 1955; Steenbeck 1966; Leighton 1969). Both of these effects depend on the rotation - the  $\Omega$ -effect because more rapidly rotating stars are expected to possess stronger internal angular velocity contrasts (Brown et al. 2008) and the  $\alpha$ -effect because it depends on the helicity of the convection which itself senses the overall rotation rate. For stars with masses less than  $\sim 0.35 M_\odot$  (spectral types later than  $\sim M3.5$ ), which are fully convective, the tachocline disappears. However, activity has been observed in such stars, suggesting a different dynamo mechanism (e.g. Rockenfeller, Bailer-Jones & Mundt 2006; Reiners & Basri 2008). Indeed, spectropolarimetric studies of fully convective M-dwarfs have shown that the magnetic field morphology appears to change with spectral type (e.g. Morin 2008; 2010). These findings have led to an alternative dynamo, the  $\alpha^2$ -dynamo, where turbulence and cyclonic convection play the main role (e.g. Chabrier & Küker 2006). West et al. (2008) find that magnetic activity is a function of subtype; earlier M-dwarf types are generally less active than late types (unless part of a close binary system). Also, they find that M-dwarf activity declines as a function of age, but extends with later subclass; activity life times in M0 dwarfs are  $0.8_{-0.5}^{+0.5}$  Gyr, and increase to as much as  $8.0_{-1.0}^{+0.5}$  Gyr for M7 type stars.

## 1.2 M-dwarfs - why study them?

M-dwarfs are very interesting objects to study for several reasons:

- M-dwarfs are an ideal stellar population for studying the structure and evolution of our Galaxy (e.g. Wielen 1977; Reid et al. 1995; Bochanski et al. 2007), and the star-formation history in the local Solar neighbourhood (e.g. Gizis et al. 2002), because of their ubiquity and very long main-sequence lifetimes. Chromospheric activity decays on time-scales of billions of years, which is a time-scale relevant for studies of Galactic

evolution. As emphasised by e.g. Reid et al. (1999), the local star formation history is one of the major requirements for modelling of the sub-stellar mass function.

- M-dwarfs also encompass many important regions of parameter space of stellar structure, not only the onset of convection, but also of significant electron degeneracy in the core, and the formation of dust and subsequent depletion of metals onto dust grains in the stellar atmosphere. Note furthermore that the equation of state for M-dwarfs, which determines internal structure and forms an important ingredient for stellar atmosphere models (e.g. Chabrier & Baraffe 1996), may even need to be (slightly) revised (e.g. Torres & Ribas 2002; Lopez-Morales 2004). Such a revision may (partially) remedy the mismatch between observed fundamental M-dwarf properties and models, but remains an interesting open question (e.g. Irwin et al. 2011).
- M-dwarfs form important ingredients for dynamical stellar evolution simulations by connecting solar-type stars and brown dwarfs, which are two mass regions that appear to have very different binary fractions. The change of these multiplicity characteristics throughout the M-dwarf regime is important to understand the evolution of both low-mass stars and brown dwarfs and their formation environment (e.g. Goodwin et al. 2007; Burgasser et al. 2007; Parker et al. 2009). Also, the observed distributions of orbital period and mass-ratios of M-dwarf binaries are constraints to models of star-formation and dynamical evolution (e.g. Bate et al. 2012). See also chapters 4 and 5.
- Exoplanet detection techniques are significantly more sensitive to planets orbiting M-dwarfs than solar-type stars, making them sensitive to rocky planets in the habitable zone. In addition they occupy a different place in parameter space and are therefore important probes for planet formation theories (see also section 1.6).
- There are still apparent discrepancies between theoretical stellar structure models for M-dwarfs and the observed fundamental M-dwarf properties (mass, luminosity, radius, effective temperature), in addition to the lack of dynamical mass-radius measurements for mid-to-late type M-dwarfs (mass below  $0.2 M_{\odot}$ ). See also chapters 3 and 5 and section 1.5.

## 1.3 Low-mass binary formation

### 1.3.1 Observational constraints

Observations of both young clusters and the field show that a significant fraction of stars are formed as multiple systems (e.g. Duquennoy & Mayor 1991; Goodwin et al. 2007; Duchene et al. 2007). Binary systems dominate the total number of multiple systems, with the relative ratios of binary, triple and higher order systems has been observed to be 75:18:4 (Duquennoy & Mayor 1991; Tokovinin & Smekhov 2002). Multiplicity characteristics provide some of the strongest observational constraints on theoretical models and numerical simulations that aim to describe star forming clusters (e.g. Clarke 2007). Any model has to be able to reproduce at the same time both the observed binary/multiple fraction amongst stars and the distributions

of mass-ratio and separation, and furthermore provide an explanation on how these properties depend on primary mass.

There is strong observational evidence that most binary formation occurs shortly after stellar birth, because the binary fraction for pre-main sequence stars has been found to be higher than that for main sequence stars (Mathieu 1994; Kraus et al. 2011). It is therefore unlikely that many new binary systems are formed on the main sequence, e.g. by capture. Recent observational work from Raghavan et al. (2010) shows that roughly half of all sun-like stars (spectral type F6-K3) are in binary or higher order multiple systems. Current data also suggests that around O and B type stars stellar companions are ubiquitous, indicating that nearly all high-mass stars are part of either a binary or a multiple system (e.g. Zinnecker & Yorke 2007; Sana et al. 2012). For M-dwarfs, the fraction of multiple stars is smaller at 26-42%, when considering data over the full range of orbital periods (Delfosse et al. 2004; Reid & Gizis 1997; Fischer & Marcy 1992). For very low mass stars (VLMS;  $M < 0.1M_{\odot}$ ) and brown dwarfs (BD), the binary frequency is only 10-30% (e.g. Bouy et al. 2003; Reid et al. 2008; Goldman et al. 2008). Observations also suggest that the mass ratio distribution of VLMSs and BDs are skewed towards equal mass binaries, whereas solar-like stars have a flatter distribution in mass ratio  $q(= M_2/M_1)$  (e.g. Burgasser et al. 2007). For M-dwarfs, Delfosse et al. (2004) argue that there is a significant difference in the mass ratio distribution between short ( $P < 50$  d) and long period M-dwarf binaries, with a strong preference for nearly equal masses ('twins') for the short orbits.

### 1.3.2 Fragmentation scenarios

Most binaries are thought to be formed by fragmentation, either of turbulent collapsing molecular cloud cores or later on in circumstellar disks. The early idea that binaries could be formed from the fision of a rotating protostar was abandoned after several hydrodynamical simulations showed that this process is not likely to occur (e.g. Bodenheimer et al. 2000). It is also believed that binaries accrete mass from their envelope via a circumbinary disk (see Figure 1.1).

The turbulent cloud scenario (a.k.a. 'prompt' fragmentation) says that non-linear perturbations within a star forming core cause a sub-region to become over-dense and collapse, which ultimately grows to become a second condensation in the cloud (a companion). Alternatively, turbulent motions of the gas (either induced by the shearing motions of stars within our Galaxy or from stellar feedback), can lead to the formation of filamentary structures, which then fragment into multiple systems. It is thought that the evolution of a gas cloud can be divided into four distinct phases, which all have a characteristic gas number density  $n_c$  that affects the scale at which binary formation through fragmentation occurs (the Jeans length): the *isothermal* phase ( $n_c < 10^{11} \text{cm}^{-3}$ ), the *adiabatic* phase ( $10^{11} < n_c < 10^{16} \text{cm}^{-3}$ ) when the gas in the centre of the cloud becomes optically thick, the *second collapse* phase ( $10^{16} < n_c < 10^{21} \text{cm}^{-3}$ ) when molecular hydrogen is dissociated and the cloud collapses rapidly, and the *protostellar* phase ( $n_c > 10^{21} \text{cm}^{-3}$ ) when the hydrogen is fully dissociated, the collapses adiabatically, and a protostar is formed. From observations, it is expected that fragmentation in the isothermal phase rarely occurs (e.g. Kandori et al. 2005; Tachihara et al. 2002). Simulations and observations suggest that a major fraction of binary forming molecular clouds might fragment in the adiabatic phase (e.g. Caselli et al. 2002; Matsumoto & Hanawa 2003; Cha & Whitworth 2003). The typical fragment separation in the isothermal and adiabatic phases are  $10$ - $10^4$  AU, and it is expected that these will evolve to wide binary systems. We discuss possible formation

mechanisms for closer binaries in Section 1.4.

Binaries could also form at later stages of the star formation process when a massive circumstellar disk around a protostar becomes unstable and fragments into one or more companions (e.g. Adams 1989; Laughlin & Bodenheimer 1994; Bonnell 1994; ). Such instabilities may be caused by close encounters with other stars or disks or without external interactions. Previous analytic work and numerical simulations suggested that disks around low-mass stars will be stable (Matzner & Levin 2005; Boley et al. 2007; Cai et al. 2008). Moreover, simulations by Offner (2010) suggested that such stars are not expected to fragment to multiple systems within disks, and turbulent fragmentation is the dominant formation mechanism. An important requirement for binary formation via disk fragmentation is that the disk is massive enough ( $\sim 0.1M_{\odot}$ ), indicating that it may be difficult to form M-dwarf companions in this way.

Generally speaking, the amount of fragmentation appears to depend on the amount of initial turbulence in the core. Two important parameters controlling when and whether this happens are the rate of rotation and the strength of the magnetic field in the initial cloud (e.g. Machida et al. 2008). Faster cloud rotation promotes fragmentation, while a stronger magnetic field delays or in some cases suppresses fragmentation through all phases of cloud evolution. Kratter et al. (2008; 2010) show that whether a disk will fragment or not can naturally be described by the two variables  $\xi$  and  $\Gamma$ . Here,  $\xi$  relates the accretion rate of material from the cloud onto the disk, whereas  $\Gamma$  measures the fraction by which accretion changes the total disk plus star mass per orbit of the disk. This indicates that high-mass stars, which generally have higher accretion, are likely to live in the disk fragmentation regime, whereas low-mass binaries have low accretion such that they may still form by turbulent fragmentation, but are unlikely to form by disk fragmentation.

## 1.4 Close binaries

### 1.4.1 Close versus wide

It is currently uncertain how and in what environments close low-mass binary systems can form, and through what physical mechanism they evolve. In this thesis we mainly discuss M-dwarf binaries that are in the eclipsing regime (roughly speaking periods shorter than 50 d), which are relatively easy to access using current radial velocity instruments. As such, they are a reliable source of mass measurements, which is the most fundamental parameter defining stars. For a binary with a system mass of  $1M_{\odot}$ , an orbital period of 10 d corresponds to a component separation of  $\sim 0.1$  AU. In this thesis, we consider M-dwarf binaries with orbital periods as low as 0.1-0.2 d, corresponding to separations of  $\sim 0.003$ -0.01 AU. Which ever way they form, it is likely that close binary formation is intimately related to significant orbital migration after core fragmentation. This is because the radius of a sub-solar mass pre-main sequence star is of the order 2-3  $R_{\odot}$  (Baraffe et al. 1998), indicating that a young binary system is restricted in its birth separation (see also chapter 4). It is difficult to reveal the earliest stages of binary formation observationally because these very young objects are deeply embedded, and formation processes are expected to be extremely short.

To properly investigate what mechanisms and processes influence binary star formation and set the observed multiplicity characteristics of stars, studies have resorted to numerical simula-

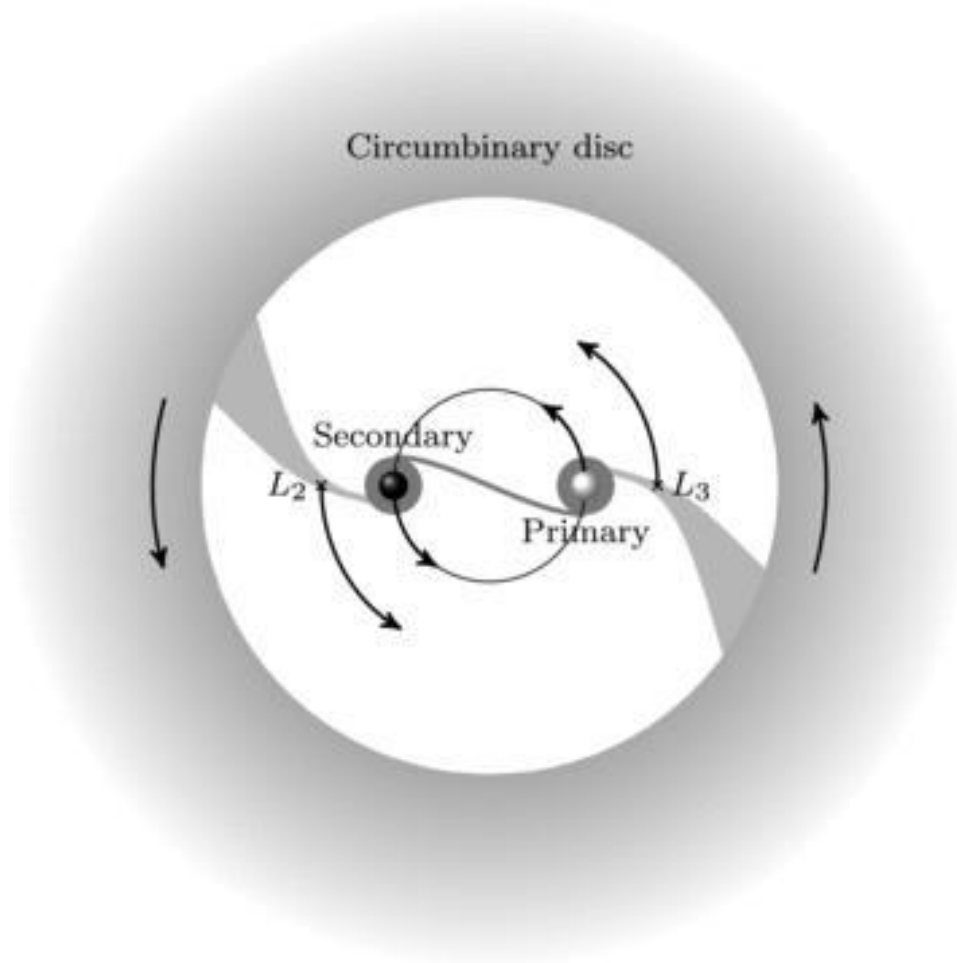


**Figure 1.1** — Diagram showing a gravitationally bound young binary system on a circular orbit surrounded by a circumbinary disc (adapted from de Val-Borro et al. 2011). The motion of the binary creates a central cavity within the disc. Material from the circumbinary disks can be accreted onto the stars, via circumstellar disks around one or both components, through the Lagrange points  $L_2$  and  $L_3$ .

tions. Machida et al. (2008) have run 147 magneto-hydrodynamic models (MHD) for isolated cloud evolution and binary fragmentation at various values of magnetic field, turbulence and rotation rate. They find that clouds with large ratio of rotational to magnetic energy yield fragmentation in the adiabatic phase, which gives 3-300 AU fragments (wide binaries). Moderate rotation to magnetic energy models induce fragmentation during the latest stages of collapse and produce  $<0.3$  AU fragments (close binaries), whereas high magnetic field models generally produce single stars. This is illustrated in Figure 1.2.

Bate et al. (2009,2012) present the largest hydrodynamic simulation of binary formation to date, that were performed on a cloud of  $500M_{\odot}$  mass, and compare the properties of the formed binary systems to results from observational surveys. Two major conclusions from their work are relevant to this thesis. First of all, they find that for decreasing mass primaries the binary frequency steeply decreases, in line with current observations. Secondly, there is a clear correlation of mass ratio with orbital period, such that closer binaries have a significantly greater fraction of near-twin systems. Such trends are expected because high angular momentum gas is

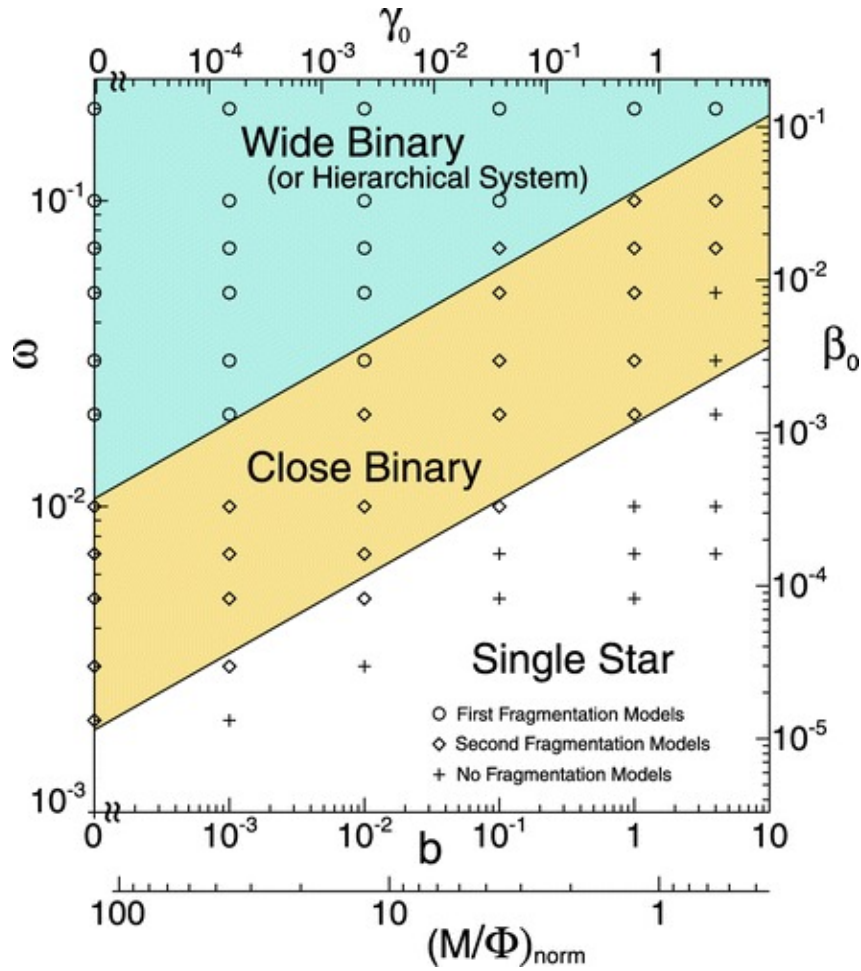


**Figure 1.2** — *The physical conditions in a star forming cloud determining the occurrence of fragmentation, as obtained in the numerical MHD simulations of Machida et al. (2008) of 147 model clouds. Open circles indicate models where fragmentation occurs in the adiabatic phase, and fragments have separations in the range of 3-300 AU (wide binaries). Open diamonds indicate models that have fragmented during the second collapse phase, with separations 0.007-0.3 AU (close binaries). Crosses indicate models that have not fragmented (i.e. formed single stars). The parameter  $\omega$  represents cloud rotation,  $\beta_0$  and  $\gamma_0$  the ratios of rotational and magnetic energy to the gravitational energy, and  $b$  traces the strength of the magnetic field.*

preferentially captured by the companion in a close binary system according to Bate & Bonnell (1997), and dynamical interactions can effectively remove the lowest mass stars and break low-mass binaries (e.g. Duchene et al. 2007; further discussed in chapter 5). One observational probe of the validity of such simulations is to determine the frequency of highly unequal-mass stellar binary systems with an M-dwarf primary. We provide the discovery of one such system in chapter 5. Another interesting reason for studying unequal-mass M-dwarf binaries is that there is a current debate about the physics of mass-accretion onto binaries. Work from e.g. de Val-Borro (2011) suggests that material from the circumbinary disk can decrease the mass-ratio, in contrast with expectations from e.g. Bate et al. (2012).

### 1.4.2 Close binary types

Close (eclipsing) binary stars come in three distinct flavours depending on their mass ratio, orbital semi-major axis  $a$ , and stellar radii ( $R_{1,2}$ ): *detached*, *semi-detached*, and *contact*. Each of these classes has a corresponding light curve shape which is influenced by the binary orbital inclination  $i$  (which determines the amplitude of the eclipses), the ratio of their effective temperatures and the ratio of their radii (which determine the ratio of primary to secondary eclipse depth). There is a critical tear-shaped equipotential surface beyond which matter is being transferred to the companion, the stellar Roche lobe. According to Eggleton (1983) the geometry of the Roche lobe can be approximately expressed as function of  $q$ :

$$r_1/a = \frac{0.49q^{2/3}}{0.6q^{2/3} + \ln(1 + q^{1/3})}, \quad (1.1)$$

which is a rising function with increasing  $q$ . Detached systems are well-separated, far from Roche lobe filling, and nearly spherical. In semi-detached systems, one of the Roche lobes in the binary has filled up, and the stars are noticeably non-spherical. Gas may be transferred to the companion. In a contact system, both components of the binary have filled their Roche lobes, and the two stars form a common envelope. The ultimate fate of such binaries is likely a merger between the two stars. Because M-dwarfs have very long lifetimes on the main sequence and their radii are relatively constant, the main reason for Roche lobe filling in M-dwarf binary systems is the shrinking of their orbits with time (decreasing  $a$ ; see chapter 4). In chapter 3 of this thesis we will describe a survey for detached M-dwarf binaries, whereas we also focus on (near-) contact binaries in chapter 4.

### 1.4.3 The close binary period distribution

The binary separation distribution has been observed to be very wide, ranging from 0.01 to  $\sim 10^4$  AU (0.01 to 5000 AU for the pre-main sequence, e.g. Mathieu 1994; Kraus et al. 2011). In Figure 1.3 we show the period distribution of eclipsing binaries (of various spectral types) in the OGLE II Survey (Devor et al. 2005; grey filled bars). Detached systems are indicated as filled black bars. The drop-off at longer periods is likely due to selection effects, but the steep drop at the short end appears to be real. A similar steep drop around 0.22 d is also noted by Norton et al. (2011) using data from the WASP Survey. A popular explanation in literature for this cut-off is that the orbital evolution of close binaries is driven by angular momentum loss on the stellar main-sequence (e.g. Stepien 1995;2006;2011). Here, binaries are expected to lose angular momentum through magnetic stellar winds. In this theory, it is predicted that no binary system with a total mass of less than 1.0-1.2  $M_{\odot}$  (i.e. M-dwarf systems) can evolve to a contact state within the given age of our Universe by losing angular momentum. As we will see later on, 0.22 d corresponds to a contact K-type binary system. An alternative model was recently put forward by Jiang et al. (2012), who explain the apparent dearth of contact M-dwarfs to an instability of mass-transfer when the components of M-dwarf binaries come close. In chapter 4, we will confront these models with our new observations of M-dwarfs.

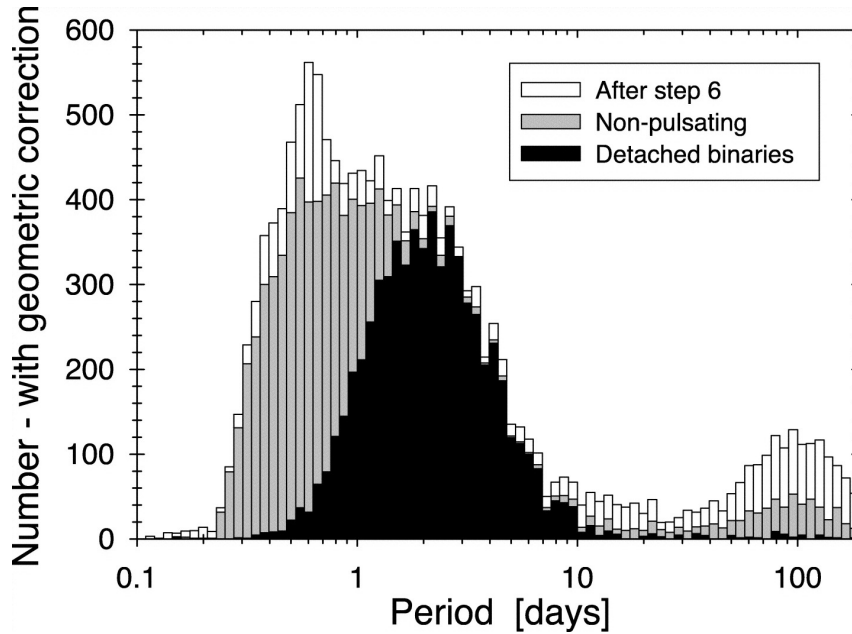


**Figure 1.3** — *The period distribution of eclipsing binary in the OGLE II Survey (grey filled bars), adapted from Devor et al. (2005).*

## 1.5 The mass-radius relation for M-dwarfs

Despite the abundance of M-dwarfs in our Milky Way there is still significant debate about even their most fundamental stellar parameters (see also thesis chapters 3,4, and 5). Precise knowledge of these parameters is not only vital to constrain evolution models for this important Galactic stellar population, but also for the accurate characterisation of their planetary companions, which provide crucial tests of planet formation theories. Accurate measurements of host star mass, radius, luminosity, effective temperature and age are all important inputs to determine exoplanet mass (density), atmospheric structure, composition and evolution. However, current stellar evolution models are unable to accurately reproduce all of the observed properties of M-dwarf stars (e.g. Hillenbrand & White 2004; Lopez-Morales & Ribas 2005), unlike most of their solar-type analogues. Detached double-lined eclipsing binaries provide the most accurate, precise and direct measurements of fundamental low-mass star properties without having to rely on model predictions. Uncertainties on stellar masses and radii can be pushed down as low as 0.5% (e.g. Andersen 1991; Morales et al. 2009). Furthermore, the coevality and shared metallicity of M-dwarf binary stars, due to their common origin, provide extra constraints on evolution models. These observations have revealed that stars in binaries have radii that are significantly larger than models predict (radii inflated by 5-10%) and effective temperatures lower by 3-5% (Torres & Ribas 2002; Lopez-Morales & Ribas 2005; Ribas 2006; Morales et al. 2010; Torres et al. 2010; Kraus et al. 2011).

Two different theories have been proposed to explain the observed discrepancies. The first theory argues that the activity of the host star, induced by fast rotation and/or strong magnetic fields, inhibits convection, which forces the star to inflate in order to retain hydrostatic equilibrium (e.g. Mullan & MacDonald 2001; Ribas 2006; Chabrier et al. 2007). Also, higher stellar activity is correlated with more cool star spots on the stellar surface which further decrease

convective efficiency and add an extra systematic source of noise to light curve solutions of eclipsing binaries. Morales et al. (2010) show that the effects of surface spots could account for uncertainties as high as 6% in derived stellar radii. It is also predicted that radius inflation is correlated with binary orbital period, such that close binaries, which are expected to be tidally synchronised and fast rotating, are more inflated than wider binaries (e.g. Kraus et al. 2011). The recently discovered M-dwarfs in Irwin et al. (2011) and Doyle et al. (2011), both with long  $\sim 41$  d orbits and likely inactive, are however significantly inflated, questioning the proposed period-activity relation. We further discuss possible trends in chapter 3 where we describe a new infra-red survey hunting for detached M-dwarf eclipsing binary systems. The second theory identified higher metallicity as the cause of the radius inflation, using interferometry to measure the radii of inactive single stars (Berger et al. 2006; Lopez-Morales 2007). An increasing abundance of metals would have the effect of enhancing the number density of molecular compounds in the atmospheres of the stars, making it harder for radiation to escape, thus inflating their radii and lowering their effective temperature. However, whereas these studies find that inactive single stars with inflated radii are on average metal-rich, no such correlation appears to exist for active single stars (see also Demory et al. 2009). Given the fact that West et al. (2008) find an activity fraction for (single) M4-M9 stars, which are the preferred hunting ground for Earth-like planets (see section 1.6), of at least 40-80%, it is vital to understand what physical mechanism(s) cause the discrepancies.

A sufficiently large sample of accurate measurements using M-dwarf eclipsing binaries, incorporating both fully and partially convective stars, is a key ingredient to unravel the effects of activity, rotation and metallicity on the observed stellar properties. This is the main motivation for setting up a photometric survey in the near-infrared (see chapters 3,4 and 5) to find M-dwarf binaries.

## 1.6 Planets around M-dwarfs

M-dwarfs are excellent targets to hunt for planets using the transit method. By fitting a transit light curve, the inclination of the planetary orbit can be determined directly, and the  $\sin(i)$  degeneracy in planet mass, that limits planet searches utilising the radial velocity method, be resolved. Also, the planet to star size ratio can be determined easily. Because the planet to star size ratio is significantly larger for M-dwarfs with respect to solar type hosts, deeper transits are possible, making the discovery of small planets feasible, even from the ground. For example, whereas 1% deep transits are expected for a Jupiter transiting a solar type host, the same transit depth corresponds to a Neptune sized planet transiting a  $\sim 0.35R_{\odot}$  star, and to an Earth transiting a  $0.1R_{\odot}$  host. Also, the gravitational pull of any planet on its host star is in theory easier to measure: an Earth around a  $0.1M_{\odot}$  M-dwarf induces a factor  $\sim 5$  higher radial velocity amplitude on its host compared to a solar-type star for the same orbital period. Because of their low luminosities, M-dwarfs have habitable zones significantly closer to their host stars than solar type stars. In fact, for M5 or later hosts this zone extends to as low as 0.05 AU ( $\sim 10$  d; e.g. Kaltenegger & Traub 2009), which is within reach of current ground-based efforts, although planets orbiting so close to their parent star may be tidally locked, which could hamper life to develop. M-dwarfs are potential test cases to verify the predictions from planet formation theories. The theory of core accretion (e.g. Laughlin et al. 2004) makes the clear prediction that

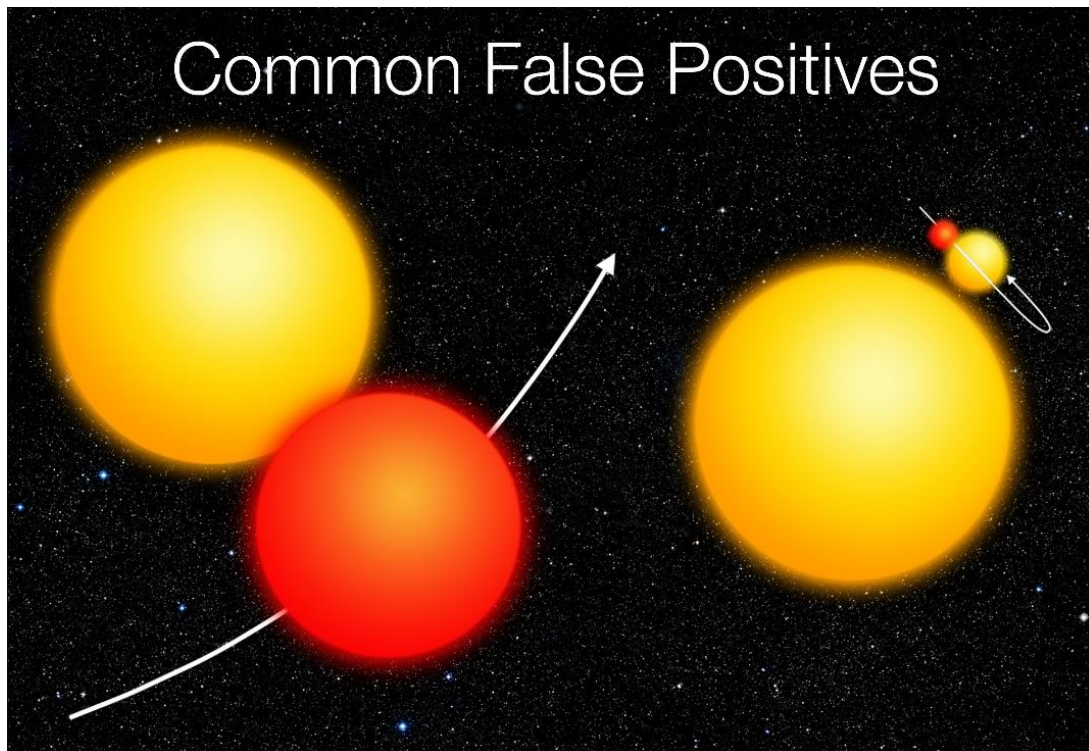


**Figure 1.4** — *Common false-positive scenarios in a transit survey for exoplanets. The left part of the figure shows a pair of grazing stellar eclipsing binaries, which can mimic the shallow eclipses of a genuine planet. Another possibility is a small star transiting a giant or another large main-sequence star. The third scenario is that of a third star blended with a background stellar binary (or a foreground binary blended with a background star), diluting the transit depth.*

Jovian planets should be rare around M-dwarfs, whereas Neptune-like and terrestrial planets may be common, which is something that (ground-based transit) observations could confirm.

There are currently only few transiting planet confirmations around M-dwarf hosts and even fewer surveys actively hunting for them. The M-*Earth* survey (Charbonneau et al. 2009) targets 2000 bright late type M-dwarfs, and has discovered one Super Earth planet transiting a M4.5V host (GJ1412b). The Kepler Mission (Borucki et al. 1997) presents several M-dwarf planet candidates from a sample comprising 1081 cool stars, of which one has received radial velocity follow-up; KOI-254 is a hot Jupiter transiting a  $0.59M_{\odot}$  host (Johnson et al. 2012). Two planets, a hot Neptune and a hot Uranus, have been observed to transit the M-dwarf hosts stars in GJ436 and GJ3470b (Gillon et al. 2007; Bonfils et al. 2012).

An important observational problem related to transit surveys is the occurrence of false-positives. Firstly, correlated noise (from the telescope or intrinsic variability of the host star) can mimic planet signals on the typical few hour time-scales expected for transiting planets. Another concern are contaminating stellar eclipsing binaries. In Figure 1.4 we show common scenarios involving such binaries. The left part of the figure shows the case of two grazing main-sequence stars mimicking the shallow eclipses of a planet. Another possibility is that of a small star (e.g. an M-dwarf) transiting an early type main-sequence star or giant. Also, the deep eclipses of a binary could be diluted by a third star, either in the background or in the foreground. We discuss in chapter 2 a method that could reduce the amount of follow-up

time needed for candidate verification, by directly fitting the discovery light curves with simple models that incorporate third light.

## 1.7 WFCAM Transit Survey

In this thesis we use data from the Wide Field Camera Transit Survey (WTS), which is a near-infra-red photometric monitoring campaign currently running on the 3.8m United Kingdom Infrared Telescope (UKIRT). As such, it is the first published survey to hunt for planets around M-dwarfs in the infra-red. In the WTS J-band, the brightness of M-dwarfs is significantly increased, because  $<0.6M_{\odot}$  stars have their peak in the spectral energy distribution at these wavelengths. For example, a M4 star ( $0.2M_{\odot}$ ) in J-band is  $\sim 4$  mag brighter than in V band and  $\sim 1.5$  mag brighter than in I-band. Secondly, because our telescope aperture is considerably larger than that used in regular (optical) transit surveys, we retain sufficient photometric precision for large samples of M-dwarfs, despite the fact that we run a deep, small solid angle, survey on stars that are on average significantly fainter. Also, in the infra-red, the contrast of cool star spots is more favourable than in the optical, which indicates that systematic effects from spot modulation on derived light curve parameters are significantly reduced. The WTS runs as a flexible queue-schedule program on UKIRT, which was designed such that it could profit from sub-optimal observing conditions when other surveys do not observe. The WTS targets four rectangular regions of sky, 1.5 square degree each, which were chosen to allow continuous accessibility throughout the year. These four fields were named the WTS 19hr, 17hr, 07hr and the 3hr fields. By pointing slightly outside the Galactic plane, dwarf numbers are optimised, while contamination from red giant stars and blended light sources is reduced. Light curves from the WTS have a root mean square scatter of  $<1\%$  between  $13 < J < 16$ , and a few mmag at the bright end of the survey, which indicates sufficient precision for the detection of Neptune sized planets around mid M-dwarfs and Jupiters around early-to-late type M-dwarfs.

One other interesting aspect of the Survey is that it has the potential to discover considerable numbers of (very) low mass eclipsing binaries, down to fainter magnitudes due to the deeper eclipses of stellar binaries. Therefore, our data also have potential for constraining the currently uncertain formation and evolution mechanisms of M-dwarfs down to the hydrogen burning limit, by studying the occurrence frequency of close low-mass binaries, with orbital periods from  $\sim 10$  d down to the regime of M-dwarf contact-systems (which cover orbits as short as 0.1 days; see chapter 4). The brightest of these binaries are potential targets for detailed follow-up to determine their masses, radii and temperatures, and calibrate low-mass stellar evolution model predictions (as presented in chapters 3 and 5). The Survey targets  $\sim 6000$  M-dwarfs between  $13 < J < 16$  for all four fields, and over 10000 M-dwarfs up to  $J=18$  (which forms the target population for chapter 4).

As per May 18, 2012, sufficient epochs ( $\sim 1000$ ) were obtained for one target field (the 19hr field). At the time of writing of this thesis, 2 planets were discovered in the WTS, one is an inflated hot Jupiter planet around a late F-type main sequence star in a 3.35 d orbit (Cappetta et al. 2011), the other is a Jupiter around a K-type star in a very short orbit of 1.05 d (Birkby et al. 2012; in prep). In the current data, no planets around M-dwarf hosts have yet been verified by follow-up. This preliminary null-detection has been interpreted in terms of the predicted occurrence of giant planets around M-dwarfs in Kovacs et al. (2012, submitted).

## 1.8 This thesis

In **chapter 2** we present a new method to eliminate false-positives from a exoplanet candidate list through direct fitting of their light curves, with the aim to minimise the vast amount of time that is spent to verify these candidates. We simulate light curves of stellar blends and transiting planet systems and find that blend scenarios can be excluded for transiting systems with low impact parameter. At high impact parameter blended and non-blended systems cannot be distinguished, meaning that they can only be eliminated by applying a cut in impact parameter. We apply our method on space-based data from the CoRoT satellite and identify the good candidates in this dataset. We argue that this method could be used on the Kepler database (e.g. Batalha et al. 2010) to study the fraction of real planets in this candidate list.

Using the high-precision infra-red light curves of the WFCAM Transit Survey, we present in **chapter 3** the discovery of 16 detached M-dwarf eclipsing binaries and provide a detailed characterisation of three of them. The radii of our binaries are inflated by 3-12% with respect to model predictions, in agreement with observed trends, despite a lower expected systematic contribution from cool star spots in the infra-red. We find there is no statistically significant evidence for radius inflation for longer orbital periods, in contrast with previous findings. Such measurements are not only important to understand the most abundant stellar population of our Milky Way, but also to allow detailed characterisation of their planetary companions.

In **chapter 4** we report on the discovery of four ultra-short period ( $P < 0.18$  d) eclipsing M-dwarf binaries from an extensive search of over 10 000 M-dwarfs in the WTS, which have orbital periods that are significantly shorter than that of any other known main-sequence binary system, and below the sharp cut-off at  $\sim 0.22$  d as seen in earlier-type binaries. Our record holder is a binary of near-twin M4 stars in a tight 2.5 hr orbit. Our detections pose a direct challenge to popular theories that explain the evolution of short-period binaries by loss of angular momentum through magnetized winds, or by unstable mass-transfer. We argue that the evolutionary time-scales of M-dwarf binaries may have been overestimated, e.g. due to a higher magnetic activity or different formation mechanism.

In **chapter 5** we present the discovery of a highly unequal-mass ( $q=0.27$ ) eclipsing M-dwarf binary, with masses  $0.505$  and  $0.139 M_{\odot}$ , providing a unique constraint of binary star formation theory and of evolutionary models for low-mass stars. The cool companion of the binary is in a very sparsely sampled and important M-dwarf mass regime for studies of Earth-like planets requiring accurate calibration of their host star radii and masses. We compare our findings with star formation simulations that suggest that close unequal M-dwarf binaries are rare, and model stellar atmosphere predictions for the measured binary properties.

## 1.9 Future work

We here discuss shortly what interesting follow-up work could be performed. The method to reduce exoplanet false-positive scenarios in Chapter 2 will be validated on the high-quality light curves of the Kepler mission, which is now starting to build an archive with rejected candidates. Currently, there is a master student in our group attempting to do this. The ultra-short period eclipsing M-dwarf binaries presented in Chapter 4 could be followed up with medium to high resolution spectroscopy to determine their component masses and radii. This may provide addi-

tional confirmation of their (near-)contact state in a binary system and a measure to what degree radii of very fast rotating (partially) convective stars are inflated. Such observations will be challenging for two reasons. Firstly, because of the short orbital periods, short exposure times on the spectra are needed to avoid radial velocity smearing of the signal. Secondly, because the binaries are synchronously rotating, absorption features normally used for radial velocity cross-correlation may be very wide. However, as work on contact solar-type eclipsing binaries using broadening functions (e.g. Duerbeck & Rucinski 2007) shows, this may still be feasible. Another avenue of new work is to probe existing or upcoming high quality photometric databases for new (very) short period eclipsing binaries around M-dwarfs (e.g. Kepler, SDSS, WASP, Palomar Transient Factory PTF, PanStars etc), and improve their orbital statistics. This will place better constraints on the formation mechanism of such systems. Also, the relation with solar type or higher mass (detached) eclipsing binaries could be investigated, in turn providing additional constraints on binary and single star formation and evolution theories. Alternatively, a new photometric survey could be set up on a wide field imaging telescope specifically tuned towards  $<0.22$  d orbital periods on a large sample of M-dwarfs. The derived mass and radius errors of the interesting highly unequal double-line eclipsing M-dwarf binary system in Chapter 5 could be reduced by obtaining multi-band photometry, which will allow to better separate the contribution of cool star spots on the derived light curve parameters. Ultimately, this work should lead to a better understanding of the formation and evolution scenarios of this important Galactic stellar population.

## 1.10 Note to Chapter 3

This Chapter 3, which is published in MNRAS, is a second-author paper. I hereby specifically state my role in the making of this paper. I was directly involved in: i) all of the follow-up observations of this chapter as an active observer, ii) the reduction and modeling of the low-resolution spectroscopy (Section 3.5), the reduction of the INT i-band data (Section 3.3.2), iii) the initial calculations and write-up of Sections 3.8 (space velocities) and Sections 3.3.2, 3.3.4, 3.5.4.

## Bibliography

- Adams, F. C., Ruden, S. P., & Shu, F. H. 1989, *ApJ*, 347, 959
- Andersen, J. 1991, *A&ARv*, 3, 91
- Batalha, N. M., Borucki, W. J., Koch, D. G., et al. 2010, *ApJ*, 713, L109
- Bate, M. R. 2009, *MNRAS*, 392, 590
- Bate, M. R. 2012, *MNRAS*, 419, 3115
- Bate, M. R., & Bonnell, I. A. 1997, *MNRAS*, 285, 33
- Baraffe, I., Chabrier, G., & Barman, T. 2008, *A&A*, 482, 315
- Baraffe, I., & Chabrier, G. 1996, *ApJ*, 461, L51
- Berger, D. H., Gies, D. R., McAlister, H. A., et al. 2006, *ApJ*, 644, 475
- Bochanski, J. J., Munn, J. A., Hawley, S. L., et al. 2007, *AJ*, 134, 2418
- Bodenheimer, P., Burkert, A., Klein, R. I., & Boss, A. P. 2000, *Protostars and Planets IV*, 675
- Boley, A. C., Durisen, R. H., Nordlund, Å., & Lord, J. 2007, *ApJ*, 665, 1254
- Bonfils, X., Gillon, M., Udry, S., et al. 2012, *A&A*, 546, A27
- Bonnell, I. A. 1994, *Clouds, Cores, and Low Mass Stars*, 65, 115
- Borucki, W. J., Koch, D. G., Dunham, E. W., & Jenkins, J. M. 1997, *Planets Beyond the Solar System and the Next Generation of Space Missions*, 119, 153
- Bouy, H., Brandner, W., Martín, E. L., et al. 2003, *Brown Dwarfs*, 211, 245
- Brown, B. P., Browning, M. K., Brun, A. S., Miesch, M. S., & Toomre, J. 2008, *ApJ*, 689, 1354
- Burgasser, A. J., Reid, I. N., Siegler, N., et al. 2007, *Protostars and Planets V*, 427
- Cai, K., Durisen, R. H., Boley, A. C., Pickett, M. K., & Mejía, A. C. 2008, *ApJ*, 673, 1138
- Cappetta, M., Saglia, R. P., Birkby, J. L., et al. 2012, *arXiv:1210.1217*
- Caselli, P., Benson, P. J., Myers, P. C., & Tafalla, M. 2002, *ApJ*, 572, 238
- Cha, S.-H., & Whitworth, A. P. 2003, *MNRAS*, 340, 91
- Chabrier, G., Gallardo, J., & Baraffe, I. 2007, *A&A*, 472, L17
- Chabrier, G., & Baraffe, I. 1997, *A&A*, 327, 1039
- Chabrier, G., & Küker, M. 2006, *A&A*, 446, 1027
- Charbonneau, D., Berta, Z. K., Irwin, J., et al. 2009, *Nature*, 462, 891
- Charbonneau, P., & MacGregor, K. B. 1997, *ApJ*, 486, 502
- Clarke, C. J. 2007, *IAU Symposium*, 240, 337
- de Val-Borro, M., Gahm, G. F., Stempels, H. C., & Pepliński, A. 2011, *MNRAS*, 413, 2679
- Delfosse, X., Beuzit, J.-L., Marchal, L., Bonfils, X.; Perrier, C.; SÁlgransan, D.; Udry, S.; Mayor, M. 2004, *Spectroscopically and Spatially Resolving the Components of the Close Binary Stars*, 318, 166
- Demory, B.-O., Ségransan, D., Forveille, T., et al. 2009, *A&A*, 505, 205
- Devor, J. 2005, *ApJ*, 628, 411
- Doyle, L. R., Carter, J. A., Fabrycky, D. C., et al. 2011, *Science*, 333, 1602
- Duchêne, G., Bontemps, S., Bouvier, J., et al. 2007, *A&A*, 476, 229
- Duerbeck, H. W., & Rucinski, S. M. 2007, *AJ*, 133, 169
- Duquennoy, A., & Mayor, M. 1991, *A&A*, 248, 485
- Eggleton, P. P. 1983, *ApJ*, 268, 368
- Fischer, D. A., & Marcy, G. W. 1992, *ApJ*, 396, 178
- Gillon, M., Pont, F., Demory, B.-O., et al. 2007, *A&A*, 472, L13
- Gizis, J. E., Reid, I. N., & Hawley, S. L. 2002, *AJ*, 123, 3356

- Goldman, B., Bouy, H., Zapatero Osorio, M. R., et al. 2008, *A&A*, 490, 763
- Goodwin, S. P., Kroupa, P., Goodman, A., & Burkert, A. 2007, *Protostars and Planets V*, 133
- Henry, T. J., Ianna, P. A., Kirkpatrick, J. D., & Jahreiss, H. 1997, *AJ*, 114, 388
- Hillenbrand, L. A., & White, R. J. 2004, *ApJ*, 604, 741
- Irwin, J. M., Quinn, S. N., Berta, Z. K., et al. 2011, *ApJ*, 742, 123
- Jiang, D., Han, Z., Ge, H., Yang, L., & Li, L. 2012, *MNRAS*, 421, 2769
- Johnson, J. A., Gazak, J. Z., Apps, K., et al. 2012, *AJ*, 143, 111
- Kaltenegger, L., & Traub, W. A. 2009, *ApJ*, 698, 519
- Kandori, R., Nakajima, Y., Tamura, M., et al. 2005, *AJ*, 130, 2166
- Kraus, A. L., Ireland, M. J., Martinache, F., & Hillenbrand, L. A. 2011, *ApJ*, 731, 8
- Kratter, K. M., Matzner, C. D., & Krumholz, M. R. 2008, *ApJ*, 681, 375
- Kratter, K. M., Matzner, C. D., Krumholz, M. R., & Klein, R. I. 2010, *ApJ*, 708, 1585
- Laughlin, G., Bodenheimer, P., & Adams, F. C. 2004, *ApJ*, 612, L73
- Laughlin, G., & Bodenheimer, P. 1994, *ApJ*, 436, 335
- Leighton, R. B. 1969, *ApJ*, 156, 1
- Lopez-Morales, M. 2004, Ph.D. Thesis
- López-Morales, M. 2007, *ApJ*, 660, 732
- López-Morales, M., & Ribas, I. 2005, *ApJ*, 631, 1120
- Machida, M. N., Tomisaka, K., Matsumoto, T., & Inutsuka, S.-i. 2008, *ApJ*, 677, 327
- Mathieu, R. D. 1994, *ARA&A*, 32, 465
- Matsumoto, T., & Hanawa, T. 2003, *ApJ*, 595, 913
- Matzner, C. D., & Levin, Y. 2005, *ApJ*, 628, 817
- Morales, J. C., Ribas, I., Jordi, C., et al. 2009, *ApJ*, 691, 1400
- Morales, J. C., Gallardo, J., Ribas, I., et al. 2010, *Binaries - Key to Comprehension of the Universe*, 435, 141
- Morin, J., Donati, J.-F., Petit, P., et al. 2008, *MNRAS*, 390, 567
- Morin, J., Donati, J.-F., Petit, P., et al. 2010, *MNRAS*, 407, 2269
- Norton, A. J., Payne, S. G., Evans, T., et al. 2011, *A&A*, 528, A90
- Mullan, D. J., & MacDonald, J. 2001, *ApJ*, 559, 353
- Offner, S. S. R., Kratter, K. M., Matzner, C. D., Krumholz, M. R., & Klein, R. I. 2010, *ApJ*, 725, 1485
- Parker, E. N. 1955, *ApJ*, 121, 491
- Parker, E. N. 1993, *ApJ*, 408, 707
- Parker, R. J., Goodwin, S. P., Kroupa, P., & Kouwenhoven, M. B. N. 2009, *MNRAS*, 397, 1577
- Raghavan, D., McAlister, H. A., Henry, T. J., et al. 2010, *ApJS*, 190, 1
- Reid, I. N., Hawley, S. L., & Gizis, J. E. 1995, *AJ*, 110, 1838
- Reid, I. N. 1999, *Star Formation 1999*, 327
- Reid, I. N., Cruz, K. L., Kirkpatrick, J. D., et al. 2008, *AJ*, 136, 1290
- Reid, I. N., & Gizis, J. E. 1997, *AJ*, 114, 1992
- Reiners, A., & Basri, G. 2008, *ApJ*, 684, 1390
- Ribas, I. 2006, *Ap&SS*, 304, 89
- Rockenfeller, B., Bailer-Jones, C. A. L., & Mundt, R. 2006, *A&A*, 448, 1111
- Sana, H., de Mink, S. E., de Koter, A., et al. 2012, *Science*, 337, 444
- Steenbeck, M., Krause, F., Rädler, K.-H. 1966, *Zeitschrift Naturforschung Teil A*, 21, 369
- Stepien, K. 1995, *MNRAS*, 274, 1019

- Stepien, K. 2006, *Acta Astron.*, 56, 347  
Stępień, K. 2011, *Acta Astron.*, 61, 139  
Tachihara, K., Onishi, T., Mizuno, A., & Fukui, Y. 2002, *A&A*, 385, 909  
Thompson, M. J., Christensen-Dalsgaard, J., Miesch, M. S., & Toomre, J. 2003, *ARA&A*, 41, 599  
Tokovinin, A. A., & Smekhov, M. G. 2002, *A&A*, 382, 118  
Torres, G., & Ribas, I. 2002, *ApJ*, 567, 1140  
Torres, G., Andersen, J., & Giménez, A. 2010, *A&ARv*, 18, 67  
West, A. A., Hawley, S. L., Bochanski, J. J., et al. 2008, *AJ*, 135, 785  
Wielen, R. 1977, *A&A*, 60, 263  
Zinnecker, H., & Yorke, H. W. 2007, *ARA&A*, 45, 481



---

## Chapter 2

---

# Minimizing follow-up for space-based transit surveys using full lightcurve analysis.

*Context.* One of the biggest challenges facing large transit surveys is the elimination of false-positives from the vast number of transit candidates. A large amount of expensive follow-up time is spent on verifying the nature of these systems.

*Aims.* We investigate to what extent information from the lightcurves can identify blend scenarios and eliminate them as planet candidates, to significantly decrease the amount of follow-up observing time required to identify the true exoplanet systems.

*Methods.* If a lightcurve has a sufficiently high signal-to-noise ratio, a distinction can be made between the lightcurve of a stellar binary blended with a third star and the lightcurve of a transiting exoplanet system. We first simulate lightcurves of stellar blends and transiting planet systems to determine what signal-to-noise level is required to make the distinction between blended and non-blended systems as function of transit depth and impact parameter. Subsequently we test our method on real data from the first IRa01 field observed by the CoRoT satellite, concentrating on the 51 candidates already identified by the CoRoT team.

*Results.* Our simulations show that blend scenarios can be constrained for transiting systems at low impact parameters. At high impact parameter, blended and non-blended systems are indistinguishable from each other because they both produce V-shaped transits. About 70% of the planet candidates in the CoRoT IRa01 field are best fit with an impact parameter of  $b > 0.85$ , while less than 15% are expected in this range considering random orbital inclinations. By applying a cut at  $b < 0.85$ , meaning that  $\sim 15\%$  of the potential planet population would be missed, the candidate sample decreases from 41 to 11. The lightcurves of 6 of those are best fit with such low host star densities that the planet-to-star size ratios imply unrealistic planet radii of  $R > 2R_{Jup}$ . Two of the five remaining systems, CoRoT1b and CoRoT4b, have been identified as planets by the CoRoT team, for which the lightcurves alone rule out blended light at 14% ( $2\sigma$ ) and 31% ( $2\sigma$ ). One system possesses a M-dwarf secondary, one a candidate Neptune.

*Conclusion* We show that in the first CoRoT field, IRa01, 85% of the planet candidates can be rejected from the lightcurves alone, if a cut in impact parameter of  $b < 0.85$  is applied, at the cost of a  $< 15\%$  loss in planet yield. We propose to use this method on the Kepler database to study the fraction of real planets and to potentially increase the efficiency of follow-up.

## 2.1 Introduction

With the CoRoT and Kepler space observatories in full swing (Baglin et al. 2006, Borucki et al. 2003), which both deliver thousands of lightcurves with unprecedented photometric precision and cadence, we have moved into an exciting new era of exoplanet research. Now, the characterisation of small, possibly rocky planets has finally become a realistic prospective (e.g. Corot-7b, Leger et al. 2009; Kepler-10b, Batalha et al. 2011). One of the biggest challenges is to separate real planets from the significant fraction of (astrophysical) false-positives that can mimic a genuine transit signal (e.g. Batalha et al. 2010). Ground-based transit surveys have revealed that stellar eclipsing binaries (EBs) blended with light from a third star are the main source of contamination (e.g. Udalski et al. 2002). Also, for Super-Earth planet candidates blends with a background transiting Jupiter-sized planet system can be important. In these systems the eclipse depth, shape and ellipsoidal light variations of an EB are diluted by the effects of chance alignment of a foreground or background star or associated companion inside a photometric aperture set by either the pixel scale or the point spread function. In addition, light from a third star in the photometric aperture can bias the fitted parameters of a planet transit system. High resolution, high signal-to-noise spectra are normally required to exclude binary scenarios by excluding their large radial velocity or bi-sector variations, a process that can be very time-consuming.

Stellar blends are common in space-based transit surveys as apertures are relatively large (e.g.  $19'' \times 21''$  for CoRoT), and target fields are crowded since the number of target stars is maximized in this way. To weed out false-positives, the CoRoT team relies on an extensive ground-based follow-up campaign for on-off photometry to identify the transited star in the CoRoT aperture (Deeg et al. 2009) and high resolution imaging observations to identify possible stars that dilute the lightcurve of a planet candidate. Even so, many candidates remain unresolved and defy easy characterisation after such a campaign. Kepler uses its unique astrometric precision to minimise the number of blends, which can be identified by a position shift of the flux centroid during transit, but will still require enormous ground-based efforts on the remaining  $\sim 1200$  candidates (e.g. Borucki et al. 2011). Together with the new influx of planet candidates from current surveys, possible future missions (such as PLATO; e.g. Catala et al. 2011) and ground-based efforts to hunt for planets around low-mass stars, the telescope demand for full follow-up may grow enormously. Therefore, any new technique or strategy that can eliminate even a moderate fraction of all candidates from the discovery lightcurves, prior to follow-up, is extremely valuable.

In this paper we investigate to what extent information from the lightcurves themselves can identify blend scenarios and eliminate them as planet candidates and on the other hand rule out blend scenarios in the case of true planet systems. Our key motivation is that *the lightcurves of blended systems can not be perfectly fit by pure transit models and neither can genuine transits be fit by blended light models*. In section 2.2 we introduce our lightcurve fitting procedure and in section 2.3 we apply it to simulated data of a transiting hot Jupiter and Super-Earth. While such a procedure provides a natural tool to distinguish blends from genuine planetary systems by lightcurve fitting, it breaks down for transits with high impact parameters. We therefore only consider transiting systems with impact parameter  $b < 0.85$ , losing potentially  $\sim 15\%$  of the planet catch, but significantly decreasing (by an order of magnitude) the required amount of follow-up observations. In section 2.4 we apply our method to the candidates of the CoRoT

IRa01 field, whose candidates are almost completely characterised through an extensive follow-up campaign, and discuss the results in section 2.5.

## 2.2 Method

### 2.2.1 Transit fitting

Several methods have been presented in the literature to identify blended systems and to select the best planet candidates. Seager & Mallen-Ornellas (2003) proposed a diagnostic that involves fitting a trapezoid to the transit lightcurve to obtain estimates for the transit parameters and subsequently identify the best candidates. In this paper we use a method very similar to that used by Snellen et al. (2009) to reject blend scenarios for the transiting hot Jupiter OGLE2-TR-L9. It involves least-square fitting of a lightcurve using the standard transit parameters (see below) plus an additional parameter representing the extra light from a third light source. If the fit is significantly better with extra light, the lightcurve is from a blended system. If this is not the case, an upper limit to the third light fraction can be set to a degree depending on the signal-to-noise of the data. This procedure is in essence similar to *Blender*, which is used by the Kepler team (e.g. Torres et al. 2011). However, *Blender* simulates physical systems involving so many parameters that it is impractical to run on a large number of candidates. Here we are not interested in the true nature of the second object (whether it is a background, foreground or physically related star), just in its possible influence on the transit lightcurve.

We assume at this point that lightcurves with obvious signs of the presence of a stellar binary, such as ellipsoidal light variations and/or secondary eclipses, have been excluded from the candidate list. Note that a useful upper limit to the amount of ellipsoidal light variation, and the likelihood of a genuine planetary secondary, can be obtained by taking a Fourier transform of the data with the transit signal removed. We therefore do not require EBOP (Popper and Etzel 1981) to model the complex binary effects in the lightcurve, but rather utilize an IDL routine that incorporates the analytical transit model of Mandel and Agol (2002;M&A). Our system simply consists of a secondary transiting a primary with possible additional light from a tertiary.

### 2.2.2 Transit parameters

We treat the transit mid-time  $T_0$  and the orbital period  $P$  as fixed parameters, resulting from the candidate selection process. For extra simplicity we keep the limb darkening parameters fixed at the tabulated solar values for CoRoT white light, assuming quadratic parameters  $(a,b)=(0.44,0.23)$  from Sing et al. (2010). Although this gives a small bias ( $<0.06$  in impact parameter) for primary stars of different stellar type, the method is not meant for precise planet characterization and does not influence the characterization of potential blended and non-blended systems. Our transit model has three free parameters; the ratio of secondary over primary radii ( $R_2/R_1$ ), the impact parameter of the transit  $b$ , which is the smallest projected distance of the centre of the secondary to that of the primary in units of  $R_1$ , and the density of the primary star  $\rho_1$ . This density can be converted to the scaled orbital radius ( $a/R_1$ ), assuming

that  $M_1 \gg M_2$ , through

$$\left(\frac{a}{R_1}\right)^3 = \frac{G \rho_1}{3\pi P^2} \quad (2.1)$$

The relative projected distances  $z$  between secondary and primary are computed from the input orbital phases  $\phi$ ,

$$z(\phi) = \sqrt{\left(\frac{a}{R_1}\right)^2 \sin(\phi)^2 + b^2 \cos(\phi)^2}, \quad (2.2)$$

Together with  $(R_2/R_1)$ , these are used as input to a custom-made IDL program, incorporating the routine from M&A, that computes the theoretical models. We introduce light to this transit system by adding the blended light fraction  $k$ ,

$$F_{total}(\phi, b, R_1/R_2, \rho_*, k) = F_{eclipse} \cdot (1 - k) + k, \quad (2.3)$$

where  $F_{eclipse}$  is the original transit lightcurve. We then devise the following chi-square statistic to compare the lightcurve to the data  $F_{obs,i}$  with uncertainty  $\sigma_{obs,i}$ ,

$$\chi^2 = \sum_i \frac{(F_{obs,i} - F_{total,i})^2}{\sigma_{obs,i}^2} \quad (2.4)$$

Note that we assume circular orbits. This has no influence on the characterization of blended and non-blended systems, but it does affect the derived host star density, and is therefore important for the estimate of the radius of the secondary object. This is further discussed in section 2.5.

### 2.2.3 MCMC

To obtain the best-matching system parameters, we use a Monte Carlo Markov Chain  $\chi^2$  optimisation technique (MCMC, e.g. Tegmark et al. 1998) to map out the probability distribution for each lightcurve parameter. MCMC is found to be a more robust technique to obtain a global parameter solution in multi-parameter space than (downhill) grid-based methods, due to the resolution inefficiency of the latter (e.g. Serra et al. 2011). In the MCMC algorithm, the parameters  $p_i$  are perturbed by an amount drawn from a normal distribution  $\mathcal{N}$  according to:  $p_{i+1} = p_i + f \cdot \mathcal{N} \cdot \sigma_p$ , where  $f$  is the jump function and  $\sigma_p$  the standard deviation of the sampling distribution for each  $p$ . Subsequently  $\chi^2$  is recalculated for these perturbed parameters and a Gaussian likelihood  $\mathcal{L} \propto \exp(-\chi^2/2)$  is determined. These random jumps in parameter space are accepted or rejected according to the Metropolis-Hastings rule (Metropolis et al. 1953; Hastings 1970). If the perturbed parameter set has a higher likelihood  $\mathcal{L}'$  than its progenitor, it will be accepted as a new chain point, otherwise it will be accepted with a probability of  $\mathcal{L}'/\mathcal{L}$ . We run the algorithm many times to build up a 'chain' of parameter values and tweak  $\sigma_p$  and  $f$  such that  $\sim 40\%$  of the jumps are accepted. After creating multiple chains from different starting conditions, we check proper model convergence and mixing of the individual chains using the Gelman & Rubin  $R$  statistic (Gelman & Rubin 1992). To save time, first  $k$  is set to zero at the minimum  $\chi^2$  determined with MCMC analysis. Subsequently  $k$  is increased in small steps (but always kept fixed during the MCMC) with the previously found parameters as starting values. In this way the parameter values (adopting the median of the distribution) and the uncertainties in the parameters are determined as function of  $k$  in an efficient way.

## 2.3 Tests on synthetic lightcurves

In this section, we test our method on synthetic lightcurves to determine the required precision to detect or exclude third light in a particular transit system. We perform these simulations for two candidate systems: (i) a hot Jupiter orbiting a solar type star and (ii) a Super-Earth around a similar host.

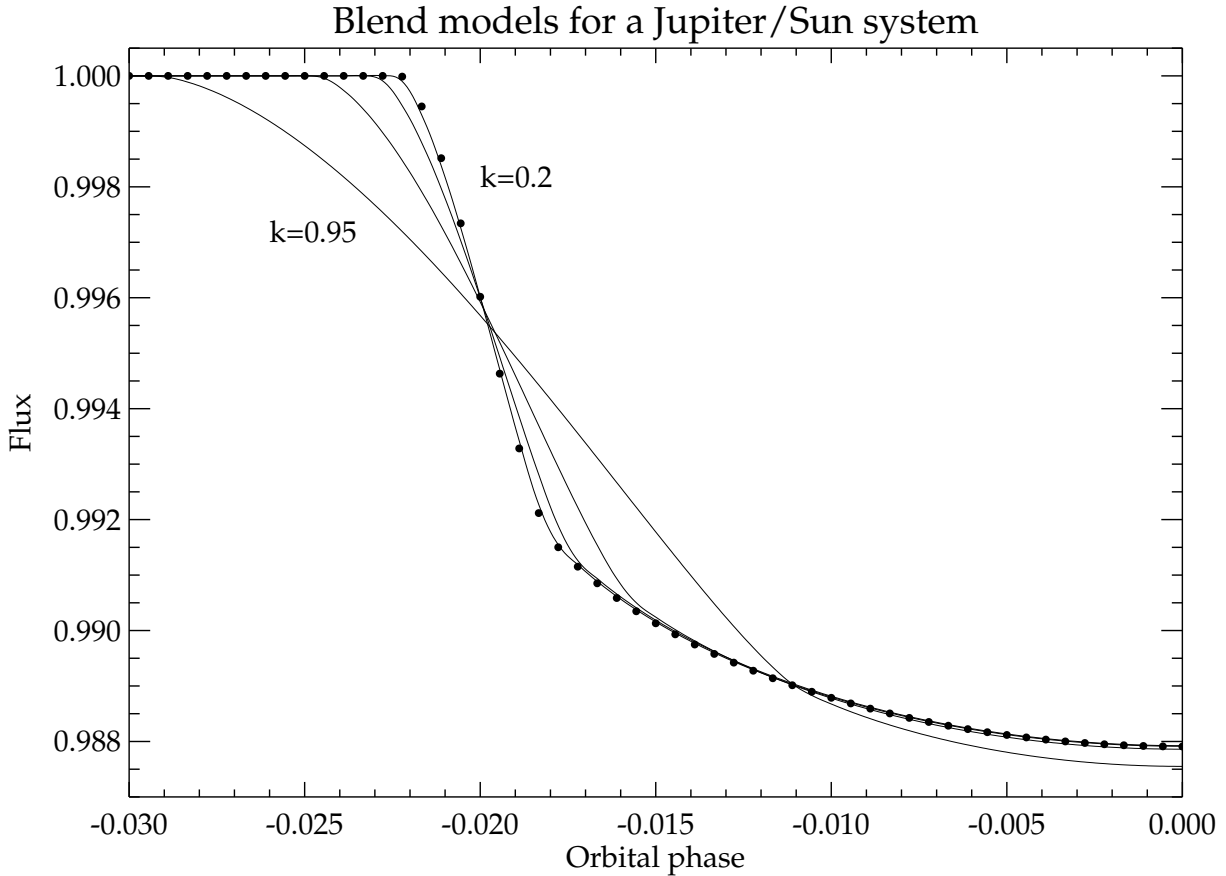


**Figure 2.1** — Simulated lightcurve for a transiting exoplanet system consisting of a hot Jupiter in a 2.5 day orbit around a solar type star with impact parameter  $b=0.2$  (black dots). The solid curves show diluted binary models with best-fit parameters determined by MCMC, for blended light fraction  $k=[0.2, 0.5, 0.8, 0.95]$ .

### 2.3.1 Transiting hot Jupiter

We simulated a set of transit lightcurves for a hot Jupiter with  $R_2 = 1R_{\text{Jup}}$  and  $P=2.5$  days, orbiting a star with a solar density, for a range of impact parameters. The lightcurve for an impact parameter of  $b = 0.2$  is shown in Figure 2.1. As explained in the previous section, our method finds the best fit for a range in blended light fraction  $k$ . Of course, in this simulation a perfect fit is obtained for  $k=0$ . As can be seen in Figure 2.1, an increasingly worse fit is obtained for increasing  $k$ , most obviously seen by comparing the  $k=0.95$  model to the synthetic data. This latter model fit assumes that 95% of the light is from a third object, meaning that

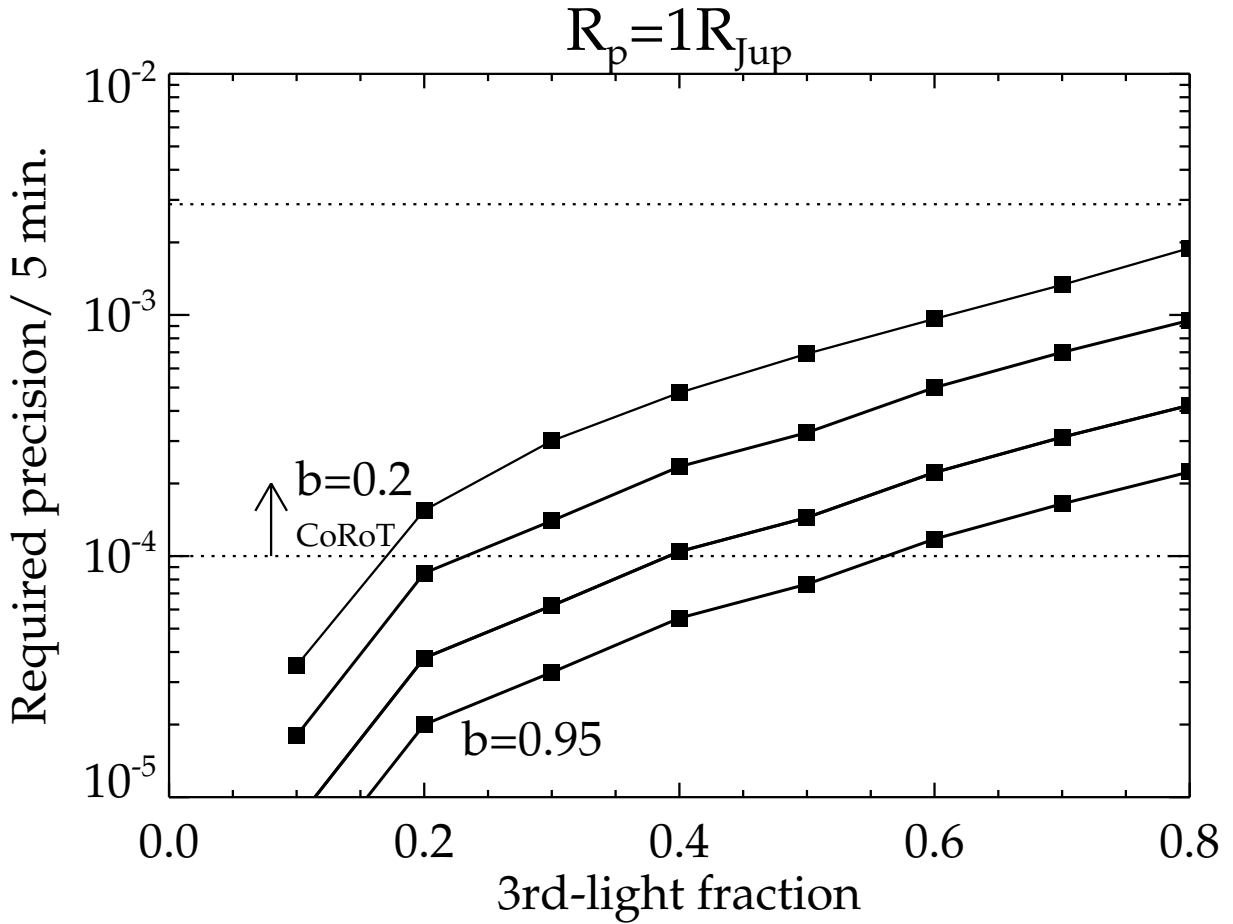


**Figure 2.2** — The photometric precision per 5 minutes required to exclude a blended light fraction  $k$  at  $3\sigma$  for a hot Jupiter around a solar type host star ( $R_2/R_1 = 0.1$  and  $\rho_* = \rho_\odot$ ), as a function of the system parameters  $b$  and  $k$ . The four solid curves are for impact parameters  $b=0.2, 0.5, 0.8,$  and  $0.95$ . The upper and lower horizontal dotted lines indicate the range in precision for objects in the IRa01 field, determined by Aigrain et al. (2009).

the unblended transit is actually a factor 20 deeper, hence 20% deep instead of 1%. It implies that  $R_2/R_1 \sim 0.45$ , resulting in a much longer duration transit unless it is grazing. This results in the best-fitting  $k=0.95$  model being much more V-shaped than the synthetic lightcurve of the planet. We can now convert the differences between the synthetic lightcurves and model fits to  $\chi^2$  values for each combination of  $b$  and  $k$  by assigning uncertainties to the synthetic data. In this way we can determine what photometric precision is required to exclude a certain blended light fraction in the lightcurves as a function of  $b$ . Figure 2.2 shows the precision per 5 minutes of data required to exclude a blended light fraction  $k$  at a  $3\sigma$  level in a system with an impact parameter of  $b=0.2, 0.5, 0.8,$  and  $0.95$ . The required precision becomes more stringent for lower values of  $k$  and higher values of  $b$ . For  $b=0.2$ , 80% blended light ( $k=0.8$ ) can be excluded in a lightcurve with a precision of only  $2 \times 10^{-3}$  per 5 minutes, while for  $b=0.8$ , 20% of blended light can only be rejected if the lightcurve has a precision of  $4 \times 10^{-5}$  per 5 minutes.

### 2.3.2 Transiting super-Earth

We performed also tests on a Super-Earth with  $R_2 = 2.5R_{\oplus}$  orbiting a sun-like star, following the same procedure as described above. Since the transit itself is a factor  $\sim 16$  more shallow than for a Jupiter-size planet, the level of precision required to reject blend scenarios is also significantly higher, as can be seen in Figure 2.3. Note however that even for a blended light fraction of  $k=0.95$ , the radius of transiting object  $R_2$  is still in the Jupiter-size regime. Hence only if the blended light fraction is very high,  $k > 0.95$ , can an eclipsing binary mimic a Super-Earth transit.

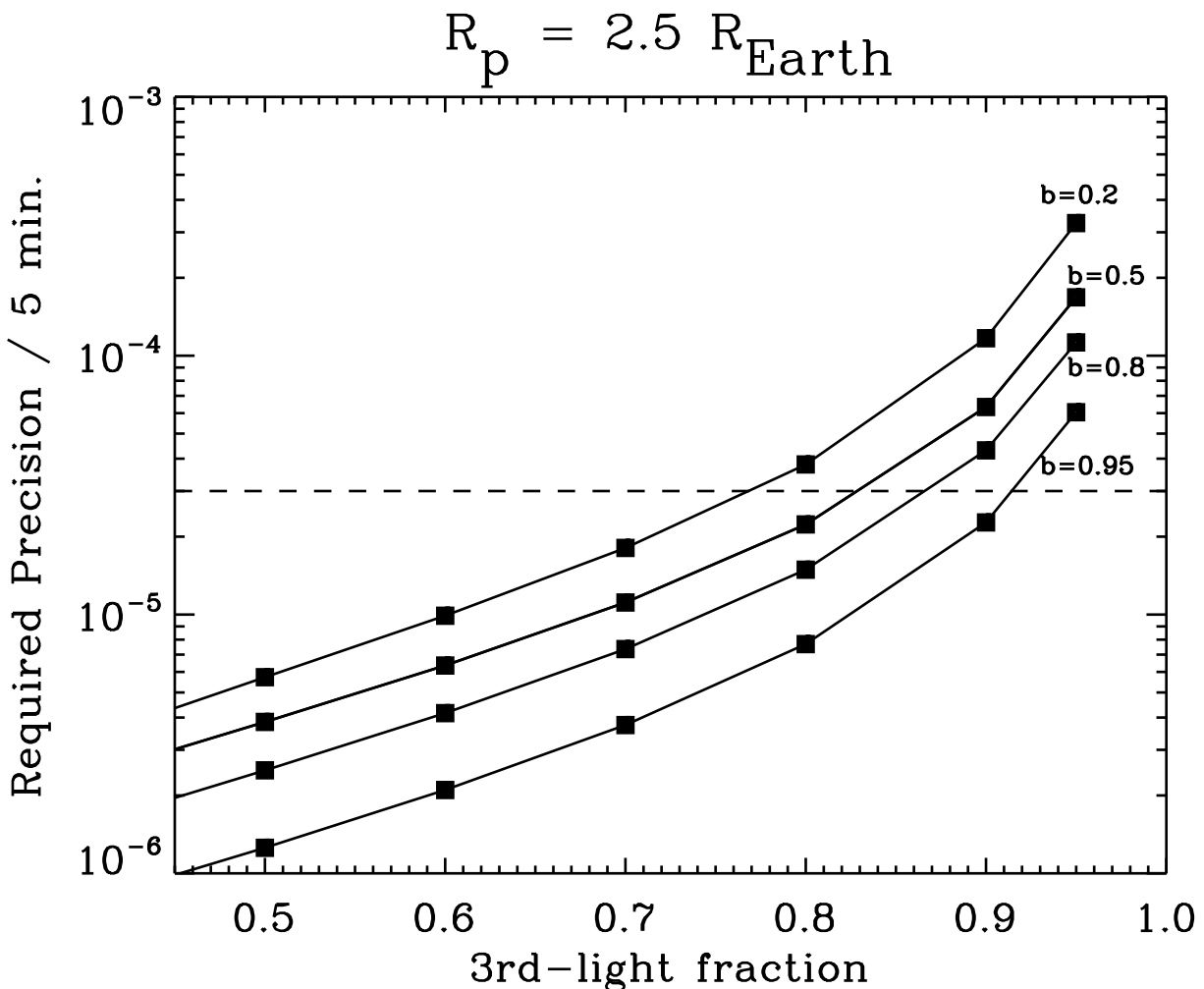


**Figure 2.3** — As for Fig. 2.2, but for a  $2.5R_{\text{Earth}}$  SuperEarth planet around a solar type host in a 2.5 day orbital. We can exclude 80% blended light at the  $3\sigma$  level at a moderate impact parameter of  $b=0.5$ . The horizontal dashed line refers to the precision reached in the discovery lightcurve of CoRoT 7b, the first rocky SuperEarth planet (Leger et al. 2009).

## 2.4 Tests on candidates in the CoRoT IRa01 field

### 2.4.1 The data set

In this section we test our method on real data, using the lightcurves of the candidates selected by the CoRoT team from CoRoT field IRa01 (Carpano et al. 2009). In this first field targeted by CoRoT, 3898 bright stars were observed in chromatic mode (with a blue, green and red channel) and another 5974 in a single monochromatic "white" band in a 66 day staring run towards the Galactic anti-center. From the 50 initial candidates, a subsample of 29 promising targets received extensive follow-up as discussed in Moutou et al. (2009). Two of these have so far been identified as genuine planets: CoRoT-1b, a low density  $R_p = 1.49R_{Jup}$  transiting hot Jupiter around a G0V host (Barge et al. 2008) and CoRoT-4b, a  $R_p = 1.19R_{Jup}$  hot Jupiter around a F8V host (Aigrain et al. 2008). Seventeen additional systems were solved using the photometric and spectroscopic follow-up observations (Moutou et al. 2009). We choose to test our method on the 45 bright candidates with more than one transit observed, using the publicly available N2-level data.

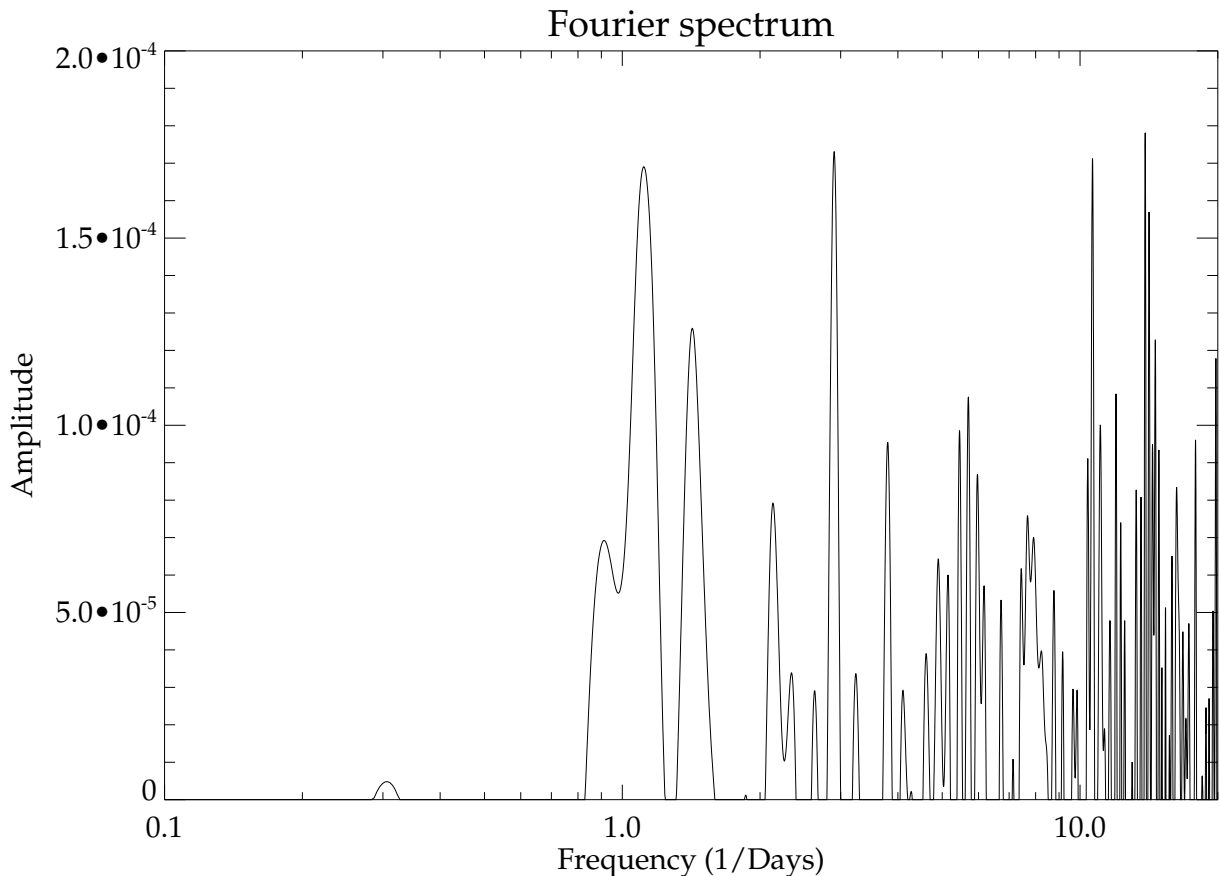


**Figure 2.4** — *Fourier diagram of an example noise spectrum prior to lightcurve cleaning. Amplitude of the best-fitting sine curve on the vertical axis is plotted against frequency. Peaks around frequencies of 1.0 and  $\sim 14$  are due to remaining systematics related to the satellite orbit and Earth's rotational period.*

## 2.4.2 Pre-cleaning of the lightcurves

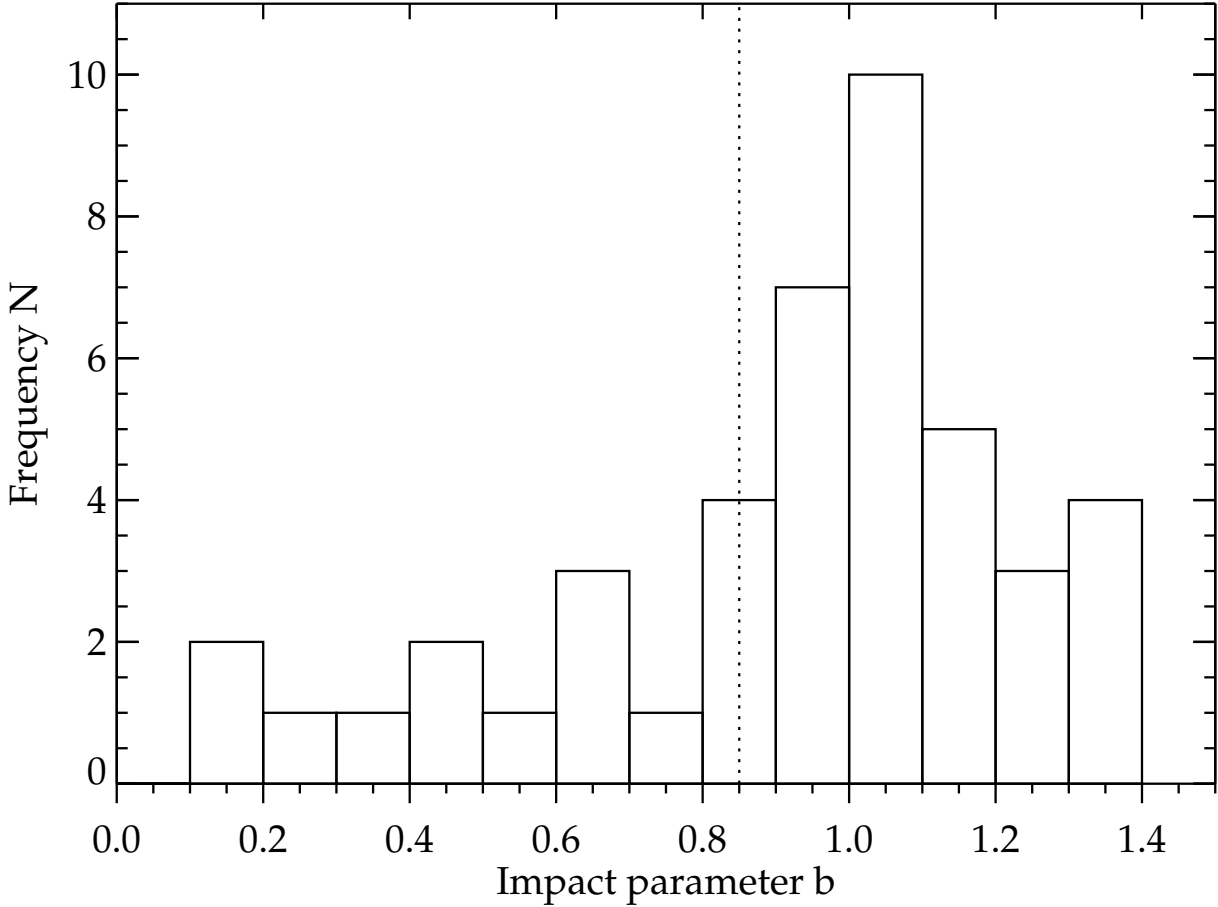
We first combine the multicolor lightcurves into one single 'white lightcurve' for each candidate under the assumption that the CoRoT analysis teams did not detect any significant variation of eclipse depth with wavelength, which would already have been a clear sign of blending effects. We first clip each lightcurve by removing outliers at the  $5\sigma$  level. These outliers are mostly associated with the epochs at which the satellite passes the South Atlantic Anomaly (SAA) or moves in/out of the Earth's shadow. We then iteratively refine the mid-times  $T_0$  and the orbital period  $P$  using the Kwee-van Woerden method (Kwee & van Woerden 1956) and cross-correlation with a theoretical transit model (e.g. Rauer et al. 2009). Individual transit events that show temporary jumps in flux, caused by the impact of energetic particles (mainly protons) onto the CCD ("hot pixels"), are excluded from our analysis. For 16 out of the initial 50 CoRoT IRa01 candidates (32%) we had to remove one or more transits from the lightcurve that were affected by such particle hits. Each individual lightcurve was then phasefolded around every transit. To normalise the data, we fit either a first order polynomial in a small range in phase ( $\pm 0.1$  from mid-transit) around each transit or a higher order polynomial (order  $n=13$ ) in a larger phase range (typically  $\pm 0.4$  in phase), depending on which approach delivers the lowest rms in and out of eclipse and the least red noise (Pont et al. 2006).

Figure 2.4 shows a typical example of the dominant frequencies still remaining after the polynomial fit. For most objects, distinct peaks exist around periods of 103 minutes and at 24 hours. We identify these peaks with remaining systematics, related to the satellite's orbit and Earth's rotational period, caused by ingress and egress of the spacecraft from Earth's shadow, variations in gravity and magnetic field and changes in the levels of thermal and reflected light from the Earth (e.g. Aigrain et al. 2009). By folding the out-of-eclipse data onto the dominant frequencies of the Fourier diagram, we then fit a sinusoidal function to the remaining systematics, followed by median averaging over all transits. We subsequently binned the lightcurves and assign errors, according to the standard deviation divided by the square root of the number of points in each bin.

## 2.4.3 Fitting the lightcurves

Each lightcurve is first fitted with the method explained in section 2.2, assuming  $k=0$ , yielding the starting parameter sets  $(R_2/R_1, b, \rho_*)$  for our blend analysis. In Figure 2.5 we show the resulting MCMC distribution of impact parameter  $b$  versus  $R_2/R_1$  for all the 45 candidates. CoRoT WinIDs (a shortcut of the CoRoT run identification number, e.g. IRa01-E1-2046) for each candidate are indicated, with yellow for the two confirmed planets CoRoT1b and CoRoT4b, in blue those candidates that have been confirmed to be blended systems by Moutou et al. (2009), and in red unsettled cases (either suspected early type stars with only few or very broad spectral lines for further radial velocity follow-up observations with HARPS or confirmed genuine EBs with non-planetary secondary masses). As can be seen, a large fraction of the candidates are, assuming no blended light, best fitted with a very high (often larger than unity) impact parameter. This is even more clear in the distribution of fitted impact parameters as shown in figure 2.6. For 32 out of the 45 ( $\sim 70\%$ ) candidates  $b > 0.85$ , while from geometric arguments it is expected that  $\sim 15\%$  of planets would be found at such a high impact parameter. Assuming that all eleven candidates at  $b < 0.85$  are non-blended systems only  $\sim 1.6$





**Figure 2.6** — *Distribution of fitted impact parameter of the CoRoT IRa01 candidates. The distribution is strongly peaked around  $b=1.0$ , indicating a significant population of (blended) EB contaminants. For a genuine planet distribution we would expect a flat histogram that falls off at high impact parameter. The dotted vertical line indicates the  $b=0.85$  cutoff we have proposed in this paper.*

out of the remaining sample since they are all fitted with a high impact parameter. For six objects a significant fraction of blended light can be excluded from the lightcurve alone, including CoRoT-1b and CoRoT-4b. It would therefore not have been necessary to check whether the variability in these candidates came from the target star or not and the follow-up could have immediately concentrated on radial velocity measurements. All parameters of the remaining candidates are shown in Table 1. An additional cut in the candidate list is made using a combination of the best fit mean stellar densities  $\rho_*$  and  $R_2/R_1$ , as shown in Figure 2.8. Six of the candidates have host stars with densities corresponding to A-stars, resulting in unrealistically large secondary radii of  $> 2.0R_{Jup}$ . Note that there is currently no consensus on the upper limit of planet size, meaning that by setting a hard limit on planet radius we may exclude very large or bloated (hot) Jupiters. However, there are currently only 4 out of 219 transiting exoplanets reported with radii larger than  $1.8R_{Jup}$  ([www.exoplanet.eu](http://www.exoplanet.eu)). Also, the probability that the secondary is a mid-type M-dwarf rather than a genuine planet increases when considering larger radii. This results in a remaining planet candidate sample of 5 objects instead of the original 45 using arguments based on the lightcurve alone. These five objects have been marked with filled symbols in Figure 2.8. Details on each system are discussed in Appendix A.

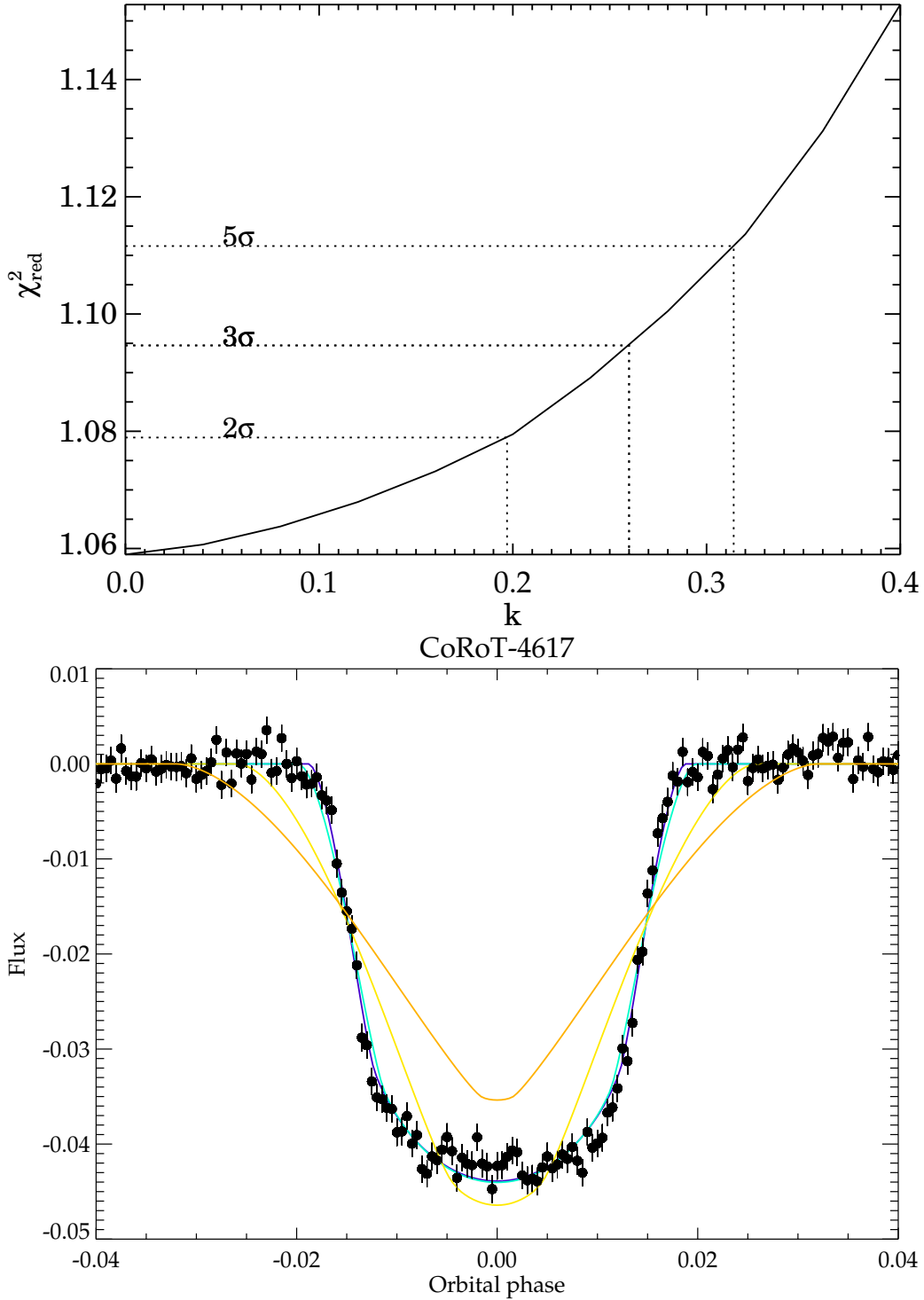


**Figure 2.7** — Panel a): The reduced  $\chi^2$  as function of blended light fraction  $k$ . The horizontal dashed line shows the  $2\sigma$ ,  $3\sigma$  and  $5\sigma$  rejection criteria. Our lightcurve model directly indicates an early type main sequence stellar host, with a  $2\sigma$  upper limit for blended light of  $k \sim 20\%$ . The low stellar density implies a large secondary radius, rejecting the planet hypothesis. Panel b): best fitting EB models with blended light fraction  $k=[0.2,0.5,0.90,0.95]$ , clearly showing that solutions with low  $k$  are favoured. Note that an orbit with an eccentricity of  $e=0.5$ , orientated in the right way, could increase the estimated stellar density to that of the Sun, and decrease  $R_2$  to  $2 R_{\text{Jup}}$ . This ambiguity can be easily removed by taking a single spectrum of the star, resolving its spectral type.

WinID+CoRoTID	P	$\left(\frac{R_2}{R_1}\right)$	$b$	$\text{Log}\left(\frac{\rho_*}{\rho_\odot}\right)$	$\left(\frac{a}{R_*}\right)$	$2\sigma$
1126 0102890318	1.51	0.14	0.43	-0.16	4.93	14%
0330 0102912369	9.20	0.10	0.18	-0.13	16.96	31%
0203 0102825481	5.17	0.18	0.62	0.04	13.09	30%
1712 0102826302	2.77	0.05	0.60	-0.88	4.27	93%
4108 0102779966	7.37	0.07	0.80	-0.06	15.41	95%
<i>(<math>R_2/R_1</math>) versus <math>\rho_*</math></i>						
4617 0102753331	19.76	0.19	0.10	-1.42	10.47	20%
2430 0102815260	3.59	0.10	0.24	-0.81	5.36	44%
4073 0102863810	15.00	0.18	0.36	-0.08	24.40	67%
1736 0102855534	21.72	0.11	0.43	-1.24	12.77	62%
3724 0102759638	12.33	0.10	0.50	-1.33	8.17	78%

**Table 2.1** — *The candidate sample that survives the impact parameter cut. The last six sources are excluded using a second cut because the fitted host star density indicates a secondary radius  $R_2 > 2R_{Jup}$ . The last column indicates the  $2\sigma$  upper limit to the blended light fraction  $k$ .*

## 2.5 Discussion

In this paper we investigated to what extent we can use the high signal-to-noise lightcurves of space-based exoplanet transit surveys to identify blended light scenarios, and eliminate them as planet candidates. We concentrated on the 51 exoplanet candidates from the first CoRoT IRa01 field (Carpano et al. 2009). About 70% of the 51 planet candidates in the CoRoT IRa01 field are best fit with an impact parameter of  $b > 0.85$ , which at face value already indicates that the candidate distribution is strongly contaminated by blended and/or grazing systems. We find that by cutting a candidate sample such that those objects with high impact parameter are removed, at the cost of losing a small fraction of potential planets, a significant reduction in required follow-up observations can be achieved. Of all candidates, only 5 remain in the final sample of which two are genuine planet systems, one is a low mass transiting M dwarf and one is a candidate Neptune.

The V-shaped lightcurves of near-grazing planet systems are strongly degenerate with blended eclipsing binary systems and can therefore not be distinguished from each other. How many planets are potentially missed by invoking the cut in impact parameter? Of the known transiting exoplanets,  $\sim 6\%$  has an impact parameter larger than 0.85 and  $\sim 16\%$  an impact parameter of more than 0.75<sup>1</sup>. The cumulative probability of a particular transit at a given impact parameter greater or equal to a cutoff value  $b_X$  and transit depth  $\Delta F$  is given by:

$$P_c(b > b_X) = \frac{1 + \sqrt{\Delta F} - b_X}{1 + \sqrt{\Delta F}} = \frac{1 + R_2/R_1 - b_X}{1 + R_2/R_1} \quad (2.5)$$

Note that this expression is different from the equation presented in Seager and Mallen-Ornellas (2003), because the maximum impact parameter in their formula is determined by the grazing condition  $b_{max} = 1 - R_2/R_1$ , yielding a minus sign in equation 5. For a  $1R_{Jup}$  planet around a solar type star  $\sim 22\%$  would potentially be missed by setting the cut in impact parameter ( $\sim 6\%$

<sup>1</sup>[www.exoplanet.eu](http://www.exoplanet.eu)

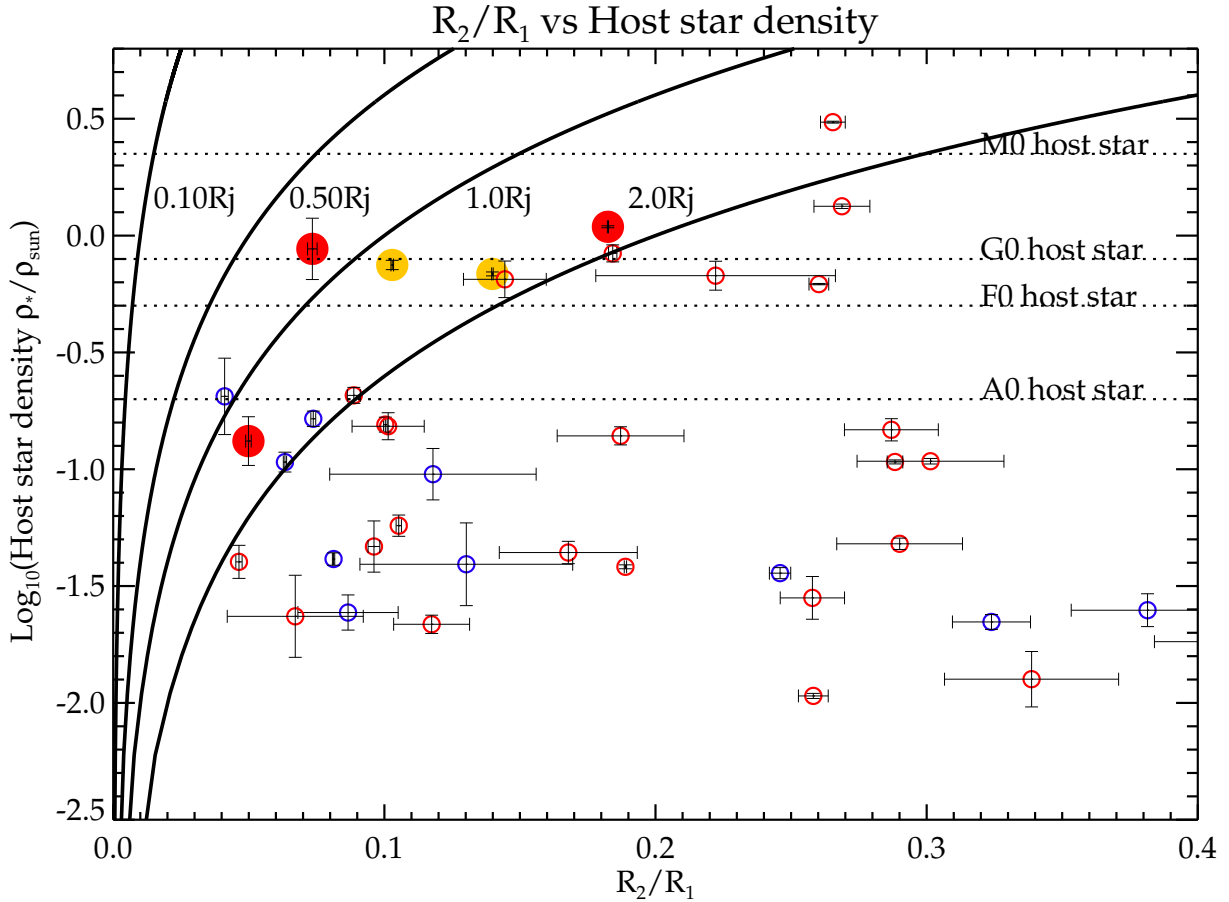


**Figure 2.8** — The  $R_2/R_1$  size ratio versus the log of the stellar density for the CoRoT candidates in the IRa01 field, assuming  $k=0$ . The dotted lines mark the densities of A to M type main-sequence hosts. The five filled dots are the candidates that survive both our cuts in impact parameter and secondary size. The two confirmed transiting hot Jupiters CoRoT1b and CoRoT4b are shown as yellow filled dots. Open circles are the candidates we have excluded using our cuts. Blue circles indicate sources which have been identified as blended EBs by the CoRoT team follow-up, and red circles are either unsettled cases in the CoRoT follow-up or systems identified as genuine EBs through their radial velocities. The four solid curves indicate  $R_2=[0.10,0.50,1.0,2.0]R_{Jup}$ , assuming the main sequence mass-radius relation of Cox (2000) for the primary.

according to Seager and Mallen-Ornellas). However, extremely grazing systems will be very shallow and of short duration and will therefore provide very limited physical information. For example, a grazing  $1R_{Jup}$  with impact parameter  $b=1.05$ , will show a transit with a duration of 30% and only 20% of the depth of a transit with  $b=0$ . Therefore, the actual planet loss fraction will be closer to the predictions of Seager and Mallen-Ornellas (2003), i.e.  $< 15\%$ .

In this paper we have made the assumption of circular orbits, but radial velocity surveys teach us that such an assumption is not valid for longer periods (e.g. Butler et al. 2006). In addition, Barnes (2007) shows that a planet with an eccentric orbit is more likely to transit by a factor of  $(1-e^2)^{-1}$  than a planet in a circular orbit with the same semi-major axis. A significant population of transiting exoplanets with an eccentric orbit is therefore expected for long duration space-based surveys. Because the planet orbital velocity varies from  $\sqrt{\frac{1+e}{1-e}}V_{circ}$  to  $\sqrt{\frac{1-e}{1+e}}V_{circ}$

between periastron and apastron in an eccentric orbit, transit duration can vary as function of  $e$  and  $\omega$  (the angle of pericenter). This leads to a wrong fit of the host star density (e.g. Kipping 2010a, Tingley et al. 2011), therefore directly affecting our estimate of the secondary radius  $R_2$ . We therefore can not reliably make the planet-to-star ratio versus host star density cut in the eccentric orbit case for longer period planets ( $P > 3.0$ days). Fortunately, the fitted impact parameter,  $R_2/R_1$  and blended light fraction  $k$  are not affected by an eccentric orbit. This means that we can still first apply a cut in impact parameter  $b < 0.85$  and remove likely blends. To subsequently determine the real host star density it is sufficient to take a single high-resolution spectrum to determine  $\rho_1$  and estimate  $R_2$ . Using this spectroscopically determined density an upper limit to  $\text{ecos}(\omega)$  can be set. One particular case in our sample is CoRoT-4617 with an orbital period of  $P=19.76$  days. Assuming a circular orbit, the host star is estimated to have a density only  $\sim 4\%$  of that of the Sun, in accordance with an early B-star. This would imply that the radius of the secondary object has  $R_2 \sim 8R_{Jup}$ . However, an orbit with an eccentricity of  $e=0.5$ , orientated in the right way, could increase the estimated stellar density to that of the Sun, and decrease  $R_2$  to  $2R_{Jup}$ . This ambiguity can be easily removed by taking a single spectrum of the star, resolving its spectral type.

The method presented here is designed to remove false-positives in candidate lists through the identification of blended light. We do not assign a likelihood of planetary nature to the remaining candidates, meaning that we do not assess whether these are genuine planet systems, we just removed those systems which are not (except for a small fraction of collateral damage). However, it is anyway interesting to link blended light fractions to the population of random background eclipsing binaries. Assuming that 1:300 of field stars are eclipsing binaries (Devor et al. 2008), and 1:1000 stars have a transiting hot Jupiter, we require an average of 0.3 background stars within the PSF, and within the magnitude range set by the limit of blended light, to have an equal likelihood for the two scenarios, and to end up with half of the remaining objects as eclipsing binaries. For a typical magnitude ( $V=14.0$ ) for the candidate star, taking into account the size of the CoRoT PSF, this is reached at a  $\Delta\text{mag} = \sim 1.5$ , corresponding to  $k=0.8$ . For 8 out of the 10 remaining targets this level of blended light is excluded at the  $>3\sigma$  level. For a typical limit of  $k < 0.6$ , the background eclipsing binary can at most be 0.5 magnitudes fainter than the target star, making this scenario a factor  $\sim 5$  less likely. Do note however that this does not take into account physical triple systems, for which radial velocity follow-up is required to exclude them. Recently, the Kepler team have announced the discovery of  $\sim 1200$  planet candidates (Burucki et al. 2011). We propose to use the method presented here on this candidate list, to identify clear blend systems to obtain a better estimate on the fraction of planet systems in this sample.

## 2.6 Conclusions

In this paper we have investigated to what extent information from lightcurves of a space-based exoplanet transit survey can identify blended light scenarios and eliminate them as planet candidates, to significantly decrease the required amount of follow-up time. If a lightcurve has sufficiently high signal-to-noise, a distinction can be made between a blended eclipsing binary and a transiting exoplanet. We first have simulated lightcurves of stellar blends and transiting planet systems to determine the required signal-to-noise as a function of impact parameter and

transit depth. Our simulations show that blend scenarios can be distinguished from transiting systems at low impact parameter. At high impact parameter, blended and non-blended systems both produce V-shaped transits and are indistinguishable from each other. We have subsequently tested our method on real data from the first IRa01 field of CoRoT, concentrating on the 51 candidates already identified by the CoRoT team (Carpano et al. 2009). We show that 70% of the planet candidates in the CoRoT IRa01 field are best fit with an impact parameter of  $b > 0.85$ , whereas  $\sim 15\%$  are expected assuming random orbital orientations. By applying a cut at  $b < 0.85$ , meaning that  $\sim 15\%$  of the potential planet population would be missed, the candidate sample decreases from 41 to 11. The lightcurves of 6 of those are best fit with such a low host star density that the planet-to-star size ratio implies an unrealistic planet radius of  $R_2 > 2R_{\text{Jup}}$ . From the remaining five, two systems, CoRoT-1b and CoRoT-4b, have been identified by the CoRoT team as planets, for which the lightcurves alone rule out blended light at a 25%( $2\sigma$ ) and 40%( $2\sigma$ ). One other candidate is also consistent with a non-blended system, but is a late M-dwarf, which will always require radial velocity follow-up for confirmation since M-dwarfs can have similar radii as Jupiter mass planets. One other system consists of a candidate Neptune around a M-dwarf according to Moutou et al. (2009). We have therefore shown that 85% of the planet candidates can be rejected for the IRa01 field from the lightcurves alone. We propose to use this method on the Kepler database to study the fraction of real planets and to potentially increase the efficiency of follow-up. For long period candidates, possible non-zero eccentricity will affect the cut in planet-to-star ratio versus host star density, effectively increasing the sample size. However a single high-resolution spectrum would be sufficient to determine the real host star density and estimate the size of transiting objects.

## Bibliography

- Aigrain, S., et al. 2008, *A&A*, 488, L43  
Aigrain, S., et al. 2009, *A&A*, 506, 425  
Baglin, A., et al. 2006, 36th COSPAR Scientific Assembly, 36, 3749  
Barge, P., et al. 2008, *A&A*, 482, L17  
Barnes, J. W. 2007, *PASP*, 119, 986  
Batalha, N. M., et al. 2010, *ApJ*, 713, L103  
Batalha, N. M., Borucki, W. J., Bryson, S. T., et al. 2011, *ApJ*, 729, 27  
Borucki, W. J., et al. 2003, *Proc. SPIE*, 4854, 129  
Borucki, W. J., et al. 2011, *ApJ*, 728, 117  
Butler, R. P., et al. 2006, *ApJ*, 646, 505  
Catala, C., Appourchaux, T., & Plato Mission Consortium, t. 2011, *Journal of Physics Conference Series*, 271, 012084  
Carpano, S., et al. 2009, *A&A*, 506, 491  
Cox, A. N., & Pilachowski, C. A. 2000, *Physics Today*, 53, 100000  
Deeg, H. J., et al. 2009, *A&A*, 506, 343  
Devor J., Charbonneau D., O'Donovan F.T., Mandushev G., Torres G., 2008, *ApJ* 135, 850  
Hastings, et al. 1970, *Biometrika*, Vol. 57, No. 1. (1 April 1970), pp. 97-109  
Geman & Rubin 1992, *Statistical Science*, Vol. 7, No. 4. (Nov., 1992), pp. 457-472  
Kipping, D. M. 2010, *MNRAS*, 407, 301  
Kwee, K. K., & van Woerden, H. 1956, *Bull. Astron. Inst. Netherlands*, 12, 327  
Léger, A., et al. 2009, *A&A*, 506, 287  
Mandel, K., & Agol, E. 2002, *ApJ*, 580, L171  
Metropolis, N., Rosenbluth, A. W., Rosenbluth, M. N., Teller, A. H., & Teller, E. 1953, *J. Chem. Phys.*, 21, 1087  
Moutou, C., et al. 2009, *A&A*, 506, 321  
Pont, F., Zucker, S., & Queloz, D. 2006, *MNRAS*, 373, 231  
Popper, D. M., & Etzel, P. B. 1981, *AJ*, 86, 102  
Rauer, H., et al. 2009, *A&A*, 506, 281  
Seager, S., & Mallén-Ornelas, G. 2003, *ApJ*, 585, 1038  
Serra, P., Amblard, A., Temi, P., Burgarella, D., Giovannoli, E., Buat, V., Noll, S., & Im, S. 2011, arXiv:1103.3269  
Sing, D. K. 2010, *A&A*, 510, A21  
Smalley, B., et al. 2011, *A&A*, 526, A130  
Snellen, I. A. G., et al. 2009, *A&A*, 497, 545  
Tingley, B., Bonomo, A. S., & Deeg, H. J. 2011, *ApJ*, 726, 112  
Torres, G., et al. 2011, *ApJ*, 727, 24  
Udalski, A., Szewczyk, O., Zebrun, K., Pietrzynski, G., Szymanski, M., Kubiak, M., Soszynski, I., & Wyrzykowski, L. 2002, *Acta Astron.*, 52, 317

## Appendix

In this Appendix we discuss in detail the sample of 10 remaining CoRoT candidates, that were selected using the cut in impact parameter and were presented in Section 2.4 and Table 1. In Figures 9-11, we show for each candidate the blended light fraction  $k$  versus reduced  $\chi^2$ , and the best fitting blended light models for  $k=0.2, 0.5, 0.9$ , and  $0.95$ . In Table 2, we show best-matching system parameters for the full CoRoT IRa01, assuming no blended light.

## Comments on individual sources

### SELECTED PLANET CANDIDATES FROM THE LIGHTCURVES ALONE

*E2-1126-0102890318*

We find a  $2\sigma$  upper limit for blended light contribution of  $k < 0.14$ , therefore a blend scenario can be excluded for this source at high confidence using the lightcurve alone. In addition, by assuming that the host star is on the main sequence, its mean density points to a  $\sim 1.5R_{\text{Jup}}$  radius, well in the range of known hot Jupiters. Of course, this source is exoplanet CoRoT-1b (Barge et al. 2008).

*E1-0330-0102912369*

We find a  $2\sigma$  upper limit for blended light contribution of  $k < 0.31$  from its lightcurve, meaning that only a small contribution of blended light is tolerated. Assuming the host star is on the main sequence, its mean density points to a  $\sim 1.2R_{\text{Jup}}$  radius for the secondary. This object is identified as exoplanet CoRoT-4b (Aigrain et al. 2008). Eventhough the CoRoT-4b host star is of similar brightness as CoRoT-1b, the significantly longer orbital period, the residual variability (caused by a spotted rotating stellar photosphere) and the 1.8 times smaller transit depth are the causes of the lower confidence on blended light.

*E2-0203-0102825481*

The  $2\sigma$  upper limit for blended light is  $k < 0.3$  from its lightcurve. Radial velocity follow-up by the CoRoT team showed this to be an eclipsing binary of a low-mass M dwarf and a G-type primary (Morales et al., in prep). Assuming the host star is on the main sequence, its mean density points to a  $\sim 1.7R_{\text{Jup}}$  radius. Although not a planet, it is consistent with a non-blended system as found from our lightcurve fitting. Such systems always require RV follow-up since late M dwarfs and Jupiter-mass planets can have similar radii.

*E2-1712-0102826302*

We find a  $2\sigma$  upper limit for blended light contribution of  $k < 0.93$ . We can therefore only exclude a high contribution of blended light for this shallow (2.4 mmag) transit. This means that at  $2\sigma$  confidence the true eclipse depth is less than 2.4% in the presence of blended light. The fitted host star mean density points to an early type or evolved system. HARPS radial velocity follow-up has confirmed that the host star is an evolved fast rotator and Moutou et al. (2009) conclude that a triple system is the most probable scenario.

*E1-4108-0102779966*

Because of the poor signal-to-noise of this transit and the relatively high impact parameter  $b=0.8$ , the  $2\sigma$  upper limit for blended light is  $k < 0.95$ , therefore only a very high contribution of blended light can be excluded for this candidate. Assuming the host star is on the main sequence, its density is slightly lower compared to the solar value, indicating a stellar radius of  $R_1 \sim 1.2R_{\odot}$ . However, spectroscopic follow-up with HARPS suggested that the host is a low

mass ( $\sim 0.8M_{\odot}$ ) star. No additional follow-up has thusfar been obtained by the CoRoT team.

### **CANDIDATES REJECTED DUE TO THEIR LARGE SIZE**

*E1-4617-0102753331*

The  $2\sigma$  upper limit for blended light is  $k < 0.20$ , therefore a blend scenario can be excluded at high confidence for this source. Assuming the host star is on the main sequence, its very low density points to an early B-type primary with a K dwarf secondary. The planet hypothesis is rejected and no additional follow-up is therefore required judging from the lightcurve alone. Note that an orbit with an eccentricity of  $e=0.5$ , orientated in the right way, could increase the estimated stellar density to that of the Sun, and decrease  $R_2$  to  $2 R_{Jup}$ . This ambiguity can be easily removed by taking a single spectrum of the star, resolving its spectral type.

*E2-2430-0102815260*

We find a  $2\sigma$  upper limit for blended light contribution of  $k < 0.44$ . Again, only a small contribution of blended light is tolerated. Assuming the host star is on the main sequence, its mean density, consistent with an A type or evolved star, points to a radius  $R_2 > 2.5R_{Jup}$ . Radial velocity follow-up by the CoRoT team showed this to be a single lined eclipsing binary of a fast rotating host star and an early type M dwarf (Moutou et al. 2009).

*E2-4073-0102863810*

For this source, we find a  $2\sigma$  upper limit for blended light of  $k < 0.67$ . This object shows  $\sim 4\%$  deep eclipses around a host star that is  $\sim 20\%$  less dense than the sun. This candidate was introduced in the original list of Carpano et al. (2009), but is not mentioned in the follow-up paper of Moutou et al. (2009). With an anticipated secondary radius of  $\sim 2.1R_{Jup}$  this object could still belong to the rare group of low mass stars or brown dwarfs. In the case of a stellar M5 secondary, the secondary eclipse would be detectable at  $\sim 3.5$  mmag in depth.

*E2-1736-0102855534*

The  $2\sigma$  upper limit for blended light is  $k < 0.62$ . The low mean density of the host star, consistent with a very early main sequence or evolved star, points to a  $> 2.0R_{Jup}$  radius. Analysis of the lightcurve reveals a secondary eclipse at the  $9\sigma$  level, which indicates the secondary is in fact a low mass star. CoRoT radial velocity follow-up has confirmed that the host star is a fast rotating early type star and the system is a single lined eclipsing binary.

*E2-3724-0102759638*

For this source, we find a  $2\sigma$  upper limit for blended light of  $k < 0.78$ . Assuming the host star is on the main sequence, its very low density points to an A type primary, therefore  $R_2 > 2.0R_{Jup}$ . This object is listed both as a planet candidate and a binary by Carpano et al. (2009).

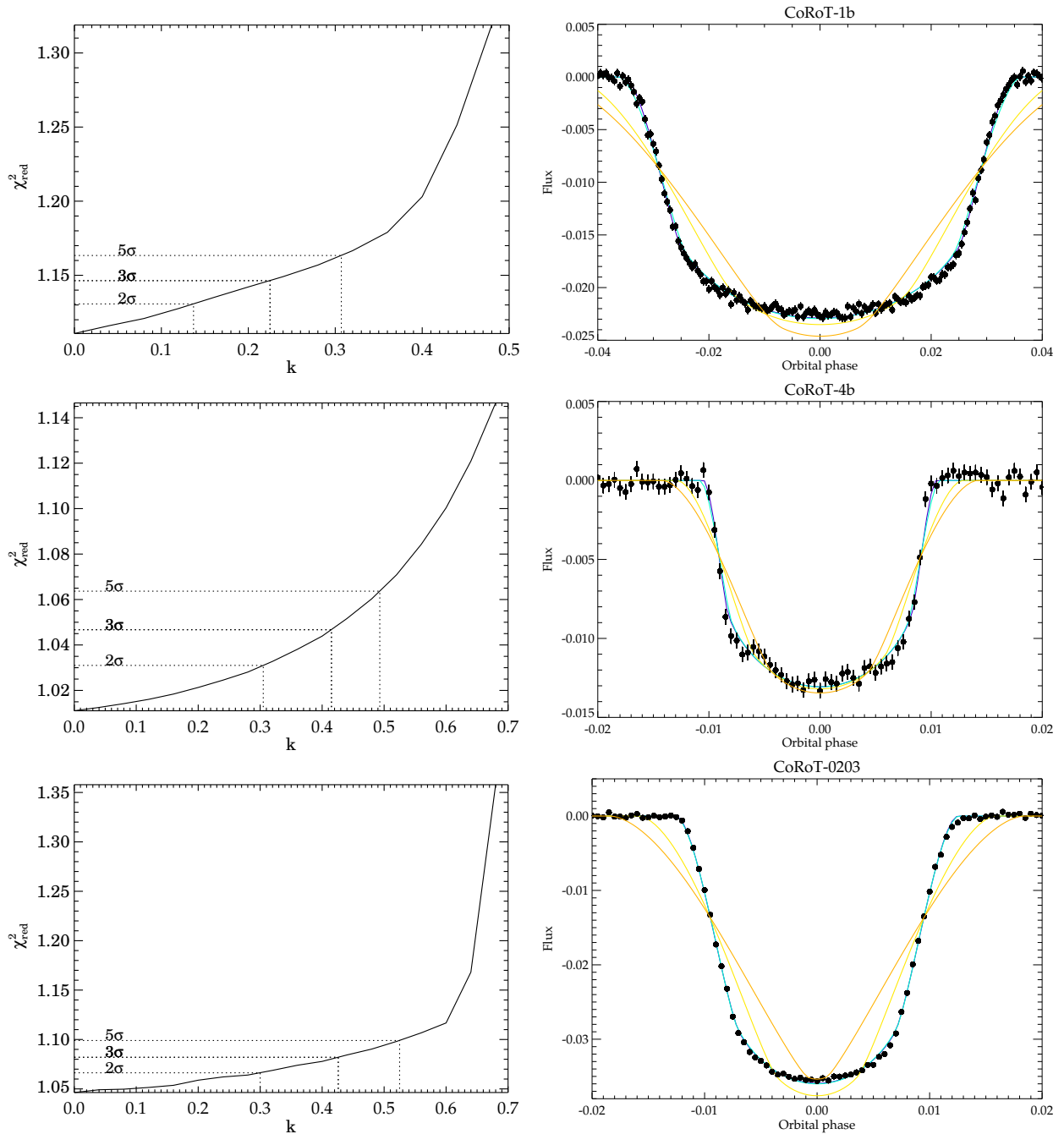


**Figure 2.9** — For each CoRoT IRa01 candidate: the blended light fraction  $k$  versus reduced  $\chi^2$  (left panels) and the best fitting blended light models for  $k=0.2, 0.5, 0.9,$  and  $0.95$ .

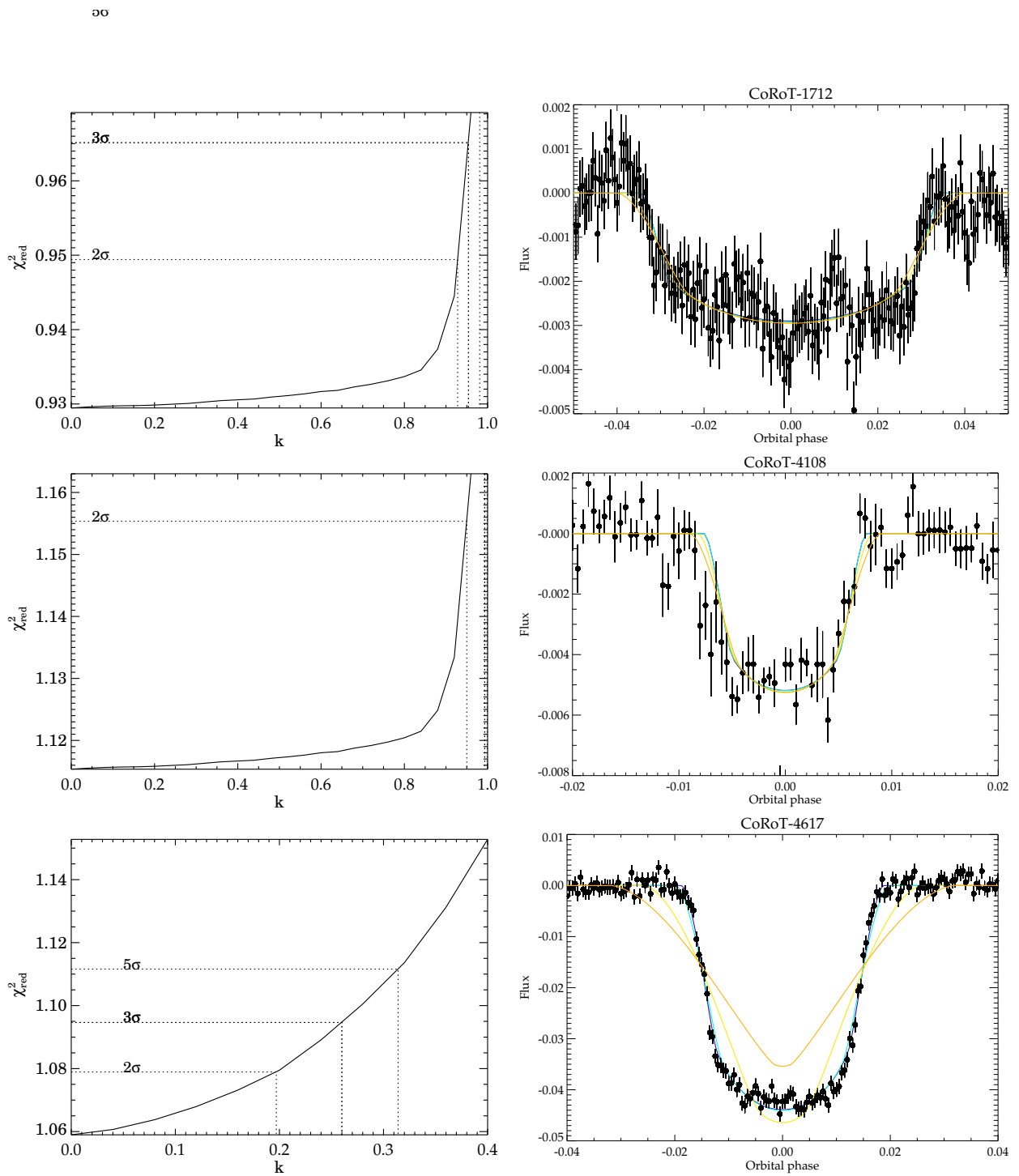


**Figure 2.10** — For each CoRoT IRa01 candidate: the blended light fraction  $k$  versus reduced  $\chi^2$  (left panels) and the best fitting blended light models for  $k=0.2, 0.5, 0.9,$  and  $0.95$ .

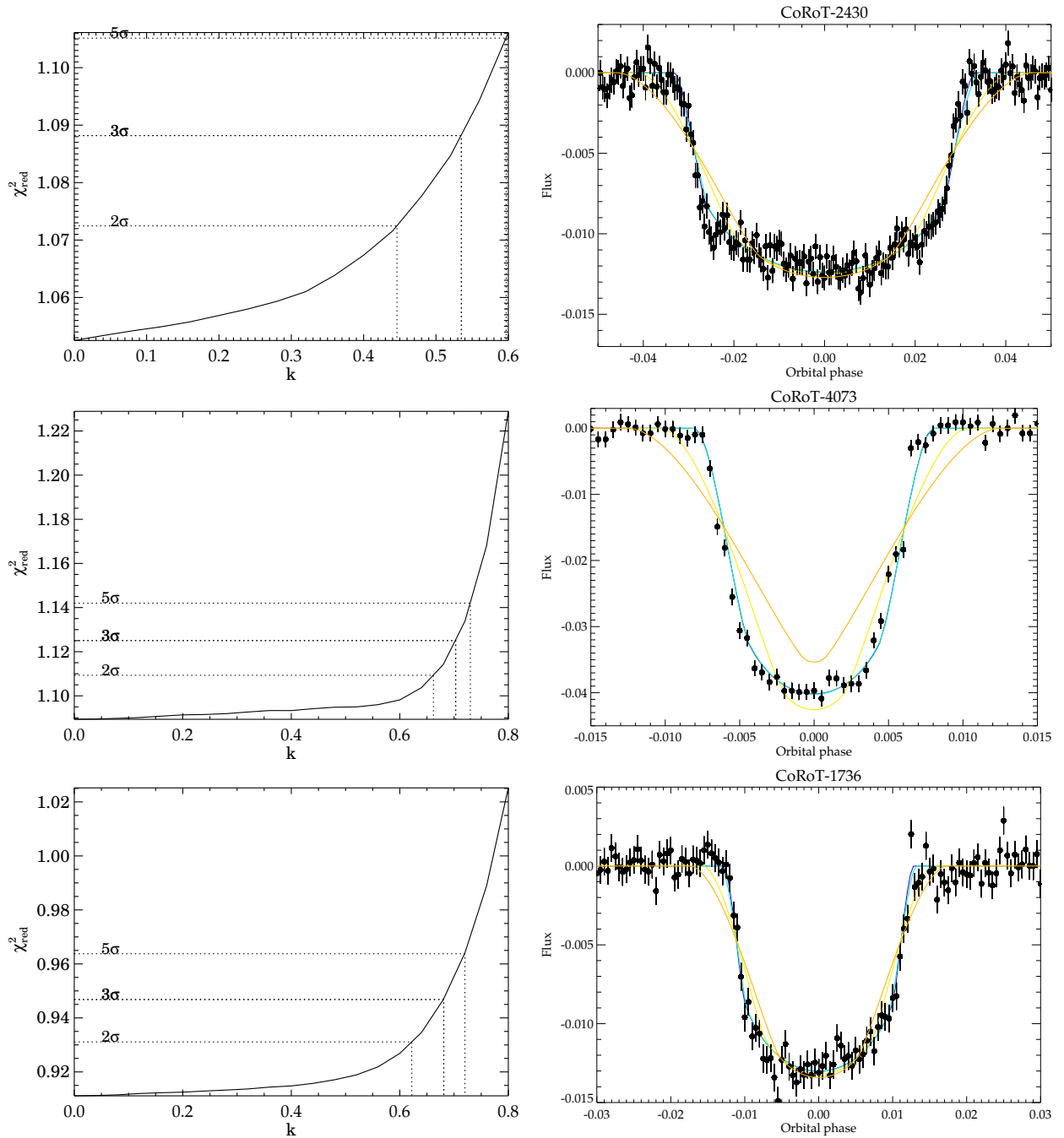


**Figure 2.11** — For each CoRoT IRa01 candidate: the blended light fraction  $k$  versus reduced  $\chi^2$  (left panels) and the best fitting blended light models for  $k=0.2, 0.5, 0.9,$  and  $0.95$ .

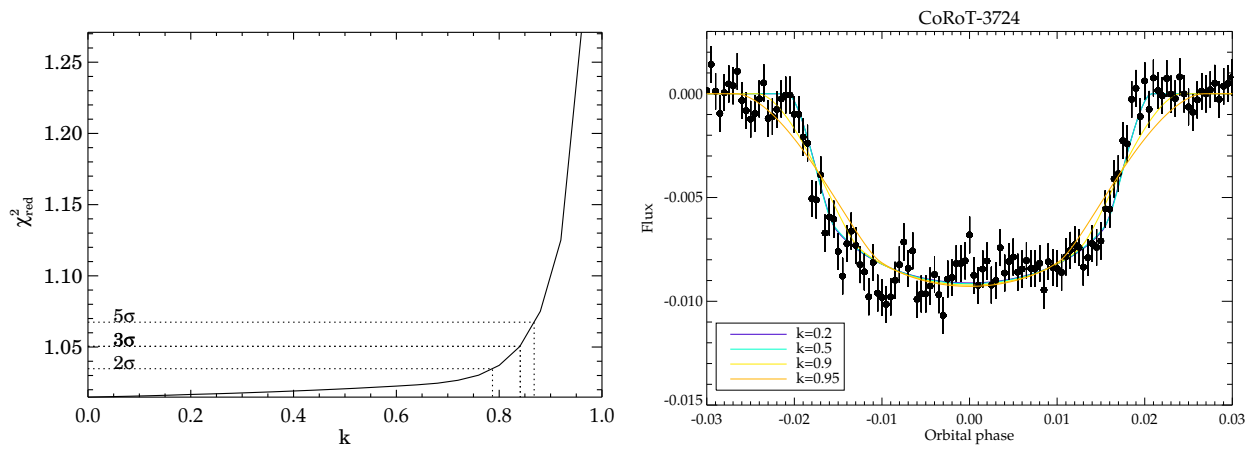


**Figure 2.12** — For each CoRoT IRa01 candidate: the blended light fraction  $k$  versus reduced  $\chi^2$  (left panels) and the best fitting blended light models for  $k=0.2, 0.5, 0.9$ , and  $0.95$ .

WinID+CoRoTID	P(days)	$\left(\frac{r_p}{r_*}\right)$	$b$	$\text{Log}\left(\frac{\rho_*}{\rho_\odot}\right)$ (error in $\left(\frac{\rho_*}{\rho_\odot}\right)$ )	$\left(\frac{a}{R_*}\right)$
1319 0102729260	1.70	0.17	1.09(0.011)	-1.36(0.004)	2.14
1158 0102763847	10.53	0.27	1.10(0.017)	0.13(0.044)	22.50
0288 0102787048	7.89	0.06	0.90(0.016)	-0.97(0.024)	8.01
3787 0102787204	0.86	0.26	1.22(0.040)	-1.55(0.002)	1.17
1857 0102798247	0.82	0.07	0.91(0.013)	-0.78(0.015)	2.04
4591 0102806520	4.30	0.29	1.21(0.085)	-0.83(0.062)	5.94
1136 0102809071	1.22	0.09	1.03(0.018)	-1.61(0.002)	1.41
2430 0102815260	3.59	0.10	0.24(0.107)	-0.81(0.014)	5.36
0203 0102825481	5.17	0.18	0.62(0.006)	0.04(0.016)	13.09
1712 0102826302	2.77	0.05	0.60(0.287)	-0.88(0.074)	4.27
0399 0102829121	33.06	0.13	0.85(0.017)	0.57(0.243)	67.81
1736 0102855534	21.72	0.11	0.43(0.119)	-1.24(0.009)	12.77
0396 0102856307	7.82	0.34	1.32(0.035)	-1.90(0.030)	3.90
1126 0102890318	1.51	0.14	0.43(0.017)	-0.16(0.017)	4.93
0330 0102912369	9.20	0.10	0.18(0.119)	-0.13(0.042)	16.96
2755 0102918586	4.39	0.26	1.01(0.005)	-0.21(0.006)	9.72
4617 0102753331	19.76	0.19	0.10(0.090)	-1.42(0.001)	10.47
3724 0102759638	12.33	0.10	0.50(0.105)	-1.33(0.008)	8.17
4290 0102777119	2.21	0.14	1.05(0.010)	-2.77(0.010)	0.86
4108 0102779966	7.37	0.07	0.80(0.085)	-0.06(0.492)	15.41
1531 0102780627	2.38	0.09	0.91(0.009)	-0.68(0.020)	4.49
2009 0102788073	10.85	0.25	1.17(0.432)	-1.44(0.045)	6.88
2774 0102798429	1.61	0.29	1.19(0.133)	-1.32(0.003)	2.12
3010 0102800106	23.21	0.22	1.00(0.127)	-0.17(0.091)	30.33
4300 0102802430	5.81	0.12	1.00(0.025)	-1.02(0.006)	6.27
2604 0102805893	3.82	0.38	1.33(0.052)	-1.60(0.009)	3.04
2648 0102812861	3.68	0.10	0.92(0.070)	-0.82(0.010)	5.42
2328 0102819021	4.51	0.12	0.97(0.037)	-1.66(0.008)	3.24
4998 0102821773	10.08	0.14	0.88(0.011)	-0.19(0.067)	17.19
3425 0102835817	1.19	0.32	1.25(0.024)	-1.65(0.008)	1.34
3854 0102841669	1.14	0.05	0.94(0.050)	-1.40(0.003)	1.59
3952 0102842120	13.48	0.08	0.85(0.356)	1.47(0.068)	74.27
1407 0102842459	5.17	0.27	1.02(0.013)	0.49(0.040)	18.45
2721 0102850921	0.61	0.29	1.18(0.017)	-0.97(0.004)	1.46
0704 0102855472	2.16	0.08	0.62(0.043)	-1.38(0.005)	2.45
4073 0102863810	15.00	0.18	0.36(0.036)	-0.08(0.047)	24.40
2329 0102869286	1.87	0.13	1.04(0.432)	-1.41(0.586)	2.19
3336 0102876631	1.39	0.04	0.84(0.110)	-0.69(0.121)	3.12
4911 0102881832	2.17	0.26	1.12(0.010)	-1.97(0.013)	1.57
4339 0102903238	1.36	0.07	1.00(0.126)	-1.63(0.062)	1.50
4124 0102926194	1.51	0.41	1.37(0.041)	-1.74(0.005)	1.47
3819 0102932089	1.57	0.30	1.07(0.035)	-0.97(0.012)	2.73
4467 0102940315	16.45	0.19	0.98(0.049)	-0.86(0.010)	14.25
3856 0102954464	16.56	0.49	1.31(0.047)	0.55(0.347)	42.02

**Table 2.2** — The fitting parameters for our blend models when applied to the CoRoT IRa01 sample, assuming  $k=0$ .

---

## Chapter 3

---

# Discovery and characterisation of detached M-dwarf eclipsing binaries in the WFCAM Transit Survey

We report the discovery of 16 detached M-dwarf eclipsing binaries with  $J < 16$  mag and provide a detailed characterisation of three of them, using high-precision infrared light curves from the WFCAM Transit Survey (WTS). Such systems provide the most accurate and model-independent method for measuring the fundamental parameters of these poorly understood yet numerous stars, which currently lack sufficient observations to precisely calibrate stellar evolution models. We fully solve for the masses and radii of three of the systems, finding orbital periods in the range  $1.5 < P < 4.9$  days, with masses spanning  $0.35 - 0.50M_{\odot}$  and radii between  $0.38 - 0.50R_{\odot}$ , with uncertainties of  $\sim 3.5 - 6.4\%$  in mass and  $\sim 2.7 - 5.5\%$  in radius. Close-companions in short-period binaries are expected to be tidally-locked into fast rotational velocities, resulting in high levels of magnetic activity. This is predicted to inflate their radii by inhibiting convective flow and increasing star spot coverage. The radii of the WTS systems are inflated above model predictions by  $\sim 3 - 12\%$ , in agreement with the observed trend, despite an expected lower systematic contribution from star spots signals at infrared wavelengths. We searched for correlation between the orbital period and radius inflation by combining our results with all existing M-dwarf radius measurements of comparable precision, but we found no statistically significant evidence for a decrease in radius inflation for longer period, less active systems. Radius inflation continues to exist in non-synchronised systems indicating that the problem remains even for very low activity M-dwarfs. Resolving this issue is vital not only for understanding the most populous stars in the Universe, but also for characterising their planetary companions, which hold the best prospects for finding Earth-like planets in the traditional habitable zone.

J.L.B. Birkby, S.V. Nefs, S.T. Hodgkin, G. Kovács, B. Sipőcz,  
, D.J. Pinfield, I.A.G. Snellen, D. Mislis, F. Murgas, N. Lodieu  
E. de Mooij, N. Goulding, P. Cruz, H. Stoev, M. Cappetta  
E. Palle, D. Barrado, R. Saglia, E. Martin, Y. Pavlenko  
*MNRAS* 426, B1507 (2012)

### 3.1 Introduction

M-dwarfs ( $M_* \lesssim 0.6M_\odot$ ) constitute more than seventy per cent of the Galactic stellar population (Henry et al. 1997) and consequently, they influence a wide-range of astrophysical phenomena, from the total baryonic content of the universe, to the shape of the stellar initial mass function. Furthermore, they are fast becoming a key player in the hunt for Earth-like planets (e.g. Nutzman & Charbonneau 2008; Koppenhoefer et al. 2009; Law et al. 2011). The lower masses and smaller radii of M-dwarfs mean that an Earth-like companion causes a deeper transit and induces a greater reflex motion in its host than it would do to a solar analogue, making it comparatively easier to detect Earths in the traditional habitable zones of cool stars. The inferred properties of exoplanet companions, such as their density, atmospheric structure and composition, currently depend on a precise knowledge of the fundamental properties of the host star, such as its mass, radius, luminosity and effective temperature at a given age. Yet, to date, no theoretical model of low-mass stellar evolution can accurately reproduce all of the observed properties of M-dwarfs (Hillenbrand & White 2004; López-Morales & Ribas 2005), which leaves their planetary companions open to significant mischaracterisation. Indeed, the characterisation of the atmosphere of the super-Earth around the M-dwarf GJ 1214 seems to depend on the spot coverage of the host star (de Mooij et al. 2012).

Detached, double-lined, M-dwarf eclipsing binaries (MEBs) provide the most accurate and precise, model-independent means of measuring the fundamental properties of low-mass stars (Andersen 1991), and the coevality of the component stars, coupled with the assumption that they have the same metallicity due to their shared natal environment, places stringent observational constraints on stellar evolution models. In the best cases, the uncertainties on the masses and radii measured using MEBs can be just 0.5% (Morales et al. 2009; Kraus et al. 2011). However, since M-dwarfs are intrinsically faint, only a small number of MEBs have been characterised so far with suitable accuracy to calibrate low-mass stellar evolution models, and there are even fewer measurements below  $\sim 0.35M_\odot$ , where stellar atmospheres are thought to transport energy purely by convection (Chabrier & Baraffe 1997).

More worryingly, existing observations show significant discrepancies with stellar models. The measured radii of M-dwarfs are inflated by 5 – 10% compared to model estimates and their effective temperatures appear too cool by 3 – 5% (see e.g. Torres & Ribas 2002; López-Morales & Ribas 2005; Ribas 2006; Morales et al. 2010; Torres et al. 2010; Kraus et al. 2011). This anomaly has been known for some time but remains enigmatic. Bizarrely, the two discrepancies compensate each other in the mass-luminosity plane such that current stellar models can accurately reproduce the observed mass-luminosity relationship for M-dwarfs. Two different physical mechanisms have been suggested as the cause of this apparent radius inflation: i) metallicity (Berger et al. 2006; López-Morales 2007) and ii) magnetic activity (Mullan & MacDonald 2001; Ribas 2006; Torres et al. 2006; Chabrier et al. 2007).

Berger et al. (2006) and López-Morales (2007) used interferometrically-measured radii of single, low-mass stars to look for correlation between inflation and metallicity. Both studies found evidence that inactive, single stars with inflated radii corresponded to stars with higher metallicity, but this did not hold true for active, fast-rotating single stars and further studies could not confirm the result (Demory et al. 2009). While metallicity may play a role in the scatter of effective temperatures for a given mass (the effective temperature depends on the bolometric luminosity which is a function of metallicity), it seems unlikely that it is the main

culprit of radius inflation.

The magnetic activity hypothesis is steered by the fact that the large majority of well-characterised MEBs are in short ( $< 2$  day) orbits. Such short period systems found in the field (i.e. old systems) are expected to be tidally-synchronised with circularised orbits (Zahn 1977). The effect of tidal-locking is to increase magnetic activity and is a notion that is supported by observations of synchronous, rapid rotation rates in MEBs, a majority of circular orbits for MEBs, plus X-ray emission and  $H\alpha$  emission from at least one of the components. It is hypothesised that increased magnetic activity affects the radius of the star in two ways. Firstly, it can inhibit the convective flow, thus the star must inflate and cool to maintain hydrostatic equilibrium. Chabrier et al. (2007) modelled this as a change in the convective mixing length, finding that a reduced mixing length could account for the inflated radii of stars in the partially-radiative mass regime, but it had negligible effect on the predicted radii of stars in the fully-convective regime. However, Jackson et al. (2009) showed that the radii of young, single, active, fully-convective stars in the open cluster NGC 2516 could be inflated by up to 50%, based on radii derived using photometrically-measured rotation rates and spectroscopically-measured projected rotational velocities. This therefore suggests that inhibition of convective flow is not the only factor responsible for the radius anomaly.

The second consequence of increased magnetic activity is a higher production of photospheric spots which has a two-fold effect: i) a loss of radiative efficiency at the surface, causing the star to inflate and ii) a systematic error in light curve solutions due to a loss of circular symmetry caused by a polar distribution of spots. Morales et al. (2010) showed that these two effects could account for  $\sim 3\%$  and  $0 - 6\%$  of the radius inflation, respectively, with any remaining excess ( $0 - 4\%$ ) produced by inhibition of convective efficiency. This however is only under certain generalisations, such as a 30% spot coverage fraction and a concentration of the spot distribution at the pole. One would perhaps expect the systematic error induced by star spots to be wavelength dependant, such that radius measurements obtained at longer wavelength would be closer to model predictions.

Kraus et al. (2011) searched for correlation between the radius anomaly and the orbital periods of MEBs, to see if the data and the models converged at longer periods ( $\sim 3$  days) where the stellar activity is less aggravated by fast rotation speeds. They found tentative evidence to suggest that this is the case but it is currently confined to the realm of small statistics. Not long after their study, the MEarth project uncovered a 41-day, non-synchronised, non-circularised, inactive MEB with radius measurements still inflated on average by  $\sim 4\%$ , despite a detailed attempt to account for spot-induced systematics (Irwin et al. 2011). They suggest that either a much larger spot coverage than the 30% they assumed is required to explain the inflation, or perhaps that the equation of state for low-mass stars, despite substantial progress (see review by Chabrier et al. 2005), is still inadequate.

Clearly, a large sample of MEBs with a wide-range of orbital periods is key to defining the magnetic activity effect and understanding any further underlying physical issues for modelling the evolution of low-mass single stars. This in turn will remove many uncertainties in the properties of exoplanets with M-dwarf host stars. With that in mind, this paper presents the discovery of many new MEBs to emerge from the WFCAM Transit Survey, including a full characterisation to reasonable accuracy for three of the systems using 4-m class telescopes, despite their relatively faint magnitudes ( $i = 16.7 - 17.6$ ).

In Section 3.2, we describe the WFCAM Transit Survey (WTS) and its observing strat-

egy, and Section 3.3 provides additional details of the photometric and spectroscopic data we used to fully characterise three of the MEBs. In Section 3.4, we outline how we identified the MEBs amongst the large catalogue of light curves in the WTS. Sections 3.5-3.7 present our analysis of all the available follow-up data used to characterise three of the MEBs including their system effective temperatures, metallicities,  $H\alpha$  emission and surface gravities, via analysis of low-resolution spectroscopy, their size-ratio and orbital elements using multi-colour light curves, and their mass ratios using radial velocities obtained with intermediate-resolution spectra. These results are combined in Section 3.8 to determine individual masses, radii, effective temperatures. We also calculate their space velocities and assess their membership to the Galactic thick and thin disks. Lastly, in Section 3.9, we discuss our results in the context of low-mass stellar evolution models and a mass-radius-period relationship, as suggested by Kraus et al. (2011).

## 3.2 The WFCAM Transit Survey

We identified our new MEBs using observations from the WFCAM Transit Survey (WTS) (Birkby et al. 2011). The WTS is an on-going photometric monitoring campaign that operates on the 3.8m United Kingdom Infrared Telescope (UKIRT) at Mauna Kea, Hawaii. Its primary and complementary science goals are: i) to provide a stringent observational constraint on planet formation theories through a statistically meaningful measure of the occurrence rate of hot Jupiters around low-mass stars (Kovacs et al. 2012; submitted) and ii) to detect a large sample of eclipsing binaries stars with low-mass primaries and characterise them to high enough accuracy such that we strongly constrain the stellar evolution models describing the planet-hosting M-dwarfs found in the survey. The WTS contains  $\sim 6,000$  early to mid M-dwarfs with  $J \leq 16$  mag, covering four regions of the sky which span a total of 6 square degrees.

We combine the large aperture of UKIRT with the Wide-Field Camera (WFCAM) infrared imaging array to observe in the  $J$ -band ( $1.25\mu\text{m}$ ), near the peak of the spectral energy distribution (SED) of a cool star. Our observing strategy takes advantage of a unique opportunity offered by UKIRT, thanks to the highly efficient queue-scheduled operational mode of the telescope. Rather than requesting continuous monitoring, we noted there was room for a flexible proposal in the queue, which did not require the very best observing conditions, unlike most of the on-going UKIRT programmes that require photometric skies with seeing  $< 1.3''$  (Lawrence et al. 2007). The WTS is therefore designed in such a way that there is always at least one target field visible and it can observe in mediocre seeing and thin cloud cover. We chose four target fields to give us year-round visibility, with each field passing within 15 degrees of zenith. To select the fields, we combined 2MASS photometry and the dust extinction maps of Schlegel et al. (1998) to find regions of sky that maximised the number of dwarf stars and maximised the ratio of dwarfs to giants (Cruz et al. 2003), while maintaining  $E(B - V) < 0.1$ . We stayed relatively close to the galactic plane to increase the number of early M-dwarfs, but restricted ourselves to  $b > 5$  degrees to avoid the worst effects of overcrowding.

The survey began on August 05, 2007, and the eclipsing systems presented in this paper are all found in just one of the four WTS fields. The field is centred on RA = 19h, Dec = +36d, (hereafter, the 19h field), for which the WTS has its most extensive coverage, with 1145 data points as of June 16, 2011. Note that this field is very close to, but does not overlap with,

the Kepler field (Batalha et al. 2006), but it is promising that recent work showed the giant contamination in the Kepler field for magnitudes in a comparable range to our survey was low ( $7 \pm 3\%$  M-giant fraction for  $K_P > 14$ ), Mann et al. 2012.

## 3.3 Observations and Data Reduction

### 3.3.1 UKIRT/WFCAM *J*-band photometry

UKIRT and the WFCAM detector provide the survey with a large database of infrared light curves in which to search for transiting and eclipsing systems. The WFCAM detector consists of four  $2048 \times 2048$   $18\mu\text{m}$  pixel HgCdTe Rockwell Hawaii-II, non-butable, infrared arrays that each cover  $13.65' \times 13.65'$  and are separated by 94% of a chip width (Casali et al. 2007). Each WTS field covers 1.5 square degrees of sky, comprising of eight pointings of the WFCAM paw print, exposing for a 9-point jitter pattern with 10 second exposures at each position, and tiled to give uniform coverage across the field. It takes 15 minutes to observe an entire WTS field ( $9 \times 10\text{s} \times 8 + \text{overheads}$ ), resulting in a cadence of 4 data points per hour (corresponding to one UKIRT Minimum Schedulable Block). Unless there are persistently bad sky conditions at Mauna Kea, due to our relaxed observing constraints the WTS usually observes only at the beginning of the night, just after twilight in  $> 1''$  seeing when the atmosphere is still cooling and settling.

The 2-D image processing of the WFCAM observations and the generation of light curves closely follows that of Irwin et al. (2007b) and is explained in detail in Kovacs et al. (2012; submitted). We refer the avid reader to these publications for an in-depth discussion of the reduction techniques but briefly describe it here. For image processing, we use the automatically reduced images from the Cambridge Astronomical Survey Unit pipeline<sup>1</sup>, which is based on the INT wide-field survey pipeline (Irwin & Lewis 2001). This provides the 2-D instrumental signature removal for infrared arrays including the removal of the dark and reset anomaly, the flat-field correction using twilight flats, deurtaining and sky subtraction. We then perform astrometric calibration using 2MASS stars in the field-of-view, resulting in an astrometric accuracy of  $\sim 20 - 50$  mas after correcting for field and differential distortion<sup>2</sup>. For photometric calibration, the detector magnitude zero-point is derived for each frame using measurements of stars in the 2MASS Point Source Catalogue that fall within the same frame (Hodgkin et al. 2009).

In order to generate a master catalogue of source positions for each field in the *J*-band filter, we stack 20 frames taken in the best conditions (i.e. seeing, sky brightness and transparency) and run our source detection software on the stacked image (Irwin 1985; Irwin & Lewis 2001). The resulting source positions are used to perform co-located, variable, ‘soft-edged’ (i.e. pro-rata flux division for boundary pixels) aperture photometry on all of the time-series images (see Irwin et al. 2007b).

For each of the four WFCAM detector chips, we model the flux residuals in each frame as a function of position using a 2-D quadratic polynomial, where the residuals are measured for each object as the difference between its magnitude on the frame in question and its median magnitude calculated across all frames. By subtracting the model fit, this frame-to-frame cor-

<sup>1</sup><http://casu.ast.cam.ac.uk/surveys-projects/wfcam/technical>

<sup>2</sup><http://casu.ast.cam.ac.uk/surveys-projects/wfcam/technical/astrometry>

rection can account for effects such as flat-fielding errors, or varying differential atmospheric extinction across each frame, which can be significant in wide-field imaging (see e.g. Irwin et al. 2007b).

Our source detection software flags any objects with overlapping isophotes. We used this information in conjunction with a morphological image classification flag also generated by the pipeline to identify non-stellar or blended objects. The plate scale of WFCAM ( $0.4''/\text{pix}$ ) is significantly smaller than those of most small aperture, ground-based transit survey instruments, such as SuperWASP (Pollacco et al. 2006), HATNet (Bakos et al. 2004) and TrES (Dunham et al. 2004), and can have the advantage of reducing the numbers of blended targets, and therefore the numbers of transit mimics, despite observing fainter stars.

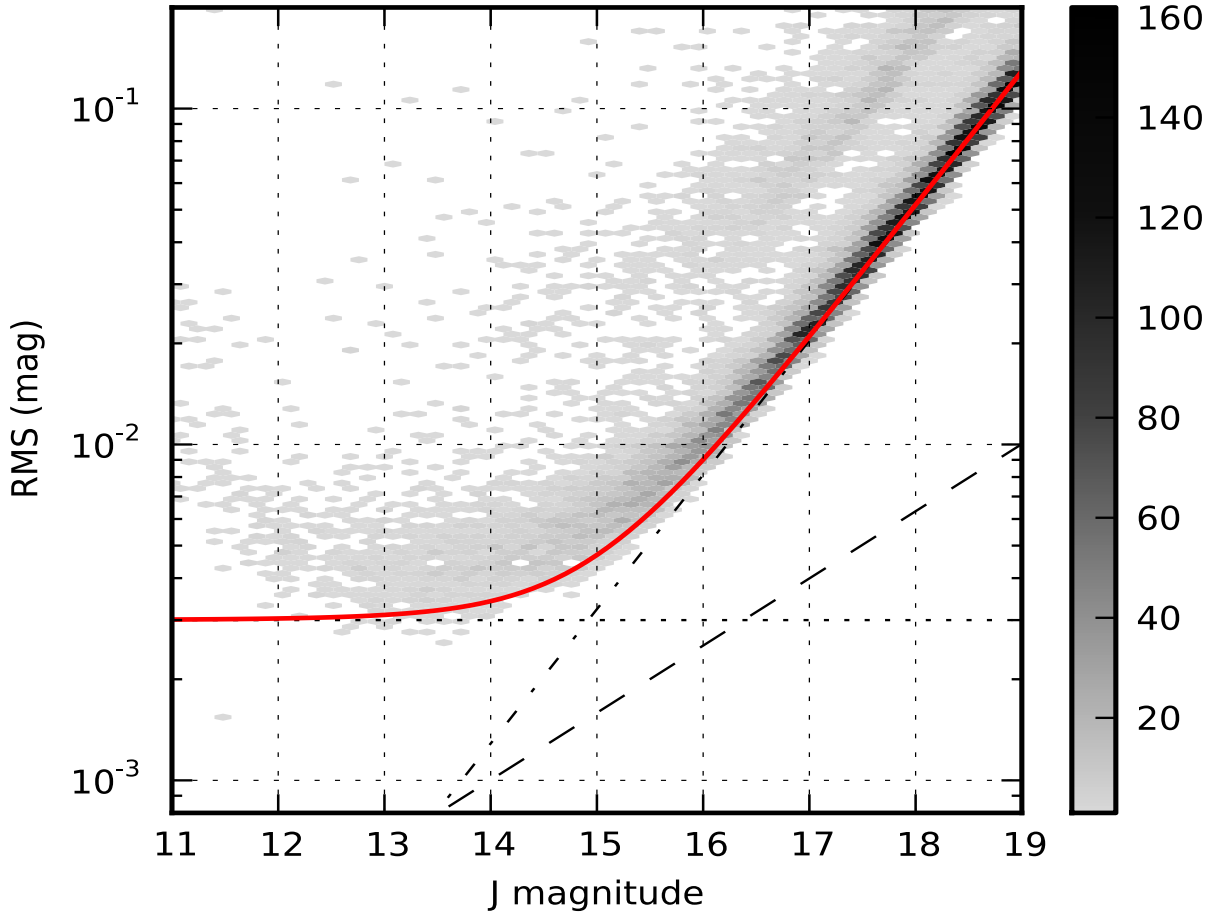
The last step in the light curve generation is to perform a correction for residual seeing-correlated effects caused by image blending that are not removed by the frame-to-frame correction. For each light curve, we model the deviations from its median flux as a function of the stellar image FWHM on the corresponding frame, using a quadratic polynomial that we then subtract. We note that this method addresses the symptoms, but not the cause, of the effects of blending.

Figure 3.1 shows the per data point photometric precision of the final light curves for the stellar sources in the 19hr field. The RMS is calculated as a robust estimator using as  $1.48 \times \text{MAD}$ , i.e. the equivalent of the Gaussian RMS, where the MAD is the median of the absolute deviations (Hoaglin et al. 1983). The upturn between  $J \sim 12 - 13$  mag marks the saturation limit, so for our brightest objects, we achieve a per data point precision of  $\sim 3 - 5$  mmag. The blue solid line shows the median RMS in bins of 0.2 mag. The median RMS at  $J = 16$  mag is  $\sim 1\%$  ( $\sim 10$  mmag), with a scatter of  $\sim 0.8 - 1.5\%$ , and only 5% of sources have an RMS greater than 15 mmag at this magnitude. Hence, for the majority of sources with  $J \leq 16$  mag, the precision is in theory suitable for detecting not only M-dwarf eclipsing binaries but also transits of mid-M stars by planets with radii  $\sim 1R_{\oplus}$  (see Kovacs et al. (2012;submitted) for the WTS sensitivity to Jupiter- and Neptune-sized planets). The 16 new MEBs are shown on the plot by the red star symbols. Note that shorter period MEBs sit higher on the RMS diagram, but that genuine longer period MEBs still have RMS values close to the median, due to our robust estimator and the long observing baseline of the survey.

For the MEB light curves characterised in this paper, we perform an additional processing step, in which we use visual examination to clip several clear outlying data points at non-consecutive epochs.

The WTS  $J$ -band light curve data for the MEBs reported in this paper are given in Table 3.1. We have adopted a naming system that uniquely identifies each source handled by our data reduction process, and thus we refer to MEBs characterised in this paper as: 19b-2-01387, 19c-3-01405, and 19e-3-08413. The first number in the naming strategy gives the Right Ascension hour the target field. The following letter corresponds to one of the eight pointings that make up the whole WTS target field. The number between the hyphens denotes which of the four WFCAM chips the source is detected on and the final 5 digits constitute the source's unique sequence number in our master catalogue of WTS sources.

Some sources in the WTS fields are observed multiple times during a full field pointing sequence due to the slight overlap in the exposed areas in the tile pattern. 19c-3-01405 is one such target, receiving two measurements for every full field sequence. The median magnitude for 19c-3-01405 on each chip differs by 32 mmag. Hodgkin et al. (2009) claim a photometric



**Figure 3.1** — The RMS scatter per data point of the WTS light curves as a function of WFCAM  $J$  magnitude, for sources in the 19hr field with stellar morphological classification. The RMS is a robust estimator calculated as  $1.48 \times$  the median of the absolute deviations. We achieve a per data point photometric precision of 3 – 5 mmag for the brightest objects, with a median RMS of  $\sim 1\%$  for  $J = 16$  mag. Saturation occurs between  $\sim 12 - 13$  mag as it varies across the field and with seeing. The dashed red horizontal line at 3 mmag marks the limit of our photometric precision. The blue solid curve shows the median RMS in bins of 0.2 mag. The red stars show the positions of the 16 WTS 19hr field MEBs. The shorter period MEBs sit higher in the plot. RMS values are given in Table 3.14

calibration error of 1.5% for WFCAM thus the median magnitudes have a  $\sim 2\sigma$  calibration error. The photometric calibration uses 2MASS stars that fall on chip in question, so different calibration stars are used for different chips and pointing. We combined the light curves from both exposures to create a single light curve with  $893 + 898 = 1791$  data points, after first subtracting the median flux from each light curve. The combined light curve has the same out-of-eclipse RMS, 8 mmag, as the two single light curves. The other two MEBs, 19b-2-01387 and 19e-3-08413, have 900 and 899 data points and an out-of-eclipse RMS of 5 mmag and 7 mmag, respectively.

We also obtained single, deep exposures of each WTS field in the WFCAM  $Z$ ,  $Y$ ,  $J$ ,  $H$  and  $K$  filters (exposure times 180, 90, 90,  $4 \times 90$  and  $4 \times 90$  seconds, respectively). These are used

Name	HJD	$J_{\text{WTS}}$ (mag)	$\sigma_{J_{\text{WTS}}}$ (mag)	$\Delta m_0^a$ (mag)	FWHM <sup>b</sup> (pix)	$x^c$ (pix)	$y^c$ (pix)
19b-2-01387	2454317.808241	14.6210	0.0047	0.0001	2.17	321.98	211.07
19b-2-01387	2454317.820311	14.6168	0.0047	0.0002	2.37	321.74	210.88
...	...	...	...	...	...	...	...

**Table 3.1** — The WTS *J*-band light curves of 19b-2-01387, 19c-3-01405 and 19e-3-08413. Magnitudes are given in the WFCAM system. Hodgkin et al. (2009) provide conversions for other systems. The errors,  $\sigma_J$ , are estimated using a standard noise model, including contributions from Poisson noise in the stellar counts, sky noise, readout noise and errors in the sky background estimation. <sup>a</sup> Correction to the frame magnitude zero point applied in the differential photometry procedure. More negative numbers indicate greater losses. See Irwin et al. (2007b). <sup>b</sup> Median FWHM of the stellar images on the frame. <sup>c</sup>  $x$  and  $y$  pixel coordinates the MEB systems on the image, derived using a standard intensity-weighted moments analysis. (This table is published in full in the online journal and is shown partially here for guidance regarding its form and content.)

in conjunction with  $g, r, i$  and  $z$  photometry from SDSS DR7 to create SEDs and derive first estimates of the effective temperatures for all sources in the field, as described in Section 3.4.1.

### 3.3.2 INT/WFC *i*-band follow-up photometry

Photometric follow-up observations to help test and refine our light curve models were obtained in the Sloan *i*-band using the Wide Field camera (WFC) on the 2.5m Isaac Newton Telescope (INT) at Roque de Los Muchachos, La Palma. We opted to use the INT’s Sloan *i* filter rather than the RGO *I*-band filter as i) it has significantly less fringing and, ii) unlike the RGO filter, it has a sharp cut-off at  $\sim 8500 \text{ \AA}$  and therefore avoids strong, time-variable telluric water vapour absorption lines, which could induce systematics in our time-series photometry (Bailer-Jones & Lamm 2003). The observing run, between July 18 - August 01, 2010, was part of a wider WTS follow-up campaign to confirm planetary transit candidates and thus only a few windows were available to observe eclipses. Using the WFC in fast mode (readout time 28 sec. for  $1 \times 1$  binning), we observed a full secondary eclipse of 19b-2-01387 and both a full primary and a full secondary eclipse of 19e-3-08413. The observations were centred around the expected times of primary and secondary eclipse, allowing at least 30 minutes of observation either side of ingress and egress to account for any uncertainty in our predicted eclipse times based on the modelling of the WTS light curves. In total, we observed 120 epochs for the secondary eclipse of 19b-2-01387 using 60s exposures, and 89 and 82 data points for the primary and secondary eclipse of 19e-3-08413, respectively, using 90s exposures.

We reduced the data using custom built IDL routines to perform the standard 2-D image processing (i.e. bias subtraction and flat-field division). Low-level fringing was removed by subtracting a scaled super sky-frame. To create the light curves, we performed variable aperture photometry using circular apertures with the IDL routine *APER*. The sky background was estimated using a  $3\sigma$ -clipped median on a  $30 \times 30$  pixel box, rejecting bad pixels. For each MEB, we selected sets of 15-20 bright, nearby, non-saturated, non-blended reference stars to create a master reference light curve. For each reference star, we selected the aperture with the smallest out-of-eclipse RMS. We removed the airmass dependence by fitting a second order polynomial

Name	HJD	$\Delta m_{i_{\text{INT}}}$ (mag)	$\sigma_{m_{i_{\text{INT}}}}$ (mag)
19b-2-01387	2455400.486275	-0.0044	-0.0034
19b-2-01387	2455400.487652	-0.0049	-0.0024
...	...	...	...

**Table 3.2** — INT  $i$ -band follow-up light curves of 19b-2-01387 and 19e-3-08413.  $\Delta m_{i_{\text{INT}}}$  are the differential magnitudes with respect to the median of the out-of-eclipse measurements such that the out-of-eclipse magnitude is  $m_{i_{\text{INT}}} = 0$ . The errors,  $\sigma_i$ , are the scaled Gaussian equivalents of the median absolute deviation of the target from the reference at each epoch i.e.  $\sigma_i \sim 1.48 \times \text{MAD}$ . (This table is published in full in the online journal and is shown partially here for guidance regarding its form and content.)

to the out-of-eclipse data.

The INT  $i$ -band light curve data is presented in Table 3.2. The RMS of the out-of-eclipse data for the primary eclipse of 19b-2-01387 is 4.4 mmag while the out-of-eclipse RMS values for the primary and secondary eclipses of 19e-3-08413 are 5.7 mmag and 7.1 mmag, respectively.

### 3.3.3 IAC80/CAMELOT $g$ -band follow-up photometry

We obtained a single primary eclipse of 19e-3-08413 in the Sloan  $g$ -band filter using the CAMELOT CCD imager on the 80cm IAC80 telescope at the Observatorio del Teide in Tenerife. The observations were obtained on the night of 08 August 2009, during a longer run to primarily follow-up WTS planet candidates. Exposure times were 60 seconds and were read out with  $1 \times 1$  binning of the full detector, resulting in a cadence of 71 seconds, making a total of 191 observations for the night.

The time-series photometry was generated using the VAPHOT package<sup>3</sup> (Deeg & Doyle 2001). The bias and flat field images were processed using standard IRAF routines in order to calibrate the raw science images. The light curve was then generated using VAPHOT, which is a series of modified IRAF routines that performs aperture photometry; these routines find the optimum size aperture that maximize the signal-to-noise ratio for each star. The user can specify whether to use a variable aperture to account for a time-variable point-spread-function (e.g. due to changes in the seeing) or to fix it for all images. For this data set, we fixed the aperture and used an ensemble of 6 stars with a similar magnitude to the target to create a master reference light curve. Finally, a second order polynomial was fitted to the out-of-eclipse data the target light curve to remove a long-term systematic trend.

The  $g$ -band light curve is shown in the bottom left panel of Figure 3.6, and the data are given in Table 3.3. The out-of-eclipse RMS for the target is 26.9 mmag, which is higher than the follow-up with the INT, due to the smaller telescope diameter.

<sup>3</sup><http://www.iac.es/galeria/hdeeg/>

HJD	$\Delta m_{g_{\text{IAC80}}}$ (mag)	$\sigma_{m_{g_{\text{IAC80}}}}$ (mag)
2455052.51020	-0.0417	0.0290
2455052.51113	-0.0091	0.0301
...	...	...

**Table 3.3** — IAC80  $g$ -band follow-up light curve of 19e-3-08413.  $\Delta m_{g_{\text{IAC80}}}$  are the differential magnitudes with respect to the median of the out-of-eclipse measurements such that the out-of-eclipse magnitude is  $m_{g_{\text{IAC80}}} = 0$ . The errors,  $\sigma_g$ , are those computed by the IRAF.PHOT package. (This table is published in full in the online journal and is shown partially here for guidance regarding its form and content.)

Name	Epoch <sup>a</sup>	$t_{\text{int}}$ (s)	Instr.	$\lambda_{\text{range}}$ (Å)	R	SNR
19b-2-01387	394.71	300	ISIS	6000-9200	1000	27
19c-3-01405	426.53	900	ACAM	3300-9100	450	30
19e-3-08413	426.54	900	ACAM	3300-9100	450	30

**Table 3.4** — Summary of low resolution spectroscopic observations at the William Herschel Telescope, La Palma. <sup>a</sup> JD-2455000.0.

### 3.3.4 WHT low-resolution spectroscopy

We carried out low-resolution spectroscopy during a wider follow-up campaign of the WTS MEB and planet candidates on several nights between July 16 and August 17, 2010, using the William Herschel Telescope (WHT) at Roque de Los Muchachos, La Palma. These spectra allow the identification of any giant contaminants via gravity sensitive spectral features, and provide estimates of the effective system temperatures, plus approximate metallicities and chromospheric activity indicators (see section 3.5).

We used the Intermediate dispersion Spectrograph and Imaging System (ISIS) and the Auxiliary-port Camera (ACAM) on the WHT to obtain our low-resolution spectra. In all instances we used a  $1.0''$  slit. We did not use the dichroic during the ISIS observations because it can induce systematics and up to 10% efficiency losses in the red arm, which we wanted to avoid given the relative faintness of our targets. Wavelength and flux calibrations were performed using periodic observations of standard lamps and spectrophotometric standard stars throughout the nights. Table 3.4 summarises our low-resolution spectroscopic observations.

The reduction of the low-resolution spectra was performed with a combination of IRAF routines and custom IDL procedures. In IDL, the spectra were trimmed to encompass the length of the slit, bias-subtracted and median-filtered to remove cosmic rays. The ACAM spectra were also flat-fielded. We corrected the flat fields for dispersion effects using a pixel-integrated sensitivity function. The IRAF.APALL routine was used to identify the spectra, subtract the background and optimally sum the flux in apertures along the trace. For the ISIS spectrum, wavelength and flux calibration was performed with the CuNe+CuAr standard lamps and ING flux standard SP2032+248. For ACAM, arc frames were used to determine the wavelength solution along the slit using a fifth order spline function fit with an RMS  $\sim 0.2\text{Å}$ . For flux-

calibration, we obtained reference spectra of the ING flux standard SP2157+261.

### 3.3.5 WHT/ISIS intermediate-resolution spectroscopy

Modelling the individual radial velocities (RVs) of components in a binary system provides their mass ratio and a lower limit on their physical separation. Combining this information with an inclination angle determined by the light curve of an eclipsing system ultimately yields the true masses and radii of the stars in the binary. We measured the RVs of the components in our MEBs using spectra obtained with the intermediate-resolution, single-slit spectrograph ISIS mounted on the WHT. We used the red arm with the R1200R grating centred on 8500Å, giving a wavelength coverage of  $\sim 8100 - 8900\text{\AA}$ . The slit width was chosen to match the approximate seeing at the time of observation giving an average spectral resolution  $R \sim 9300$ . The spectra were processed entirely with IRAF, using the CCDPROC packages for instrumental signature removal. We optimally extracted the spectra for each object on each night and performed wavelength and flux calibration using the semi-automatic KPNO.DOSLIT package. Wavelength calibration was achieved using CuNe arc lamp spectra taken after each set of exposures and flux calibration was achieved using observations of spectrophotometric standards.

#### Radial velocities via cross-correlation

The region 8700 – 8850Å contains a number of relatively strong metallic lines present in M-dwarfs and is free of telluric absorption lines making it amenable for M-dwarf RV measurements (Irwin et al. 2009). We used the IRAF implementation of the standard 1-D cross-correlation technique, FXCOR, to extract the RV measurements for each MEB component using synthetic spectra from the MARCS<sup>4</sup> spectral database (Gustafsson et al. 2008) as templates. The templates had plane-parallel model geometry, a temperature range from 2800-5500K incremented in 200K steps, solar metallicity, surface gravity  $\log(g) = 5.0$  and a 2 km/s micro-turbulence velocity, which are all consistent with low-mass dwarf stars. The best-matching template i.e. the one that maximised the cross-correlation strength of the primary component for each object, was used to obtain the final RVs of the system, although note that the temperature of the best-matching cross-correlation template is not a reliable estimate of the true effective temperature. The saturated near-infrared Ca II triplet lines at 8498, 8542 and 8662Å were masked out during the cross-correlation. A summary of our observations and the extracted radial velocities are given in table 3.5.

## 3.4 Identification of M-dwarf Eclipsing Binaries

### 3.4.1 The M-dwarf sample

It is possible to select M-dwarfs in WTS fields using simple colour-colour plots such as those shown in Figure 3.2, which were compiled using our deep WFCAM photometry plus magnitudes from SDSS DR7, which has a fortuitous overlap with the 19hr field. Jones et al. (1994) showed that the  $(i - K)$  colour is a reasonable estimator for the effective temperature, however

---

<sup>4</sup><http://marcs.astro.uu.se/>

Name	HJD	Slit ( $''$ )	$t_{int}$ ( $n \times \text{sec}$ )	SNR	Phase	RV <sub>1</sub> (km/s)	RV <sub>2</sub> (km/s)
19b-2-01387	2455395.55200	1.2	$2 \times 1200$	22.7	0.1422	-143.2	8.0
19b-2-01387	2455396.46471	0.7	$3 \times 600$	6.22	0.7513	23.7	-158.0
19b-2-01387	2455407.52383	1.0	$3 \times 900$	14.0	0.1314	-137.9	-4.2
19b-2-01387	2455407.62644	1.0	$3 \times 1200$	8.0	0.1998	-155.3	25.1
19b-2-01387	2455408.38324	1.0	$3 \times 900$	9.1	0.7049	14.5	-157.6
19b-2-01387	2455408.51689	1.0	$3 \times 1200$	12.8	0.7941	15.1	-153.7
19b-2-01387	2455408.63070	1.0	$3 \times 1200$	13.4	0.8700	-9.8	-139.2
19b-2-01387	2455409.38673	1.0	$3 \times 1200$	14.3	0.3745	-128.4	-4.8
19c-3-01405	2455407.43073	1.0	$1200 + 630$	6.4	0.2244	-62.5	57.0
19c-3-01405	2455407.47937	1.0	$3 \times 1200$	5.3	0.2343	-57.0	52.7
19c-3-01405	2455407.58012	1.0	$3 \times 1200$	5.3	0.2547	-63.8	54.6
19c-3-01405	2455408.46929	1.0	$3 \times 1200$	6.0	0.4347	-21.7	22.0
19c-3-01405	2455409.56881	1.0	$3 \times 1200$	6.0	0.6573	47.3	-52.6
19c-3-01405	2455409.68190	0.8	$3 \times 1200$	5.1	0.6802	42.5	-64.4
19c-3-01405	2455409.47707	0.8	$3 \times 1200$	7.5	0.6387	46.4	-43.6
19e-3-08413	2455408.42993	1.0	$3 \times 1200$	7.1	0.6640	108.0	-46.5
19e-3-08413	2455408.56307	1.0	$3 \times 1200$	8.7	0.7435	113.1	-58.4
19e-3-08413	2455409.43629	1.0	$3 \times 1200$	8.9	0.2654	-24.8	140.9
19e-3-08413	2455409.52287	0.8	$3 \times 1200$	7.5	0.3171	-27.6	125.6
19e-3-08413	2455409.61343	0.8	$3 \times 1200$	7.5	0.3712	-9.4	109.1

**Table 3.5** — Summary of intermediate-resolution spectroscopic observations. All observations were centred on  $8500\text{\AA}$ .

the eclipsing nature of the systems we are interested in can cause irregularities in the colour indices, especially since the WFCAM photometry was taken at different epochs to each other and the SDSS photometry. For example, a system of two equal mass stars in total eclipse result is 0.75 mag fainter compared to its out-of-eclipse magnitude. We made a more robust sample of M-dwarfs by estimating the effective temperature of each source in the 19h field via SED fitting of all the available passbands i.e. SDSS  $g, r, i$  and  $z$ -band plus WFCAM  $Z, Y, J, H$  and  $K$ -band. By rejecting the most outlying magnitudes from the best SED fit, one becomes less susceptible to errors from in-eclipse observations. Note that the SDSS  $u$ -band magnitudes of our redder sources are affected by the known red leak in the  $u$  filter and are hence excluded from the SED fitting process.

To perform the SED fitting, we first put all the observed photometry to the Vega system (see Hewett et al. 2006 and Hodgkin et al. 2009 for conversions). Although the WFCAM photometry is calibrated to 1.5 – 2% with respect to 2MASS (Hodgkin et al. 2009), the 2MASS photometry also carries its own systematic error, so we assumed an extra 3% systematic error added in quadrature to the photometric errors for each source to account for calibration errors between different surveys. We used a simple  $\chi^2$  fitting routine to compare the data to a set of solar metallicity model magnitudes at an age of 1 Gyr from the stellar evolution models of Baraffe et al. (1998). We linearly interpolated the model magnitudes onto a regular grid of 5 K intervals from 1739 – 6554 K, to enable a more precise location of the  $\chi^2$  minimum. If the worst fitting

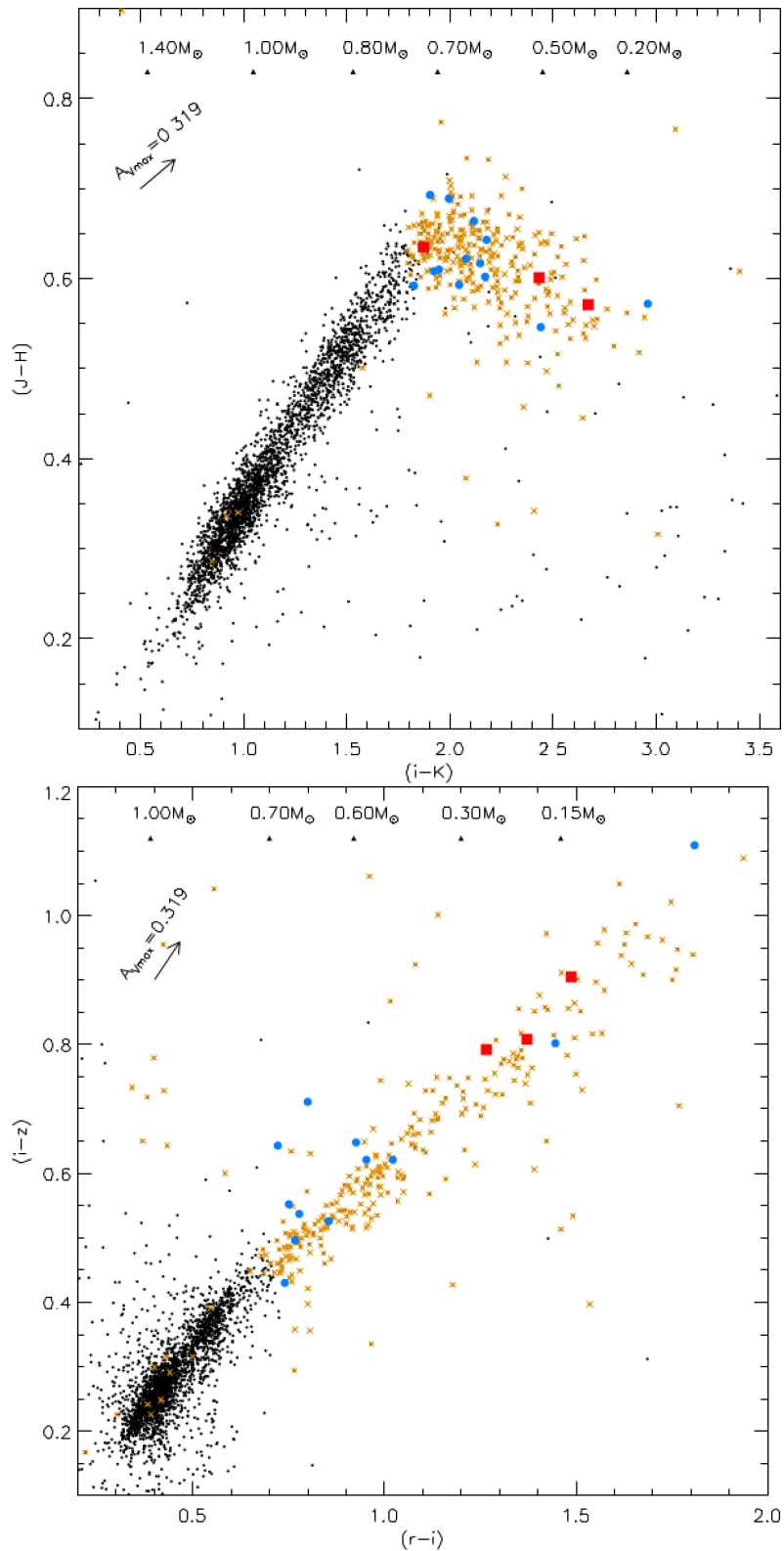


**Figure 3.2** — Colour-colour plots of the sources in one of the WFCAM pointings for the 19hr field (black +), overlaid with the full 19hr field sample of detached MEB candidates (blue filled circles and red filled squares). The filled red squares mark the three MEB systems characterised in this paper. The orange crosses mark the M-dwarf candidate sources in the pointing (see Section 3.4.1). The triangles mark the masses for the given colour index, derived from the 1 Gyr solar metallicity isochrone of the Baraffe et al. (1998) low-mass stellar evolution models. The arrows mark the maximum reddening vector, assuming a distance of 1 kpc.

Parameter	19b-2-01387	19c-3-01405	19e-3-08413
$\alpha_{J2000}$	19:34:15.5	19:36:40.7	19:32:43.2
$\delta_{J2000}$	36:28:27.3	36:42:46.0	36:36:53.5
$\mu_{\alpha \cos \delta}$ ("/yr)	$0.023 \pm 0.003$	$-0.002 \pm 0.004$	$0.008 \pm 0.004$
$\mu_{\delta}$ ("/yr)	$0.032 \pm 0.003$	$-0.001 \pm 0.004$	$-0.007 \pm 0.004$
$g$	$19.088 \pm 0.010$	$20.342 \pm 0.024$	$20.198 \pm 0.020$
$r$	$17.697 \pm 0.006$	$18.901 \pm 0.012$	$18.640 \pm 0.009$
$i$	$16.651 \pm 0.004$	$17.634 \pm 0.008$	$17.488 \pm 0.005$
$z$	$16.026 \pm 0.007$	$16.896 \pm 0.012$	$16.847 \pm 0.010$
$Z$	$15.593 \pm 0.005$	$16.589 \pm 0.007$	$16.156 \pm 0.006$
$Y$	$15.188 \pm 0.006$	$16.432 \pm 0.011$	$15.832 \pm 0.008$
$J$	$14.721 \pm 0.004$	$15.706 \pm 0.006$	$15.268 \pm 0.005$
$H$	$14.086 \pm 0.003$	$15.105 \pm 0.006$	$14.697 \pm 0.005$
$K$	$14.414 \pm 0.006$	$14.836 \pm 0.007$	$14.452 \pm 0.006$

**Table 3.6** — A summary of photometric properties for the three MEBs, including our photometrically derived effective temperatures and spectral types. The proper motions  $\mu_{\alpha \cos \delta}$  and  $\mu_{\delta}$  are taken from the SDSS DR7 database. SDSS magnitudes  $g, r, i$  and  $z$  are in AB magnitudes, while the WFCAM  $Z, Y, J, H$  and  $K$  magnitudes are given in the Vega system. The errors on the photometry are the photon-counting errors and do not include the extra 3% systematic error we add in quadrature when performing the SED-fitting. Conversions of the WFCAM magnitudes to other systems can be found in Hodgkin et al. (2009). Note that the WFCAM  $K$ -band magnitude for 19b-2-01387 was obtained during an eclipse event and does not represent the total system magnitude.

data point in the best  $\chi^2$  fit was more than a  $5\sigma$  outlier, we excluded that data point and re-ran the fitting procedure. This makes the process more robust to exposures taken in eclipse. The errors on the effective temperatures include the formal  $1\sigma$  statistical errors from the  $\chi^2$  fit (which are likely to be under-estimated) plus an assumed  $\pm 100$  K systematic uncertainty. This error also takes into account the known missing opacity issue in the optical bandpasses in the Baraffe et al. (1998) models.

Our M-dwarf sample is conservative. It contains any source with an SED effective temperature  $\leq 4209$  K, magnitude  $J \leq 16$  mag and a stellar class morphology flag (as determined by the data reduction pipeline). The maximum effective temperature corresponds to a radius of  $0.66R_{\odot}$  at the typical field star age of 1 Gyr, according to the stellar evolution models of Baraffe et al. (1998). We opted to restrict our MEB search to  $J \leq 16$  mag because the prospects for ground-based radial velocity follow-up are bleak beyond  $J = 16$  mag ( $I \sim 18$  mag, Aigrain et al. 2007) if we wish to achieve accurate masses and radii that provide useful constraints on stellar evolution models. We found a total of 2,705 M-dwarf sources in the 19hr field. Table 3.6 gives the single epoch, deep photometry from SDSS and WFCAM, plus the proper motions from the SDSS DR7 database (Munn et al. 2004, 2008) for the systems characterised in this paper. Their SED-derived system effective temperatures,  $T_{\text{eff,SED}}$  are given in Table 3.7.

### Interstellar reddening

The photometry for the 19hr field is not dereddened before performing the SED fitting. The faint magnitudes of our M-dwarf sources implies they are at non-negligible distances and that extinction along the line-of-sight may be significant. This means that our M-dwarf sample may contain hotter sources than we expect. At  $J \leq 16$  mag, assuming no reddening, the WTS is distance-limited to  $\sim 1$  kpc for the earliest M-dwarfs ( $M_J = 6$  mag at 1 Gyr for M0V,  $M_* = 0.6M_\odot$ , using the models of Baraffe et al. 1998). We investigated the reddening effect in the direction of the 19hr field using a model for interstellar extinction presented by Drimmel et al. (2003). In this model, extinction does not have a simple linear dependency on distance but is instead a three-dimensional description of the Galaxy, consisting of a dust disk, spiral arms as mapped by HII regions, plus a local Orion-Cygnus arm segment, where dust parameters are constrained by COBE/DIRBE far infrared observations. Using this model, we calculate that  $A_V = 0.319$  mag ( $E(B - V) = 0.103$  mag) at 1 kpc in the direction of the 19hr field. We used the conversion factors in Table 6 of Schlegel et al. (1998) to calculate the absorption in the UKIRT and SDSS bandpasses, finding  $A_g = 0.370$  mag,  $A_K = 0.036$  mag,  $E(r - i) = 0.065$ ,  $E(i - z) = 0.059$  and  $E(J - H) = 0.032$ . The reddening affect along the line-of-sight to the field thus appears to be small. We show this maximum reddening vector as an arrow in Figure 3.2.

For the most interesting targets in the WTS (EBs or planet candidates), we obtain low-resolution spectra to further characterise the systems and check their dwarf-like nature (see Section 3.5). Effective temperatures based on spectral analysis suffer less from the effects of reddening effects because the analysis depends not only on the slope of the continuum but also the shape of specific molecular features, unlike the SED fitting. Therefore, the SED effective temperatures are only a first estimate and we will later adopt values derived by fitting model atmospheres to low-resolution spectra of our MEBs (see Section 3.5.4).

### 3.4.2 Eclipse detection

We made the initial detection of our MEBs during an automated search for transiting planets in the WTS light curves, for which we used the Box-Least-Squares (BLS) algorithm, OCCFIT, as described in Aigrain & Irwin (2004), and employed by Miller et al. (2008). The box represents a periodic decrease in the mean flux of the star over a short time scale (an upside-down top hat). The in-occultation data points in the light curves fall into a single bin,  $I$ , while the out-of-occultation data points form the ensemble  $O$ . This single bin approach may seem simplistic but in the absence of significant intrinsic stellar variability, such as star spot modulation, it becomes a valid approximation to an eclipse and is sufficient for the purpose of *detection*. Given the relatively weak signal induced by star spot activity in the  $J$ -band, we did not filter the light curves for stellar variability before executing the detection algorithm. We ran OCCFIT on the M-dwarf sample light curves in the 19h field. Our data invariably suffer from correlated ‘red’ noise, thus we adjust the OCCFIT detection statistic,  $S$ , which assesses the significance of our detections, with the procedure described by Pont et al. (2006) to derive a new statistic,  $S_{\text{red}}$ . This process is explained in detail for OCCFIT detections in Miller et al. (2008).

### 3.4.3 Candidate selection

To automatically extract the MEB candidates from results of running OCCFIT on the M-dwarf sample light curves, we required that  $S_{\text{red}} \geq 5$  and that the detected orbital period must not be near the common window-function alias at one day i.e.  $0.99 > P > 1.005$  days. This gave 561 light curves to eyeball, during which we removed objects with spurious eclipse-like features associated with light curves near the saturation limit.

In total, we found 26 sources showing significant eclipse-features in the 19h field, of which 16 appear to be detached and have full-phase coverage, with well-sampled primary and secondary eclipses. The detached MEB candidates are marked on the colour-colour plot in Figure 3.2 by the blue filled circles and red filled squares. The orbital periods of the MEBs corresponding to the blue filled circles are given in Table 3.14 and their folded light curves are shown in Figures 3.13 and 3.14. The MEBs corresponding to the red filled squares are the subjects of the remaining detailed analysis in this paper.

## 3.5 Low-resolution spectroscopic analysis

Low-resolution spectra of our three characterised MEBs, as shown in Figure 3.3, permit a further analysis of their composite system properties and provide consistency checks on the main-sequence dwarf nature of the systems.

### 3.5.1 Surface Gravity

Slesnick et al. (2006) and Lodieu et al. (2011) have shown that the depths of alkaline absorption lines between  $6300 - 8825\text{\AA}$  can highlight low surface gravity features in low-mass stars. We used the spectral indices  $\text{Na}_{8189}$  and  $\text{TiO}_{7140}$  to search for any giant star contaminants in the MEBs and found that all three MEBs have indices consistent with dwarf star gravity. We note that our low-resolution spectra were not corrected for telluric absorption, which is prevalent in the  $\text{Na}_{8189}$  region, and thus our measured indices may not be completely reliable. However a visual inspection of the spectra also reveals deep, clear absorption by the NaI doublet at  $8183\text{\AA}$ ,  $8195\text{\AA}$  as highlighted in Figure 3.3, which is not seen in giant stars. For comparison, we also observed an M4III giant standard star, [R78b] 115, shown at the top of Figure 3.3, with the same set up on the same night. It lacks the deep Na I doublet absorption lines found in dwarfs and its measured spectral indices are  $\text{TiO}_{7140} = 2.0 \pm 0.2$  and  $\text{Na}_{8189} = 0.97 \pm 0.04$ , which places it in the low-surface gravity region for M4 spectral types in Figure 11 of Slesnick et al. (2006). The gravity-sensitive spectral index values for our MEBs are given in Table 3.7.

### 3.5.2 Metallicity

The profusion of broad molecular lines in M-dwarf spectra, caused by absorbing compounds such as Titanium Oxide and Vanadium Oxide redwards of  $6000\text{\AA}$  (Kirkpatrick et al. 1991), make it difficult to accurately define the continuum level, which complicates M-dwarf metallicity measurements. However, recent work shows that the relative strengths of metal hydride and metal oxide molecular bands in low-resolution optical wavelengths can be used to separate metal-poor subdwarfs from solar-metallicity systems. For example, Woolf et al. (2009)

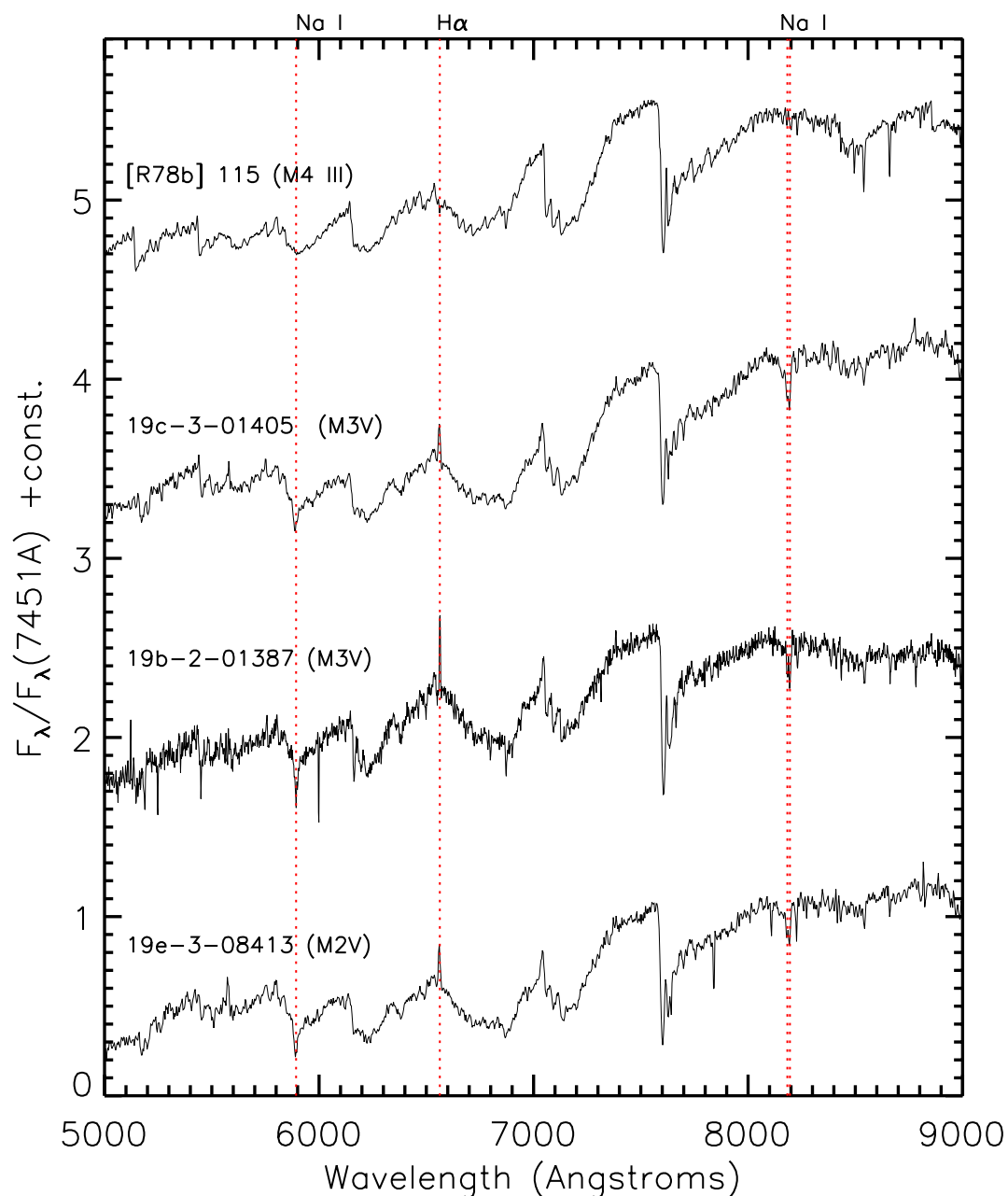


**Figure 3.3** — Low-resolution spectra of our three new MEBs plus a known M-giant star (top spectrum) for comparison. The TiO absorption band at  $7100\text{\AA}$  signifies the onset of the M-dwarf spectral types. The dotted vertical lines, from left to right, mark the Na I,  $H\alpha$  and the Na I doublet rest wavelengths in air. The Na I doublet is strong in dwarfs while the Calcium infrared triplet at  $8498, 8542$  and  $8662\text{\AA}$  is strongest in giants. The deep features at  $7594$  and  $7685\text{\AA}$  are telluric  $O_2$  absorption.  $H\alpha$  emission is clearly present in all three MEBs.

provided a set of equal metallicity contours in the plane of the CaH2+CaH3 and TiO5 spectral indices defined by Reid et al. (1995), and they mapped the metallicity index  $\zeta_{\text{TiO/CaH}}$  described by Lépine et al. (2007) onto an absolute metallicity scale, calibrated by metallicity measurements from well-defined FGK stars with M-dwarf companions, albeit with a significant scatter of  $\sim 0.3$  dex. Dhital et al. (2011) have refined the coefficients for  $\zeta_{\text{TiO/CaH}}$  after finding a slight bias for higher metallicity in early M-dwarfs. We measured the CaH2+CaH3 and TiO5 indices in our MEB spectra and compared them with these works. We found that all three of our systems are consistent with solar metallicity. The measured values of the metallicity-sensitive indices for our MEBs are given in Table 3.7.

One should note that further progress has been made in M-dwarf metallicity measurements by moving to the infrared and using both low-resolution *K*-band spectra (Rojas-Ayala et al. 2010; Muirhead et al. 2011) and high-resolution *J*-band spectra (Önehag et al. 2011; Del Burgo et al. 2011). These regions are relatively free of molecular lines, allowing one to isolate atomic lines (such as Na I and Ca I) and thus achieve a precise continuum placement. However, in the spectra of M-dwarf short period binary systems, one must be aware that the presence of double-lines and rotationally-broadened features further increase the uncertainty in their metallicity estimates.

### 3.5.3 H $\alpha$ Emission

All three of our MEBs show clear H $\alpha$  emission in their low-resolution spectra, although it is not possible to discern if both components are in emission. The equivalent widths of these lines, which are a measure of the chromospheric activity, are reported in Table 3.7, where a negative symbol denotes emission. H $\alpha$  emission can be a sign of youth, but we do not see any accompanying low-surface gravity features. The strength of the H $\alpha$  emission seen in our MEBs is comparable with other close binary systems (e.g. Kraus et al. 2011) and thus is most likely caused by high magnetic activity in the systems. None of the systems have equivalent widths  $< -8\text{\AA}$ , which places them in the non-active accretion region of the empirically derived accretion criterion of Barrado y Navascués & Martín (2003).

### 3.5.4 Spectral type and effective temperature

Our low-resolution spectra permit an independent estimate of the spectral types and effective temperatures of the MEBs to compare with the SED fitting values. Initially, we assessed the spectral types using the HAMMER<sup>5</sup> spectral-typing tool, which estimates MK spectral types by measuring a set of atomic and molecular features (Covey et al. 2007). One can visually inspect the automatic fit by eye and adjust the fit interactively. For the latest-type stars (K and M), the automated characterisation is expected to have an uncertainty of  $\sim 2$  subclasses. We found that 19b-2-01387 has a visual best-match with an M2V system, while the other two MEBs were visually closest to M3V systems. M-dwarf studies (Reid et al. 1995; Gizis 1997) have found that the TiO5 spectral index could also be used to estimate spectral types to an accuracy of  $\pm 0.5$  subclasses for stars in the range K7V-M6.5V. The value of this index and the associated spectral

<sup>5</sup><http://www.astro.cornell.edu/~kcovey/thehammer.html>

type (SpT) are given for each of our three MEBs in Table 3.7. We find a reasonable agreement between the spectral index results, the visual estimates and the SED derived spectral types.

Woolf & Wallerstein (2006) derived a relationship between the CaH2 index and the effective temperatures of M-dwarfs in the range  $3500\text{K} < T_{\text{eff}} < 4000\text{K}$ . Table 3.7 gives the value of this index and the associated effective temperatures, labelled  $T_{\text{eff}}(\text{CaH2})$ , for our three MEBs. Woolf & Wallerstein (2006) do not quote an uncertainty on the relationship, so we assumed errors of  $\pm 150\text{K}$ . Within the assumed errors, the effective temperatures derived from the spectral indices and the SED fitting agree, but the relationship between the CaH2 index and  $T_{\text{eff}}$  has not been robustly tested for the CaH2 values we have measured.

Instead, we have determined the system effective temperatures for our MEBs by directly comparing the observed spectra to cool star model atmospheres using a  $\chi^2$ -minimisation algorithm. This incorporated the observational errors, which were taken from the error spectrum produced during the optimal extraction of the spectra. We used a grid of NextGen atmospheric models (Allard et al. 1997) interpolated to the same resolution as our low-resolution spectra. The models had increments of  $\Delta T_{\text{eff}} = 100\text{K}$ , solar metallicity and a surface gravity  $\log(g) = 5.0$  (a typical value for early-type field M-dwarfs), and spanned  $5000 - 8500\text{\AA}$ . During the fitting, we masked out the strong telluric  $\text{O}_2$  features at  $7594, 7685\text{\AA}$  and the  $\text{H}\alpha$  emission line at  $6563\text{\AA}$  as these are not present in the models, although we found that their inclusion had a negligible affect on the results. All the spectra were normalised to their continuum before fitting. We fitted the  $\chi^2$ -distribution for each MEB with a six-order polynomial to locate its minimum. The corresponding best-fitting  $T_{\text{eff}}$  (atmos., adopted) is given in Table 3.7. Assuming systematic correlation between adjacent pixels in the observed spectrum, we multiplied the formal  $1\sigma$  errors from the  $\chi^2$ -fit by  $\sqrt{3}$  to obtain the final errors on the system effective temperatures.

From here on, our analysis is performed with system effective temperatures derived from model atmosphere fitting. Although our different methods agree within their errors, the model atmosphere fitting is more robust against reddening effects, even if this effect is expected to be small, as discussed earlier.

## 3.6 Light curve analysis

Light curves of an eclipsing binary provide a wealth of information about the system, including its orbital geometry, ephemeris, and the relative size and relative radiative properties of the stars. We used the eclipsing binary software, JKTEBOP<sup>6</sup> (Southworth et al. 2004b,c), to model the light curves of our MEBs. JKTEBOP is a modified version of EBOP (Eclipsing Binary Orbit Program; Nelson & Davis 1972; Popper & Etzel 1981; Etzel 1980). The algorithm is only valid for well-detached eclipsing binaries with small tidal distortions, i.e near-spherical stars with oblateness  $< 0.04$  (Popper & Etzel 1981). A first pass fit with JKTEBOP showed that this criterion is satisfied by all three of our MEBs.

The light curve model of a detached, circularised eclipsing binary is largely independent of its radial velocity model, which allowed us to perform light curve modelling and derive precise orbital periods on which to base our follow-up multi-wavelength photometry and radial velocity measurements. The RV-dependent part of the light curve model is the mass ratio,  $q$ , which controls the deformation of the stars. In our initial analysis to determine precise orbital

<sup>6</sup><http://www.astro.keele.ac.uk/~jkt/>

Name	$T_{\text{eff}}$ (SED)	$T_{\text{eff}}$ (atmos., adopted)	$T_{\text{eff}}$ (CaH2)	SpT (TiO5)	TiO5	CaH2 (Å)
19b-2-01387	$3494 \pm 116$	$3590 \pm 100$	$3586 \pm 150$	$M2.7 \pm 0.5$	0.52	0.52
19c-3-01405	$3389 \pm 110$	$3307 \pm 130$	$3514 \pm 150$	$M2.8 \pm 0.5$	0.50	0.48
19e-3-08413	$3349 \pm 111$	$3456 \pm 140$	$3569 \pm 150$	$M2.3 \pm 0.5$	0.54	0.51

Name	CaH3	TiO <sub>7140</sub>	Na <sub>8189</sub>	EW(H $\alpha$ )
19b-2-01387	0.73	1.46	0.89	-3.2
19c-3-01405	0.75	1.60	0.87	-4.3
19e-3-08413	0.73	1.46	0.90	-4.1

**Table 3.7** — A summary of the spectral indices, derived effective temperatures and spectral types (SpT) for the three characterised MEBs. The photometric estimates are labelled with (SED). They have the smallest errors, which include the formal uncertainties plus a 100 K systematic uncertainty, but they potentially suffer from reddening effects and under-estimation of the errors. Our adopted effective temperatures are marked (atmos., adopted). They are derived from comparison with the NextGen model atmosphere spectra (Allard et al. 1997) and are more robust against reddening effects. The (TiO5) and (CaH2) labels mark values derived from the spectral index relations of Reid et al. (1995) and Woolf & Wallerstein (2006), respectively. We use  $T_{\text{eff}}$  (atmos., adopted) for all subsequent analysis in this paper.

periods, we assumed circular stars, which is reasonable for detached systems, but the observed mass ratios (see Section 3.7) were adopted in the final light curve analysis.

JKTEBOP depends on a number of physical parameters. We allowed the following parameters to vary for all three systems during the final fitting process: i) the sum of the radii as a fraction of their orbital separation,  $(R_1 + R_2)/a$ , where  $R_j$  is the stellar radius and  $a$  is the semi-major axis, ii) the ratio of the radii,  $k = R_2/R_1$ , iii) the orbital inclination,  $i$ , iv) the central surface brightness ratio,  $J$ , which is essentially equal to the ratio of the primary and secondary eclipse depths, v) a light curve normalisation factor, corresponding to the magnitude at quadrature phase, vi)  $e \cos \omega$ , where  $e$  is the eccentricity and  $\omega$  is the longitude of periastron, vii)  $e \sin \omega$ , viii) the orbital period,  $P$  and ix) the orbital phase zero-point,  $T_0$ , corresponding to the time of mid-primary eclipse. The starting values of  $P$  and  $T_0$  are taken from the original OCCFIT detection (see Section 3.4.2). In the final fit, the observed  $q$  value is held fixed. The reflection coefficients were not fitted, instead they were calculated from the geometry of the system. The small effect of gravity darkening was determined by fixing the gravity darkening coefficients to suitable values for stars with convective envelopes ( $\beta = 0.32$ ) (Lucy 1967). JKTEBOP will allow for a source of third light in the model, whether it be from a genuine bound object or from some foreground or background contamination, so we initially allowed the third light parameter to vary but found it to be negligible in all cases and thus fixed it to zero in the final analysis.

Our light curves, like many others, are not of sufficient quality to fit for limb darkening, so we fixed the limb darkening coefficients for each component star. JKTLTD is a subroutine of JKTEBOP that gives appropriate limb darkening law coefficients for a given bandpass based on a database of coefficients calculated from available stellar model atmospheres. We used the PHOENIX model atmospheres (Claret 2000, 2004) and the square-root limb darkening law in all cases. Studies such as van Hamme (1993) have shown that the square-root law is the most accurate at infrared wavelengths. For each star, we assumed surface gravities of  $\log(g) = 5$ , a

Parameter	19b-2-01387	19c-3-01405	19e-3-08413
WTS <i>J</i> -band			
P (days)	1.49851768 ±0.00000041	4.9390945 ±0.0000015	1.67343720 ±0.00000048
$T_0$ (HJD)	245332.889802 ±0.000077	245393.80791 ±0.00022	245374.80821 ±0.00016
$(R_1 + R_2)/a$	0.17818 ± 0.00040	0.07023 ± 0.00035	0.1544 ± 0.0016
$k$	0.967 ± 0.044	0.987 ± 0.081	0.782 ± 0.070
$J$	0.9307 ± 0.0043	0.993 ± 0.013	0.8162 ± 0.0084
$i$ (°)	88.761 ± 0.051	89.741 ± 0.053	87.59 ± 0.26
$e \cos \omega$	-0.00020 ± 0.00017	0.000060 ± 0.000068	-0.00014 ± 0.00017
$e \sin \omega$	-0.0007 ± 0.0026	-0.0041 ± 0.0059	0.0112 ± 0.0062
Norm.(mag)	14.64726 ± 0.00017	0.00003 ± 0.00020	15.22776 ± 0.00020
$R_1/a$	0.0906 ± 0.0020	0.0354 ± 0.0014	0.0867 ± 0.0027
$R_2/a$	0.0875 ± 0.0021	0.0348 ± 0.0015	0.0676 ± 0.0040
$L_2/L_1$	0.871 ± 0.076	0.97 ± 0.15	0.503 ± 0.090
$e$	0.0066 ± 0.0026	0.0058 ± 0.0043	0.0114 ± 0.0062
$\omega$ (°)	268.0 ± 1.7	180.5 ± 90.9	91.1 ± 1.2
$\sigma_J$ (mmag)	5.2	8.4	8.7
INT <i>i</i> -band			
$J$	0.8100	—	0.63
$\sigma_i$ (mmag)	5.7	—	12.1
IAC80 <i>g</i> -band			
$J$	—	—	0.6455
$\sigma_i$ (mmag)	—	—	29.9

**Table 3.8** — Results from the *J* and *i*-band light curve analysis. Only perturbed parameters are listed. The light curve parameter errors are the 68.3% confidence intervals while the model values are the means of the 68.3% confidence level boundaries, such that the errors are symmetric.  $T_0$  corresponds to the epoch of mid-primary eclipse for the first primary eclipse in the *J*-band light curve. Errors on 19e-3-08413 are from residual permutation analysis as they were the largest, indicating time-correlated systematics.  $\sigma_{J,i}$  give the RMS of the residuals to the final solutions, where all parameters in the fit are fixed to the quoted values and the reflection coefficients calculated from the system geometry.

solar metallicity and micro-turbulence of 2 km/s, and used estimated effective temperatures for the component stars:  $[T_{\text{eff},1}, T_{\text{eff},2}] = [3500\text{K}, 3450\text{K}]$  for 19b-2-01387,  $[T_{\text{eff},1}, T_{\text{eff},2}] = [3300\text{K}, 3300\text{K}]$  for 19e-3-08413, and  $[T_{\text{eff},1}, T_{\text{eff},2}] = [3525\text{K}, 3350\text{K}]$  for 19c-3-01405. Note that we did not iterate the limb darkening coefficients with the final derived values of  $T_1$  and  $T_2$  (see Section 3.8) as they only differed by  $\sim 30$  K ( $< 1\sigma$ ) from the assumed values. This would be computationally intensive to do and would result in a negligible effect on the final result.

The phase-folded *J*-band light curves for the MEBs and their final model fits are shown in Figures 3.4, 3.5 and 3.6, while the model values are given in Table 3.8.

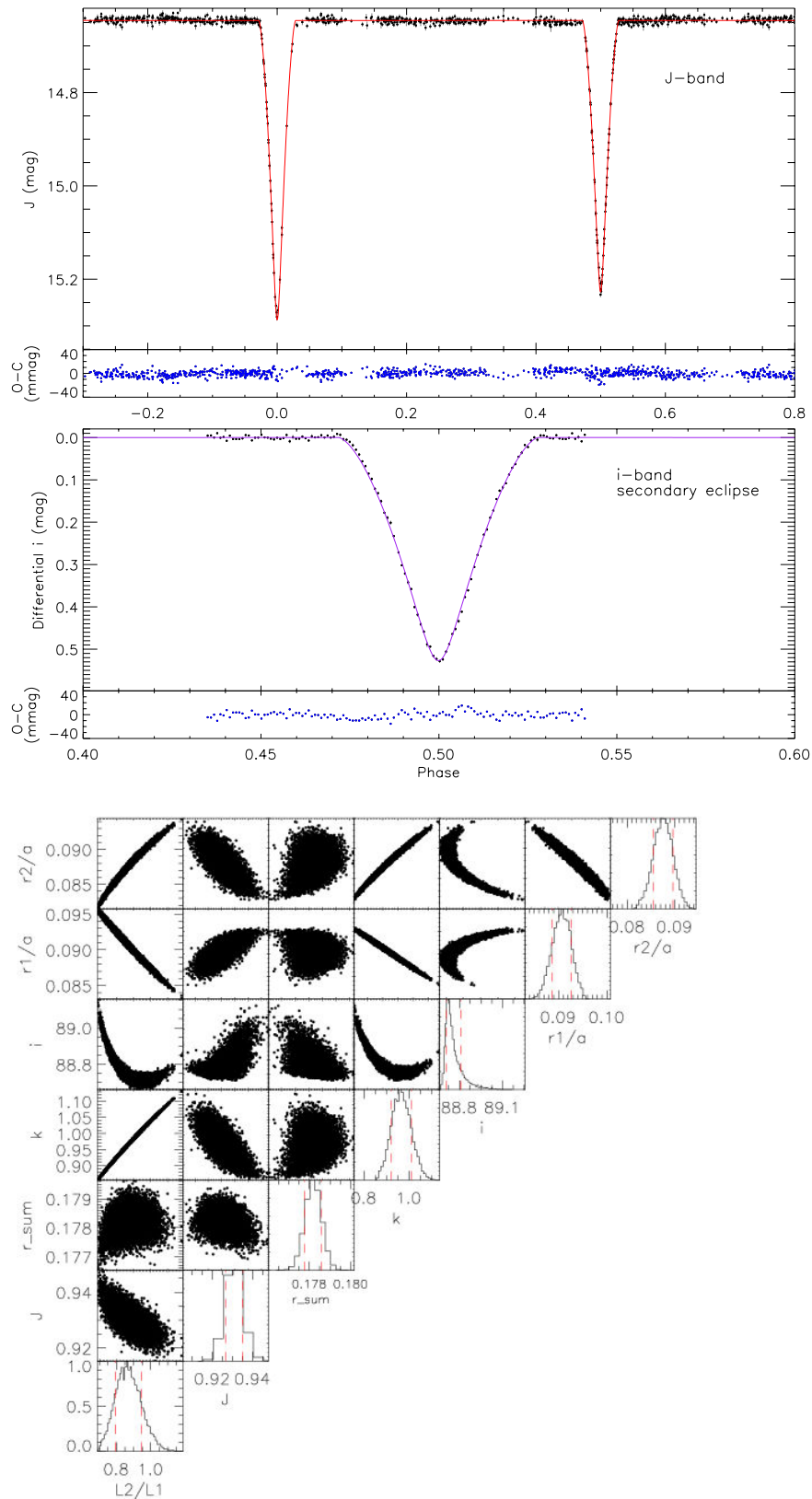


**Figure 3.4** — 19b-2-01387 Top panel: full phase WFCAM *J*-band light curve. Middle panel: the INT/WFC *i*-band light curve at secondary eclipse. The solid red and purple lines show the best-fit from JKTEBOP. The blue data points in the smaller panels show the residuals after subtracting the model. Bottom panel: Parameter correlations from Monte Carlo simulations and histograms of individual parameter distributions. The red dashed vertical lines mark the 68.3% confidence interval. For a high resolution plot please refer to the online paper.

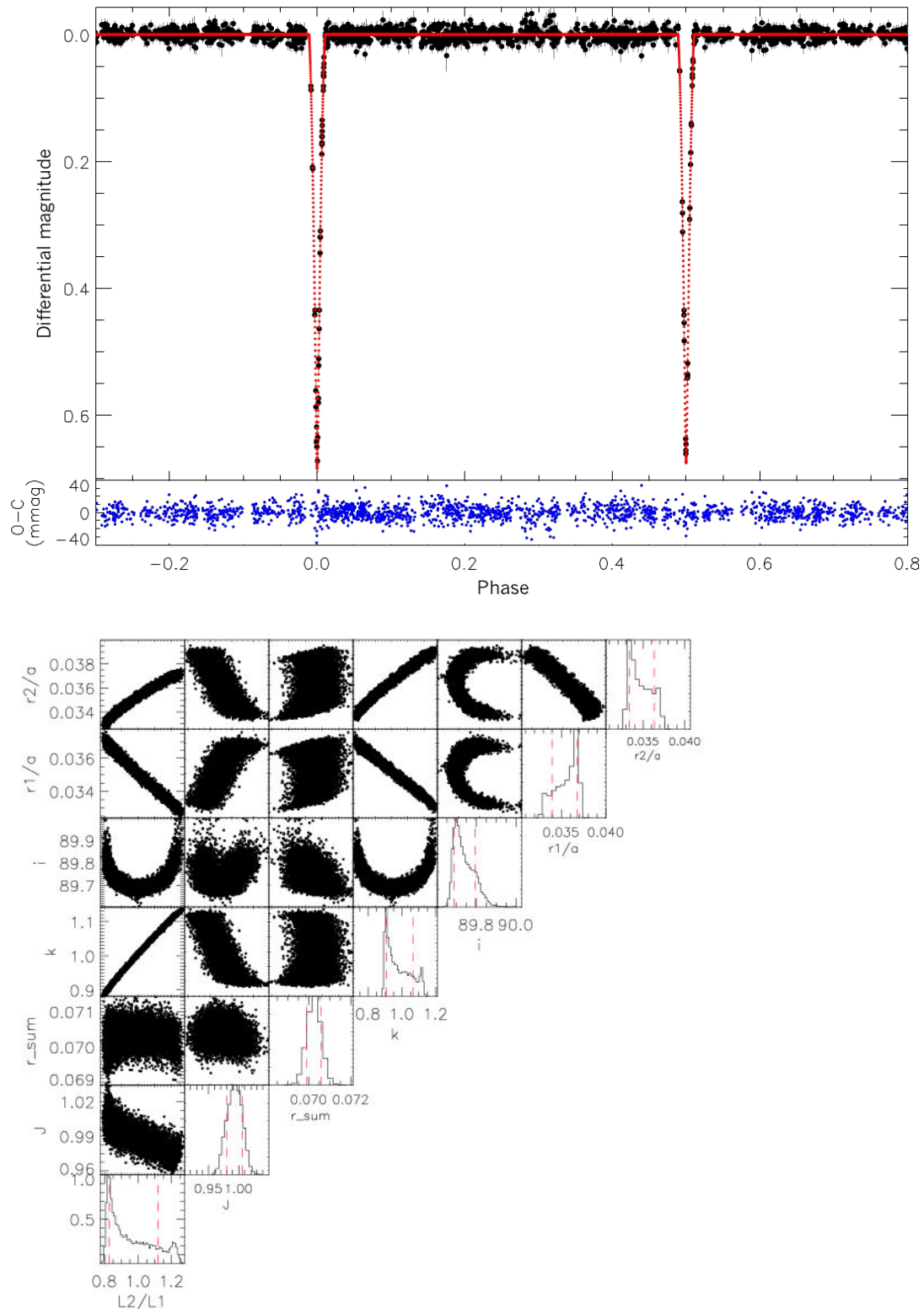


**Figure 3.5 — 19c-3-01405** Top panel: WFCAM  $J$ -band light curve. Lines and panels as in Figure 3.4. The magnitude scale is differential as we have combined light curves from two different WFCAM chips. Bottom panel: Monte Carlo results with lines as in Figure 3.4. Our inability to constrain the model with follow-up data results in strong correlation between the radius ratio and light ratio and parameter distributions that are significantly skewed. There are also degeneracies in the inclination which is expected given the near identical eclipse depths. For a high resolution MCMC plot please refer to the online paper.

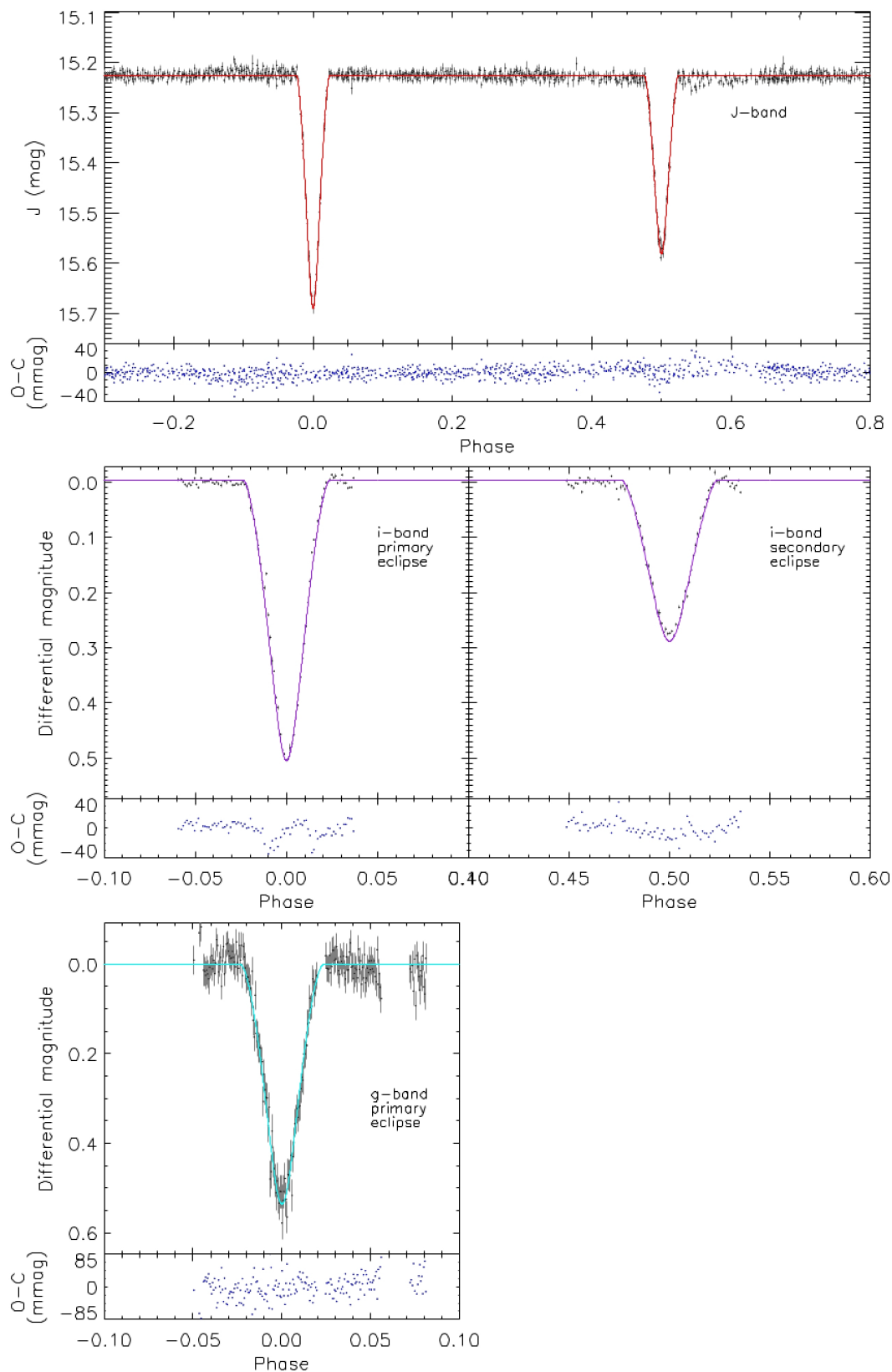


**Figure 3.6 — 19e-3-08413** Top panel: full phase WFCAM *J*-band light curve. Middle panels: INT/WFC *i*-band light curves of a primary and a secondary eclipse. Bottom panel: IAC80 *g*-band light curve of a primary eclipse. The solid red, purple, and cyan lines show the best-fit from JKTEBOP. For a high resolution MCMC plot please refer to the online paper. Parameter correlations from residual permutations, which gave the larger errors on the model parameters than the Monte Carlo simulations, indicating time-correlated systematics. There are strong correlations between the light ratio, radius ratio and inclination.

### 3.6.1 Error analysis

JKTEBOP uses a Levenberg–Marquardt minimisation algorithm (Press et al. 1992) for least-squares optimisation of the model parameters; however, the formal uncertainties from least-squares solutions are notorious for underestimating the errors when one or more model parameters are held fixed, due to the artificial elimination of correlations between parameters. JKTEBOP provides a method for assessing the  $1\sigma$  uncertainties on the measured light curve parameters through Monte Carlo (MC) simulations. In these simulations, a synthetic light curve is generated using the best-fitting light curve model at the phases of the actual observations. Random Gaussian noise is added to the model light curve which is then fitted in the same way as the data. This process is repeated many times and distribution of the best fits to the synthetic light curves provide the  $1\sigma$  uncertainties on each parameter. Southworth et al. (2005b) showed this technique is robust and gives similar results to Markov Chain Monte Carlo techniques used by others, under the (reasonable) assumption that the best fit to the observations is a good fit. JKTEBOP can also perform a residual permutation (prayer bead) bead error analysis which is useful for assigning realistic errors in the presence of correlated noise (Southworth 2008). For each MEB, we have performed both MC simulations (using 10,000 steps) and a prayer bead analysis. The reported errors are those from the method that gave the largest uncertainties. The correlations between the parameter distributions from the MC and prayer bead analysis are shown in Figures 3.4, 3.5 and 3.6 along with histograms of the distributions of individual parameters. The distributions are not perfectly Gaussian and result in asymmetric errors for the 68.3% confidence interval about the median. As we wish to propagate these errors into the calculation of absolute dimension, we have symmetrized the errors by adopting the mean of the 68.3% boundaries (the 15.85% and 84.15% confidence limits) as the parameter value and quoting the 68.3% confidence interval as the  $\pm 1\sigma$  errors. These errors are given in Table 3.8 for each MEB.

Our follow-up  $g$ - and  $i$ -band light curves (where available) were used to check the  $J$ -band solution by modelling them with the derived  $J$ -band parameters, but allowing the surface brightness ratio and the light curve normalisation factor to vary. The limb darkening coefficients were changed to those appropriate for the respective  $g$ - and  $i$ -band and the reflection coefficients were again determined by the system geometry. The RMS values of these fits are given in Table 3.8 along with the derived  $g$ - and  $i$ -band surface brightness ratio for completeness. The  $g$ - and  $i$ -band phase-folded data is shown overlaid with the models in Figure 3.4 and 3.6. We find that the  $J$ -band solutions are in good agreement with the  $g$ - and  $i$ -band data.

### 3.6.2 Light ratios

All three of our MEBs exhibit near equal-depth eclipses, implying that the systems have components with similar mass. This is promising because it suggests relatively large reflex motions that will appear as well-separated peaks in a cross-correlation function from which we derive RVs. However, it is well-known for systems with equal size components that the ratio of the radii, which depends on the depth of the eclipses, is very poorly determined by the light curve (Popper 1984), even with the high photometric precision and large number epochs in the WTS (see Andersen et al. (1980); Southworth et al. (2007a) for other excellent examples of this phenomenon). Conversely,  $(R_1 + R_2)/a$ , is often very well-constrained because it depends mainly

on the duration of the eclipses and the orbital inclination of the system. The reason that the ratio of the radii is so poorly constrained stems from the fact that quite different values of  $R_2/R_1$  result in very similar eclipse shapes.

Unfortunately, we found that all three of our MEBs presented problems associated with poorly constrained  $R_2/R_1$ , revealed in the initial modelling as either a large skew in the errors on the best-fit parameters or best-fit solutions that were physically implausible. For example, for 19b-2-01387, the initial best-fit gave  $L_2/L_1 > 1$  and  $R_2/R_1 > 1$  while  $T_2/T_1 < 1$ . We know from our low-resolution spectroscopy that these stars are very likely to be ordinary main-sequence M-dwarfs and while their exact radii may be under-estimated by models, they generally obey the trend that less massive stars are less luminous, smaller and cooler. We note that Stassun et al. (2007) found a temperature reversal in a system of two young brown dwarfs where the less massive component was hotter but smaller and fainter than its companion. In their case the more massive component, although cooler, had an RV curve and eclipse depth that were consistent. In our cases, the most massive component (smallest  $K_*$ ) comes towards us (blue-shift) after the deepest (primary) eclipse, so it must be the more luminous component. The uncertainty in our modelling is most likely to be due to insufficient coverage of the mid-eclipse points.

However, we can try to use external data as an additional constraint in the fit. Some authors employ a spectroscopically derived light ratio as an independent constraint on  $k$  in the light curve modelling (Southworth et al. 2004a, 2007b; Nordstrom & Johansen 1994). JKTEBOP allows the user to incorporate an input light ratio in the model and propagates the errors in a robust way. The input light ratio adds a point in the flux array at a specific phase (Southworth et al. 2007b). If this is supplied with a very small error, the point is essentially fixed. We have tried several methods to estimate the light ratio for each of our three systems, although we stress here that none of the estimates should be considered as significant. One requires high resolution spectra to extract precise light ratios, via the analysis of the equivalent width ratios of metallic lines, which will be well-separated if observed at quadrature (Southworth et al. 2005b). With a high resolution spectrum, one can disentangle the components of the eclipsing binary and perform spectral index analysis on the separate components (e.g. Irwin et al. 2007a).

19b-2-01387 is our brightest system and subsequently has the highest signal-to-noise in our intermediate-resolution spectra. The best spectrum is from the first night of observations. For this system, we estimated the light ratio in three ways: i) by measuring the ratio of the equivalent widths of the lines in the Na II doublet (shown in Figure 3.7), ii) by using the two-dimensional cross-correlation algorithm, TODCOR (Zucker & Mazeh 1994), which weights the best-matching templates by the light ratio and, iii) by investigating the variation in the goodness-of-fit for a range of input light ratios in the model.

For the first method, the IRAF.SPLOT task was used to measure the equivalent width of the Na I doublet feature with rest wavelength  $8183.27\text{\AA}$  for each star. Note that this assumes the components have the same effective temperature. The ratio was  $EW(2)/EW(1) = 0.3582/0.4962 = 0.7219$ . In the second method, we found that only the spectrum from the first night contained sufficient SNR to enable TODCOR to correctly identify the primary and secondary components. It is known that TODCOR does not perform as well for systems with similar spectral features (Southworth & Clausen 2007) so we do not use it to derive RVs for our nearly equal mass systems. The TODCOR estimated light ratio was  $L_2/L_1 = 0.846$ . In the final method, we iterated JKTEBOP across a grid of initial light ratios between 0.6-1.1, in steps

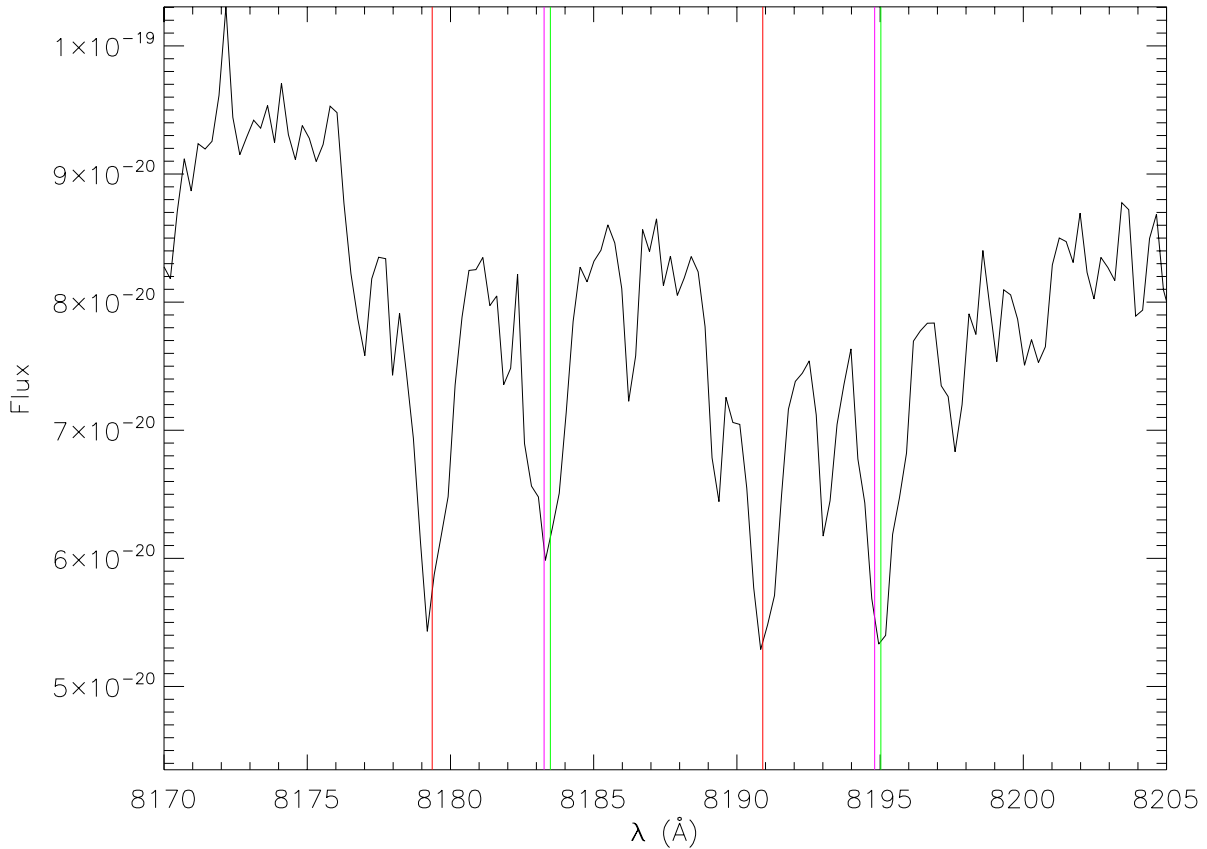


**Figure 3.7 — 19b-2-01387:** A high signal-to-noise intermediate resolution spectrum taken near quadrature phase of 19b-2-01387 in the Na II doublet wavelength region which we used to measure equivalent widths to estimate the light ratio. The purple vertical lines show the rest frame wavelength of the doublet at  $\lambda 8183.27\text{\AA}$ ,  $\lambda 8194.81\text{\AA}$ . The red lines mark the doublet for primary object and the green lines mark the secondary doublet lines, based on the RVs derived in Section 3.7.

of 0.01, with very small errors while allowing all our usual parameters to vary. The resulting  $\chi^2$ -distribution is not well-behaved. There is a local and global minimum at  $L_2/L_1 = 0.72$  and  $L_2/L_1 = 0.97$ , respectively, but the global minimum is bracketed on one side by a significant jump to a much larger  $\chi^2$  suggesting numerical issues. We opted to use the light ratio derived with TODCOR as the input to the model. This value lies half-way between the two minimums of the  $\chi^2$  distribution, so we supplied it with a  $\sim 15\%$  error to allow the parameter space to be explored, given the uncertainty in our the measurement. Our follow-up *i*-band data of a single secondary eclipse also prefers a light ratio less than unity, but the lack of phase coverage does not give a well-constrained model. The resulting parameter distributions, shown in Figure 3.4, show strong correlation between the light ratio and  $R_2/R_1$  as expected. The resulting  $1\sigma$  error boundary for the light ratio, which is computed from  $k$  and  $J$ , is in broad agreement with the methods used to estimate it.

For 19e-3-08413, we obtained additional *i*-band photometry of a primary and secondary eclipse, plus a further primary eclipse in the *g*-band. Here, we have estimated the light ratio

by fitting our two datasets in these wavebands separately, using appropriate limb darkening coefficients for the *i*- and *g*-bands in each case, and allowing all our usual parameters to vary. We find best-fit values from the *i*- and *g*-bands of  $L_2/L_1 = 0.29$  and  $L_2/L_1 = 0.36$ , respectively. This confirms a light ratio less than unity, but as the light ratio depends on the surface brightness ratio, which in turn is wavelength dependent, we adopted  $L_2/L_1 = 0.29$  with input with an error of  $\pm 0.5$  in the final fit to the *J*-band data. Note we chose to use the *i*-band value as it is closer in wavelength to the *J*-band and the light curve was of higher quality.

In the case of 19c-3-01405, we could not derive a light ratio from the low SNR spectra, nor do we have follow-up *i*-band photometry (due to time scheduling constraints). The eclipses are virtually identical so we supplied an input light ratio of  $L_2/L_1 = 1.0$  with an error of 50%. Unfortunately, the final error distributions for the parameters are still quite skewed, as shown in Figure 3.5.

### 3.6.3 Star spots

For 19e-3-08413, we found that the residual permutation analysis gave larger errors, indicating time-correlated systematics. We have not allowed for spot modulation in our light curve model thus the residuals systematics may have a stellar origin. As mentioned previously, we expect star spot modulation in the *J*-band to be relatively weak as the SED of the spot and the star at these wavelengths are more similar than at shorter wavelengths. It is difficult to test for the presence of spots in the *g*- and *i*-band data as we do not have suitable coverage out-of-eclipse. We only have full-phase out-of-eclipse observations in a single *J*-bandpass therefore any physical spot model will be too degenerate between temperature and size to be useful. Furthermore, our *J*-band data span nearly four years, yet spot size and location are expected to change on much shorter timescales, which leads to a change in the amplitude and phase of their sinusoidal signatures. Stable star spot signatures over the full duration of our observations would be unusual. The WTS observing pattern therefore makes it difficult to robustly fit simple sinusoids, as one would need to break the light curve into many intervals in order to have time spans where the spots did not change significantly (e.g. three week intervals), and these would consequently consist of few data points. Nevertheless, we have attempted to test for spot modulation in a very simplistic manner by fitting the residuals of our light curve solutions as a function of time ( $t$ ) with the following sinusoid:

$$f(t) = a_0 + a_1 \sin(2\pi(t/a_2) + a_3), \quad (3.1)$$

where the systemic level ( $a_0$ ), amplitude ( $a_1$ ), and phase ( $a_3$ ) were allowed to vary in the search for the best-fit, while the period ( $a_2$ ) was held fixed at the orbital period as we expect these systems to be synchronised (see Table 3.11 for the theoretical synchronisation timescales). Once the best-fit was found, the values were used as starting parameters for the IDL routine MPFITFUN, to refine the fit and calculate the errors on each parameter. Table 3.9 summarises our findings.

There is evidence to suggest a low-level synchronous sinusoidal modulation in 19b-2-01387 and 19e-3-08413 with amplitude  $\sim 1.8 - 3.5$  mmag, but we do not find significant modulation for our longest period MEB (19c-3-01405). The modulation represents a source of systematic error that if modelled and accounted for, could reduce the errors our radius measurements.

Name	Amplitude (mmag)	Phase	$\gamma$ (mmag)	$\chi^2_{v,\text{before}}$	$\chi^2_{v,\text{after}}$	RMS <sub>before</sub> (mmag)	RMS <sub>after</sub> (mmag)
19b-2-01387	$1.83 \pm 0.23$	$2.53 \pm 0.012$	$0.19 \pm 0.15$	1.11	1.04	5.2	4.9
19c-3-01405	$0.22 \pm 0.27$	$-1.5 \pm 1.3$	$0.23 \pm 0.20$	0.87	0.87	8.4	8.4
19e-3-08413	$3.47 \pm 0.32$	$-0.143 \pm 0.050$	$0.39 \pm 0.22$	1.32	1.19	7.8	7.5

**Table 3.9** — Results of modelling the light curve model residuals with the simple sinusoid defined by Equation 3.1, to test for the presence of spot modulation. The terms ‘before’ and ‘after’ refer to the reduced  $\chi^2$  and RMS values before subtracting the best-fit sine curve and then after the subtraction. Note: mmag =  $10^{-3}$  mag. The RMS<sub>before</sub> value for 19e-3-08413 is different to Table 3.8 as one data point was clipped due to it being a significant outlier.

However, with only one passband containing out-of-eclipse variation, we cannot provide a useful non-degenerate model. Good-quality out of eclipse monitoring is required and given that spot modulation evolves, contemporaneous observations are needed, preferably taken at multiple wavelengths to constrain the spot temperatures (Irwin et al. 2011). It is surprising that the apparent spot modulation in our MEBs persists over the long baseline of the WTS observations and perhaps an alternate explanation lies in residual ellipsoid variations from tidal effects between the two stars. We note here that our limiting errors in comparing these MEBs to the mass-radius relationship in Section 3.9.1 are on the masses, not the radii.

### 3.7 Radial velocity analysis

To extract the semi-amplitudes ( $K_1, K_2$ ) and the centre-of-mass (systemic) velocity,  $\gamma$ , of each MEB system, we modelled the RV data using the IDL routine MPFITFUN (Markwardt 2009), which uses the Levenberg–Marquardt technique to solve the least-squares problem. The epochs and periods were fixed to the photometric solution values as these are extremely well-determined from the light curve. Circular orbits were assumed ( $e = 0$ ) for all three systems as the eccentricity was negligible in all light curve solutions. We fitted the primary RV data first using the following model:

$$RV_1 = \gamma - K_1 \sin(2\pi\phi) \quad (3.2)$$

where  $\phi$  is the phase, calculated from the light curve solution, and  $K$  is the semi-amplitude. To obtain  $K_2$ , we then fitted the secondary RV data points using the equation above, but this time fixed  $\gamma$  to the value determined from the primary RV data.

$$RV_2 = \gamma + K_2 \sin(2\pi\phi) \quad (3.3)$$

The errors on each RV measurement are weighted by the RV error given by IRAF.FXCOR and then scaled until the reduced  $\chi^2$  of the model fit is unity. The RMS of the residuals is quoted alongside the derived parameters in Table 3.10, and is treated as the typical error on each RV data point. The RMS ranges from  $\sim 2 - 5$  km/s between the systems and for the

Parameter	19b-2-01387	19c-3-01405	19e-3-08413
$K_1$ (km/s)	$90.7 \pm 1.6$	$55.2 \pm 2.2$	$72.1 \pm 2.0$
$K_2$ (km/s)	$94.0 \pm 2.3$	$60.2 \pm 1.4$	$95.2 \pm 3.0$
$\gamma$ (km/s)	$-70.7 \pm 1.3$	$-4.8 \pm 2.0$	$43.8 \pm 1.8$
RMS <sub>1</sub> (km/s)	1.8	3.7	2.7
RMS <sub>2</sub> (km/s)	5.4	2.5	5.0
$q$	$0.965 \pm 0.029$	$0.917 \pm 0.042$	$0.757 \pm 0.032$
$a \sin i$ ( $R_\odot$ )	$5.472 \pm 0.083$	$11.27 \pm 0.25$	$5.53 \pm 0.12$
$M_1 \sin^3 i$ ( $M_\odot$ )	$0.498 \pm 0.019$	$0.410 \pm 0.021$	$0.462 \pm 0.025$
$M_2 \sin^3 i$ ( $M_\odot$ )	$0.480 \pm 0.017$	$0.376 \pm 0.023$	$0.350 \pm 0.018$

**Table 3.10** — Results from radial velocity analysis.

given magnitudes of our systems is the same as the predictions of Aigrain et al. (2007) who calculated the limiting RV accuracy for ISIS on the WHT, when using 1 hour exposures and an intermediate resolution grating centred on  $8500\text{\AA}$ .

The RV curves for the primary and secondary components of the three MEBs are shown in Figure 3.8 along with the residuals of each fit. The error bars are the scaled errors from IRAF.FXCOR and serve as an indicator of the signal-to-noise in the individual spectra and the degree of mismatch with the best template.

### 3.8 Absolute dimensions and space velocities

Combining the results of the light curve and RV curve modelling allows us to derive the absolute masses and radii of our MEB components. Table 3.11 gives these dimensions along with the separations, individual effective temperatures, surface gravities, and bolometric luminosities for each binary system. The masses and radii lie within the ranges  $0.35 - 0.50M_\odot$  and  $0.37 - 0.5R_\odot$  respectively, and span orbital periods from 1 – 5 days. The derived errors on the masses and radii are  $\sim 3.5 - 6.4\%$  and  $\sim 2.7 - 5.5\%$ , respectively.

Eclipsing binaries are one of the first rungs on the Cosmic Distance Ladder and have provided independent distance measurements within the local group e.g. to the Large Magellanic Cloud and to the Andromeda Galaxy (Guinan et al. 1998; Ribas et al. 2005; Bonanos 2007). The traditional method for measuring distances to eclipsing binaries is to compute the bolometric magnitude using the luminosity, radius and effective temperature found from the light curve and RV curve analysis. This is combined with a bolometric correction and the system apparent magnitude to compute the distance. While this can yield quite accurate results, the definitions for effective temperature and the zero points for the absolute bolometric magnitude and the bolometric correction must be consistent (Bessell et al. 1998; Girardi et al. 2002). However, we have opted to use a different method to bypass the uncertainties attached to bolometric corrections. We used JKTDSDIM (Southworth et al. 2005a), a routine that calculates distances using empirical relations between surface brightness and effective temperature. These relations are robustly tested for dwarfs with  $T_{\text{eff}} > 3600$  K and there is evidence that they are valid in the infrared to  $\sim 3000$  K (Kervella et al. 2004). The scatter around the calibration of the relations in the infrared is on the 1% level. The effective temperature scales used for the EB analysis

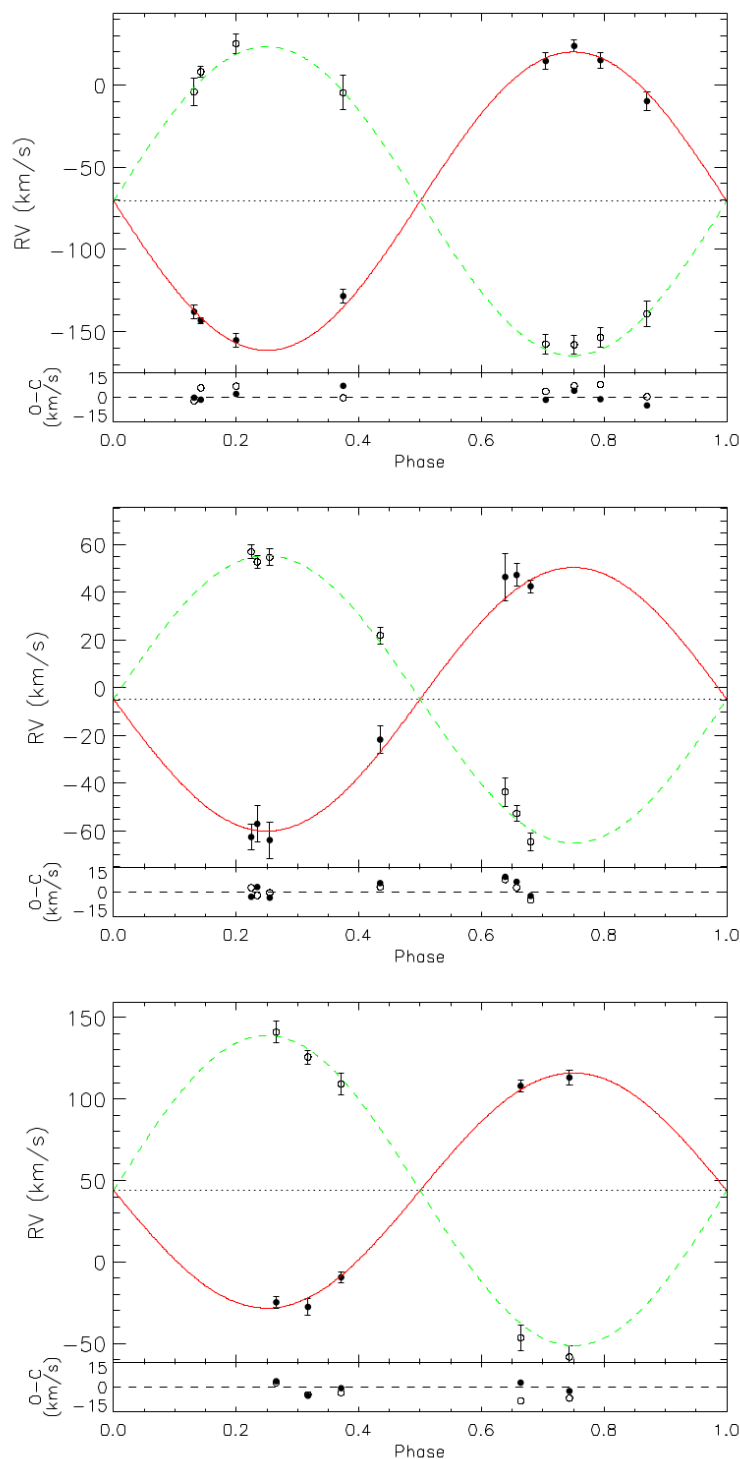


**Figure 3.8** — Primary and secondary RV curves for the MEBs. Top: **19b-2-01387**; Middle: **19c-3-01405**; Bottom: **19e-3-08413**. The solid black circles are RV measurements for the primary star, while open circles denote the secondary star RV measurements. The solid red lines are the model fits to the primary RVs and the dashed green lines are the fits to the secondary RVs, fixed to the systemic velocity of their respective primaries. The horizontal dotted lines mark the systemic velocities. The error bars are from IRAF.FXCOR but are scaled so that the reduced  $\chi^2$  of the model fit is unity. They are merely an indication of the signal-to-noise of the individual spectra and the mismatch between the template and data. Under each RV plot is a panel showing the residuals of the best-fits to the primary and secondary RVs. Note the change in scale for the y-axis. The typical RV error for each component is given in Table 3.10 by the RMS of their respective residuals.

Parameter	19b-2-01387	19c-3-01405	19e-3-08413
$M_1$ ( $M_\odot$ )	$0.498 \pm 0.019$	$0.410 \pm 0.023$	$0.463 \pm 0.025$
$M_2$ ( $M_\odot$ )	$0.481 \pm 0.017$	$0.376 \pm 0.024$	$0.351 \pm 0.019$
$R_1$ ( $R_\odot$ )	$0.496 \pm 0.013$	$0.398 \pm 0.019$	$0.480 \pm 0.022$
$R_2$ ( $R_\odot$ )	$0.479 \pm 0.013$	$0.393 \pm 0.019$	$0.375 \pm 0.020$
$a$ ( $R_\odot$ )	$5.474 \pm 0.083$	$11.27 \pm 0.27$	$5.54 \pm 0.12$
$\log(g_1)$	$4.745 \pm 0.039$	$4.851 \pm 0.055$	$4.742 \pm 0.053$
$\log(g_2)$	$4.760 \pm 0.035$	$4.825 \pm 0.064$	$4.834 \pm 0.051$
$T_{\text{eff},1}$ (K)	$3498 \pm 100$	$3309 \pm 130$	$3506 \pm 140$
$T_{\text{eff},2}$ (K)	$3436 \pm 100$	$3305 \pm 130$	$3338 \pm 140$
$L_{\text{bol},1}$ ( $L_\odot$ )	$0.0332 \pm 0.0042$	$0.0172 \pm 0.0031$	$0.0314 \pm 0.0058$
$L_{\text{bol},2}$ ( $L_\odot$ )	$0.0289 \pm 0.0037$	$0.0166 \pm 0.0031$	$0.0167 \pm 0.0033$
$M_{1,\text{bol}}$	$8.45 \pm 0.14$	$9.16 \pm 0.20$	$8.51 \pm 0.19$
$M_{2,\text{bol}}$	$8.60 \pm 0.14$	$9.20 \pm 0.20$	$9.26 \pm 0.23$
$V_{1\text{rot,sync}}$ (km/s)	$16.73 \pm 0.45$	$4.08 \pm 0.19$	$14.51 \pm 0.55$
$V_{2\text{rot,sync}}$ (km/s)	$16.73 \pm 0.45$	$4.01 \pm 0.20$	$11.31 \pm 0.70$
$t_{\text{sync}}$ (Myrs)	0.05	6.3	0.1
$t_{\text{circ}}$ (Myrs)	2.6	1480	4.0
$d_{\text{adopted}}$ (pc)	$545 \pm 29$	$645 \pm 53$	$610 \pm 52$
$U$ (km/s)	$-63.6 \pm 7.0$	$-2.4 \pm 9.0$	$30.9 \pm 8.6$
$V$ (km/s)	$1.0 \pm 7.8$	$1.3 \pm 12.2$	$-10.2 \pm 11.8$
$W$ (km/s)	$-37 \pm 6.4$	$-4.2 \pm 8.5$	$30.1 \pm 8.1$

**Table 3.11** — Derived properties for the three MEBs.  $V_{\text{rot,sync}}$  are the rotational velocities assuming the rotation period is synchronised with the orbital period.  $t_{\text{sync}}$  and  $t_{\text{circ}}$  are the theoretical tidal synchronisation and circularisation timescales from Zahn (1975, 1977)

and the calibration of its relation with surface brightness should be the same to avoid systematic errors but this is a more relaxed constraint than required by bolometric correction methods (Southworth et al. 2005a). The infrared  $J$ ,  $H$  and  $K$ -bands are relatively unaffected by interstellar reddening but we have shown in Section 3.4.1 that we expect a small amount. In the distance determination, we have calculated the distances at zero reddening and at the maximum reddening ( $E(B - V) = 0.103$  at 1 kpc for early M-dwarfs with  $J \leq 16$  mag). Our adopted distance,  $d_{\text{adopted}}$ , reported in Table 3.11 is the mid-point of the minimum and maximum distance values at the boundaries of their the individual errors, which includes the propagation of the effective temperature uncertainties. The MEBs lie between  $\sim 550 - 650$  pc.

With a full arsenal of kinematic information (distance, systemic velocities, proper motions and positions) we can now derive the true space motions,  $UVW$ , for the MEBs and determine whether they belong to the Galactic disk or halo stellar populations. We used the method of Johnson & Soderblom (1987) to determine  $UVW$  values with respect to the Sun (heliocentric) but we adopt a left-handed coordinate system to be consistent with the literature, that is,  $U$  is positive away from the Galactic centre,  $V$  is positive in the direction of Galactic rotation and  $W$  is positive in the direction of the north Galactic pole. We use the prescription of Johnson & Soderblom (1987) to propagate the errors from the observed quantities and the results are summarised in Table 3.11.

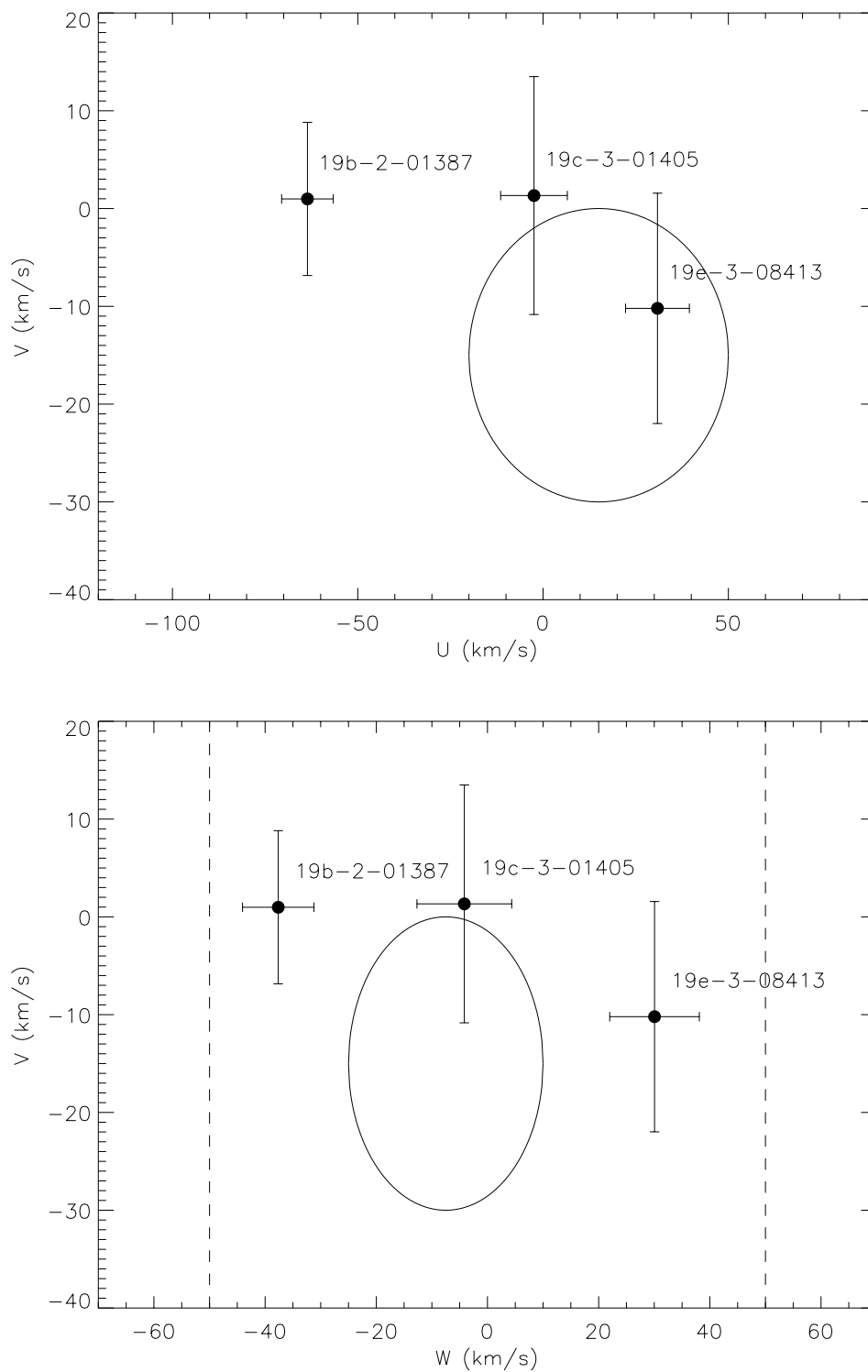
Figure 3.9 shows the MEBs in relation to the error ellipse for the Galactic young disk as defined by Leggett (1992) ( $-20 < U < 50$ ,  $-30 < V < 0$ ,  $-25 < W < 10$  w.r.t the Sun). 19c-3-01405 is consistent within its error with the young disk. 19b-2-01387 is an outlier to the young disk criterion. Instead, Leggett (1992) define objects around the edges of the young disk ellipse as members of the young-old disk population, which has a sub-solar metallicity ( $-0.5 < [m/H] < 0.0$ ). 19e-3-08413 exceeds the allowed  $W$  range for the young disk, despite overlap in the  $UV$  plane. Leggett (1992) assign these objects also to the young-old disk group. This suggest that two of our MEBs could be metal-poor but our spectral index measurements in Section 3.5 are not accurate enough to confirm this. We would require, for example, higher resolution,  $J$ -band spectra to assess the metallicities in detail (Önehag et al. 2011). Comparisons with space motions of solar neighbourhood moving groups do not reveal any obvious associations (Soderblom & Mayor 1993).

## 3.9 Discussion

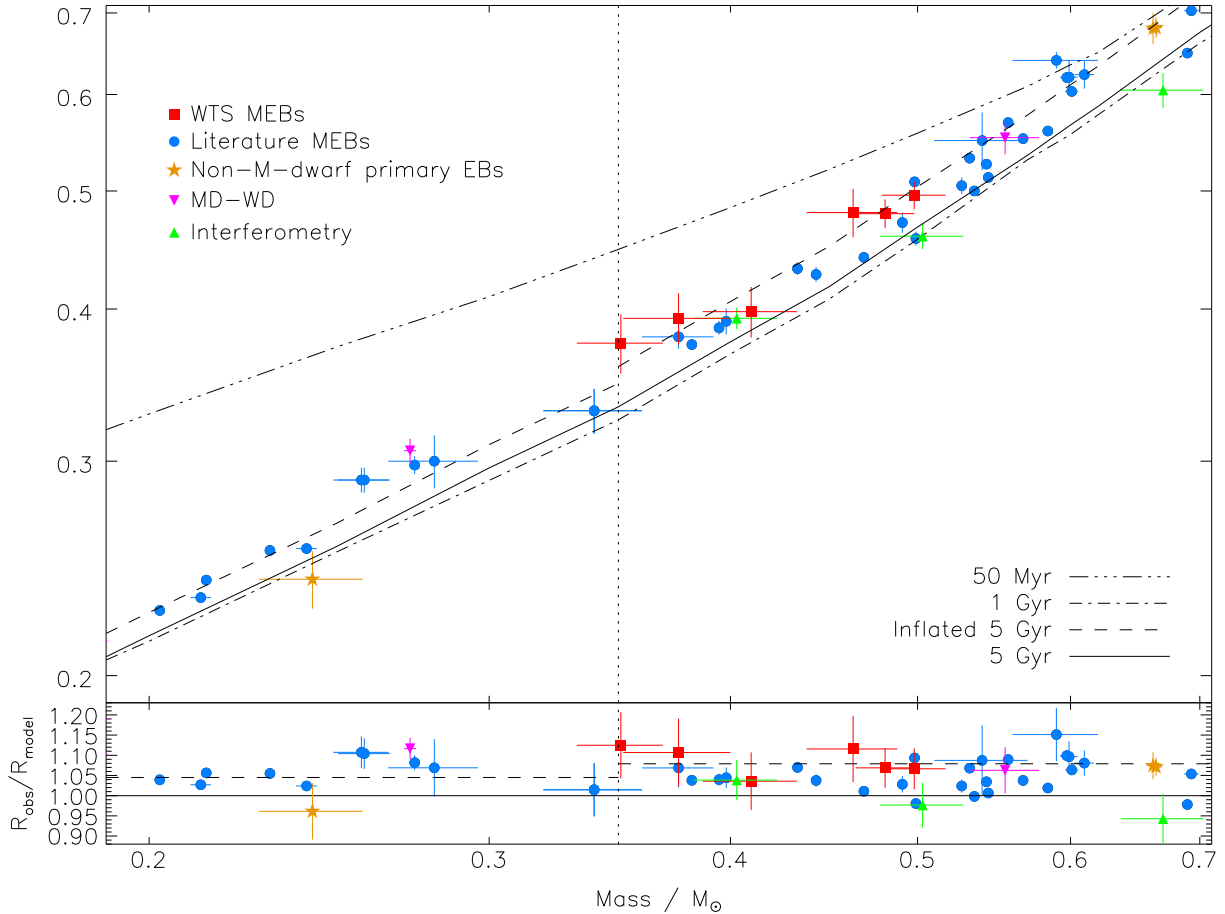
### 3.9.1 The mass-radius diagram

Figure 3.10 shows the positions of our MEBs in the mass-radius plane and compares them to literature mass-radius measurements derived from EBs with two M-dwarfs, EBs with an M-dwarf secondary but hotter primary, eclipsing M-dwarf - white dwarf systems, and inactive single stars measured by interferometry. We only show values with reported mass and radius errors comparable to or better than our own errors. The solid line marks the 5 Gyr, solar metallicity isochrone from the Baraffe et al. (1998) models (solid line), with a convective mixing length equal to the scale height ( $L_{\text{mix}} = H_p$ ), while the dash-dot line shows the corresponding 1 Gyr isochrone.

It is clear that some MEBs, both in the WTS and in the literature, have an excess in radius above the model predictions, and although there is no evidence to say that all MEBs disagree with the models, the scatter in radius at a given mass is clear, indicating a residual dependency on other parameters. Knigge et al. (2011) measured the average fractional radius excess below  $0.7M_{\odot}$ , but based on the findings of Chabrier et al. (2007) and Morales et al. (2010), split the sample at the fully-convective boundary to investigate the effect of inhibited convection. The dashed line in Figure 3.10 marks the average radius inflation they found with respect to the 5 Gyr isochrone for the fully-convective mass region below  $0.35M_{\odot}$  and in the partially-convective region above (7.9% for  $> 0.35M_{\odot}$ , but only by 4.5% for  $> 0.35M_{\odot}$ ). The WTS MEBs sit systematically above the 5 Gyr isochrone but appear to have good agreement with the average radius inflation for their mass range. It is interesting to note that we find similar radius excesses to the literature despite using infrared light curves. At these wavelengths, we crudely expect lower contamination of the light curves by sinusoidal star spots signals and less loss of circular symmetry, on account of the smaller difference between the spectral energy distributions of the star and the spots in the  $J$ -band. If one could eliminate the  $\sim 3\%$  systematic errors in MEB radii caused by polar star spots (Morales et al. 2010) by using infrared data, yet still see similar excess, this would be evidence for a larger effect from magnetic fields (or another hidden parameter) than currently thought. Unfortunately, the errors on our radii do not allow for a robust claim of this nature, but it is an interesting avenue for the field.



**Figure 3.9** — The UVW space motions with respect to the Sun for our MEBs. The errors have been propagated according to Johnson & Soderblom (1987). The solid ellipses are the error ellipses for the young disk defined by Leggett (1992). The dashed vertical lines in the lower plot mark the  $W$  boundary within which the young-old disk population is contained (Leggett 1992).



**Figure 3.10** — The mass-radius diagram for low-mass stars. The filled circles show literature MEB values with reported mass errors  $< 6\%$  and radius errors  $< 6.5\%$ . Also shown are literature values for i) the low-mass secondaries of eclipsing binaries with primary masses  $> 0.6M_{\odot}$ , ii) M-dwarfs found in M-dwarf - white dwarf eclipsing binaries (MD-WD), and iii) radius measurements of single M-dwarfs from interferometric data. The red squares mark the new WTS MEBs. The diagonal lines show model isochrones from the Baraffe et al. (1998) models ( $[m/H] = 0$ ,  $Y = 0.275$  and  $L_{mix} = H_p$ ), while the vertical dotted line marks the onset of fully-convective envelopes (Chabrier & Baraffe 1997). The dashed line shows the 5 Gyr isochrone plus the average radius excess found by Knigge et al. (2011), assuming a discontinuity at the fully-convective transition. Above  $0.35M_{\odot}$ , the model is inflated by 7.9%, but below it is only inflated by 4.5%. The bottom panel shows the radius anomaly,  $R_{obs}/R_{model}$  computed using the 5 Gyr isochrone and again the dashed line shows the corresponding average radius excess found by Kni11. The literature data used in these plots are given in Table 3.16.

The components of our new MEBs do not seem to converge towards the standard 5 Gyr isochrone as they approach the fully-convective region. In fact, our lowest mass star, which has a mass error bar that straddles the fully-convective boundary, is the most inflated of the six components we have measured. The lower panel of Figure 3.10 illustrates this inflation more clearly by showing the radius anomaly  $R_{\text{obs}}/R_{\text{model}}$  as a function of mass, as computed with the standard 5 Gyr isochrone. The errors on the radius anomaly include the observed error on the radius and the observed error on the mass (which propagates into the value of  $R_{\text{model}}$ ), added in quadrature. The spread in radii at a given mass is clearer here, and we discuss why stars of the same mass could be inflated by different amounts in Section 3.9.3 by considering their rotational velocities.

A comparison of the measured radii of all known MEBs to the model isochrones shown in Figure 3.10 might lead one to invoke young ages for most of the systems, because stars with  $M_{\star} \lesssim 0.7M_{\odot}$  are still contracting onto the pre-main sequence at an age  $\lesssim 200$  Myr and therefore have larger radii. While young stars exist in the solar neighbourhood (as shown by e.g. Jeffries & Jewell (1993) who found an upper limit of 10-15 young stars within 25pc), it is highly unlikely that all of the known MEBs are young. Indeed, the derived surface gravities for our MEBs are consistent with older main-sequence stars. We see emission of H $\alpha$  in all three systems, which can be an indicator of youth, but close binary systems are known to exhibit significantly more activity than wide binaries or single stars of the same spectral type (see e.g. Shkolnik et al. 2010). We therefore do not have independent evidence to strongly associate the inflated radii of our MEBs with young ages.

### 3.9.2 The mass- $T_{\text{eff}}$ diagram

As discussed in Section 3.1, there is some evidence for a radius-metallicity correlation (Berger et al. 2006; López-Morales 2007) amongst M-dwarfs. Model values for effective temperatures depend on model bolometric luminosities, which are a function of metallicity. Metal-poor stars are less opaque so model luminosities and effective temperatures increase while the model radii shrink by a small amount (Baraffe et al. 1998). Figure 3.11 shows our MEBs in the mass- $T_{\text{eff}}$  plane plus the same literature systems from Figure 3.10 where effective temperatures are available. The two lines show the standard 5 Gyr isochrone of the Baraffe et al. (1998) models for solar metallicity stars (solid line) and for metal-poor stars (dot-dash line).

The large errors in the mass- $T_{\text{eff}}$  plane for M-dwarfs mean that it is not well-constrained. Section 3.5 has already highlighted some of the difficulties in constraining effective temperatures and metallicities for M-dwarfs, but one should also note that effective temperatures reported in the literature are determined using a variety of different methods, e.g. broad-band colour indices, spectral indices, or model atmosphere fitting using several competing radiative transfer codes. It also involves a number of different spectral type -  $T_{\text{eff}}$  relations, and as Reyle et al. (2011) have demonstrated, these can differ by up to 500 K for a given M-dwarf subclass.

While the intrinsic scatter in the effective temperatures at a given mass may be caused by metallicity effects, the overall trend is that models predict temperatures that are too hot compared to observed values, especially below  $0.45M_{\odot}$ . Our new MEBs, which we determined to have metallicities consistent with the Sun, also conform to this trend. Furthermore, several studies of the inflated CM Dra system have found it to be metal-poor (Viti et al. 1997, 2002), whereas models would suggest it was metal-rich for its mass, based on its cooler temperature

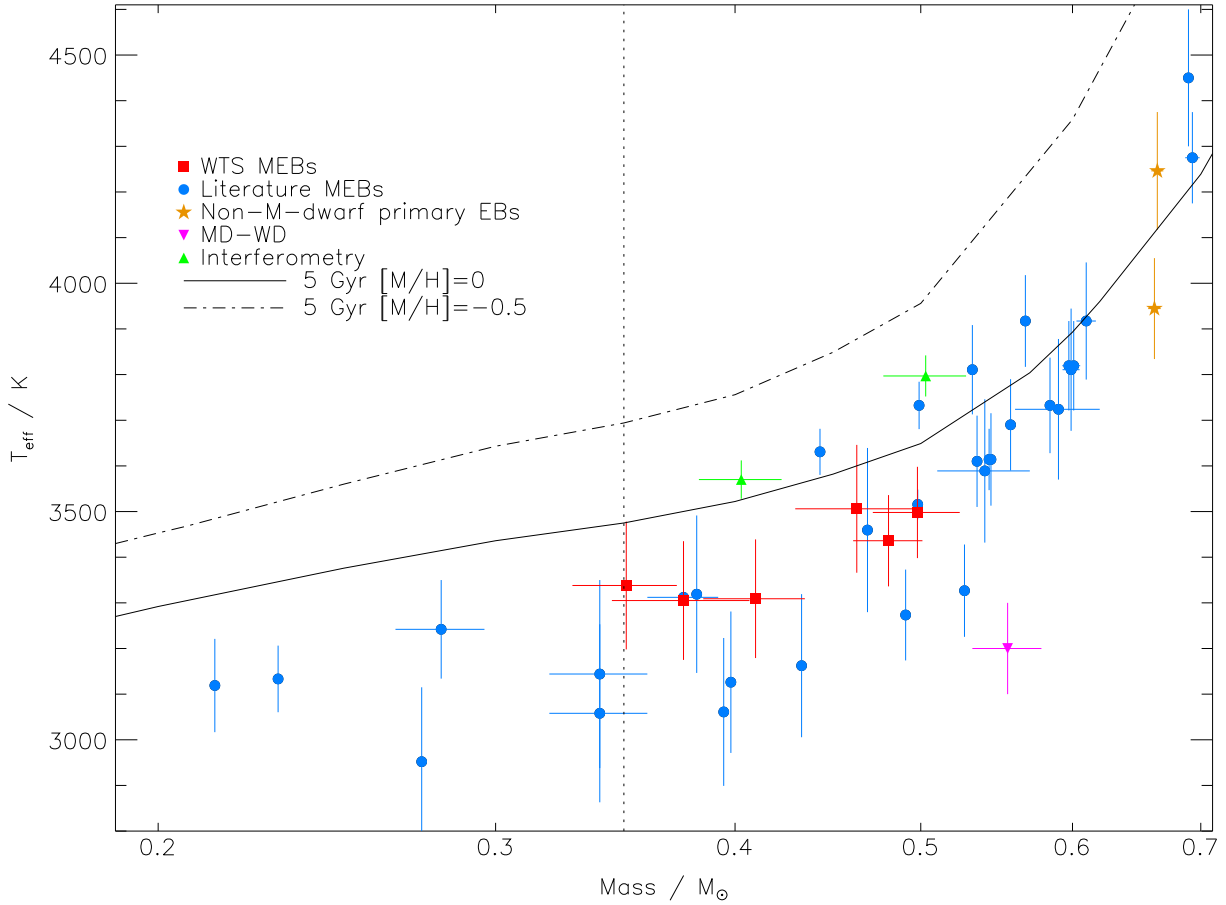


**Figure 3.11** — The mass- $T_{\text{eff}}$  diagram for low mass stars. Two different metallicity isochrones from the Baraffe et al. (1998) 1 Gyr models are over-plotted to show the effect of decreasing metallicity. The vertical dotted line marks the fully-convective boundary (Chabrier & Baraffe 1997). The data used in this plot are given in Table 3.16.

and larger radius (see Table 3.16 for data). In this case, the very precisely measured inflated radius of CM Dra cannot be explained by a high metallicity effect. In fact, the tentative association of two of our new MEBs with the slightly metal-poor young-old disk population defined by Leggett (1992), would also make it difficult to explain their inflated radii using the metallicity argument.

The scatter in the mass- $T_{\text{eff}}$  plane can also arise from spot coverage due to the fact that very spotty stars have cooler effective temperatures at a given mass, and consequently larger radii for a fixed luminosity. Large spot coverage fractions are associated with high magnetic activity, which is induced by fast rotational velocities. Table 3.11 gives the synchronous rotational velocities of the stars in our MEBs along with their theoretical timescales for tidal circularisation and synchronisation. Among our new systems, 19c-3-01405 contains the slowest rotating stars ( $\sim 4$  km/s) on account of its longer orbital period, and its components have stellar radii that are the most consistent with the standard 5 Gyr model. The other faster rotating stars in our MEBs have radii that deviate from the model by more than  $1\sigma$ . We discuss this tentative trend between radius inflation and rotational velocity (i.e. orbital period, assuming the systems are tidally-locked) in the next section.

Period	$\bar{\mu}$	$\pm \frac{\sigma}{\sqrt{N}}$	$\sigma$
All	103.7%	0.5%	3.3%
$P \leq 1.0$	106.2%	0.9%	4.0%
$P > 1.0$	102.6%	0.4%	2.4%

**Table 3.12** — A statistical analysis of the mean radius inflation for different period ranges.  $\sigma$  is the weighted sample standard deviation.

### 3.9.3 A mass-radius-period relationship?

In a recent paper, Kraus et al. (2011) presented six new MEBs with masses between  $0.38 - 0.59M_{\odot}$  and short orbital periods spanning  $0.6 - 1.7$  days. Their measurements combined with existing literature revealed that the mean radii of stars in systems with orbital periods less than 1 were different at the  $2.6\sigma$  level to those at longer periods. Those with orbital periods  $< 1$  day were systematically larger than the predicted radii by  $4.8 \pm 1\%$ , whereas for periods  $> 1.5$  days the deviation from the Baraffe et al. (1998) models are much smaller ( $1.7 \pm 0.7\%$ ). The implication is that a very short orbital period, i.e. very high level of magnetic activity, leads to greater radius inflation, and one then expects the level of radius inflation to decrease at longer periods. Figure 3.12 shows the radius anomaly ( $R_{obs}/R_{model}$ ) as a function of period for our new MEBs plus literature values whose reported errors are compatible with our own measurements ( $\sigma_{M_{obs}} < 6\%$  and  $\sigma_{R_{obs}} < 6.5\%$ ). We used the 5 Gyr, solar metallicity isochrone from the Baraffe et al. (1998) models, with  $L_{mix} = H_p$ , to derive the radius anomalies. The models were linearly interpolated onto a finer grid with intervals of  $0.0001M_{\odot}$ , and the model photospheric radii were calculated using  $R_{model} = \sqrt{L_{model}/4\pi\sigma T_{eff,model}^4}$ .

Despite the small sample, we have performed an error weighted statistical analysis of the period distribution, including our new measurements, to compare to the unweighted analysis presented in Kraus et al. (2011). Table 3.12 reports the weighted mean ( $\bar{\mu}$ ) and weighted sample standard deviation ( $\sigma$ ) of the radius anomaly for three different period ranges: i) all periods, ii) periods  $\leq 1$  day and, iii) periods  $> 1$  day. The boundary between the ‘short’ and ‘long’ period samples was chosen initially to match the analysis by Kraus et al. (2011). A T-test using the weighted mean and variances of the short and long period samples shows that their mean radii are distinct populations at a  $4.0\sigma$  significance, in support of Kraus et al.’s findings. However, the significance level is strongly dependent on the chosen period boundary, and is skewed by the cluster of very precisely measured values near 1.5 days. For example, a peak significance of  $4.8\sigma$  is found when dividing the sample at 1.5 days, but sharply drops to  $\sim 1\sigma$  for periods of 1.7 days or longer. At short periods, it rises gradually towards the peak from  $1\sigma$  at 0.3 days.

Instead, we have attempted to find a very basic mathematical description for any correlation between radius inflation and orbital period, but we appreciate our efforts are hampered by small number statistics. We fitted the distribution of the radius anomaly as a function of period, using first a linear model and then as an exponentially decaying function. We used the IDL routine MPFITFUN to determine an error weighted best-fit and the  $1\sigma$  errors of the model parameters. The results are reported in Table 3.13 and the best-fit models are over-plotted in Figure 3.12, but neither model is a good fit (although the exponential fits moderately better). While there is marginal evidence for greater inflation in the shortest period systems, we find that the ex-

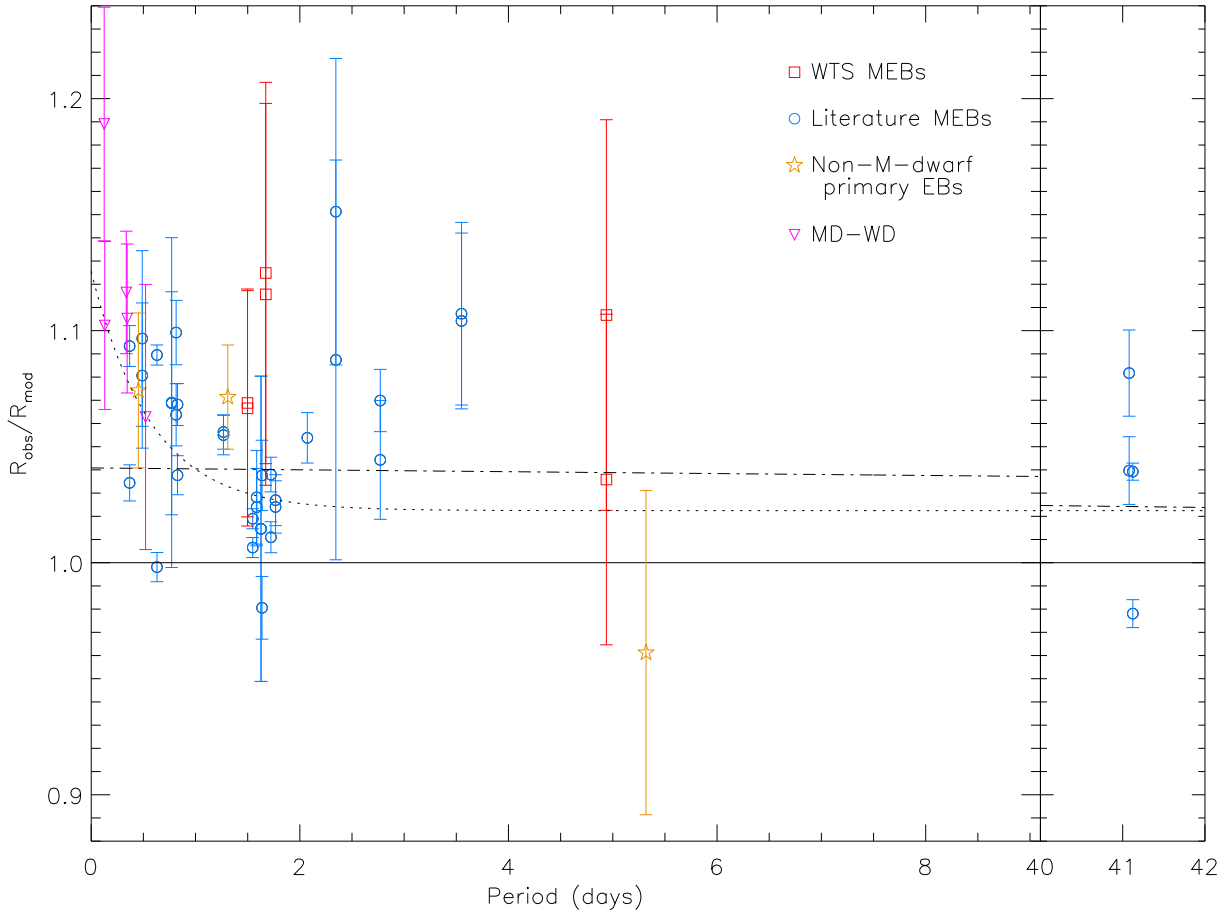


**Figure 3.12** — The radius anomaly as a function of orbital period using the 5 Gyr solar-metallicity isochrone from the Baraffe et al. (1998) models. Our new MEBs are shown by the red open squares. Literature radius anomalies with radius errors  $< 6.5\%$  are also plotted. The errors are a quadrature sum of the measured radius error plus a propagated error from the observed mass which determines the model radius. The dashed and dotted lines show the best-fit from a straight-line and exponentially decaying model to the data, respectively. The coefficients and goodness of fit for these fits are given in Table 3.13. The data used in this plot are given in Table 3.16.

pected convergence towards theoretical radius values for longer period, less active systems is not significantly supported by the available observation data.

There are two pertinent observations worth addressing, namely the low-mass eclipsing binaries LSPM J1112+7626 and Kepler-16 (Irwin et al. 2011; Doyle et al. 2011; Bender et al. 2012), which were announced after the Kraus et al. (2011) study. These systems significantly extended the observed orbital period range, with almost identical 41-day orbital periods, and both containing one fully-convective component ( $M_{\star} \sim 0.35M_{\odot}$ , Chabrier & Baraffe 1997) and one partially convective component (see Table 3.16). The radius inflation differs significantly between these two systems, as shown on the right-hand side of Figure 3.12. While the more massive, partially-convective component of Kepler-16 is well-described by the 1 Gyr model isochrone Baraffe et al. (1998) (see Figure 3.10), the other three stars suffer significant radius inflation, with no obvious correlation between the amount of inflation and the masses, even though one of them is a partially-convective star. This residual inflation, particularly for the

Model ( $R_{\text{obs}}/R_{\text{mod}} =$ )	$a_0$	$a_1$	$a_2$	$\chi^2$	DOF	$\chi^2_{\nu}$
$a_0 + a_1 P$	$1.0408 \pm 0.0017$	$-0.000406 \pm 0.000086$	–	514.5	49	10.5
$a_0 + a_1 e^{a_2 P}$	$1.0224 \pm 0.0027$	$0.103 \pm 0.017$	$-1.75 \pm 0.34$	405.0	48	8.4

**Table 3.13** — Results from an error weighted modelling of the radius anomaly as a function of period.  $a_i$  are the coefficients of the models and  $P$  is the orbital period in days. Neither of these simple models provide a statistically good fit, indicating a more complex relationship between the radius anomaly and orbital period.

fully-convective stars at long periods, may pose a challenge to the magnetic activity hypothesis as the sole reason for discrepancies between models and observations, especially given the extremely high-quality measurements of Kepler-16. However, one should note that other studies have suggested that the presence of a strong magnetic field can alter the interior structure of a low-mass star, such that it pushes the fully-convective mass limit for very active stars to lower values (Mullan & MacDonald 2001; Chabrier et al. 2007), so these stars may still suffer from a significant inhibition of convective flow.

The radius anomaly raises concern over the usefulness of the known MEBs in calibrating models for the evolution of singular M-dwarf stars that are the favoured targets of planet-hunting surveys searching for habitable worlds. Kraus et al. (2011) argue that the high-activity levels in very close MEBs make them poor representatives of typical single low-mass stars and that the observed radius discrepancies should not be taken as an indictment of stellar evolution models. However, we have seen that radius inflation remains in MEBs systems with low magnetic activity and furthermore, the inflated components of LSPM J1112+7626 do not exhibit  $H\alpha$  emission that is typically associated with the high activity levels in MEBs with inflated radii. West et al. (2011) used  $H\alpha$  emission as an activity indicator to determine that the fraction of single, active, early M-dwarfs is small ( $< 5\%$ ), but increases to 40 – 80% for M4-M9 dwarfs. Yet, it may be that the amount of activity needed to inflate radii to the measured values in MEBs is small and therefore below the level where observable signatures appear in  $H\alpha$  emission. This would then question the reliability of  $H\alpha$  emission as an activity indicator, meaning the fraction of ‘active’, single M-dwarfs may be even higher than the West et al. (2011) study. Given that these very small stars are a ripe hunting-ground for Earth-size planets, we must be able to constrain stellar evolution models in the presence of magnetic activity if we are to correctly characterise planetary companions. We note that even the very precisely-calibrated higher-mass stellar evolution models (Andersen 1991; Torres et al. 2010) do not reproduce the radii of active stars accurately (see Morales et al. (2009) who found 4 – 8% inflation in a G7+K7 binary with a 1.3 day orbit).

In order to establish a stringent constraint on the relationship between mass, period and radius, we need further measurements of systems that i) include ‘active’ and ‘non-active’ stars that span the fully-convective and partially-convective mass regimes, and ii) a better sampled range of orbital periods beyond 5 days to explore systems that are not synchronised. We may ultimately find that activity does not account for the full extent of the radius anomaly, and as suggested by Irwin et al. (2011), perhaps the equation of state for low-mass stars can still be improved. On the other hand, perhaps the importance of tidal effects between M-dwarfs in binaries with wider separations has been underestimated, as it has been shown that the orbital evolution of M-dwarf binary systems is not well-described by current models (Nefs et al. 2012).

### 3.10 Conclusions

In this paper, we have presented a catalogue of 16 new low-mass, detached eclipsing binaries that were discovered in the WFCAM Transit Survey. This is the first time dynamical measurements of M-dwarf EBs have been detected and measured primarily with infrared data. The survey light curves are of high quality, with a per epoch photometric precision of 3 – 5 mmag for the brightest targets ( $J \sim 13$  mag), and a median RMS of  $\lesssim 1\%$  for  $J \lesssim 16$  mag. We have reported the characterisation of three of these new systems using follow-up spectroscopy from ground-based 2 – 4 m class telescopes. The three systems ( $i = 16.7 - 17.6$  mag) have orbital periods in the range 1.5 – 4.9 days, and span masses 0.35 – 0.50 $M_{\odot}$  and radii 0.38 – 0.50 $R_{\odot}$ , with uncertainties of  $\sim 3.5 - 6.4\%$  in mass and  $\sim 2.7 - 5.5\%$  in radius. Two of the systems may be associated with the young-old disk population as defined by Leggett (1992) but our metallicity estimates from low-resolution spectra do not confirm a non-solar metallicity.

The radii of some of the stars in these new systems are significantly inflated above model predictions ( $\sim 3 - 12\%$ ). We analysed their radius anomalies along with literature data as a function of the orbital period (a proxy for activity). Our error-weighted statistical analysis revealed marginal evidence for greater radius inflation in very short orbital periods  $< 1$  day, but neither a linear nor exponentially decay model produced a significant fit to the data. As a result, we found no statistically significant evidence for a correlation between the radius anomaly and orbital period, but we are limited by the small sample of precise mass and radius measurements for low-mass stars. However, it is clear that radius inflation exists even at longer orbital periods in systems with low (or undetectable) levels of magnetic activity. A robust calibration of the effect of magnetic fields on the radii of M-dwarfs is therefore a key component in our understanding of these stars. Furthermore, it is a limiting factor in characterising the planetary companions of M-dwarfs, which are arguably our best targets in the search for habitable worlds and the study of other Earth-like atmospheres.

More measurements of the masses, radii and orbital periods of M-dwarf eclipsing binaries, spanning both the fully convective regime and partially convective mass regime, for active and non-active stars, across a range of periods extending beyond 5 days, are necessary to provide stringent observational constraints on the role of activity in the evolution of single low-mass stars. However, the influence of spots on the accuracy to which we can determine the radii from light curves will continue to impede these efforts, even in the most careful of cases (see e.g. Morales et al. 2010; Irwin et al. 2011).

This work has studied only one third of the M-dwarfs in the WFCAM Transit Survey. Observations are on-going and we expect our catalogue of M-dwarf eclipsing binaries to increase. This forms part of the legacy of the WTS and will provide the low-mass star community with high-quality MEB light curves. Furthermore, the longer the WTS runs, the more sensitive we become to valuable long-period, low-mass eclipsing binaries. These contributions plus other M-dwarf surveys, such as MEarth and PTF/M-dwarfs, will ultimately provide the observational calibration needed to anchor the theory of low-mass stellar evolution.

## Acknowledgements

We would like to thank I. Baraffe for providing the model magnitudes for our SED fitting in the appropriate filters, and S. Aigrain for the use of the OCCFIT transit detection algorithm. This work was greatly improved by several discussions with J. Irwin, as well as J. Southworth, K. Stassun and R. Jeffries. We thank the referee for their insightful comments which have improved this work and we also thank C. del Burgo for his comments on the original manuscript. JLB acknowledges the support of an STFC PhD studentship during part of this research. We thank the members of the WTS consortium and acknowledge the support of the RoPACS network. GK, BS, PC, NG, and HS are supported by RoPACS, while JLB, BN, SH, IS, DP, DB, RS, EM and YP have received support from RoPACS during this research, a Marie Curie Initial Training Network funded by the European Commission's Seventh Framework Programme. NL is supported by the national program AYA2010-19136 funded by the Spanish ministry of science and innovation. Finally, we extend our thanks to the fantastic team of TOs and support staff at UKIRT, and all those observers who clicked on U/CMP/2.

The United Kingdom Infrared Telescope is operated by the Joint Astronomy Centre on behalf of the Science and Technology Facilities Council of the U.K. This article is based on observations made with the INT, WHT operated on the island of La Palma by the ING in the Spanish Observatorio del Roque de los Muchachos, and with the IAC80 on the island of Tenerife operated by the IAC in the Spanish Observatorio del Teide. This research uses products from SDSS DR7. Funding for the SDSS and SDSS-II has been provided by the Alfred P. Sloan Foundation, the Participating Institutions, the National Science Foundation, the U.S. Department of Energy, the National Aeronautics and Space Administration, the Japanese Monbukagakusho, the Max Planck Society, and the Higher Education Funding Council for England. The SDSS Web Site is <http://www.sdss.org/>. This publication makes use of data products from the Two Micron All Sky Survey, which is a joint project of the University of Massachusetts and the Infrared Processing and Analysis Center/California Institute of Technology, funded by the National Aeronautics and Space Administration and the National Science Foundation. This work also makes use of NASA's Astrophysics Data System (ADS) bibliographic services, and the SIMBAD database, operated at CDS, Strasbourg, France. IRAF is distributed by the National Optical Astronomy Observatory, which is operated by the Association of Universities for Research in Astronomy (AURA) under cooperative agreement with the National Science Foundation.

## Appendix

In Table 3.14, we present the periods, epochs, effective temperatures,  $J$ -band and  $i$ -band magnitudes of the 13 remaining 19hr detached, well-sampled M-dwarf eclipsing binaries found with this study ( $J \leq 16$  mag). The temperatures are based on the SED fitting described in Section 3.4.1 and may be under-estimated. The periods and epochs are based only on least-square fitting which under-estimates the errors. These results are accurate to  $\sim 30$  minutes and we recommend to anyone planning to observe these objects in a time critical manner that they check these values themselves with the light curve data provided with this paper. Note that 19g-4-02069 is the subject of a near future publication (Nefs et al. *in prep.*) using RVs follow-up already obtained with GNIRS/GEMINI. The phase-folded light curves are shown in Figures 3.13. and 3.14, and the light curve data are provide in Table 3.15.

Name	RA (deg)	Dec (deg)	$N_{\text{epochs}}$	RMS (mag)	$P$ (days)	$T_0$ (HJD)	$J$ (Vega) (mag)	$i$ (Vega) (mag)	$T_{\text{eff,SED}}$ (K)
19a-1-02980	292.71276	36.312725	893	5.8	2.103525	2454318.65422	14.861	16.166	3946
							$\pm 0.004$	$\pm 0.004$	$\pm 100$
19c-3-08647	294.30659	36.815037	893	15.0	0.867466	2454318.50614	14.812	16.171	3883
							$\pm 0.004$	$\pm 0.004$	$\pm 100$
19c-4-11480	293.81149	36.902880	893	20.4	0.681810	2454317.89071	15.850	17.208	3946
							$\pm 0.006$	$\pm 0.007$	$\pm 100$
19d-2-07671	294.58622	36.386467	891	48.9	0.614540	2454317.99692	15.971	17.101	4209
							$\pm 0.007$	$\pm 0.007$	$\pm 100$
19d-2-09173	294.50246	36.365239	891	22.4	3.345469	2454320.15668	15.185	16.343	4209
							$\pm 0.005$	$\pm 0.005$	$\pm 100$
19e-2-02883	293.32813	36.241312	898	10.6	0.810219	2454317.90290	15.976	17.272	3946
							$\pm 0.007$	$\pm 0.007$	$\pm 100$
19f-1-07389	292.89403	36.143865	904	18.3	0.269868	2454317.97411	15.504	16.575	4209
							$\pm 0.005$	$\pm 0.005$	$\pm 100$
19f-4-05194	292.81253	36.590539	904	35.0	0.589530	2454318.10730	16.013	17.070	4209
							$\pm 0.007$	$\pm 0.006$	$\pm 100$
19g-1-13215	293.63655	36.249009	898	10.2	2.843515	2454318.34495	15.985	17.589	3374
							$\pm 0.007$	$\pm 0.008$	$\pm 100$
19g-2-08064	294.16931	36.162723	898	14.8	1.720410	2454317.94781	14.466	15.596	4209
							$\pm 0.003$	$\pm 0.004$	$\pm 100$
19g-4-02069	293.76480	36.521247	898	11.2	2.441759	2454321.78532	14.843	16.911	3054
							$\pm 0.004$	$\pm 0.006$	$\pm 100$
19h-2-00357	294.66466	36.272874	885	8.3	7.004082	2454320.79766	15.531	16.808	3946
							$\pm 0.005$	$\pm 0.006$	$\pm 100$
19h-2-01090	294.62103	36.262345	886	11.5	5.285051	2454322.78131	15.681	16.843	4209
							$\pm 0.006$	$\pm 0.006$	$\pm 100$

**Table 3.14** — The first release of the WTS M-dwarf Eclipsing Binary Catalogue detailing the remaining MEBs in the WTS 19hr field with  $J \leq 16$  mag that are not characterised in this paper. Note that 19g-4-02069 is the subject for a near future publication by Nefs et al. (*in prep.*) using RV follow-up from GNIRS/GEMINI. Please see appendix text for caveats on the quoted ephemerides.

Name	HJD	$J_{\text{WTS}}$ (mag)	$\sigma_{J_{\text{WTS}}}$ (mag)
19a-1-02980	2454317.82863842	14.846761	0.004826
19a-1-02980	2454317.84010834	14.844511	0.004894
...	...	...	...

**Table 3.15** — The WTS  $J$ -band light curves for the remainder of the WTS MEB catalogue given in Table 3.14. Magnitudes are given in the WFCAM system. Hodgkin et al. (2009) provide conversions for other systems. The errors,  $\sigma_J$ , are estimated using a standard noise model, including contributions from Poisson noise in the stellar counts, sky noise, readout noise and errors in the sky background estimation. (This table is published in full in the online journal and is shown partially here for guidance regarding its form and content.)

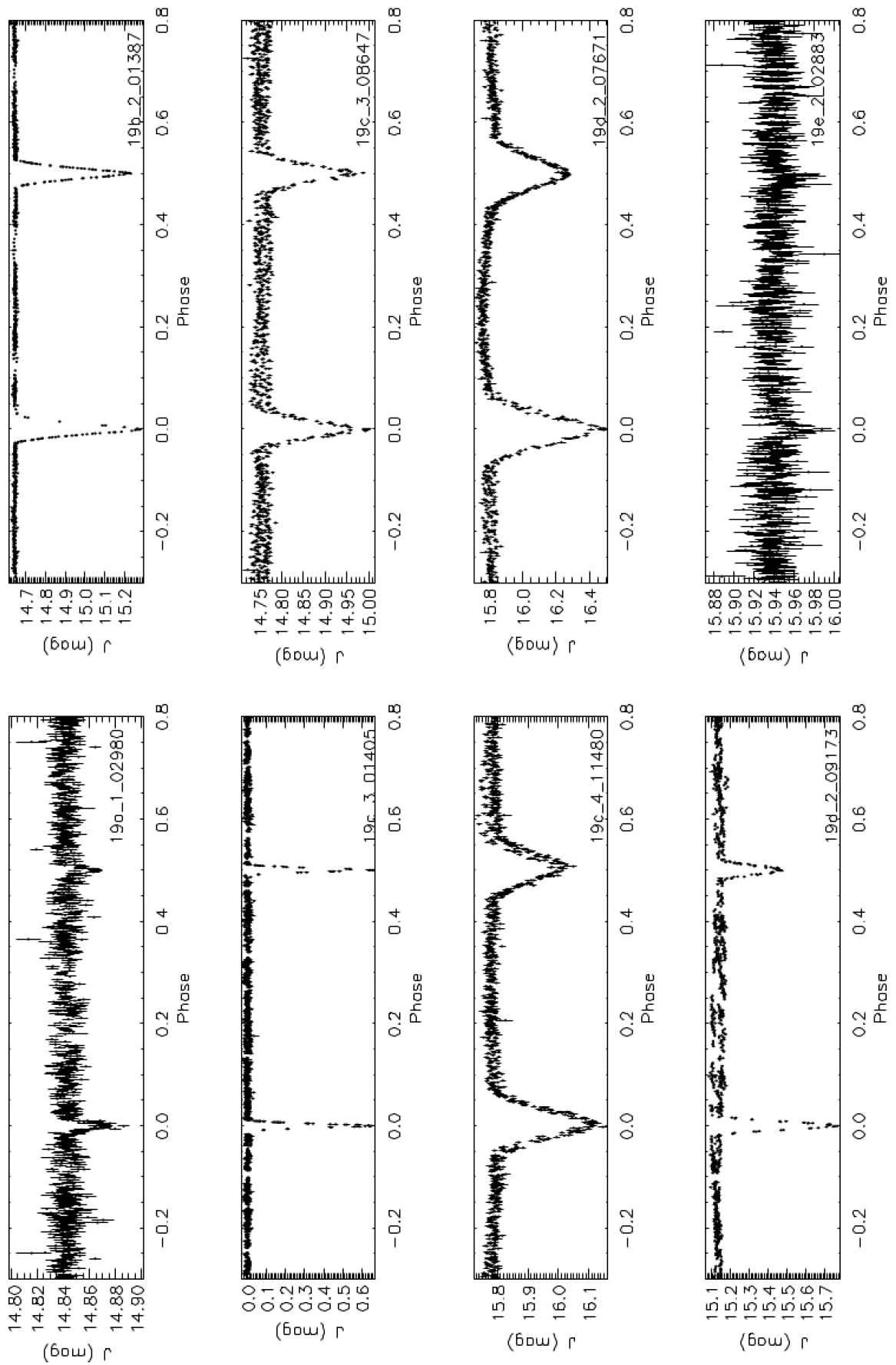


**Figure 3.13** — Phase-folded light curves of the MEBs discovered in the WTS 19hr field with  $J \leq 16$  mag...

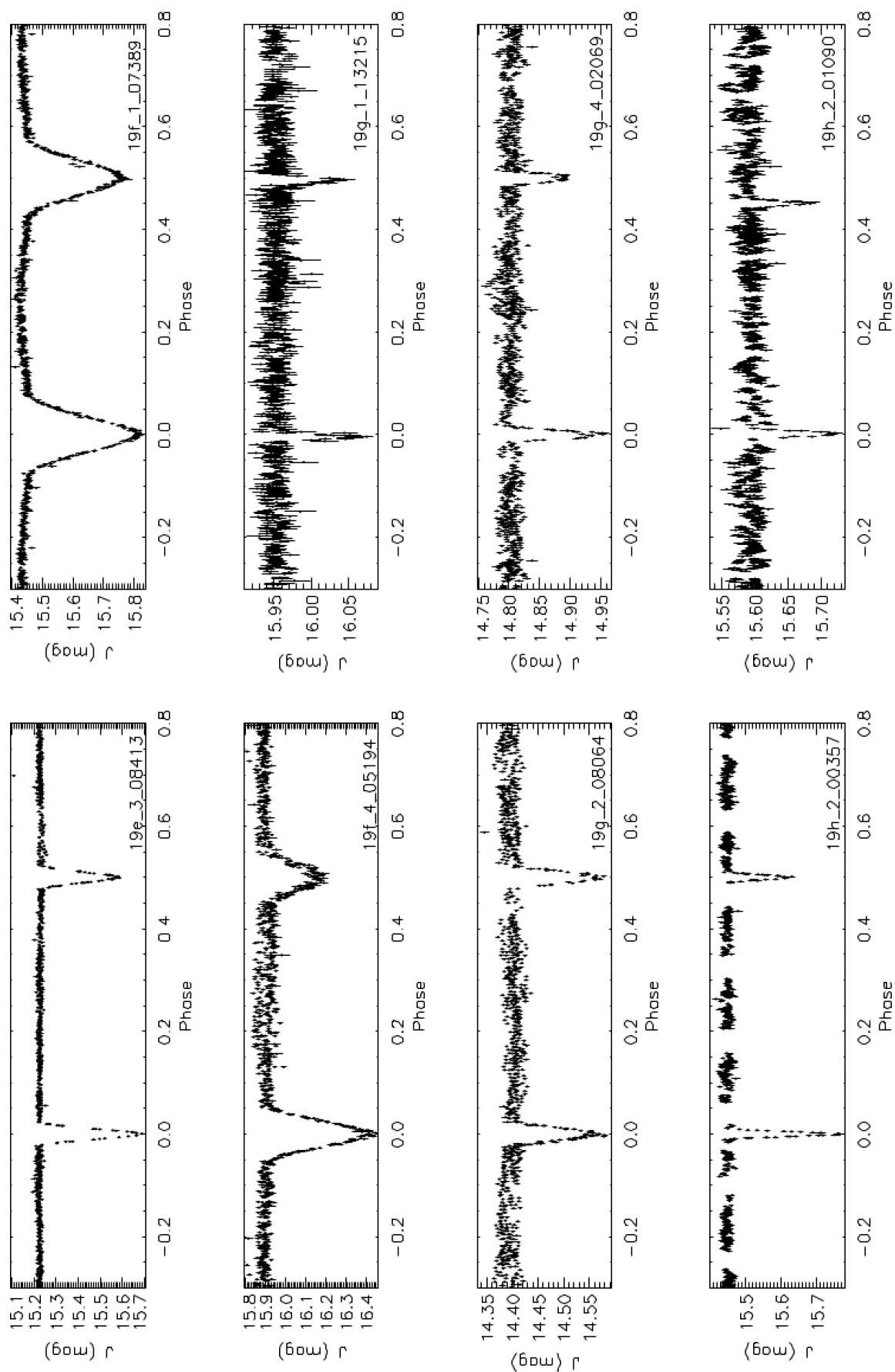


**Figure 3.14** — cont... Phase-folded light curves of the MEBs discovered in the WTS 19hr field with  $J < 16$  mag.

Table 3.16 contains the literature data used to create Figures 3.10, 3.11 and 3.12. The literature data was selected with the following filters: mass errors  $< 6.4\%$  and radius errors  $< 5.5\%$  (comparable to or better than the errors we presented for the three characterised MEBs in this paper), and in the range  $0.19 \leq M_\star \leq 0.71$  and  $0.19 \leq R_\star \leq 0.71$ .

**Table 3.16** — Literature values for systems used in Figures 3.10, 3.11 and 3.12

Name	Period (days)	Mass ( $M_\odot$ )	$\sigma_M$ ( $M_\odot$ )	Radius ( $R_\odot$ )	$\sigma_R$ ( $R_\odot$ )	$T_{\text{eff}}$ (K)	$\sigma_{T_{\text{eff}}}$ (K)	Ref
<b>MEBs</b>								
NSVS01031772A	0.368	0.5428	0.0028	0.5260	0.0028	3614.1	67.2	(1)
NSVS01031772B	0.368	0.4982	0.0025	0.5087	0.0031	3515.6	32.5	(1)
GUB <sub>oo</sub> A	0.489	0.6100	0.0071	0.6230	0.0163	3917.4	128.3	(1)
GUB <sub>oo</sub> B	0.489	0.5990	0.0061	0.6200	0.0203	3810.7	133.9	(1)
MG1-1819499A	0.6303135	0.557	0.001	0.569	0.002	3690.0	100.0	(2)
MG1-1819499B	0.6303135	0.535	0.001	0.500	0.003	3610.0	100.0	(2)
GJ3236A	0.77126	0.376	0.016	0.3795	0.0084	3312.0	110.0	(3)
GJ3236B	0.77126	0.281	0.015	0.300	0.015	3242.0	108.0	(3)
YYGemA	0.814	0.5974	0.0047	0.6196	0.0057	3819.4	98.0	(1)
YYGemB	0.814	0.6009	0.0047	0.6035	0.0057	3819.4	98.0	(1)
MG1-116309A	0.8271425	0.567	0.002	0.552	0.004	3917.4	100.5	(2)
MG1-116309B	0.8271425	0.532	0.002	0.532	0.004	3810.7	97.8	(2)
CMDraA	1.268	0.2310	0.0009	0.2534	0.0019	3133.3	73.0	(1)
CMDraB	1.268	0.2141	0.0009	0.2396	0.0015	3118.9	102.2	(1)
MG1-506664A	1.5484492	0.584	0.002	0.560	0.001	3732.5	104.6	(2)
MG1-506664B	1.5484492	0.544	0.002	0.513	0.001	3614.1	101.3	(2)
MG1-78457A	1.5862046	0.5270	0.0019	0.505	0.008	3326.6	101.1	(2)
MG1-78457B	1.5862046	0.491	0.002	0.471	0.009	3273.4	99.5	(2)
LP133-373A	1.6279866	0.34	0.02	0.330	0.014	3144.0	206.0	(4)
LP133-373B	1.6279866	0.34	0.02	0.330	0.014	3058.0	195.0	(4)
MG1-646680A	1.6375302	0.499	0.002	0.457	0.006	3732.5	51.9	(2)
MG1-646680B	1.6375302	0.443	0.002	0.427	0.006	3630.8	50.5	(2)
MG1-2056316A	1.7228208	0.4690	0.0021	0.441	0.002	3459.4	179.8	(2)
MG1-2056316B	1.7228208	0.382	0.002	0.374	0.002	3318.9	172.5	(2)
KOI126B	1.76713	0.2413	0.0030	0.2543	0.0014	—	—	(5)
KOI126C	1.76713	0.2127	0.0026	0.2318	0.0013	—	—	(5)
HIP96515Aa	2.3456	0.59	0.03	0.64	0.01	3724.0	154.0	(6)
HIP96515Ab	2.3456	0.54	0.03	0.55	0.03	3589.0	157.0	(6)
CUCncA	2.771	0.4333	0.0017	0.4317	0.0052	3162.3	156.7	(1)
CUCncB	2.771	0.3980	0.0014	0.3908	0.0095	3126.1	154.9	(1)
1RXSJ154727A	3.5500184	0.2576	0.0085	0.2895	0.0068	—	—	(7)
1RXSJ154727B	3.5500184	0.2585	0.0080	0.2895	0.0068	—	—	(7)
LSPMJ1112A	41.03236	0.3946	0.0023	0.3860	0.005	3061.0	162.0	(8)
LSPMJ1112B	41.03236	0.2745	0.0012	0.2978	0.005	2952.0	163.0	(8)

Continued on next page

Table 3.16 – continued from previous page

Name	Period	Mass	$\sigma_M$	Radius	$\sigma_R$	$T_{\text{eff}}$	$\sigma_{T_{\text{eff}}}$	Ref
Kepler16A	41.079220	0.6897	0.0035	0.6489	0.0013	4450	150	(9)
Kepler16B	41.079220	0.20255	0.00066	0.22623	0.00059	–	–	(9)
<b>Non-M-dwarf</b>								
<b>primary EBs</b>								
NGC-2204-S892B	0.452000	0.6621	0.0050	0.6800	0.0203	3944.6	110.5	(1)
IM-VirB	1.309000	0.6644	0.0048	0.6809	0.0131	4246.2	129.0	(1)
RXJ0239B	2.072016	0.693	0.006	0.703	0.002	4275.0	109.0	(10)
<b>MD-WD EBs</b>								
SDSS 1210	0.12448976	0.158	0.006	0.2135	0.003	–	–	(11)
NNSerB	0.13008017	0.111	0.004	0.149	0.002	–	–	(12)
SDSS 0123	0.33587114	0.273	0.002	0.306	0.007	–	–	(13)
GKVir	0.34433083	0.116	0.003	0.155	0.003	–	–	(13)
RXJ2130	0.5210356	0.555	0.023	0.553	0.017	3200.0	100.0	(10)
<b>Interferometry</b>								
GJ411	–	0.403	0.020	0.393	0.008	3570.0	42.0	(14)
GJ380	–	0.670	0.033	0.605	0.020	–	–	(14)
GJ887	–	0.503	0.025	0.459	0.011	3797.0	45.0	(15)

**Table 3.16** — Literature values for systems used in Figures 3.10, 3.11 and 3.12 with mass errors  $< 6.4\%$  and radius errors  $< 5.5\%$ , in the range  $0.19 \leq M_\star \leq 0.71$  and  $0.19 \leq R_\star \leq 0.71$ . Temperatures are given when available in the literature, but those without are not included in Figure 3.10. There are no rotation periods given for the interferometric measurements therefore these are excluded from Figure 3.12. References: (1) DEBCat and references therein ([www.astro.keele.ac.uk/jkt/debcats/](http://www.astro.keele.ac.uk/jkt/debcats/)), (2) Kraus et al. (2011), (3) Irwin et al. (2009), (4) Vaccaro et al. (2007), (5) Carter et al. (2011), (6) Huéllamo et al. (2009), (7) Hartman et al. (2011), (8) Irwin et al. (2011), (9) Doyle et al. (2011), (10) Knigge et al. (2011) and references therein, (11) Pyrzas et al. (2012), (12) Parsons et al. (2010), (13) Parsons et al. (2012), (14) Ségransan et al. (2003), (15) Demory et al. (2009).

## Bibliography

- Aigrain, S., Hodgkin, S., Irwin, J., et al. 2007, *MNRAS*, 375, 29
- Aigrain, S. & Irwin, M. 2004, *MNRAS*, 350, 331
- Allard, F., Hauschildt, P. H., Alexander, D. R., & Starrfield, S. 1997, *ARA&A*, 35, 137
- Andersen, J. 1991, *A&A Rev.*, 3, 91
- Andersen, J., Clausen, J. V., & Nordstrom, B. 1980, in *IAU Symposium*, Vol. 88, *Close Binary Stars: Observations and Interpretation*, ed. M. J. Plavec, D. M. Popper, & R. K. Ulrich, 81–86
- Bailer-Jones, C. A. L. & Lamm, M. 2003, *MNRAS*, 339, 477
- Bakos, G., Noyes, R. W., Kovács, G., et al. 2004, *PASP*, 116, 266
- Baraffe, I., Chabrier, G., Allard, F., & Hauschildt, P. H. 1998, *A&A*, 337, 403
- Barrado y Navascués, D. & Martín, E. L. 2003, *AJ*, 126, 2997
- Batalha, N. M., Borucki, W., Caldwell, D. A., et al. 2006, in *Bulletin of the American Astronomical Society*, Vol. 38, *American Astronomical Society Meeting Abstracts*, 210.08
- Bender, C. F., Mahadevan, S., Deshpande, R., et al. 2012, [arXiv:1205.0259](https://arxiv.org/abs/1205.0259)
- Berger, D. H., Gies, D. R., McAlister, H. A., et al. 2006, *ApJ*, 644, 475
- Bessell, M. S., Castelli, F., & Plez, B. 1998, *A&A*, 333, 231
- Birkby, J., Hodgkin, S., Pinfield, D., & WTS consortium. 2011, in *Astronomical Society of the Pacific Conference Series*, Vol. 448, *Astronomical Society of the Pacific Conference Series*, ed. C. Johns-Krull, M. K. Browning, & A. A. West, 803
- Bonanos, A. Z. 2007, in *IAU Symposium*, Vol. 240, *IAU Symposium*, ed. W. I. Hartkopf, E. F. Guinan, & P. Harmanec, 79–87
- Carter, J. A., Fabrycky, D. C., Ragozzine, D., et al. 2011, *Science*, 331, 562
- Casali, M., Adamson, A., Alves de Oliveira, C., et al. 2007, *A&A*, 467, 777
- Chabrier, G. & Baraffe, I. 1997, *A&A*, 327, 1039
- Chabrier, G., Baraffe, I., Allard, F., & Hauschildt, P. H. 2005, [arXiv:astro-ph/0509798](https://arxiv.org/abs/astro-ph/0509798)
- Chabrier, G., Gallardo, J., & Baraffe, I. 2007, *A&A*, 472, L17
- Claret, A. 2000, *A&A*, 363, 1081
- Claret, A. 2004, *A&A*, 428, 1001
- Covey, K. R., Ivezić, Ž., Schlegel, D., et al. 2007, *AJ*, 134, 2398
- Cruz, K. L., Reid, I. N., Liebert, J., Kirkpatrick, J. D., & Lowrance, P. J. 2003, *AJ*, 126, 2421
- de Mooij, E. J. W., Brogi, M., de Kok, R. J., et al. 2012, *A&A*, 538, A46
- Deeg, H. J. & Doyle, L. R. 2001, in *Third Workshop on Photometry*, ed. W. J. Borucki & L. E. Lasher, 85
- Del Burgo, C., Deshpande, R., Martín, E. L., et al. 2011, *Research, Science and Technology of Brown Dwarfs and Exoplanets: Proceedings of an International Conference held in Shanghai on Occasion of a Total Eclipse of the Sun, Shanghai, China*, Edited by E.L. Martin; J. Ge; W. Lin; EPJ Web of Conferences, Volume 16, id.04006, 16, 4006
- Demory, B., Ségransan, D., Forveille, T., et al. 2009, *A&A*, 505, 205
- Dhital, S., West, A. A., Stassun, K. G., et al. 2011, [arXiv:1112.2670](https://arxiv.org/abs/1112.2670)
- Doyle, L. R., Carter, J. A., Fabrycky, D. C., et al. 2011, *Science*, 333, 1602
- Drimmel, R., Cabrera-Lavers, A., & López-Corredoira, M. 2003, *A&A*, 409, 205
- Dunham, E. W., Mandushev, G. I., Taylor, B. W., & Oetiker, B. 2004, *PASP*, 116, 1072
- Etzel, P. B. 1980, *Information Bulletin on Variable Stars*, 1900, 1
- Girardi, L., Bertelli, G., Bressan, A., et al. 2002, *A&A*, 391, 195

- Gizis, J. E. 1997, *AJ*, 113, 806
- Guinan, E. F., Fitzpatrick, E. L., Dewarf, L. E., et al. 1998, *ApJ*, 509, L21
- Gustafsson, B., Edvardsson, B., Eriksson, K., et al. 2008, *A&A*, 486, 951
- Hartman, J. D., Bakos, G. Á., Noyes, R. W., et al. 2011, *AJ*, 141, 166
- Henry, T. J., Ianna, P. A., Kirkpatrick, J. D., & Jahreiss, H. 1997, *AJ*, 114, 388
- Hewett, P. C., Warren, S. J., Leggett, S. K., & Hodgkin, S. T. 2006, *MNRAS*, 367, 454
- Hillenbrand, L. A. & White, R. J. 2004, *ApJ*, 604, 741
- Hoaglin, D. C., Mosteller, F., & Tukey, J. W. 1983, *Understanding robust and exploratory data analysis* (Wiley)
- Hodgkin, S. T., Irwin, M. J., Hewett, P. C., & Warren, S. J. 2009, *MNRAS*, 394, 675
- Huélamo, N., Vaz, L. P. R., Torres, C. A. O., et al. 2009, *A&A*, 503, 873
- Irwin, J., Aigrain, S., Hodgkin, S., et al. 2007a, *MNRAS*, 380, 541
- Irwin, J., Charbonneau, D., Berta, Z. K., et al. 2009, *ApJ*, 701, 1436
- Irwin, J., Irwin, M., Aigrain, S., et al. 2007b, *MNRAS*, 375, 1449
- Irwin, J. M., Quinn, S. N., Berta, Z. K., et al. 2011, *ApJ*, 742, 123
- Irwin, M. & Lewis, J. 2001, *New Astronomy Review*, 45, 105
- Irwin, M. J. 1985, *MNRAS*, 214, 575
- Jackson, R. J., Jeffries, R. D., & Maxted, P. F. L. 2009, *MNRAS*, 399, L89
- Jeffries, R. D. & Jewell, S. J. 1993, *MNRAS*, 264, 106
- Johnson, D. R. H. & Soderblom, D. R. 1987, *AJ*, 93, 864
- Jones, H. R. A., Longmore, A. J., Jameson, R. F., & Mountain, C. M. 1994, *MNRAS*, 267, 413
- Kervella, P., Thévenin, F., Di Folco, E., & Ségransan, D. 2004, *A&A*, 426, 297
- Kirkpatrick, J. D., Henry, T. J., & McCarthy, Jr., D. W. 1991, *ApJS*, 77, 417
- Knigge, C., Baraffe, I., & Patterson, J. 2011, arXiv:1102.2440
- Koppenhoefer, J., Afonso, C., Saglia, R. P., & Henning, T. 2009, *A&A*, 494, 707
- Kraus, A. L., Tucker, R. A., Thompson, M. I., Craine, E. R., & Hillenbrand, L. A. 2011, *ApJ*, 728, 48
- Law, N. M., Kraus, A. L., Street, R. R., et al. 2011, arXiv:1101.0630
- Lawrence, A., Warren, S. J., Almaini, O., et al. 2007, *MNRAS*, 379, 1599
- Leggett, S. K. 1992, *ApJS*, 82, 351
- Lépine, S., Rich, R. M., & Shara, M. M. 2007, *ApJ*, 669, 1235
- Lodieu, N., Dobbie, P. D., & Hambly, N. C. 2011, *A&A*, 527, A24
- López-Morales, M. 2007, *ApJ*, 660, 732
- López-Morales, M. & Ribas, I. 2005, *ApJ*, 631, 1120
- Lucy, L. B. 1967, *Zeitschrift fur Astrophysik*, 65, 89
- Mann, A. W., Gaidos, E., Lépine, S., & Hilton, E. 2012, arXiv:1202.5394
- Markwardt, C. B. 2009, in *Astronomical Society of the Pacific Conference Series*, Vol. 411, *Astronomical Data Analysis Software and Systems XVIII*, ed. D. A. Bohlender, D. Durand, & P. Dowler, 251
- Miller, A. A., Irwin, J., Aigrain, S., Hodgkin, S., & Hebb, L. 2008, *MNRAS*, 387, 349
- Morales, J. C., Gallardo, J., Ribas, I., et al. 2010, *ApJ*, 718, 502
- Morales, J. C., Ribas, I., Jordi, C., et al. 2009, *ApJ*, 691, 1400
- Muirhead, P. S., Hamren, K., Schlawin, E., et al. 2011, arXiv:1109.1819
- Mullan, D. J. & MacDonald, J. 2001, *ApJ*, 559, 353
- Munn, J. A., Monet, D. G., Levine, S. E., et al. 2004, *AJ*, 127, 3034

- Munn, J. A., Monet, D. G., Levine, S. E., et al. 2008, *AJ*, 136, 895
- Nefs, S. V., Birkby, J. L., Snellen, I. A. G., et al. 2012, arXiv:1206.1200
- Nelson, B. & Davis, W. D. 1972, *ApJ*, 174, 617
- Nordstrom, B. & Johansen, K. T. 1994, *A&A*, 291, 777
- Nutzman, P. & Charbonneau, D. 2008, *PASP*, 120, 317
- Önehag, A., Heiter, U., Gustafsson, B., et al. 2011, arXiv:1112.0141
- Parsons, S. G., Marsh, T. R., Copperwheat, C. M., et al. 2010, *MNRAS*, 402, 2591
- Parsons, S. G., Marsh, T. R., Gänsicke, B. T., et al. 2012, *MNRAS*, 420, 3281
- Pollacco, D. L., Skillen, I., Cameron, A. C., et al. 2006, *PASP*, 118, 1407
- Pont, F., Zucker, S., & Queloz, D. 2006, *MNRAS*, 373, 231
- Popper, D. M. 1984, *Mitteilungen der Astronomischen Gesellschaft Hamburg*, 62, 19
- Popper, D. M. & Etzel, P. B. 1981, *AJ*, 86, 102
- Press, W. H., Teukolsky, S. A., Vetterling, W. T., & Flannery, B. P. 1992, *Numerical recipes in FORTRAN. The art of scientific computing* (Cambridge: University Press, 1992, 2nd ed.)
- Pyrzas, S., Gänsicke, B. T., Brady, S., et al. 2012, *MNRAS*, 419, 817
- Reid, I. N., Hawley, S. L., & Gizis, J. E. 1995, *AJ*, 110, 1838
- Reyle, C., Rajpurohit, A. S., Schultheis, M., & Allard, F. 2011, arXiv:1102.1263
- Ribas, I. 2006, *Ap&SS*, 304, 89
- Ribas, I., Jordi, C., Vilardell, F., et al. 2005, *ApJ*, 635, L37
- Rojas-Ayala, B., Covey, K. R., Muirhead, P. S., & Lloyd, J. P. 2010, *ApJ*, 720, L113
- Schlegel, D. J., Finkbeiner, D. P., & Davis, M. 1998, *ApJ*, 500, 525
- Ségransan, D., Kervella, P., Forveille, T., & Queloz, D. 2003, *A&A*, 397, L5
- Shkolnik, E. L., Hebb, L., Liu, M. C., Reid, I. N., & Collier Cameron, A. 2010, *ApJ*, 716, 1522
- Slesnick, C. L., Carpenter, J. M., & Hillenbrand, L. A. 2006, *AJ*, 131, 3016
- Soderblom, D. R. & Mayor, M. 1993, *AJ*, 105, 226
- Southworth, J. 2008, *MNRAS*, 386, 1644
- Southworth, J., Bruntt, H., & Buzasi, D. L. 2007a, *A&A*, 467, 1215
- Southworth, J., Bruntt, H., & Buzasi, D. L. 2007b, *A&A*, 467, 1215
- Southworth, J. & Clausen, J. V. 2007, *A&A*, 461, 1077
- Southworth, J., Maxted, P. F. L., & Smalley, B. 2004a, *MNRAS*, 349, 547
- Southworth, J., Maxted, P. F. L., & Smalley, B. 2004b, *MNRAS*, 351, 1277
- Southworth, J., Maxted, P. F. L., & Smalley, B. 2005a, *A&A*, 429, 645
- Southworth, J., Smalley, B., Maxted, P. F. L., Claret, A., & Etzel, P. B. 2005b, *MNRAS*, 363, 529
- Southworth, J., Zucker, S., Maxted, P. F. L., & Smalley, B. 2004c, *MNRAS*, 355, 986
- Stassun, K. G., Mathieu, R. D., & Valenti, J. A. 2007, *ApJ*, 664, 1154
- Torres, G., Andersen, J., & Giménez, A. 2010, *A&A Rev.*, 18, 67
- Torres, G., Lacy, C. H., Marschall, L. A., Sheets, H. A., & Mader, J. A. 2006, *ApJ*, 640, 1018
- Torres, G. & Ribas, I. 2002, *ApJ*, 567, 1140
- Vaccaro, T. R., Rudkin, M., Kawka, A., et al. 2007, *ApJ*, 661, 1112
- van Hamme, W. 1993, *AJ*, 106, 2096
- Viti, S., Jones, H. R. A., Maxted, P., & Tennyson, J. 2002, *MNRAS*, 329, 290
- Viti, S., Jones, H. R. A., Schweitzer, A., et al. 1997, *MNRAS*, 291, 780
- West, A. A., Morgan, D. P., Bochanski, J. J., et al. 2011, *AJ*, 141, 97
- Wolf, V. M., Lépine, S., & Wallerstein, G. 2009, *PASP*, 121, 117

- Woolf, V. M. & Wallerstein, G. 2006, PASP, 118, 218  
Zahn, J. 1977, A&A, 57, 383  
Zahn, J.-P. 1975, A&A, 41, 329  
Zucker, S. & Mazeh, T. 1994, ApJ, 420, 806

---

## Chapter 4

---

# Four ultra-short period eclipsing M-dwarf binaries in the WFCAM Transit Survey.

We report on the discovery of four ultra-short period ( $P \leq 0.18$  days) eclipsing M-dwarf binaries in the WFCAM Transit Survey. Their orbital periods are significantly shorter than of any other known main-sequence binary system, and are all significantly below the sharp period cut-off at  $P \sim 0.22$  days as seen in binaries of earlier type stars. The shortest-period binary consists of two M4 type stars in a  $P = 0.112$  day orbit. The binaries are discovered as part of an extensive search for short-period eclipsing systems in over 260,000 stellar lightcurves, including over 10,000 M-dwarfs down to  $J=18$  mag, yielding 25 binaries with  $P \leq 0.23$  days. In a popular paradigm, the evolution of short period binaries of cool main-sequence stars is driven by loss of angular momentum through magnetised winds. In this scheme, the observed  $P \sim 0.22$  day period cut-off is explained as being due to timescales that are too long for lower-mass binaries to decay into tighter orbits. Our discovery of low-mass binaries with significantly shorter orbits implies that either these timescales have been overestimated for M-dwarfs, e.g. due to a higher effective magnetic activity, or that the mechanism for forming these tight M-dwarf binaries is different from that of earlier type main-sequence stars.

S.V.Nefs, J.L. Birkby, I.A.G. Snellen, S.T. Hodgkin, D. J. Pinfield, B. Sipőcz, G. Kovacs, D. Mislis, R. P. Saglia, J. Koppenhoefer, P. Cruz, D. Barrado, E. L. Martin, N. Goulding, H. Stoev, J. Zendejas, C. del Burgo, M. Cappetta, Y.V.Pavlenko  
*MNRAS* 425, N950 (2012)

## 4.1 Introduction

The period distribution of close binary star systems (e.g. Devor 2005; Derekas et al. 2007) contains important information on binary formation and evolutionary processes. Observations have revealed that there is a sharp cut-off in the period distribution at  $\sim 0.22$  days (e.g. Rucinski 1992, Norton et al. 2011), and very few binaries have thus far been discovered with significantly shorter periods (GSC 2314-0530 0.192 days; Dimitrov & Kjurkchieva 2010 and OGLE BW3 V38 0.198 days; Maceroni & Montalban 2004). Searching for binaries beyond this cut-off is interesting because their frequency of occurrence, and the ratio of detached versus contact binary systems, provide direct constraints on theories that model the formation and migration history of low-mass stars, a mass regime that has been fairly poorly characterised so far. It has even been proposed that very short period low-mass binaries could be the progenitors of stellar mergers which may lead to the observed population of very hot Jupiters (Martin et al. 2011), and which could explain events such as Nova Sco 2008, where a contact binary with an orbital period of 1.4 days merged into a single star (Tylenda et al. 2010).

There are several theories that aim to explain the observed cut-off and the apparent lack of systems beyond it. In the first theory, near-contact binaries are formed from initially well-detached systems that undergo angular momentum loss (AML) via a magnetised wind on Gyr timescales. Evidence for such winds, especially in low-mass, short-period binary systems, is provided by observations of extensive cool spot coverage, rapid rotation in tidally locked orbits, strong  $H\alpha$  emission, flares and high activity rates (e.g. Morales et al. 2010, Vida et al. 2009). Stepien (1995; 2006; 2011) estimated the timescale required for the components of a detached binary to both reach Roche-lobe overflow through AML, i.e. to become a contact binary. He proposed that the AML timescale is much longer for low-mass systems, such that M-dwarf binaries (except in the most extreme mass-ratio cases) can not reach Roche-lobe overflow within the age of the Universe. The 0.22 day cut-off therefore corresponds to a lower limit in total binary mass of  $\sim 1.0\text{-}1.2M_{\odot}$  for contact systems. However, detached low-mass ultra-short period binary systems are also extremely difficult to form by this mechanism. In Section 4.2, we will further explain and quantify the AML evolution for M-dwarf binaries.

Proposing an alternative theory, Jiang et al. (2011) suggest that an instability in mass transfer, when the primary fills its Roche lobe, is responsible for the observed short-period cut-off. This instability is predicted to occur if the primary star has a significant convection zone, implying that binaries with a primary mass lower than  $0.63M_{\odot}$  would merge too quickly to form stable contact systems. In this scheme, M-dwarf binaries in the contact phase are short-lived and are therefore extremely rare. Unlike the AML model of Stepien (2011), detached low-mass short-period binaries are permitted in the mass transfer instability model because its timescale for angular momentum loss is significantly shorter.

However, third-body interactions in the birth environment may be responsible for accelerating the orbital evolution of low-mass binaries beyond the previous predictions. Here, energy is drained from the binary by either ejection of the lowest-mass companion in a low-N ‘mini-cluster’ (e.g. Reipurth & Clarke 2001, Goodwin et al. 2004) or through the Kozai mechanism (e.g. Eggleton & Kiseleva 2001, Fabrycky & Tremaine 2007). Interestingly, an adaptive optics search for companions around solar-mass contact systems by Rucinski et al. (2007) found that the fraction of short-period binaries in hierarchical triples is at least  $59\%(\pm 8\%)$  (see also Tokovinin et al. 2006), indicating that a significant amount of short-period binaries are found

in triple systems.

With these competing scenarios in mind, it is interesting to characterise the low-mass M-dwarf population of ultra short-period binaries. Although M-dwarfs form the most common stellar population in our Galaxy ( $\sim 70\%$  by number; Henry et al. 1997), their intrinsic faintness is a challenge when trying to obtain a sufficiently large M-dwarf sample from a magnitude limited optical survey in order to study their binary characteristics. In this paper we describe a search for the shortest period eclipsing binary systems in the WFCAM Transit Survey (WTS) down to  $J=18$ . The WTS is an infrared photometric monitoring survey running on the 3.8m United Kingdom Infrared Telescope (UKIRT) with its main goal to find planets transiting M-dwarfs. Because M-dwarf spectral energy distributions (SEDs) peak in the infrared, the WTS is sensitive to redder eclipsing systems, with a significant population of binary systems down to  $\sim M5$ .

In Section 4.2 we will expand on our motivation of this work. In Section 4.3 we describe our observations and data reduction, including the WTS survey itself and low resolution spectroscopic follow-up of some of the candidates. In Section 4.4 we use a variability statistic to find stars with correlated variability and select eclipsing binary candidates from the WTS data. We subsequently determine orbital periods using box-fitting and Fourier techniques. With simple colour cuts we then pre-select binaries with primary mass  $\mathcal{M}_1 < 0.7M_\odot$  (K5). In Section 4.5 we obtain estimates of the binary effective temperature through broadband SED fitting and spectral template matching. By fitting Fourier series to the data we identify (semi-)detached and contact systems. In Section 4.6, we compare our results with expectations from the evolution scenarios of low-mass short period binaries.

## 4.2 Motivation

### 4.2.1 The AML timescale argument

Single stars with masses  $< 1.5M_\odot$  have an outer convective layer and can be chromospherically very active. This activity is expected to cause the loss of angular momentum through a magnetised wind of material that is forced to co-rotate with the star. The rotation rate of a star is found to correlate with the activity. Young active stars rotate rapidly but their rotation slows down with time leading to a decrease in their activity (e.g. Irwin et al. 2011). In a close binary, with synchronised orbits and spins, the angular momentum loss due to the spin-down of the individual stars causes a decrease of the binary orbital angular momentum, which tightens the orbit, but this then spins up the stars. A popular scenario is that when given enough time, the loss of angular momentum will bring the two stars into contact.

Stepien (1995, 2006, 2011) estimated timescales required for a detached binary to reach Roche-lobe overflow through AML and to evolve into a contact system, concluding that for a solar-type, equal-mass binary with a starting separation that corresponds to a period  $P_0=2.0$  days this timescale is  $\sim 6.5$ Gyr. He proposed that the AML timescale is significantly longer for decreasing mass systems and that therefore Roche-lobe overflow will not occur within the Hubble time for binaries with an initial primary mass of less than  $\sim 0.7M_\odot$ , again assuming an initial orbital period of 2.0 days (an assumption which is further explained below). The 0.22 day period cut would therefore correspond to a lower limit on the total mass of contact systems of

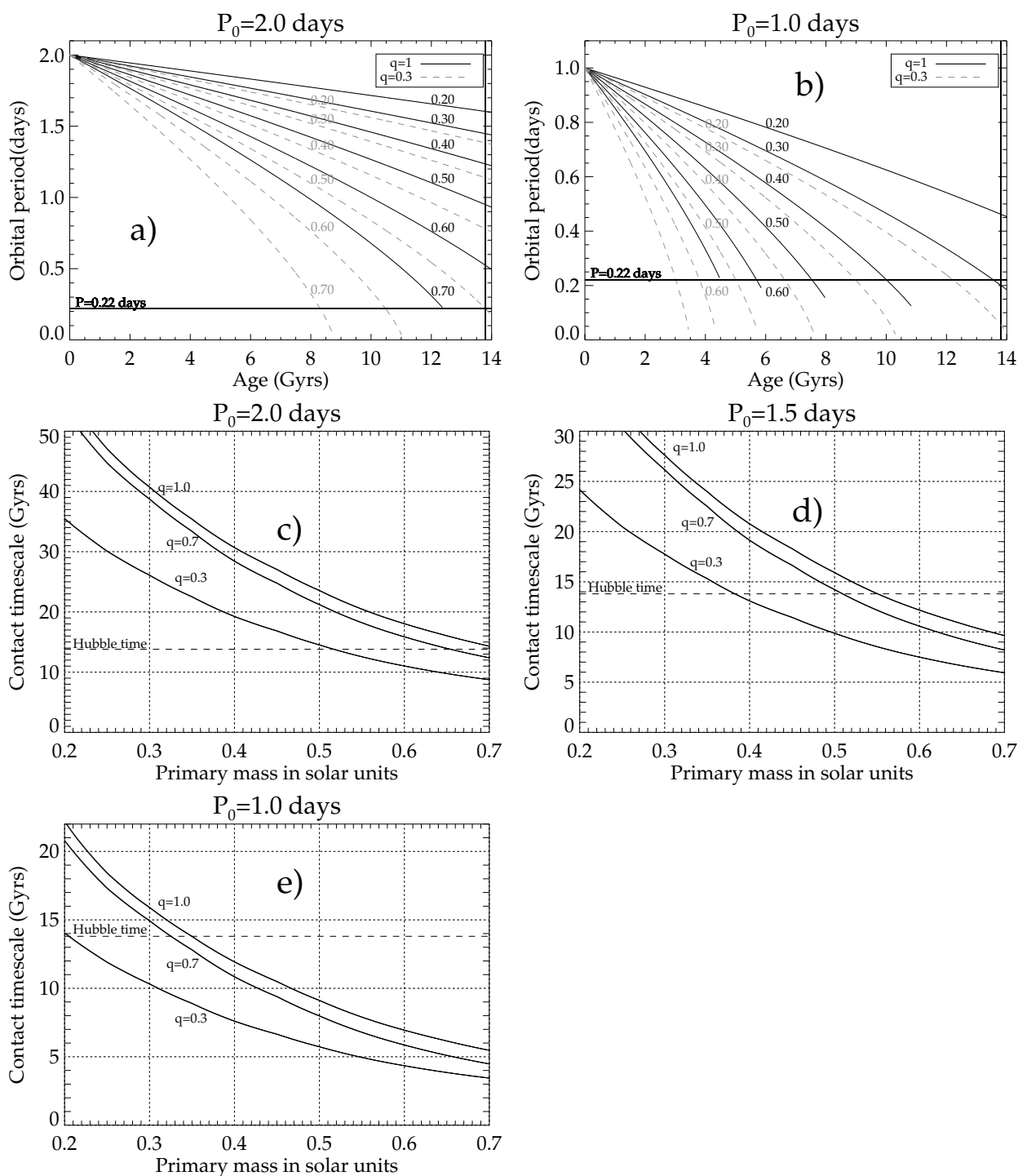


**Figure 4.1 — Panel a):** The orbital evolution of M-dwarf binaries, assuming  $P_0 = 2.0$  days and  $q = 1.0$ , plotted for decreasing primary stellar mass from  $0.7$  to  $0.2 M_\odot$  in steps of  $0.1 M_\odot$  (black solid curve). The dashed grey curves are models with mass ratio  $q = 0.3$ . The models are cut off at the point of Roche lobe overflow, which depends on total mass and the mass-ratio. The horizontal line indicates the 0.22 day period cut-off, whereas the vertical line shows the Hubble time. Binaries with mass less than  $\sim 0.65 M_\odot$  could not have reached contact. **Panel b):** same models, but for  $P_0 = 1.0$  day. **Panels c) through e):** the timescales to reach contact as a function of primary mass for  $P_0 = 2.0, 1.5$  and  $1.0$  days and mass ratios  $q = 1.0, 0.7$ , and  $0.3$ .

1.0-1.2 $M_{\odot}$  (i.e. a binary consisting of two M0 dwarfs). This suggests that evolution timescales are too long for M-dwarf binaries to decay into tight orbits within the age of the Universe.

One solution to this is to choose a shorter starting period ( $P_0$ ). To calculate the orbital evolution for M-dwarfs, and to investigate this evolution for different starting periods and mass ratios, we equate the change in the total binary orbital angular momentum ( $H_{orb}$ ), which scales with the orbital frequency  $\omega$  as  $dH_{orb}/dt \sim \omega^{-4/3}\dot{\omega}$ , to the change in the sum of spin angular momenta ( $H_{spin}$ ) for the binary components,  $dH_{spin}/dt \sim \omega$ , following the derivation in Section 4.3 of Stepien (1995). We assume that mass-loss is small over the Hubble time for M-dwarfs and that the orbit remains circular and synchronised throughout binary evolution. The change in the orbital period as function of time can then be written as:

$$\frac{dP}{dt} = -\mathcal{A}(r_1, \mathcal{M}_1, r_2, \mathcal{M}_2)P^{-1/3}, \quad (4.1)$$

where  $\mathcal{A}$  is constant with time and  $r_{1,2}$  and  $\mathcal{M}_{1,2}$  are the radii and masses of the primary and secondary binary components. This equation has the solution:

$$P(t) = (P_0^{4/3} - \frac{4}{3}\mathcal{A}t)^{3/4}, \quad (4.2)$$

where  $P_0$  is the starting period at formation (in days) and  $P(t)$  is the observed orbital period at time  $t$ .

In panel a) of Figure 4.1 we show the orbital evolution of M-dwarfs, assuming  $P_0=2.0$  days and  $q(=\mathcal{M}_2/\mathcal{M}_1)=1.0$ , plotted for decreasing primary stellar mass from 0.7 to 0.2 $M_{\odot}$  in steps of 0.1 $M_{\odot}$ . In the same panel, we show the evolution for M-dwarfs with  $q=0.3$  (grey dashed curves). Binary evolution is significantly faster for low-mass ratio systems. Clearly, unless a low mass-ratio is assumed, there is insufficient AML over the Hubble time for any M-dwarf binary to reach contact. In panel b) of Figure 4.1 we plot the same binary evolution for M-dwarfs but with  $P_0=1.0$  day, showing that a shorter starting period results in faster evolution.

In panels c) through e) of Figure 4.1 we show the time required to reach contact as a function of primary mass assuming  $P_0=2.0, 1.5,$  and 1.0 days for mass ratios  $q=1.0, 0.7,$  and 0.3. Clearly, in the  $P_0=1.0$  day model, evolution is much faster and  $q=1$  systems with primaries more massive than  $\sim 0.35M_{\odot}$  could be brought into contact within the Hubble time. This means that the upper limit on the total mass of contact systems would shift to masses corresponding to later-type M-dwarfs, assuming that the formation mechanism for such binaries is the same as that of earlier-type stars. Also, even for a 0.5+0.5 $M_{\odot}$  binary the evolution timescale is  $\sim 8$  Gyrs in the fastest model, which would mean that such binaries would be some of the oldest objects in our current universe.

We have calculated what  $P_0$  is minimally required to bring a given M-dwarf binary into a given orbital period today, within a given time-frame. We show this as a function of primary mass, derived using Equation 2, in Figure 4.2 for equal-mass binaries, assuming observed orbits of 0.10, 0.15, 0.20 and 0.25 days. For example, a minimum starting period of  $P_0=1.0$  day is required for a 0.3+0.3 $M_{\odot}$  binary to reach  $P=0.2$  days within the Hubble time. For a typical 5.0 Gyr thin disk binary, the required  $P_0$  is 0.4 days for the same system. Clearly, to constrain AML theory, it is vital to assess from observations what is the actual frequency of (ultra)short-period M-dwarf binaries.

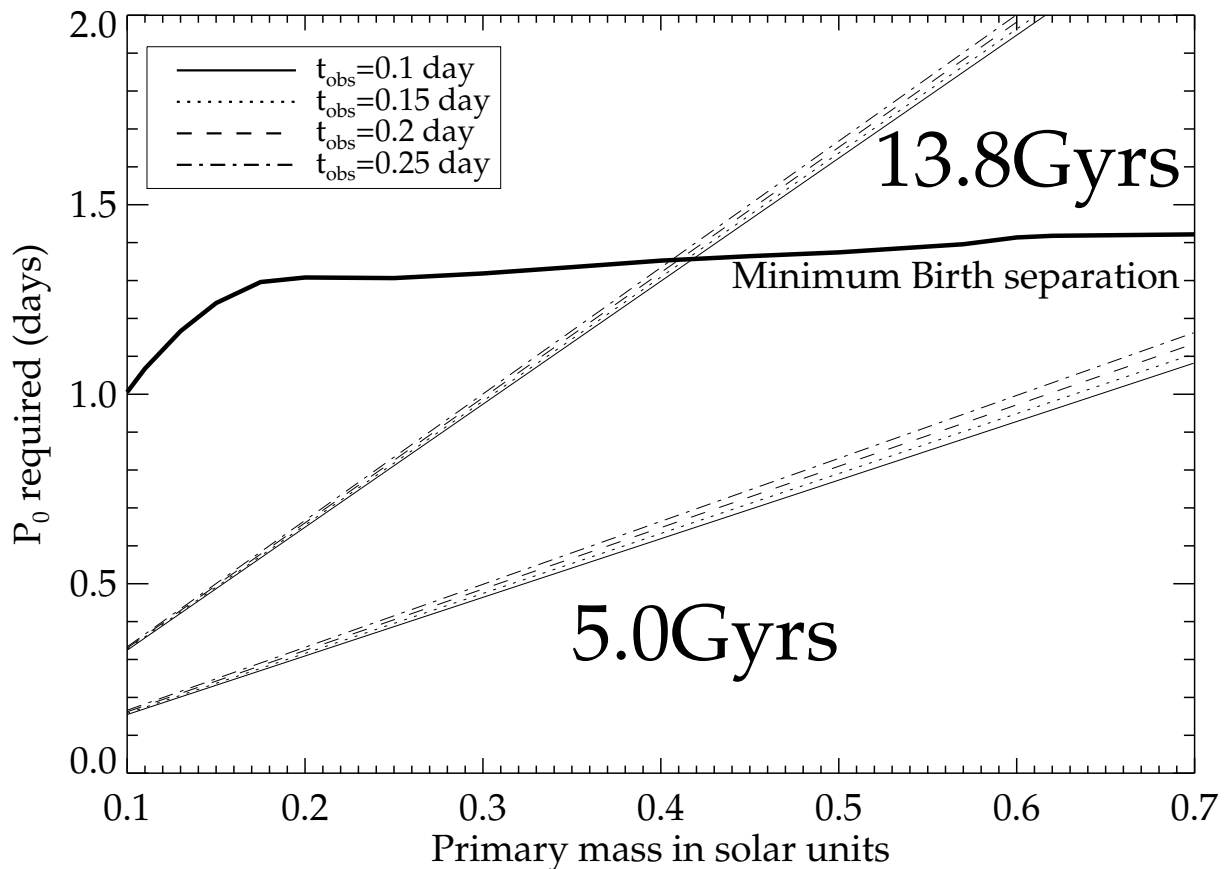


**Figure 4.2** — The starting period  $P_0$  required to bring an equal-mass binary of given primary mass into a currently observed orbit of 0.1, 0.15, 0.2, and 0.25 days (the four lines, observed period increasing from bottom to top) for  $t = 13.8$  Gyr (upper set of four lines) and  $t = 5.0$  Gyr (lower set of four lines). The thick black solid curve indicates the estimated minimum possible separation period at birth for a binary using 1.0 Myr Baraffe models.

Although shorter starting periods could at least partly explain the existence of ultra-short period M-dwarf systems within the AML framework, binaries with these short starting periods should then be found abundantly in young cluster environments. However, pre-main sequence binary progenitors with  $P_0 \leq 2.5$  days appear to be very rare, with 4 currently observed. HD15555 (a G5+K1 in a 1.7 day orbit), MML53 (a G2+K2 in a 2.1 day orbit), V4046Sgr (K5+K7; 2.42 days) and 155913-2233 (K5+K5; 2.42 days) are the only known (Melo et al. 2000, Hebb et al. 2010). Also, contact binaries of any spectral type are extremely rare in open clusters younger than  $\sim 4$  Gyr, only TXCnC (0.38 day orbit; Zhang et al. 2009) is linked to the intermediate-age open cluster Presepe ( $\sim 600$  Myr). Cargile et al. (2008) report the discovery of a 4.7 day eclipsing pre-main sequence M-dwarf with masses 0.39 and  $0.40 M_{\odot}$ , which suggests that shorter-period pre-main sequence M-dwarfs are not subject to observational bias.

The minimum possible orbital separation of a close binary during the fragmentation of a protostellar cloud is an important constraint on the assumed  $P_0$  as it prevents explaining ultra-short period binaries as simply forming very close together. This is because T-Tauri stars of subsolar mass have radii of  $\sim 2-3 R_{\odot}$  (Baraffe et al. 1998). A pile-up of detached binaries with periods of 2-3 days is also expected because the Kozai mechanism in a triple system can

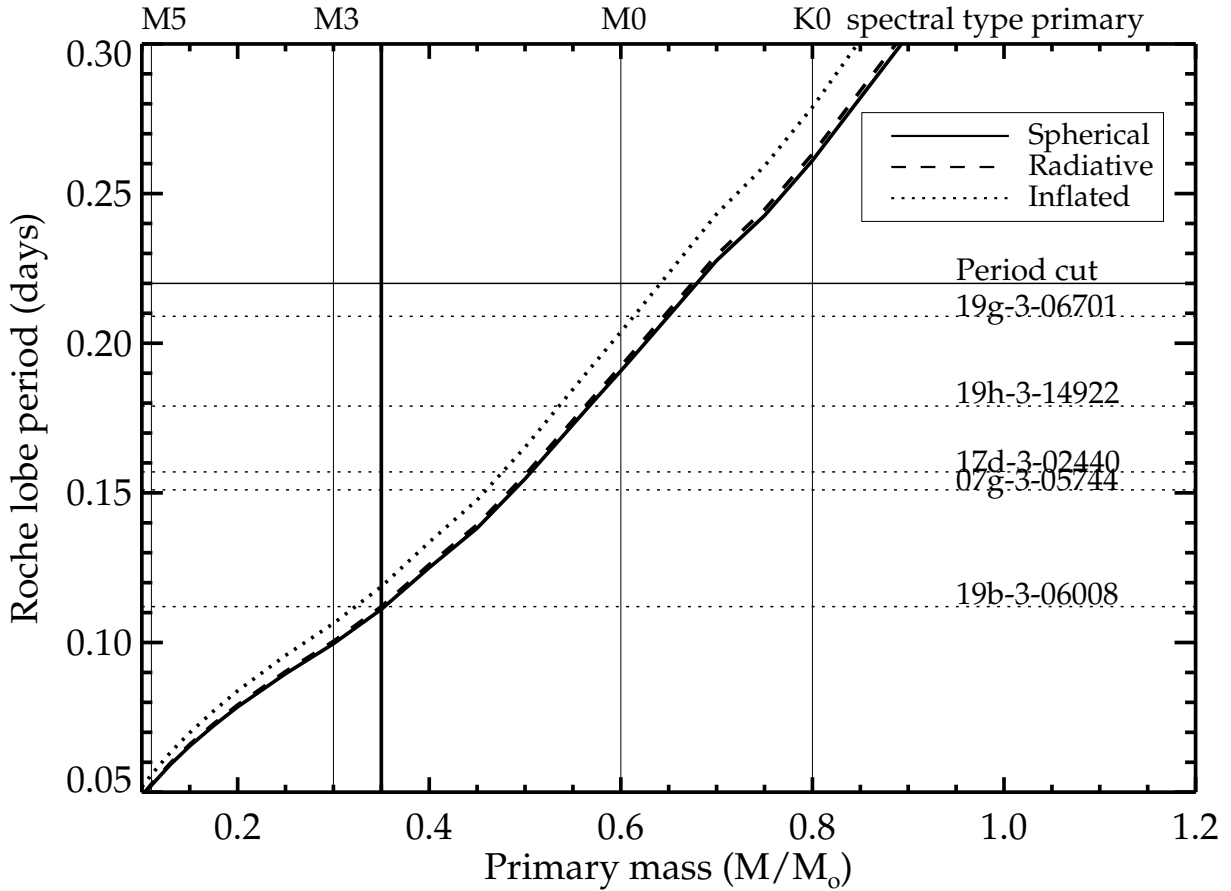


**Figure 4.3** — The estimated binary orbital period (Roche lobe period) for low-mass  $q=1$  contact binary systems, plotted as function of primary mass for three different models, all assuming the Baraffe et al. (1998) 1Gyr mass-radius relation: i) a spherical model without distorted radius (solid line); ii) a fully radiative  $n=3$  polytrope model (dashed line; no distortion) and iii) a fully convective stellar atmosphere with distortion due to tidal effects and rotation (Knigge et al. 2011; dotted line). The thick vertical line indicates the full convection limit ( $\sim 0.35 M_{\odot}$ ), whereas we also indicate approximate K0, M0, M3 and M5 type stars. Also shown are the 0.22 day period cut (horizontal solid line) and the five shortest period ( $P \leq 0.21$  days) eclipsing binaries from the WTS red binary sample (presented in Section 4.6).

effectively produce such binaries within 50 Myrs (e.g. Fabrycky and Tremaine 2007), but is less efficient for shorter periods. We approximately estimate the shortest possible  $P_0$  assuming pre-main sequence stellar radii using Baraffe (1998) 1.0 Myr models (the thick black solid curve in Figure 4.2). Note that for the lowest mass M-dwarfs no  $P_0$  can yield very short-period binaries. This makes it difficult to justify any starting period of  $P_0 < 1.5$  days.

#### 4.2.2 Periods at contact

We estimated the typical orbital periods we would expect for M-dwarf contact binary systems in order to focus our search for these systems. To do this, we determined their critical Roche lobe size  $r_{1,2}$  (e.g. Eggleton 1983). For example, for an equal-mass binary this is approximately given by  $r_1 = r_2 \sim 0.379a$ , where  $a$  is the binary separation. Using the main-sequence mass-

radius relation for low mass stars at 1Gyr of age (Baraffe et al. 1998) and Keplers law we calculate corresponding critical Roche lobe periods  $P_{Roche}$ . For illustration this  $P_{Roche}$  is plotted as a function of primary mass in Figure 4.3 (solid curve). For a binary of two M0 stars (assuming a primary mass of  $0.6M_{\odot}$ ; Baraffe & Chabrier 1996),  $P_{Roche}$  is  $\sim 0.19$ - $0.21$  days, for a twin M5 system  $\sim 0.05$ - $0.07$  days and  $\sim 0.35$  days for a solar type binary. The Roche period is also a function of  $q$ ; for a  $0.6M_{\odot}$  system with  $q=0.8$ ,  $P_{Roche}$  is  $\sim 0.13$  days and  $\sim 0.07$  days for a  $q=0.5$  system. This indicates that binaries with lower  $q$  have even shorter  $P_{Roche}$ . The dotted curve in Figure 4.3 is computed from the expression for the radius of a tidally and rotationally deformed Roche-lobe filling star (Knigge et al. 2011, Section 5.2.2). For such a star  $P_{Roche}$  is higher because the equilibrium radius of each star is now affected by the deformation. Note that there is still considerable uncertainty in the mass, radius,  $T_{\text{eff}}$ , spectral type calibration (e.g. Baraffe & Chabrier 1996), and magnetic activity may be a contributing factor to radius inflation in a tight low mass binary system (e.g. Rozyczka et al. 2009), which in turn increases the length of  $P_{Roche}$ .

Therefore, to critically test the predictions of AML and other paradigms, it is essential to determine from observations the abundance of M-dwarf binaries that are near contact, i.e. binary stars which are expected to have ultra-short orbital periods on the order of only a few hours. Because of the intrinsic faintness of M-dwarfs and the strong line broadening induced by rapid stellar rotation it is difficult to find such binaries using data from current radial velocity surveys. We therefore present the results of a campaign utilising photometric measurements obtained by the WFCAM Transit Survey, which has both the cadence and sensitivity to detect and characterise ultra-short period binaries in the uncharted M-dwarf regime.

## 4.3 Observations and data reduction

### 4.3.1 WTS J band time-series photometry

The WFCAM Transit Survey (WTS) is an ongoing photometric monitoring campaign operating on the 3.8m United Kingdom Infrared Telescope (UKIRT) at Mauna Kea, Hawaii, since August 2007. The Survey uses the Wide-Field Camera (WFCAM), which has four  $2048 \times 2048$   $18\mu\text{m}$  HgCdTe Rockwell Hawaii-II, infrared imaging arrays which each cover  $13.65' \times 13.65'$  ( $0.4''/\text{pixel}$ ), and are separated by 94% of a chip width<sup>1</sup> (Casali et al. 2007). Observations for the WTS are obtained in the J-band ( $1.25\mu\text{m}$ ), near the peak of the spectral energy distribution (SED) of a typical M-dwarf.

The WTS is primarily designed to find planets transiting red dwarf stars and to detect low mass eclipsing binaries, by observing  $\sim 6000$  early to mid M-dwarfs with  $J \leq 16$  (in this paper we consider stars down to  $J=18$ ). The WTS observing strategy uses the queue-schedule mode of UKIRT and can operate in mediocre seeing and thin cloud cover. Four target fields, 1.5 square degree each and passing within 15 degrees of zenith, were selected to give year-round visibility. The fields were selected as regions of the sky where the ratio of dwarfs to giants was maximized, reddening relatively low ( $E(B-V)$  between 0.057 and 0.234) and overcrowding reduced by observing close to but outside the galactic plane ( $b > 5^\circ$ ). In Table 4.1 we summarise the main properties of the four survey fields (the 03hr field, 07hr field, 17hr field and 19hr

<sup>1</sup><http://casu.ast.cam.ac.uk/surveys-projects/wfcam>

Name	(RA)	(DEC)	#stars	#epochs	#cand.
03hr field	03 <sup>h</sup> 39 <sup>m</sup>	+39 <sup>d</sup> 14 <sup>m</sup>	10827(36306)	392	74
07hr field	07 <sup>h</sup> 05 <sup>m</sup>	+12 <sup>d</sup> 56 <sup>m</sup>	16623(56070)	626	140
17hr field	17 <sup>h</sup> 14 <sup>m</sup>	+03 <sup>d</sup> 44 <sup>m</sup>	9621(39879)	709	68
19hr field	19 <sup>h</sup> 35 <sup>m</sup>	+36 <sup>d</sup> 29 <sup>m</sup>	34452(130320)	1154	375

**Table 4.1** — The main properties of the four WTS survey fields. Indicated are the approximate centres of the fields (right ascension and declination), the total number of stars with  $J \leq 16$  ( $J \leq 18$  in brackets), the number of epochs as of September 7th 2011, and the number of binary candidates per field.

field). A field is observed by dithering the four detectors of WFCAM (a paw print) through 8 pointings, where each pointing is labeled with a single letter from *a* to *h* (e.g. '19a'), which are then tiled to give uniform coverage across the field. In itself, each single pointing consists of a 9-point jitter pattern with 10 second exposures at each jitter position. In this way, the near-infrared lightcurves have an average cadence (including overheads) of 15 min. Typically, WTS observations are taken only at the beginning of a night, just after twilight in  $>1''$  seeing.

Data reduction of the raw 2D J-band images is performed using the Cambridge Astronomical Survey Unit (CASU) pipeline, which is based on the INT wide-field survey pipeline (Irwin & Lewis 2001). Astrometric and photometric calibration is obtained using 2MASS. Source detection is done on stacks of the 20 best exposures (the 'master frame') and aperture photometry is performed as described in Irwin et al. (2007). The brightest stars (saturation occurs around  $J=12-12.5$ ) have a precision of  $\sim 3$  mmag per data point, whereas 1% photometry is still achieved for  $J=16$  ( $\sim 7\%$  for  $J=18$ ).

The short-period eclipsing binary candidates described in this paper were obtained from WTS lightcurves reduced on 7 September 2011 of all four survey fields. The 19hr field had the most extensive coverage ( $\sim 1100$  data points). For each field, we also obtained single deep exposures in WFCAM *ZYJHK*. These will be used together with *griz* photometry from the Sloan Digitized Sky Survey (SDSS) where available to create SEDs and estimate the effective temperature of the candidates.

### 4.3.2 INT broad-band photometry

The 17hr field in the WTS is not covered by SDSS, therefore we obtained optical photometry of this field to use in our SED fitting and effective temperature estimates. We used the Wide Field Camera (WFC) on the 2.5m Isaac Newton Telescope (INT) in La Palma on the nights of 8,10 July 2009 and 26 July 2010 to obtain *g*, *r* and *i* photometry of this field. The smaller field-of-view of WFC compared to WFCAM required 14 pointings to cover the entire field. We used the following exposure times for each pointing: *g*  $2 \times 250$  seconds, *r* 500 seconds, and *i* 100 seconds, in order to match the typical depth achieved by SDSS. The data were reduced using custom-made IDL procedures to bias-subtract, flat-field (and de-fringe in the case of the *i*-band, where the fringe-frame was created from a number of deep exposures of the moonless sky). We used the IDL procedures *find.pro* to identify the sources and *aper.pro* to extract the photometry, calibrating to SDSS magnitudes using INT observations of the 19hr field in the same filters.

### 4.3.3 Low resolution spectroscopy

As an independent check on the effective temperatures derived for our binary candidates in Section 4.2, from broad-band colour fitting of their SEDs, we obtained low resolution spectral observations of three of our targets. Optical spectra of 19h-3-14922 ( $P=0.1798$  days,  $(r-i)=1.65$ ) and 19g-3-06701 ( $P=0.2090$  days,  $(r-i)=1.01$ ), were taken with the 4.2m WHT on the night of August 17 2010. We used the red arm and the R158 grism of the ISIS dual beam spectrograph, giving a dispersion of  $\sim 1.8\text{\AA}/\text{pixel}$  using a slit width of  $1.0''$  matching the seeing. In addition, a spectrum of 07e-2-03887 ( $P=0.2734$  days,  $(r-i)=1.0$ ) was obtained with ACAM ( $\sim 3.3\text{\AA}/\text{pixel}$ ) on the night of 08 September 2011. The spectra were reduced using a combination of IRAF (the *apall* package) and custom IDL routines. In IDL, the spectra were trimmed to encompass the length of the slit, bias-subtracted, flat field corrected and median-filtered to remove cosmic rays. Background subtraction and optimal extraction of the 1D spectra was performed in IRAF. We used frames taken with the CuNe+CuAr standard lamp to determine the wavelength solution. For flux-calibration, we obtained reference spectra of standard stars.

## 4.4 Sample selection

### 4.4.1 Variability statistic

The WTS 3.0 release consists of  $\sim 262,000$  stellar lightcurves with  $J \leq 18$ . First, we select only those lightcurves that have less than 20% bad datapoints and clip the bad data before further processing. We define as bad data a J-band measurement that either has infinite value (saturation, near-edge detections) or a photometric error larger than 1.0 magnitudes. We subsequently use the Stetson  $J_S$ -statistic (Stetson 1996) as a quantitative estimator for photometric variability, analogous to Pepper & Burke (2006). The Stetson statistic weights photometric observations that are correlated in time using subsets of data that are separated by less than 0.03 days. For a nonvariable star showing only random (Gaussian) noise, this statistic will be around 0, whereas it will be positive for stars with correlated (physical) variability. As an example in Figure 4.4 we show the  $J_S$  variability index for one WFCAM detector in WTS paw 19h. To select candidate variable stars, we apply a conservative cut of  $J_{S,cut} > 0.2$ . We determine this cut by examining the length of our candidate lists for random WTS paws for values of  $J_{S,cut}$  from 0 to 0.5. We subsequently checked each candidate lightcurve and obtain a cutout thumbnail image from the stacked WFCAM J band master frame to eliminate the most obvious false-positives through visual inspection. These false-positives are caused by blending effects from nearby stars, extended wings and bleed trails from bright stars or detector defects. This step eliminates 80-90% of the candidates and typically 20 to 40 objects per individual detector pass the inspection stage. In total, we find 656 variables with  $J \leq 18$  in this way. 375 candidates are from the 19hr field (which contributes 49.6% of the total number of lightcurves with  $J \leq 18$ ), 68 from the 17hr field (15.2%), 140 from the 07hr field (21.4%) and finally 74 candidates are from the 03hr field (13.8%). In Figure 4.5 we show a plot of the candidate fraction as a function of J band magnitude. At  $J=16$ , roughly 0.5% of the high quality lightcurves is classified as a candidate, but for fainter magnitudes this fraction quickly decreases, reflecting the poorer photometry. For this reason, we have not investigated any lightcurves with  $J \geq 18$ .

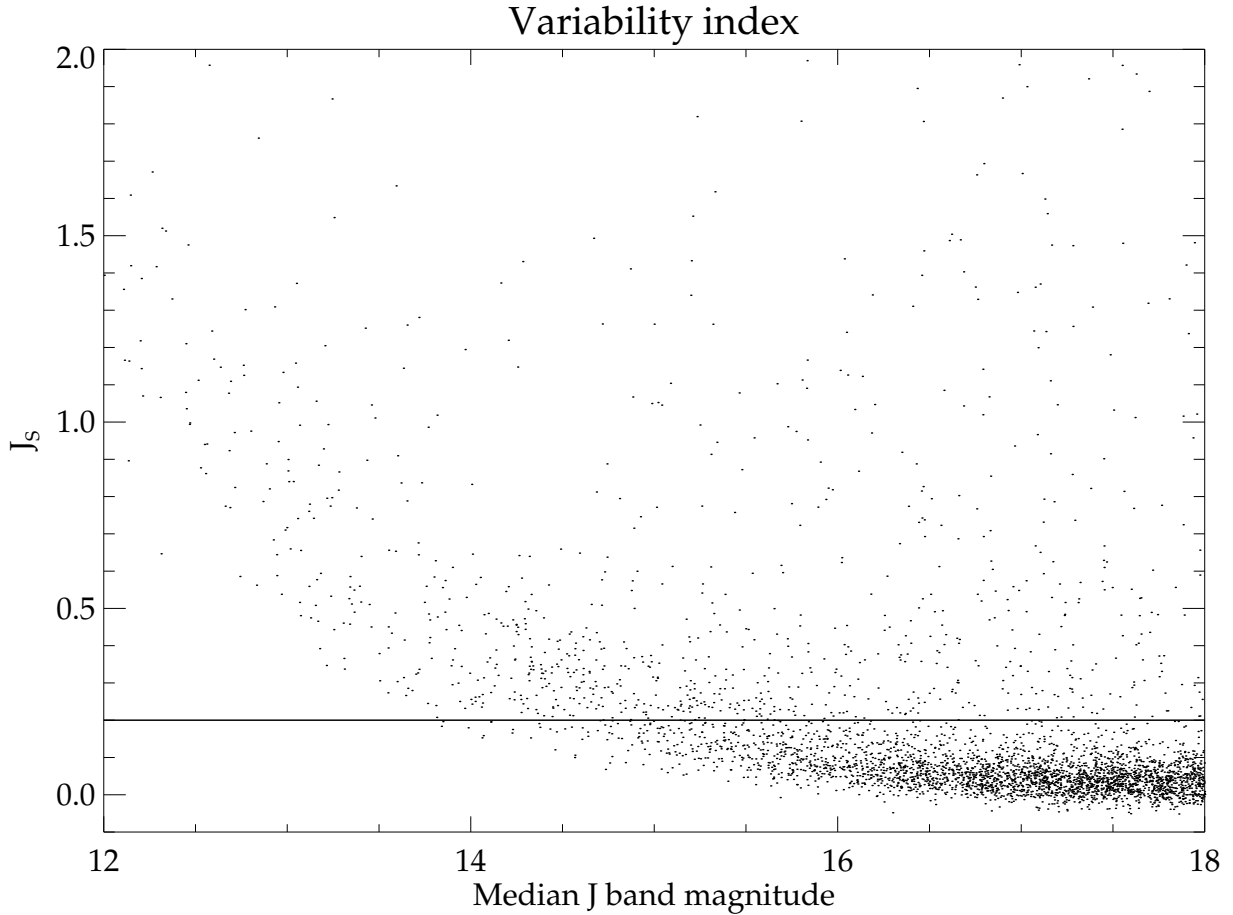


**Figure 4.4** — The Stetson  $J_s$  variability statistic for one detector of the 19h WTS paw, plotted as a function of WFCAM J band magnitude. We use a cut  $J_s > 0.2$  to select candidate eclipsing binaries. At the brightest magnitudes, outliers are dominated by systematic effects. These are removed through visual inspection.

#### 4.4.2 Orbital period determination

To determine periods for all binary candidates we adopt a simple box-fitting algorithm (Kovacs et al. 2002), such as used by Collier-Cameron et al. (2006). We limit our search to  $P \geq 0.1$  days because our frequency spectra are very noisy at the shortest periods, which we suspect is due to strong aliasing caused by the peculiar form of the WTS window function. Note that shorter period systems could still be detected as an alias of the real period. We phase-fold the lightcurves over 20,000 periods between 0.1 and 1.0 days and for every period we vary the primary eclipse epoch  $T_0$  and box width, and calculated the error-weighted signal compared to white noise (S/N). We then refined our analysis by selecting the period and epoch with the highest significance and re-iterate the box-fitting procedure with a smaller range of parameters, centered around the frequency peak. In this way, we generally achieve uncertainties in period of better than  $\sim 10^{-5}$  days and better than  $\sim 10^{-4}$  days on  $T_0$ . In this procedure we exclude periods within 10 minutes of 0.33, 0.5 and 1.0 days. In the case the algorithm confuses the secondary with the primary eclipse, this is picked up through visual inspection. In these cases the lightcurves are folded on several period aliases. As a crosscheck on the performance of

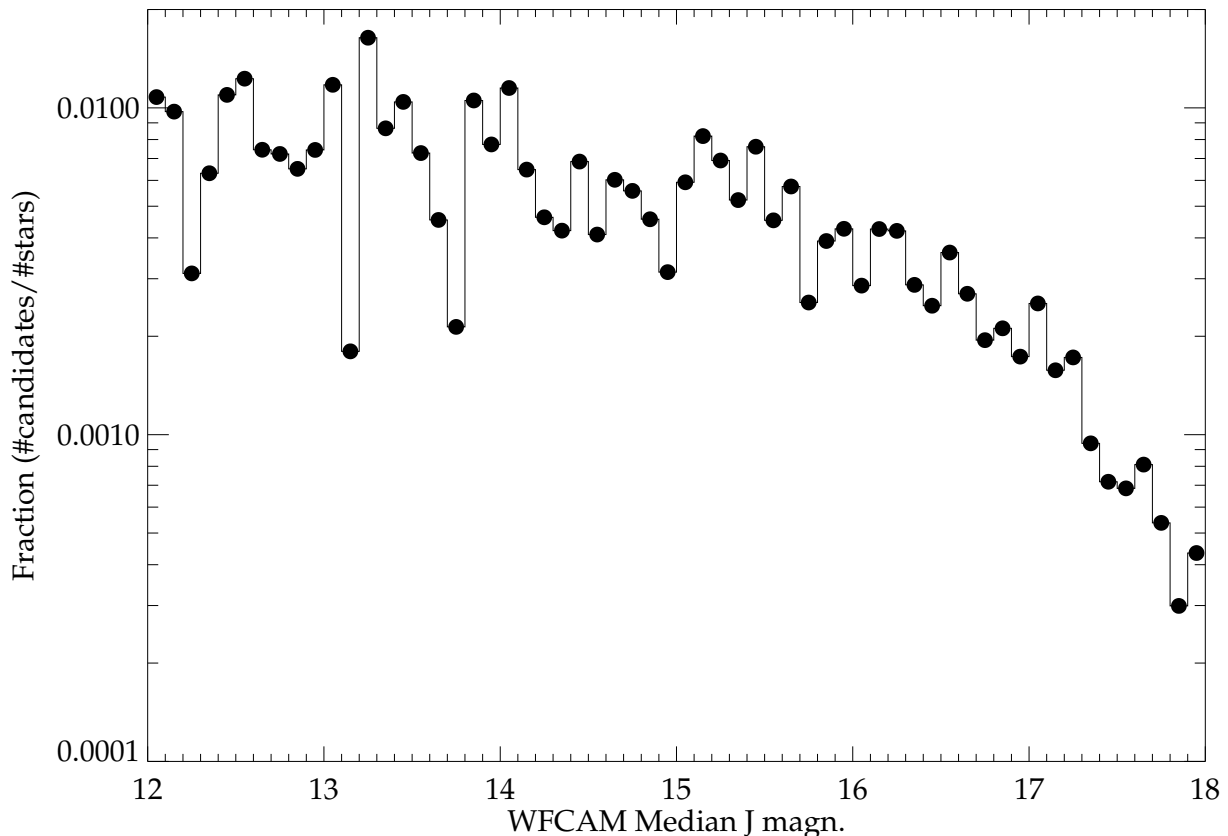


**Figure 4.5** — The ratio of binary star candidates over the number of available good quality WFCAM lightcurves as a function of WFCAM J magnitude. Each black dot indicates this fraction determined in 0.1 magnitude bins. The plot is truncated at  $J=12$  because of saturation effects for brighter stars.

the box-fitting algorithm, we also compute the Lomb-Scargle power spectrum (Scargle 1982) between 1 hr and 2 days (with a period sampling of 0.0001 days) for each candidate. Since the Lomb-Scargle method uses Fourier analysis, it is mostly sensitive to W Uma variables, pulsators and rotators, and less sensitive to the narrow eclipses that are expected for (semi-)detached systems. In the end we adopt the method that provides the lowest rms in the phase-folded lightcurve.

### 4.4.3 Selection of the final sample

We applied a first-pass colour cut using SDSS photometry (Kowalski et al. 2009) to select late K and M-dwarf short-period eclipsing binaries, which is verified using the fitting of the broadband SEDs in Section 4.2. SDSS photometry is available for three WTS survey fields, the 03hr field, 07hr field and 19hr field. For the 17hr field, which does not have SDSS coverage, we use *gri* photometry obtained on the INT. We made cuts at  $(r-i) \geq 0.50$  and  $(i-z) \geq 0.25$  and selected orbital periods with  $P \leq 0.3$  days. This defines our ‘red’ sample, the principal focus of this paper. In addition we use the well-calibrated SDSS colour selection criteria from Sesar et al. (2007) to exclude RR Lyrae. As there may be overlap in estimated effective temperature between late K-type stars and early M stars we also kept binaries which have  $P \leq 0.23$  days ( $\sim 20,000$  seconds,

analogous to the sample of Norton et al. (2011) that are bluer than our cut, but are excluded as pulsators using the Sesar et al. (2007) colour criteria. This is our ‘blue’ sample. We have removed objects from our red and blue samples that have sinusoidal phase-folded light curves with a large scatter in their amplitude, which would indicate variability caused by star spots (the amplitude depends on the spot-size which is expected to vary on timescales shorter than the 4 year observing span of the WTS). Note that this could remove a small fraction of genuine grazing equal-mass contact systems at our faintest magnitudes where our photometry is less precise.

In Figure 4.6 we show our red and blue samples in a (r-i) versus (i-z) SDSS colour-colour diagram. The light grey lines indicate the median M dwarf stellar types, as presented in Kowalski et al. (2009). The colours of these spectral types generally have a  $1\sigma$  uncertainty of 0.05-0.15. Dark grey filled dots and light grey stars indicate objects from our red sample, whereas dark grey filled squares represent the blue sample. The lightcurves and the optical colours of all of our candidates do not show features which would suggest they are M-dwarf white dwarf systems (Covey et al. 2005).

### Reddening estimates

We have investigated the reddening effect for the 19hr field using a model for interstellar extinction presented by Amores & Lepine (2005). At  $J < 17$ , assuming no reddening, the WTS is distance-limited to  $\sim 1800$  pc for the earliest M-dwarfs. At 1.8 kpc, the reddening model gives an extinction of  $A_V = 0.37$  mag ( $E(B-V) = 0.12$  mag) in the direction of the 19hr field, and using relations presented in Table 6 of Schlegel et al. (1998), we converted between filters to find  $A_g = 0.43$  mag,  $A_K = 0.042$  mag,  $E(r-i) = 0.076$ ,  $E(i-z) = 0.069$  and  $E(J-H) = 0.037$ . The reddening effect along the line-of-sight to the field thus appears to be small, and similar results are obtained for the other three WTS fields. This makes it unlikely that any of our short-period red binary candidates are highly reddened pulsators. Also note that the pulsation periods of giant stars are inversely proportional to the square root of the mean stellar density, meaning that the low densities of giant stars result in significantly longer pulsation periods than we detect in our candidates. Rodriguez-Lopez et al. (2012) suggested that M-dwarfs may be pulsating, however it is not clear if such M-dwarf pulsations are stable and whether they could be detected in M-dwarfs with Gyr ages. They have not been confirmed observationally to date. Note that any pulsation would also have to be stable on the order of four years (the span of the WTS observing campaign).

## 4.5 Characterisation of the eclipsing binary systems

### 4.5.1 Binary classification

For a crude initial classification of a binary in the three categories *detached*, *semi-detached* or *(over)contact*, we follow Rucinski (1993) and decompose the phased lightcurve  $m(\Phi)$  into Fourier components with coefficients  $a_i$  and  $b_i$ :

$$m(\Phi) = m_0 + \sum_{i=1}^{10} [a_i \cos(2\pi i \Phi) + b_i \sin(2\pi i \Phi)], \quad (4.3)$$

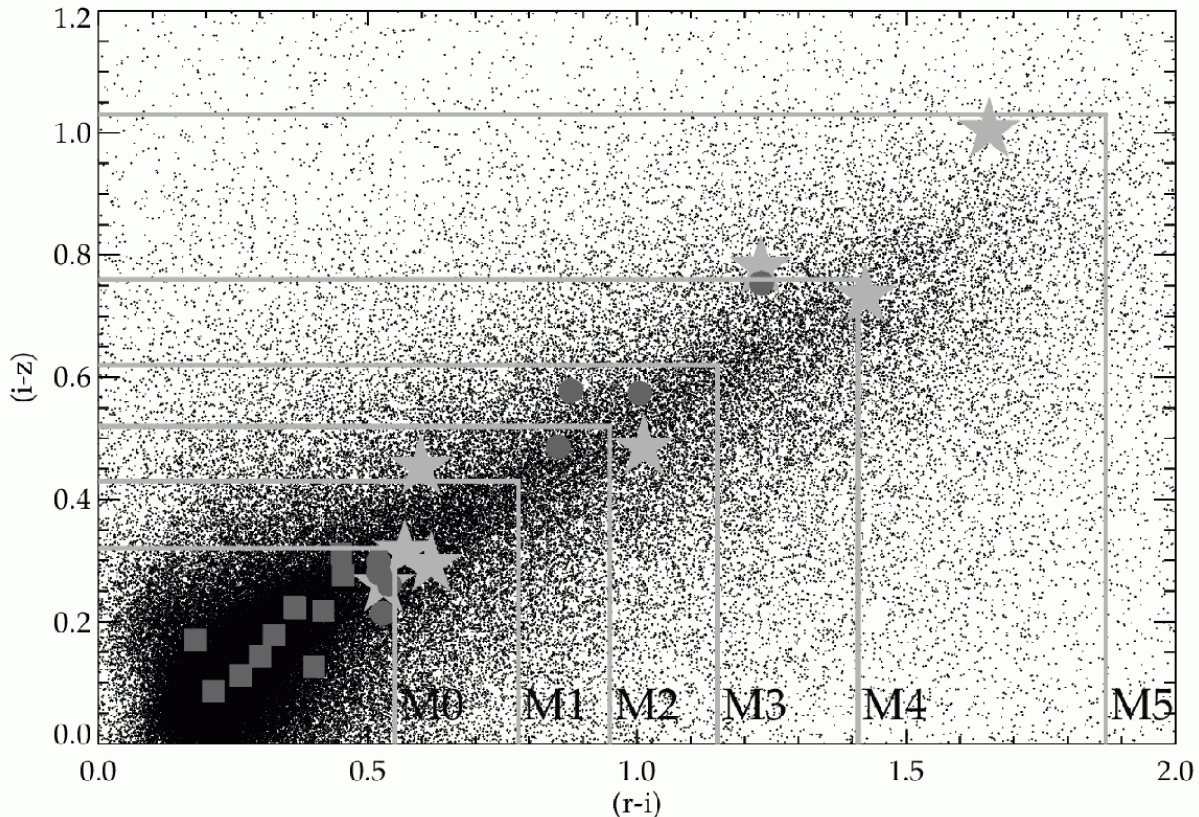


**Figure 4.6** — SDSS colour-colour diagram for objects in the 19hr field, showing  $(r-i)$  versus  $(i-z)$ . The light grey solid lines indicate the median average M-dwarf spectral types from Kowalski et al. (2009). Note that these averages generally have  $1\sigma$  uncertainty of 0.05 to 0.15 in  $(r-i)$  and  $(i-z)$ . Black dots are objects in the WTS 19hr field (for plotting purposes we only show one field), which have SDSS DR7 photometry. Dark grey squares indicate our 'blue' short period EB sample ( $P \leq 0.23$  days), dark grey filled dots indicate our red sample, where the light grey stars in the figure are red sample binaries (with  $P \leq 0.23$  days).

where  $m_0$  is the mean lightcurve magnitude. The number of Fourier components is limited to 10, because for higher  $i$  the quality of the fit does not improve for the typical uncertainties reached. For the fitting of the Fourier coefficients we use the IDL routines *fourfit* and *fourfunc* from Marc Buie's IDL archive<sup>2</sup>. Based on a grid of coefficients derived from fits to model eclipsing binary lightcurves the  $a_2$  and  $a_4$  coefficients allow a distinction to be made between the three categories by plotting the sources in the  $(a_2, a_4)$  plane (Figure 4.7). The coefficient  $a_2$  is related to the depth of the eclipses, which depends on the inclination of the orbit and the mass ratio. For example, we find  $a_2 \sim 0.036$  for 19b-3-06008, a relatively shallow semi-detached binary, whereas deep eclipse systems such as 07c-4-05645, 19e-4-00861 and 19c-2-08140 have  $a_2 \sim 0.13 - 0.16$ . The coefficients  $a_1$  and  $a_3$  are related to the ratio of primary versus secondary eclipse depths and  $b_1$  to the difference in the lightcurve maxima at phase 0.25 and 0.75 (star spots or mass transfer can bias this value). Pulsating variables can be distinguished from genuine eclipsing systems, in addition to the colour cuts previously described, by using the  $b_2$  and  $b_4$  coefficients (e.g.

<sup>2</sup>Available at <http://www.boulder.swri.edu/~buie/idl/>



Pojmanski 2002). Our candidates have  $b_2$  and  $b_4$  consistent with non-pulsating stars.

## 4.5.2 The effective temperature

We estimate the effective temperature  $T_{\text{eff}}$  of the sources in our sample using an 8-band weighted SED fit to combined SDSS griz and WFCAM YJHK photometry. We  $\chi^2$  fit the observed SED to a grid regularly spaced by 50 K in  $T_{\text{eff}}$  with theoretical broad-band colours based on Baraffe et al. (1998) 1Gyr,  $\log(g)=5.0$ , solar metallicity models. In this process, we re-iterate the fitting procedure after removing the band that gives the largest outlier from the initial  $\chi^2$  fit. For three sources we obtain an independent check on our results using low resolution spectra from the WHT (Section 4.2). For the spectroscopy data we  $\chi^2$  fit NexTGen model spectra (Allard et al. 1997) with steps in effective temperature  $\Delta T_{\text{eff}}=100\text{K}$ , solar metallicity and surface gravity  $\log(g)=5.0$  to our observed spectra resulting in uncertainties in spectral type of about one subclass (corresponding to  $\sim 100\text{-}150\text{K}$ ). We mask out the strong telluric ozone bandhead around 7600 Å and the  $H_\alpha$  emission line at 6563 Å.

In Figure 4.8 we show our three low resolution spectra (solid black lines) with overplotted best-fit model spectra (grey lines). In this figure we indicate approximate spectral types for the binary components by crude estimates based on the simplified assumption that the stars radiate as blackbodies. We use the relative depths of the primary and secondary eclipses to obtain the ratio of surface brightness and together with the ratio of radii, which we estimate from the square of the primary and secondary eclipse depths, we solve for the individual temperatures  $T_{1,2}$ , analogous to Coughlin et al. (2011). For the conversion to spectral type we use the tabulated model spectral types as a function of  $T_{\text{eff}}$  from Baraffe & Chabrier (1996). Note that the models consistently underpredict the flux around 6900 Å, which may be related to missing opacities of TiO (Titanium-Oxide) in the code we use. We find that the  $T_{\text{eff}}$  derived from the SED fitting is generally lower than the corresponding temperature from the spectral template matching, typically by one to two subclasses, corresponding to 100-300 K, which we attribute to missing opacities in the optical. However, given that we estimate typical errors of 200-300K on the SED result, the two methods are still in agreement. In Table 2 we show  $T_{\text{eff}}$  for each binary candidate.

All three binaries show significant  $H_\alpha$  emission, which indicates chromospheric activity (the absence of the Lithium absorption line appears to rule out accretion from young stars). Using the IDL routine *feature* we estimate the equivalent width (EW) of the  $H_\alpha$ . The calculated EW values ( -7.9 Å for 19h-3-14922, -3.8 Å for 07e-2-03887 and -5.7 Å for 19g-3-06701) are consistent with or slightly higher than those corresponding to active single stars with similar spectral types (Riaz et al. 2006). The three systems have equivalent widths between 30-70% of the empirical accretor/non-accretor division for their estimated spectral types (Barrado y Navascues & Martin 2003). The presence of the Na (Sodium) absorption doublet around 8200 Å and the absence of a strong Ca (Calcium) triplet in the near-IR indicate that the three candidates are high gravity objects, i.e. M-dwarfs and not giants.

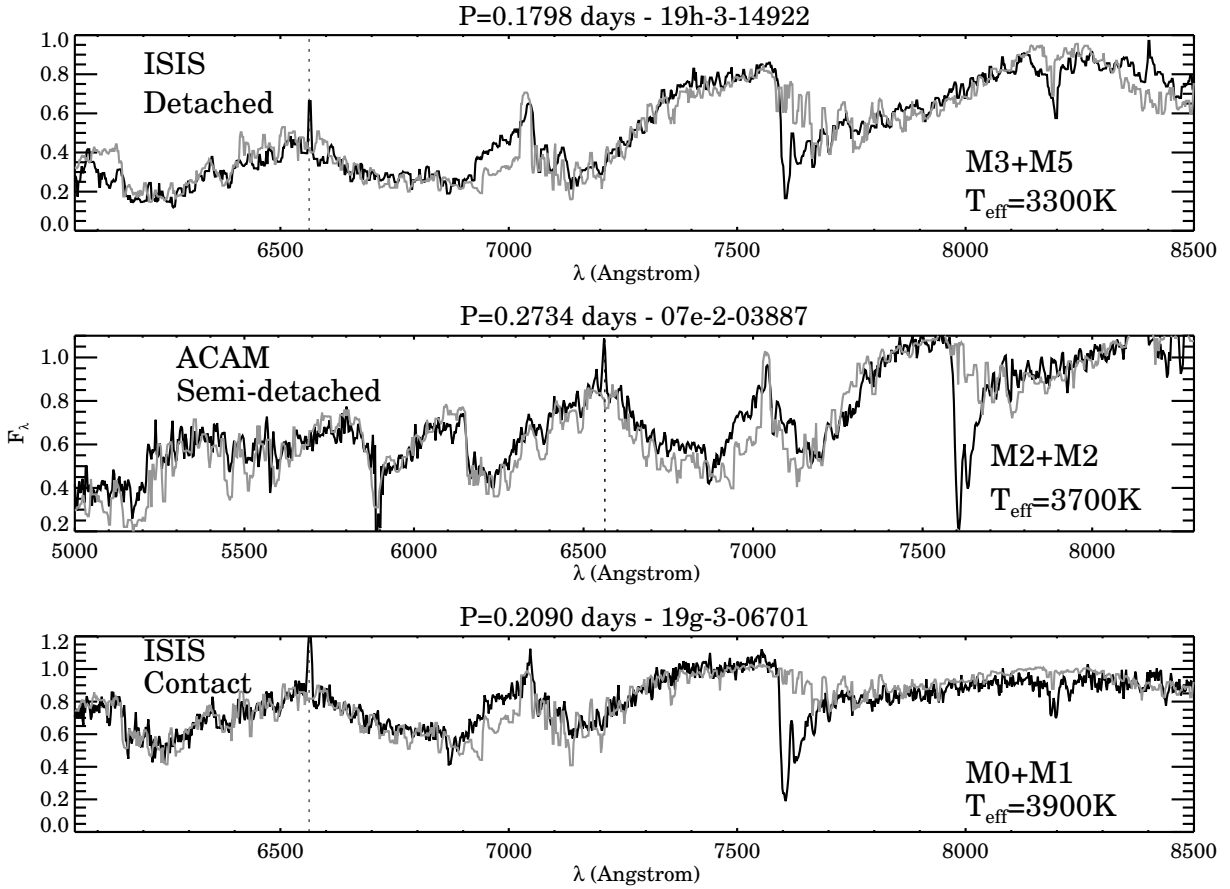


**Figure 4.8** — Two low resolution WHT ISIS red arm spectra and one ACAM spectrum of our short period binaries. The spectra are flux calibrated and normalised. **Top panel:** 19h-3-14922, a detached system of  $\sim$ M3 and M5 stars. **Middle panel:** 07e-2-03887, a (semi-)detached system of M2 stars. **Lower panel:** 19g-3-06701 a contact system of  $\sim$ M0 and M1 stars. The grey curves are best-fit NextGen model spectra for solar metallicity,  $\log(g)=5.0$  and age 1.0 Gyrs. The dotted vertical line indicates the position of the  $H_\alpha$  line at  $6563 \text{ \AA}$ , which is related to emission from the stellar chromospheres induced by spun up rotation in the binary.

## 4.6 Results & Discussion

The final sample consists of 25 eclipsing binary systems with orbital periods shorter than 0.23 days (20,000 seconds), of which 9 have optical to near-infrared colours or optical spectra consistent with M-dwarfs. Four of these 9 have periods shorter than any known main-sequence binary. In Figure 4.9 we show the WFCAM J band lightcurves of these four binaries phase-folded to the best-fit epoch and period determined from the box-fitting algorithm. Five binaries from the red sample with periods shorter than 0.23 days have Fourier coefficients ( $a_2, a_4$ ) typical of a contact system ('C'), two binaries are identified as semi-detached systems ('SD'), whereas two other systems are detached ('D'). From the blue sample, 9 out of 14 binaries ( $\sim 64\%$ ) are identified as contact systems. We have summarised the binary characteristics for both the red sample and the blue sample in Table 5.4, including the Fourier classification. For all of the 25 binaries, lightcurves are shown and coordinates are given (in Table 3) in the Appendix.

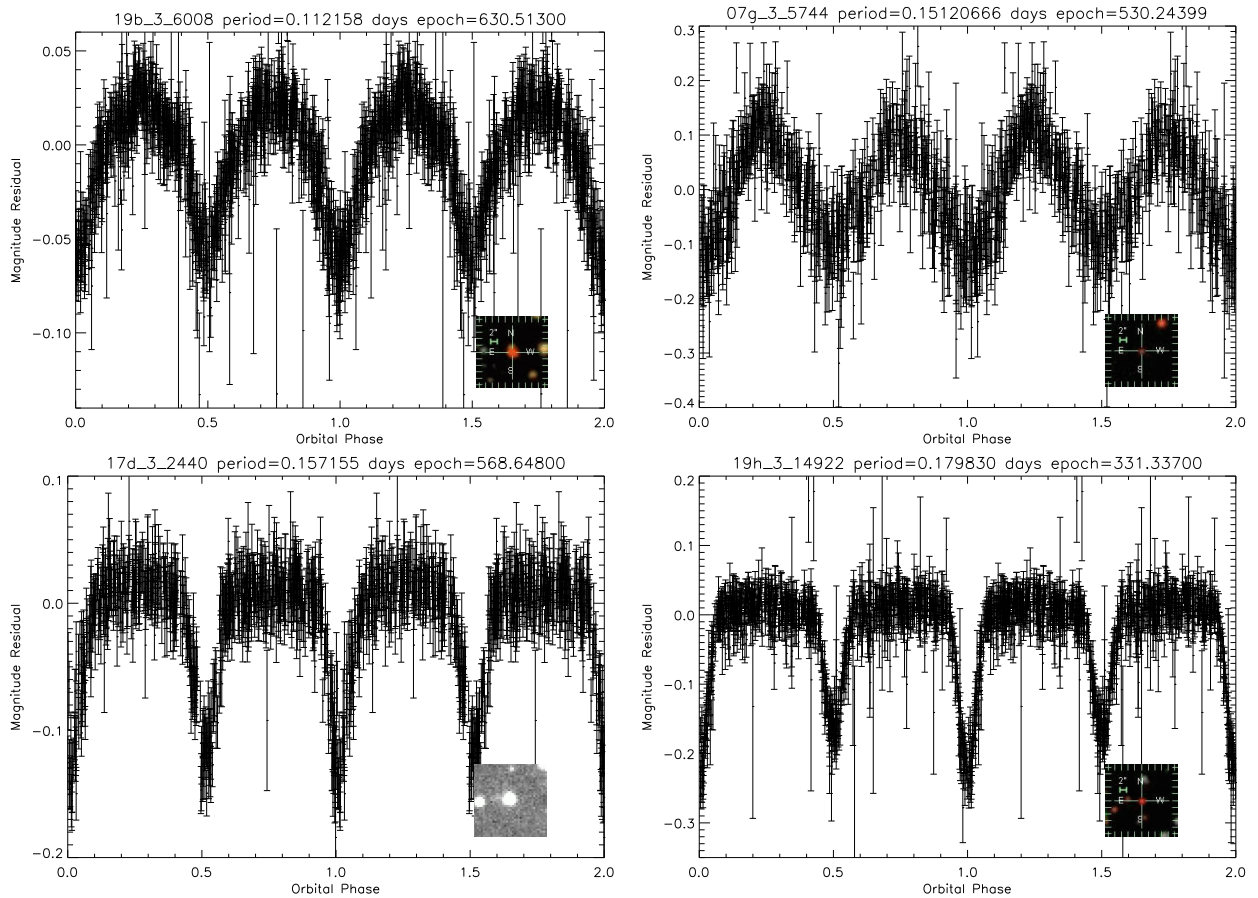


**Figure 4.9** — The (median subtracted) WFCAM J band lightcurves of the four candidate ultra-short period eclipsing M-dwarfs binaries, phase-folded to the best-fit primary eclipse epoch and orbital period. The boxes in the lower right corner of each plot show a three colour SDSS composite image of each source. For 17d-3-02440, which does not have SDSS coverage, we show the WFCAM J band image. A colour version of the thumbnails is available in the online paper.

The shortest period system, 19b-3-06008, is a binary consisting of two  $\sim M4$  stars ( $T_{\text{eff}} \sim 3150$  K) with  $P \sim 0.1121$  days. This binary appears to be close to contact. Assuming orbital synchronisation, the estimated masses and radii for this binary correspond to a fast rotational velocity between 15-25% of the breakup speed (Herbst et al. 2001), but slow enough to keep the system stable. A second system, 07g-3-05744, has a period of  $\sim 0.151$  days, shows slightly unequal eclipses and a  $T_{\text{eff}}$  of 3400 K, suggesting this is a binary with spectral types of  $\sim M2-3$ . This system is identified as a contact system by the Fourier decomposition. Two other systems, 17d-3-02440 ( $\sim M1.5$ ) and 19h-3-14922 (WHT ISIS spectrum indicating  $\sim M3$  and  $M5$  stars) with periods  $\sim 0.1572$  and  $\sim 0.1798$  days, are detached binaries with unequal ratio of primary versus secondary eclipse depth. Figure 4.3 illustrates why these binaries are classified as detached systems despite their ultra-short periods, whereas 07d-2-02291 (a blue sample K type binary with  $P \sim 0.2013$  days) is a contact system; the critical Roche lobe period for contact depends on primary mass. Nevertheless, significant out-of-eclipse variability in the lightcurves of the four ultra-short period binaries indicates there is significant tidal interaction between the primary

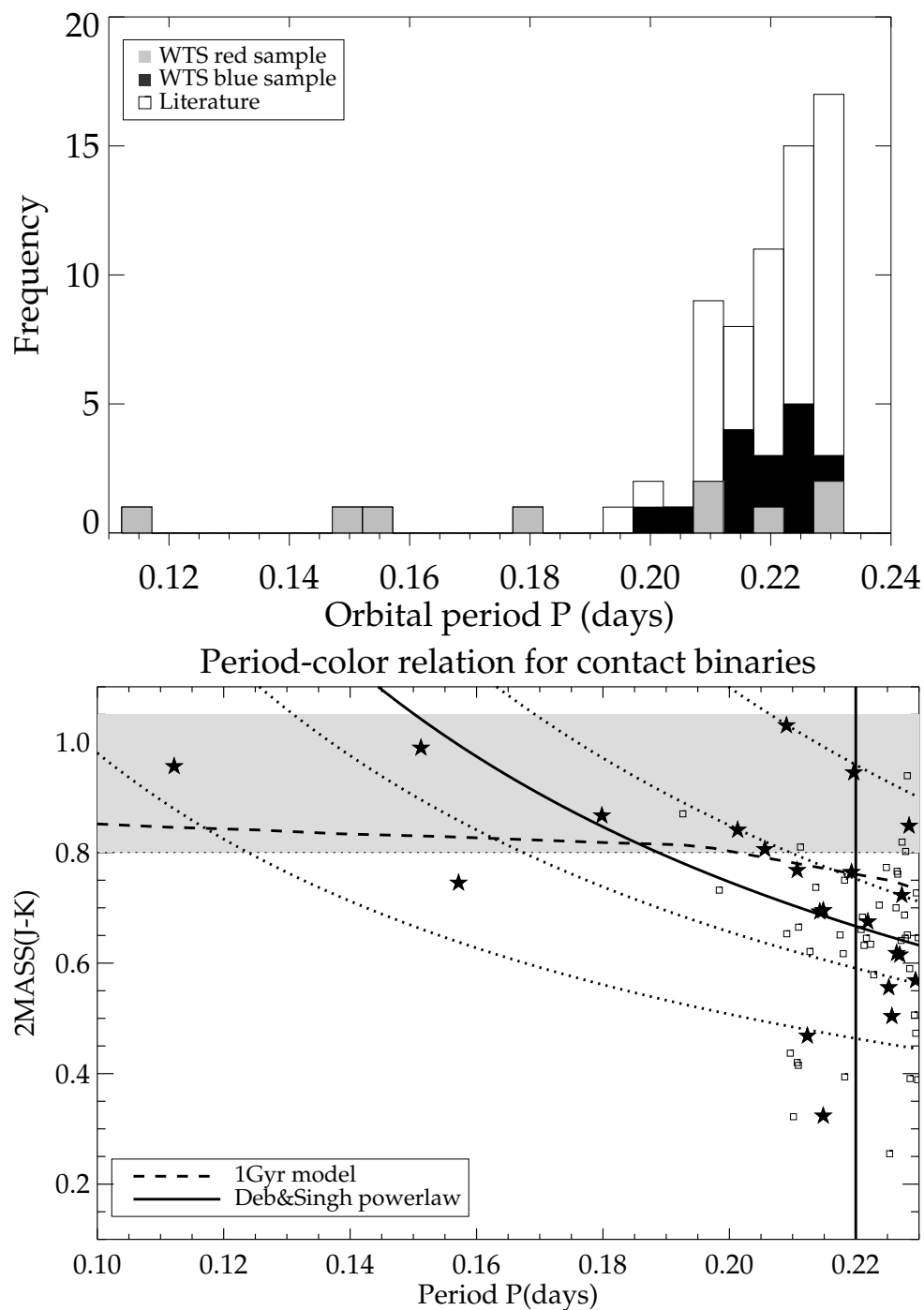


**Figure 4.10** — **Upper panel:** Period histogram of the WTS short period binaries (grey and black filled bars), combined with sources from the literature (white bars). **Lower panel:** The black stars indicate our WTS eclipsing binary sample with  $P \leq 0.23$  days, whereas open boxes are sources from the literature. The period-colour (J-K) power-law relationship for contact binaries from Deb & Singh (2010) is indicated by the solid black curve. The dotted curves show the 1 and  $3\sigma$  boundaries on the power-law index of the correlation. The dashed curve shows the theoretically predicted colours for periods at Roche lobe overflow using Baraffe 1Gyr single star models. The grey band indicates the range of (J-K) colours for a sample of nearby active M-dwarfs classified as M4 (Riaz et al. 2006).

and secondary in every system.

### 4.6.1 Comparison with previous studies

This study probes for the first time the low-mass regime of ultra-short period eclipsing binaries in an extensive way. Recently, Norton et al. (2011) presented 43 eclipsing binary candidates identified in the SuperWASP Survey with periods shorter than 0.23 days, but only three objects in their sample have  $(J-K) \geq 0.8$  ( $\sim M0$  spectral type). Their shortest period system is GSC2314-0530 ( $P \sim 0.1926$  days), which was modelled by Dimitrov & Kjurkchieva (2010) as a semi-detached M-dwarf binary with components of  $0.51M_{\odot}$  and  $0.26M_{\odot}$  (corresponding to spectral types of  $\sim M0$  and  $M4$ ). Two other binaries in their sample have  $P \leq 0.21$  days (0.20908 and 0.20964 days). Maceroni & Montalban (2004) found an almost twin  $M3$  system (OGLE BW3 V38; semi-detached,  $P=0.1984$  days) with strong chromospheric emission and masses of 0.44 and  $0.41M_{\odot}$ . Other surveys found only binaries with  $P > 0.21$  days. Miller et al. (2010) found seven candidate contact binaries with periods between 0.2109 and 0.23 days in a 0.25 square degree Galactic plane survey with the ESO 2.2m telescope, and Wel Drake et al. (2004) found a  $P=0.2155$  day system in the globular cluster 47 Tuc, whereas Pribulla et al. (2009) report a  $P=0.211249$  day system. The left panel of Figure 4.10 shows a histogram of all literature binaries plus our new systems with  $P \leq 0.23$  days (where grey and black filled bars indicate those from the WTS). The WTS sample follows the literature distribution, but suggests that rather than a sharp cut-off at 0.22 days, the population extends into a tail of significantly shorter periods for lower-mass systems.

### 4.6.2 The period-colour relation

Our observations suggest a correlation between spectral type and the shortest possible binary period. This is in line with the period-colour relation as found by Eggen (1967) for contact binaries, implying that bluer systems have longer orbital periods. This is because for main-sequence stars the effective temperature (colour) is linked with stellar radius, and as a consequence orbital period for a contact binary. The period-colour relation can be used to identify genuine contact systems and weed out pulsating stars with comparable periods (i.e.  $\delta$  Sct and  $\gamma$  Dor) and has been used for distance estimates (e.g. Rucinski 2007).

Recently the same relation was presented for infrared colours by Deb & Singh (2010) using 2MASS (J-K) photometry, which is relatively free from extinction effects. We have collected (J-K) colours from the literature of  $P \leq 0.23$  days binary systems and combined them with our WTS results in a period-near-infrared colour diagram in Figure 4.10 (right panel). In this figure the stars indicate WTS objects, whereas the open boxes are literature sources. We have converted the WFCAM infrared photometry to 2MASS colours using the equations in Hodgkin et al. (2009). We extrapolated the best-fit powerlaw period-colour relation of Deb & Singh (black solid line) to the ultrashort periods of our WTS binaries. The dotted curves show the 1 and  $3\sigma$  boundaries of this power-law index. There is significant scatter in the period versus colour sample, yet,  $\sim 65\%$  of all systems with  $P \leq 0.23$  days fall within the  $1\sigma$  limits of the correlation, indicating that the majority of our systems are consistent with (near-)contact binaries rather than pulsators. However, we believe this scatter is intrinsic (the 2MASS J and K bands are obtained at the same epoch) and could be due to varying degrees of contact or age differences within

Red sample ( $P \leq 0.23$ days) 9 objects															
Name	period	epoch	$\frac{d_2}{d_1}$	u	g	r	i	z	J	H	K	(r-i)	(i-z)	State	$T_{eff}$
19b-3-06008	0.11215791	630.51306	0.83	24.43	20.74	19.26	17.83	17.10	15.75	15.16	14.80	1.43	0.73	SD	3150
07g-3-05744	0.15120666	530.20618	0.93	23.16	22.26	21.53	20.30	19.52	17.91	17.48	16.96	1.23	0.78	C	3400
17d-3-02440	0.15715549	568.64622	0.97	-	21.08	19.81	18.76	-	16.91	16.38	16.21	1.05	-	D	3600
19h-3-14922	0.17983010	331.33704	0.86	24.83	23.06	21.16	19.51	18.50	16.87	16.23	16.05	1.65	1.00	D	3300
19g-3-06701	0.20903132	320.24438	0.77	24.52	20.62	19.07	18.05	17.57	16.20	15.61	15.22	1.01	0.49	C	3700
07c-4-05645	0.21072274	578.31655	0.91	21.85	19.18	17.85	17.28	16.97	15.62	14.94	14.89	0.57	0.32	C	4150
19e-3-05704	0.21968029	323.13207	0.91	24.81	21.92	19.45	18.85	18.40	17.19	16.51	16.30	0.60	0.45	SD	3950
19c-2-08140	0.22728102	321.37419	0.97	21.18	18.54	17.43	16.90	16.64	15.59	15.00	14.86	0.53	0.26	C	4300
19e-4-00861	0.22842771	332.28102	0.80	23.57	20.35	18.95	18.33	18.04	16.74	16.02	15.95	0.62	0.29	C	4100
Red sample ( $P \leq 0.30$ days) 8 objects															
19c-1-09997	0.24660068	335.22912	0.91	23.90	19.73	18.46	17.92	17.66	16.83	16.37	16.35	0.54	0.26	C	4350
03f-1-01082	0.25016408	518.31103	0.99	23.67	21.11	19.51	18.63	18.05	16.55	16.34	15.63	0.88	0.58	C	3400
03b-3-02411	0.26251989	1050.5354	0.61	23.71	21.88	20.15	18.92	18.17	16.76	16.21	16.03	1.23	0.75	D	3250
19f-1-07389	0.26986911	324.49300	0.89	21.19	18.72	17.48	16.95	16.73	15.43	14.95	14.64	0.53	0.21	D	4250
07h-4-03156	0.27032161	551.23573	0.71	20.28	17.91	16.71	16.19	15.89	14.75	14.10	13.91	0.52	0.30	C	4200
19d-4-05861	0.27219697	336.29275	0.70	21.96	19.73	18.83	18.31	18.03	17.14	16.41	16.49	0.52	0.28	C	4650
07e-2-03887	0.27335648	533.21993	0.95	21.69	19.51	18.10	17.10	16.52	15.25	14.68	14.39	1.01	0.57	SD	3700
19a-4-04542	0.29367660	324.31748	0.74	22.53	20.22	18.73	17.88	17.39	16.08	15.40	15.64	0.85	0.49	D	3900
Blue sample ( $P \leq 0.23$ days) 14 objects															
07d-2-02291	0.20130714	594.33319	1.00	21.20	19.35	18.45	18.13	17.95	16.80	16.01	16.00	0.33	0.18	C	4650
07f-1-05360	0.20561088	783.57709	0.90	22.96	20.52	19.42	19.01	18.79	17.66	17.13	16.90	0.42	0.22	SD	4450
07b-4-06173	0.21233759	785.57965	1.00	20.89	18.74	17.79	17.39	17.26	16.04	15.58	15.61	0.40	0.13	C	4750
07a-1-03517	0.21430452	553.24191	0.81	19.63	17.64	16.82	16.45	16.23	15.05	14.60	14.36	0.37	0.22	C	4800
07c-3-05395	0.21484877	528.30800	0.85	21.30	19.10	18.20	17.83	17.61	16.59	16.21	16.30	0.36	0.22	SD	4850
07g-3-04935	0.21484957	876.36140	0.96	21.30	19.10	18.20	17.83	17.61	16.63	16.23	15.97	0.36	0.22	SD	4800
03e-4-02972	0.21931536	1155.4332	0.92	22.07	19.73	18.79	18.36	18.42	17.06	16.35	16.36	0.42	-0.06	C	4650
03e-4-03812	0.22189564	534.24769	0.90	19.27	18.01	17.53	17.31	17.23	16.26	16.06	15.56	0.22	0.09	SD	5600
19h-1-10160	0.22338883	374.31584	0.85	21.09	21.12	18.03	17.58	17.27	15.77	-	-	0.45	0.31	C	-
19c-3-12555	0.22521823	324.36446	0.18	18.77	17.40	16.76	16.49	16.38	15.30	14.99	14.74	0.27	0.11	C	5250
19b-2-05229	0.22570901	336.39181	0.97	21.78	19.39	18.38	17.92	17.65	16.68	16.24	16.22	0.46	0.28	C	4650
19a-2-10658	0.22645761	334.36200	0.89	18.72	17.15	16.54	16.36	16.19	15.17	14.79	14.56	0.18	0.17	C	5300
07g-3-00820	0.22695102	528.30249	0.87	17.10	15.32	14.60	14.30	14.15	13.23	12.76	12.63	0.30	0.14	C	5100
19g-4-11051	0.22945028	317.38529	0.97	20.26	18.28	17.50	17.16	16.96	16.14	15.63	15.61	0.35	0.20	SD	4900

**Table 4.2** — Source property table for our red short period sample,  $P \leq 0.30$  days and  $(r-i) \geq 0.5$  and  $(i-z) \geq 0.25$ , and our blue sample with  $P \leq 0.23$  days. The epoch column shows MJD-245000. The ratio  $d_2/d_1$  indicates the secondary eclipse depth over the primary eclipse depth in the phasefolded J band lightcurve, determined by median averaging the data in a phase range of  $\pm 0.01$  around phase 1.0 and 0.5. Quoted magnitudes are SDSS DR7 ugriz and WFCAM JHK, rounded off to two decimals. Our full SEDs have 8 band grizYJHK photometry. The state column indicates the estimate from Fourier fitting (Section 4.5) of the morphological state of the binary ('D' for detached, 'SD' for semi-detached and 'C' for contact.).

the sample. Our shortest period binary system (19b-3-06008,  $P \sim 0.1121$  days) is an outlier, indicating that a simple powerlaw is not sufficient at ultra-short periods. This is because for mid- and late M-dwarfs (J-K) colour is nearly constant with spectral type and as a result the period-colour relation breaks down. We used Baraffe (1998) models to convert the maximum binary mass for a certain period to the corresponding infrared colours for a single star with the same  $T_{eff}$  as the binary. We plot this for equal-mass binaries as a dashed line in the right-hand panel of Figure 4.10. It is consistent with the Deb & Singh relation down to  $\sim 0.20$  days within their  $1\sigma$  uncertainties, but is a better fit to the data at shorter periods. Riaz et al. (2008) performed a spectroscopic study of 1080 nearby active M-dwarfs and obtained 2MASS colours. The grey shaded region indicates (J-K) colours for their M-dwarfs classified as M4, showing that the infrared colours for the ultra-short period binaries are consistent with observations of active single mid-type M-dwarfs.

### 4.6.3 Constraints to binary evolution scenarios

Our results imply that for M-dwarf binaries the orbital periods can extend significantly beyond the proposed period cut-off of  $\sim 0.22$  days. For our (near-)contact M-dwarf system 19b-3-06008, the fitted  $T_{eff} \sim 3150$  K, which corresponds to a mass of  $0.15-0.25 M_{\odot}$ , implies that there is insufficient angular momentum loss over the Hubble time within the AML framework to explain the observed orbital period with starting periods of  $P_0=2.0-1.5$  days. For the  $P_0=1.0$  day model and a mass-ratio of  $\sim 0.3$  the contact timescale is of the order of the Hubble time. However, the near-equal ratio of secondary to primary eclipse depths suggests that this binary is rather near-equal-mass, unless the secondary is extremely bloated in radius with respect to its mass. Also, a mass-ratio of 0.3 and a primary mass of  $0.2 M_{\odot}$  would bring the secondary mass uncomfortably close to the hydrogen burning limit, whereas an intrinsically dark and low-mass secondary such as a brown dwarf would be unlikely to produce the observed secondary eclipse depth and the out-of-eclipse variations. Again, for the other three ultra-short period binaries only the  $P_0=1.0$  day model can reproduce the observed orbits for the estimated primary mass, under the requirement that we assume  $M_1 > 0.35 M_{\odot}$  and/or an extreme mass ratio, the latter which may be the case for 19h-3-14922 (where we estimate that  $q$  could be as low as 0.5). Given our estimates of the minimum birth separation for M-dwarfs (Figure 4.2), it seems unlikely that these binaries were formed at such short periods.

Another possibility is that the evolution of M-dwarf binaries is faster than expected. M-dwarfs are known to be active and flaring stars. West et al. (2011) find an activity fraction of 40-80% for M4-M9 dwarfs, which implies that scaling solar type stars to M-dwarfs is not trivial. It is possible that because of the (near-)convective nature of mid-to-late type M-dwarfs that the ultra-short periods of our binaries, when synchronised with the stellar rotation, cause the magnetic field lines to be significantly twisted (the  $\alpha^2$  dynamo; Radler et al. 1990). In other words, the topology of the magnetic fields could be significantly different from that of solar-type stars, which may directly affect the overall activity and as a consequence the rate at which angular momentum is lost.

Alternatively, the formation mechanism for M-dwarfs may be different from that of earlier type main sequence stars. It is possible that during the pre-main sequence phase an excess amount of angular momentum is removed which accelerates the orbital evolution. Possible sources of such enhanced evolution could be dynamical interactions with other stars, accretion of the surrounding material and/or interaction with a circumbinary disk (Pringle 1991; Artymowicz et al. 1991; Bate & Bonnell 1997). The hydrodynamical calculations of binary formation by fragmentation of Bate et al. (2002) indicate that proto-binaries potentially form with large separations ( $\geq 10$  AU) and go through a phase of accretion and orbital evolution towards tighter orbits ( $\sim 1$  AU). Less is known about the later phases of orbital evolution. In this paper, we have demonstrated that periods of  $\sim 1.0$  day would be required at early age to explain the observed ultra-short periods for our M-dwarf binaries, if magnetic braking is the dominant mechanism by which low-mass stars evolve over Gyrs timescales.

Recall that Jiang et al. (2011) concluded that contact M-dwarf binaries (primary mass  $\leq 0.63 M_{\odot}$ ) are short-lived and thus detections of them during this ‘special’ phase of their evolution would be rare. This is because they predict an instability in mass-transfer at the point at which the primary fills its Roche lobe which merges the system almost instantaneously. In combination with the findings by Ge et al. (2010), who show that the instability of mass transfer

occurs promptly upon Roche lobe filling of the primary (a semi-detached binary) for stars with a significant convection zone, it seems that the existence of our new near-contact M-dwarf systems, 19b-3-06008 and 07g-3-05744, among  $\sim 10,000$  M-dwarf sources in the WTS Survey, is unusual. However, detached short-period low-mass binaries are allowed in this model, because the angular momentum loss timescale is significantly shorter than in the Stepien AML model for M-dwarfs. Our detached ultra-short period systems, 17d-3-02440 and 19h-3-14922, thus appear to fit within the Jiang et al. model predictions.

## 4.7 Conclusion

In this paper we have presented the results of an extensive search for short-period low-mass eclipsing binary systems in the near-infrared J-band lightcurves of the WFCAM Transit Survey. Probing over 10,000 M-dwarfs down to  $J=18$  we report on the discovery of four ultra-short period ( $P \leq 0.18$  days) M-dwarf binaries. Their periods are significantly shorter than of any other known main-sequence binary system. All four are below the observed sharp period cut-off at  $P \sim 0.22$  days as seen in binaries of earlier type stars. The shortest-period binary consists of two M4 type stars in a  $P = 0.112$  day orbit. In total, we find 25 binaries with orbital periods shorter than 0.23 days of which 9 are identified as likely M-dwarf systems through their broad-band colours or spectra. Of these 9 systems, 5 are indicated as potential contact systems. These detections pose a direct challenge to popular theories that explain the evolution of short period binaries by loss of angular momentum through magnetised winds, or by unstable mass-transfer, which predict timescales that are either too long for their formation, or timescales that are too short to observe them in the contact phase. Our discovery of binaries with significantly shorter orbital periods than the previously observed cut-off implies that either these timescales have been overestimated for M-dwarfs, e.g. due to a higher effective magnetic activity, or that the mechanism for forming these tight M-dwarf binaries is different from that of earlier type main-sequence stars.

## Acknowledgments

We thank the anonymous referee, whose comments led to a significant improvement of the manuscript. SVN, JLB, IAGS, SH, DJP, RPS, JK, DB, ELM, CdB and YVP have received support from RoPACS during this research, and BS, GK, DM, PC, NG, HS, JZ and MC are supported by RoPACS, a Marie Curie Initial Training Network funded by the European Commission's Seventh Framework Programme. CdB acknowledges the Fundacao para a Ciencia e a Tecnologia (FCT) through the project Pest-OE/EEI/UI0066/2011.

## Bibliography

- Allard, F., Hauschildt, P. H., Alexander, D. R., & Starrfield, S. 1997, *ARA&A*, 35, 137
- Amôres, E. B., & Lépine, J. R. D. 2005, *AJ*, 130, 659
- Artymowicz, P., Clarke, C. J., Lubow, S. H., & Pringle, J. E. 1991, *ApJ*, 370, L35
- Baraffe, I., Chabrier, G., Allard, F., & Hauschildt, P. H. 1998, *A&A*, 337, 403
- Baraffe, I., & Chabrier, G. 1996, *From Stars to Galaxies: the Impact of Stellar Physics on Galaxy Evolution*, 98, 209
- Bate, M. R., & Bonnell, I. A. 1997, *MNRAS*, 285, 33
- Boss, A. P. 1993, *ApJ*, 410, 157
- Cargile, P. A., Stassun, K. G., & Mathieu, R. D. 2008, *ApJ*, 674, 329
- Casali, M., Adamson, A., Alves de Oliveira, C., et al. 2007, *A&A*, 467, 777
- Collier Cameron, A., Pollacco, D., Street, R. A., et al. 2006, *MNRAS*, 373, 799
- Coughlin, J. L., López-Morales, M., Harrison, T. E., Ule, N., & Hoffman, D. I. 2011, *AJ*, 141, 78
- Covey, K. R., Ivezić, Z., Schlegel, D., et al. 2005, *Bulletin of the American Astronomical Society*, 37, 502
- Deb, S., & Singh, H. P. 2011, *MNRAS*, 412, 1787
- Derekas, A., Kiss, L. L., & Bedding, T. R. 2007, *ApJ*, 663, 249
- Devor, J. 2005, *ApJ*, 628, 411
- Dimitrov, D. P., & Kjurkchieva, D. P. 2010, *MNRAS*, 406, 2559
- Eggen, O. J. 1967, *MNRAS*, 70, 111
- Eggleton, P. P. 1983, *ApJ*, 268, 368
- Eggleton, P. P., & Kiseleva-Eggleton, L. 2001, *ApJ*, 562, 1012
- Fabrycky, D., & Tremaine, S. 2007, *ApJ*, 669, 1298
- Ge, H., Hjellming, M. S., Webbink, R. F., Chen, X., & Han, Z. 2010, *ApJ*, 717, 724
- Goodwin, S. P., Whitworth, A. P., & Ward-Thompson, D. 2004, *A&A*, 414, 633
- Hebb, L., Stempels, H. C., Aigrain, S., et al. 2010, *A&A*, 522, A37
- Henry, T. J., Ianna, P. A., Kirkpatrick, J. D., & Jahreiss, H. 1997, *AJ*, 114, 388
- Herbst, W., Bailer-Jones, C. A. L., & Mundt, R. 2001, *ApJ*, 554, L197
- Hodgkin, S. T., Irwin, M. J., Hewett, P. C., & Warren, S. J. 2009, *MNRAS*, 394, 675
- Irwin, M., & Lewis, J. 2001, *NewAR*, 45, 105
- Irwin, J., Irwin, M., Aigrain, S., et al. 2007, *MNRAS*, 375, 1449
- Irwin, J., Berta, Z. K., Burke, C. J., et al. 2011, *ApJ*, 727, 56
- Jiang, D., Han, Z., Ge, H., Yang, L., & Li, L. 2011, arXiv:1112.0466
- Knigge, C., Baraffe, I., & Patterson, J. 2011, *ApJS*, 194, 28
- Kovács, G., Zucker, S., & Mazeh, T. 2002, *A&A*, 391, 369
- Kowalski, A. F., Hawley, S. L., Hilton, E. J., et al. 2009, *AJ*, 138, 633
- Landolt, A. U. 1992, *AJ*, 104, 340
- Maceroni, C., & Montalbán, J. 2004, *A&A*, 426, 577
- Martin, E. L., Spruit, H. C., & Tata, R. 2011, *A&A*, 535, A50
- Melo, C. H. F., Soares, B. B., Miranda, A. C., da Silva, J. R. P., & de Medeiros, J. R. 2000, *The Light Elements and their Evolution*, 198, 508
- Miller, V. R., Albrow, M. D., Afonso, C., & Henning, T. 2010, *A&A*, 519, A12
- Morales, J. C., Gallardo, J., Ribas, I., et al. 2010, *Binaries - Key to Comprehension of the Universe*, 435, 141
- Norton, A.J., Payne, S.G., Evans, T., et al. 2011, *A&A*, 528, A90
- Pepper, J., & Burke, C. J. 2006, *AJ*, 132, 1177
- Pojmanski, G. 2002, *AcA*, 52, 397

- Pribulla, T., Vanko, M., & Hambalek, L. 2009, *Information Bulletin on Variable Stars*, 5886, 1
- Pringle, J. E. 1991, *MNRAS*, 248, 754
- Raedler, K.-H., Wiedemann, E., Brandenburg, A., Meinel, R., & Tuominen, I. 1990, *A&A*, 239, 413
- Reid, I. N., Hawley, S. L., & Gizis, J. E. 1995, *AJ*, 110, 1838
- Reipurth, B., & Clarke, C. 2001, *AJ*, 122, 432
- Riaz, B., Gizis, J. E., & Harvin, J. 2006, *AJ*, 132, 866
- Rozyczka, M., Kaluzny, J., Pietrukowicz, P., et al. 2009, *AcA*, 59, 385
- Rucinski, S. M. 1992, *AJ*, 103, 960
- Rucinski, S. M. 1993, *PASP*, 105, 1433
- Rucinski, S. M., Pribulla, T., & van Kerkwijk, M. H. 2007, *AJ*, 134, 2353
- Scargle, J. D. 1982, *ApJ*, 263, 835
- Schlegel, D. J., Finkbeiner, D. P., & Davis, M. 1998, *ApJ*, 500, 525
- Sesar, B., Ivezić, Ž., Lupton, R. H., et al. 2007, *AJ*, 134, 2236
- Stepien, K. 1995, *MNRAS*, 274, 1019
- Stepien, K. 2006, *AcA*, 56, 347
- Stępień, K. 2011, *AcA*, 61, 139
- Stetson, P. B. 1996, *PASP*, 108, 851
- Tylenda, R., Hajduk, M., Kamiński, T., et al. 2011, *A&A*, 528, A114
- Tokovinin, A., Thomas, S., Sterzik, M., & Udry, S. 2006, *A&A*, 450, 681
- Vida, K., Oláh, K., Kővári, Z., et al. 2009, *A&A*, 504, 1021
- Weldrake, D. T. F., Sackett, P. D., Bridges, T. J., & Freeman, K. C. 2004, *AJ*, 128, 736
- West, A. A., Morgan, D. P., Bochanski, J. J., et al. 2011, *AJ*, 141, 97
- Zhang, X. B., Deng, L., & Lu, P. 2009, *AJ*, 138, 680

## **Appendix**

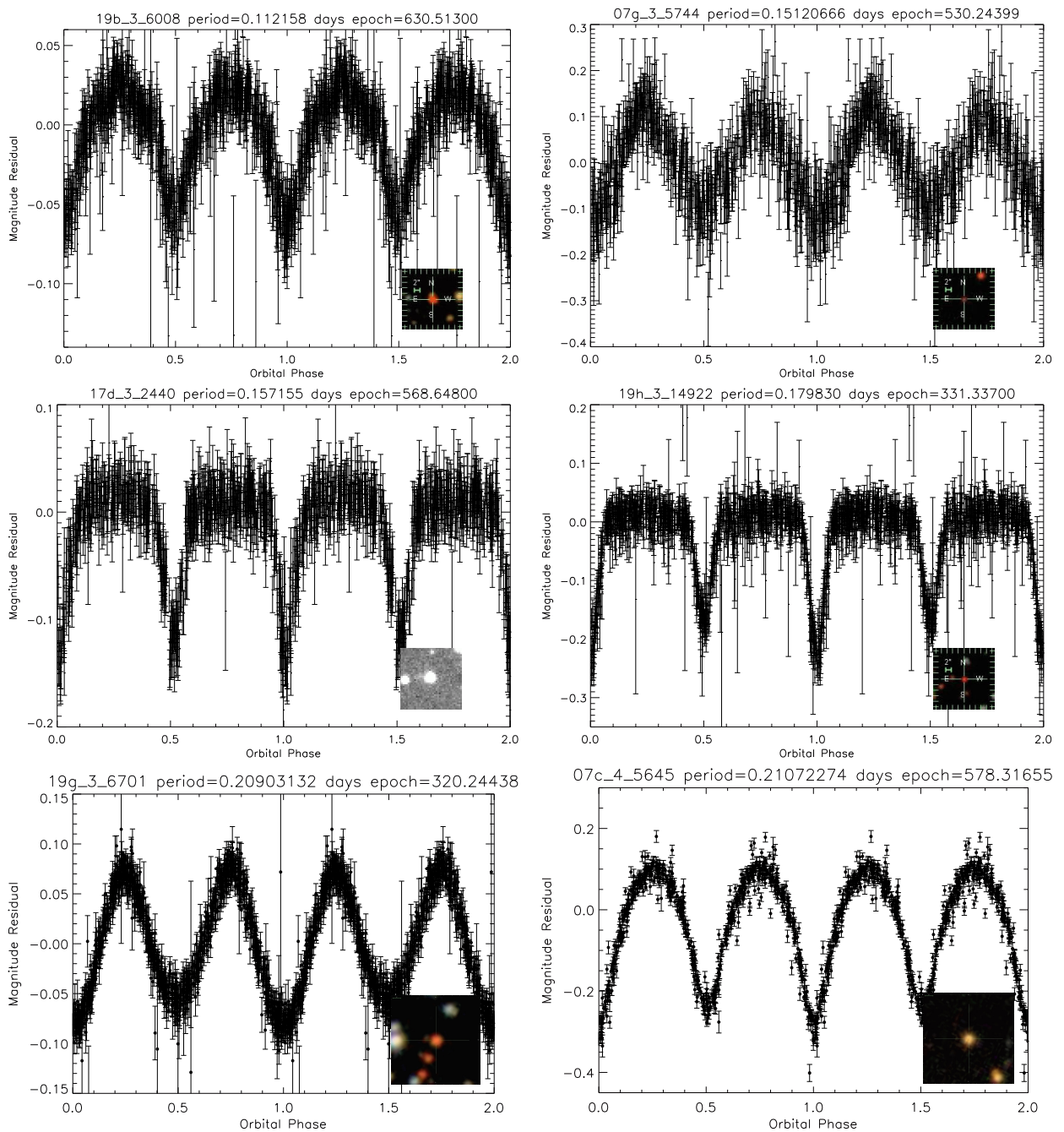


**Figure 4.11** — The red sample of candidate eclipsing binaries, which satisfies the colour constraints  $(r-i) \geq 0.5$  and  $(i-z) \geq 0.25$ , ordered by increasing period  $P \leq 0.23$  days. We plot two full binary orbits. The boxes in the lower right corner of each plot show a three colour SDSS composite image of each source. For 17d-3-02440, which does not have SDSS coverage, we show the WFCAM J band image. A colour version of the thumbnails is available in the online paper.

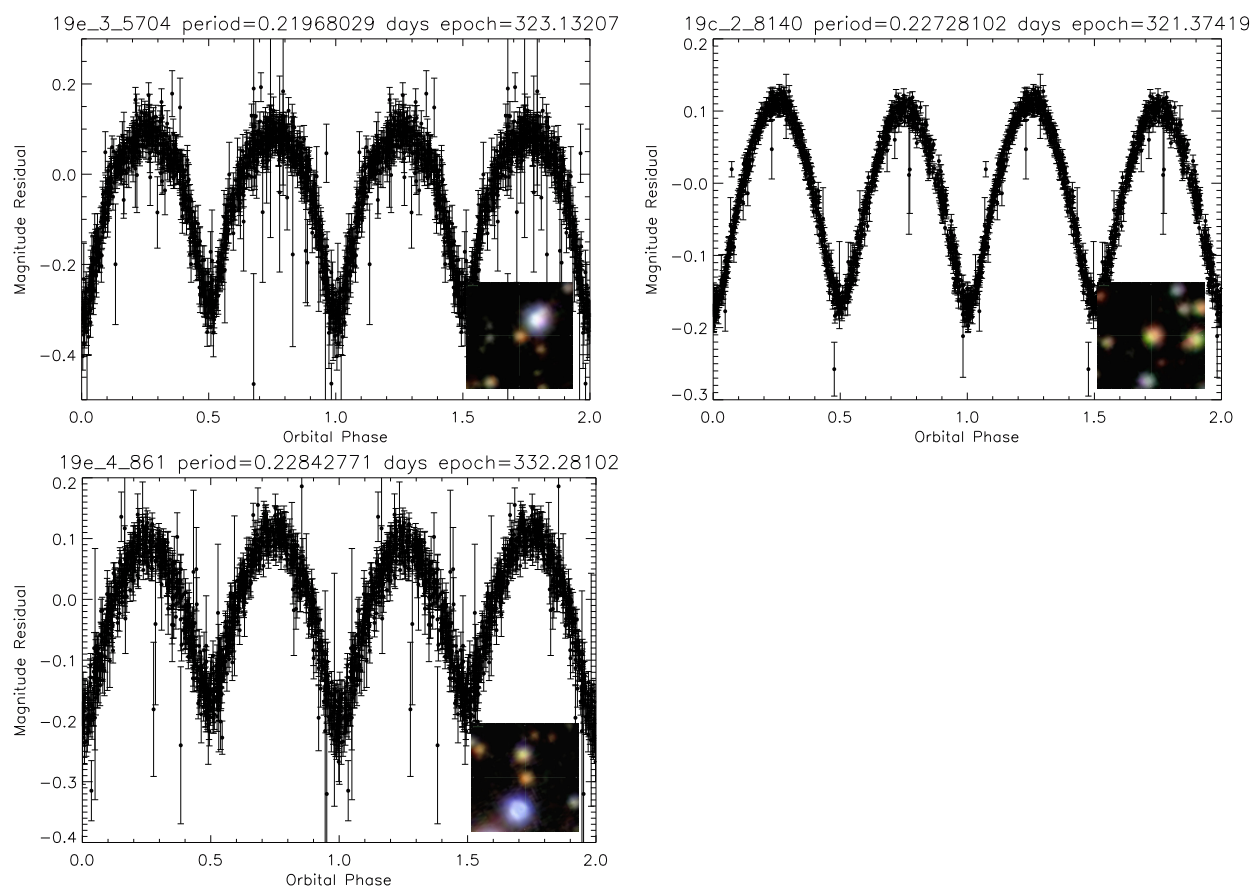


**Figure 4.12** — Red sample with  $P \leq 0.23$  days continued.

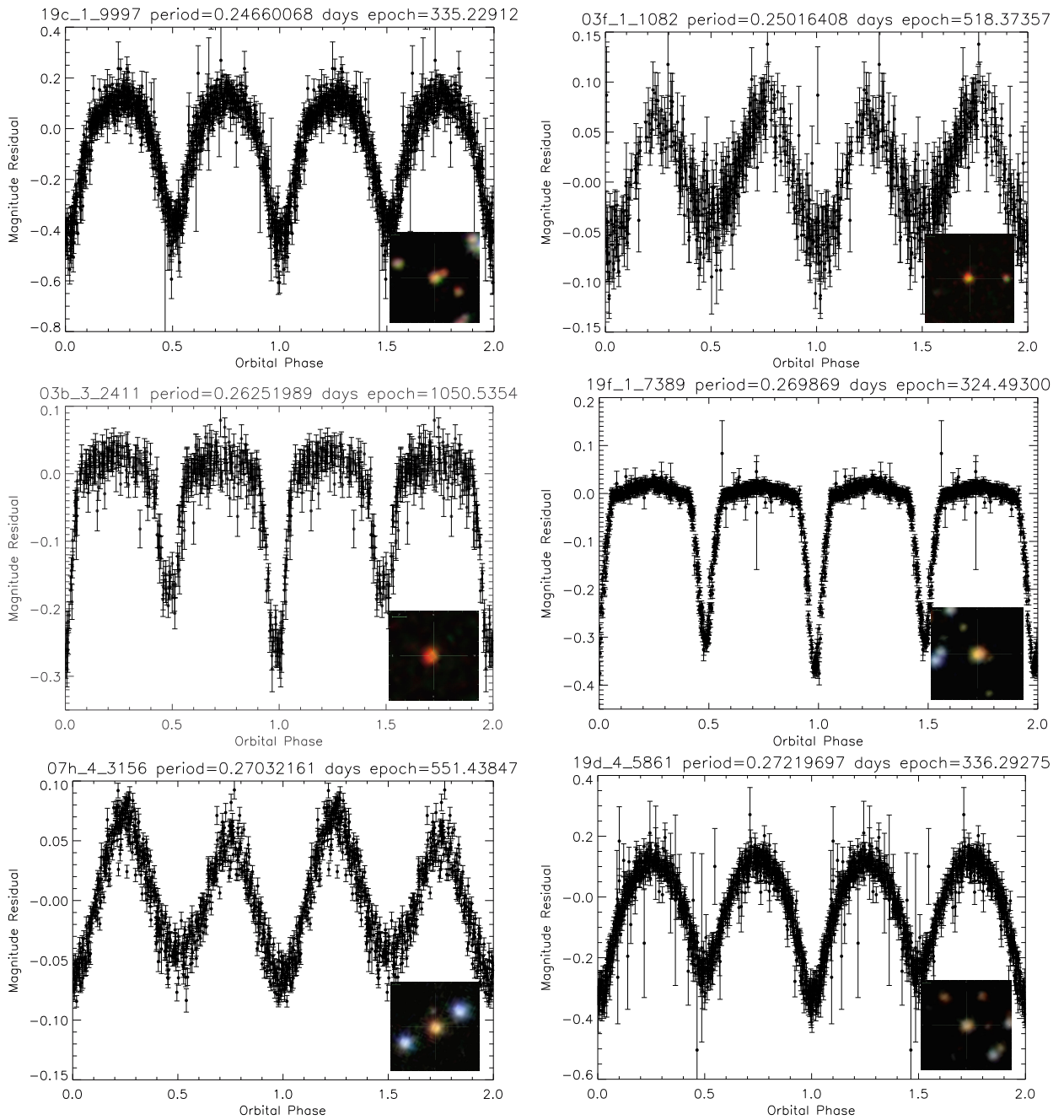
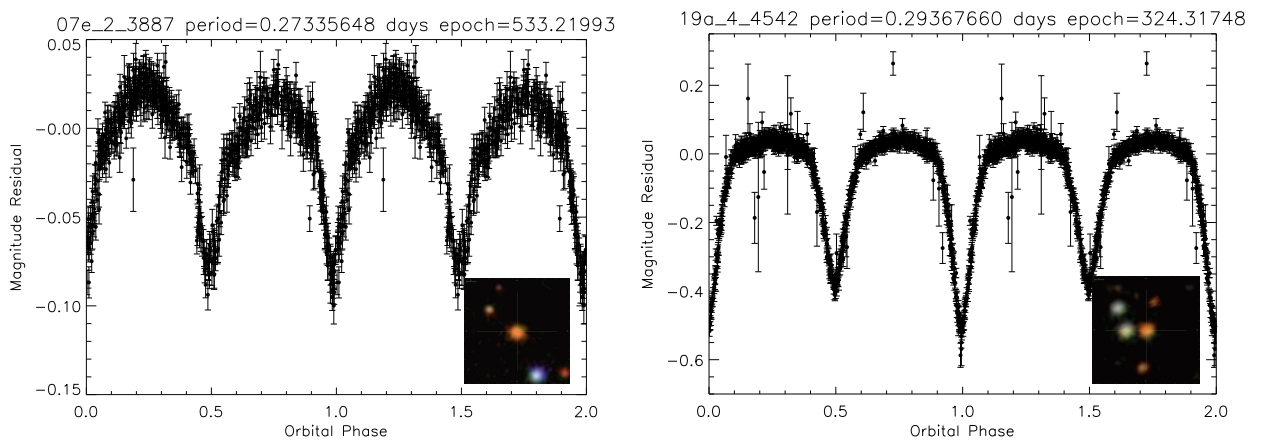


Figure 4.13 — Red sample with  $0.23 < P \leq 0.3$  days.



**Figure 4.14** — Red sample with  $0.23 < P \leq 0.3$  days continued.

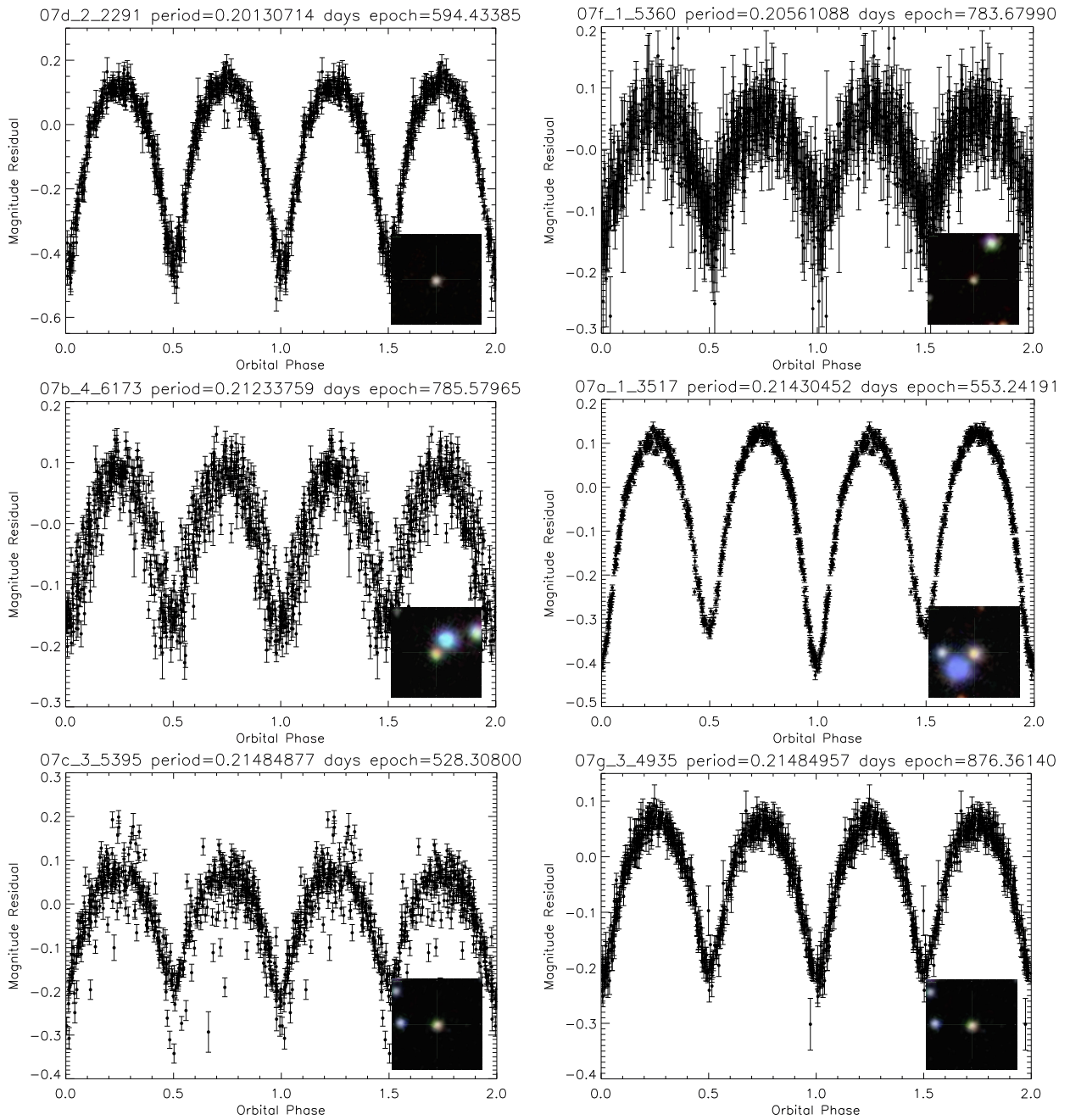


Figure 4.15 — Blue sample with  $P \leq 0.23$  days.

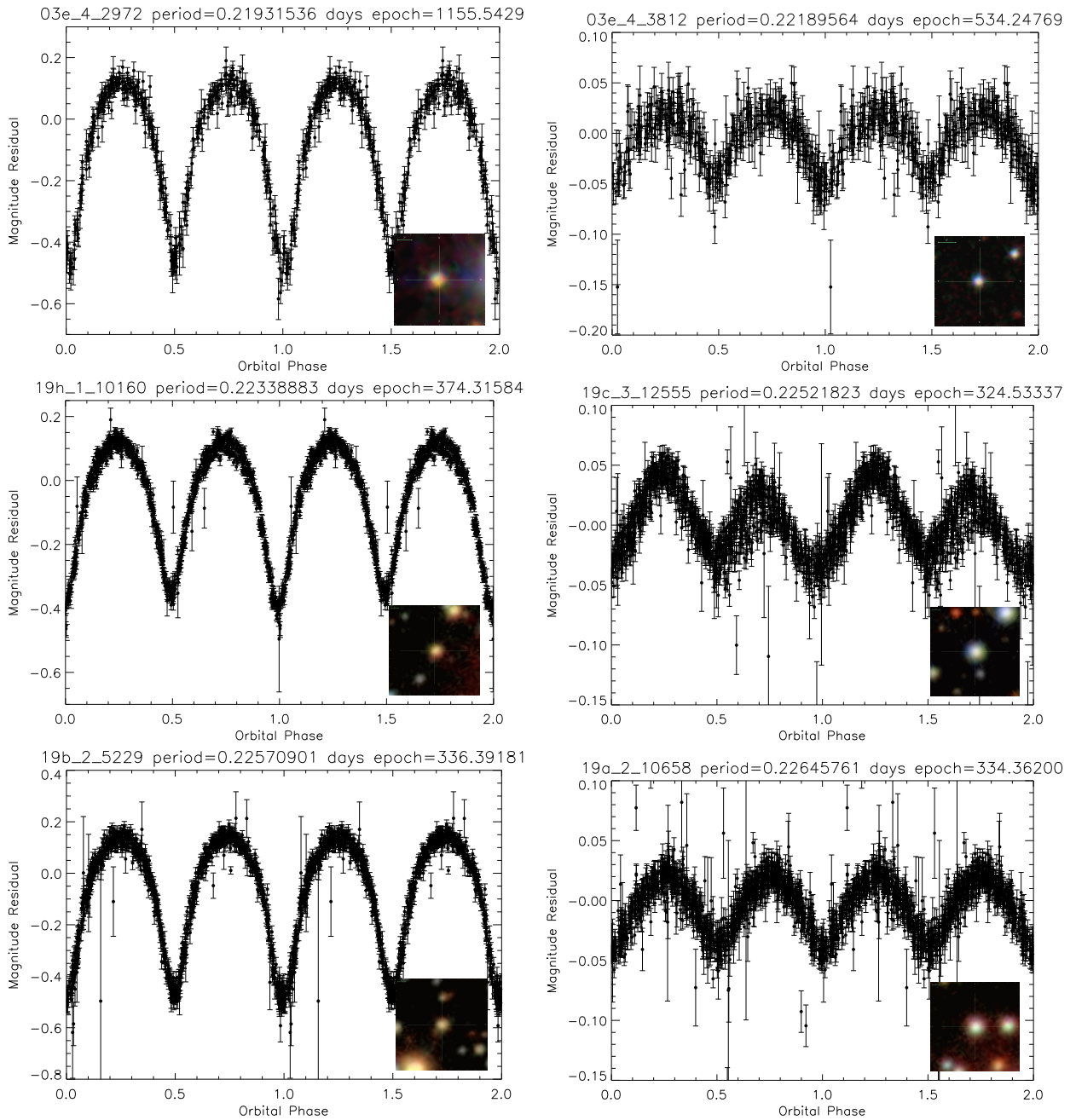


Figure 4.16 — Blue sample with  $P \leq 0.23$  days continued

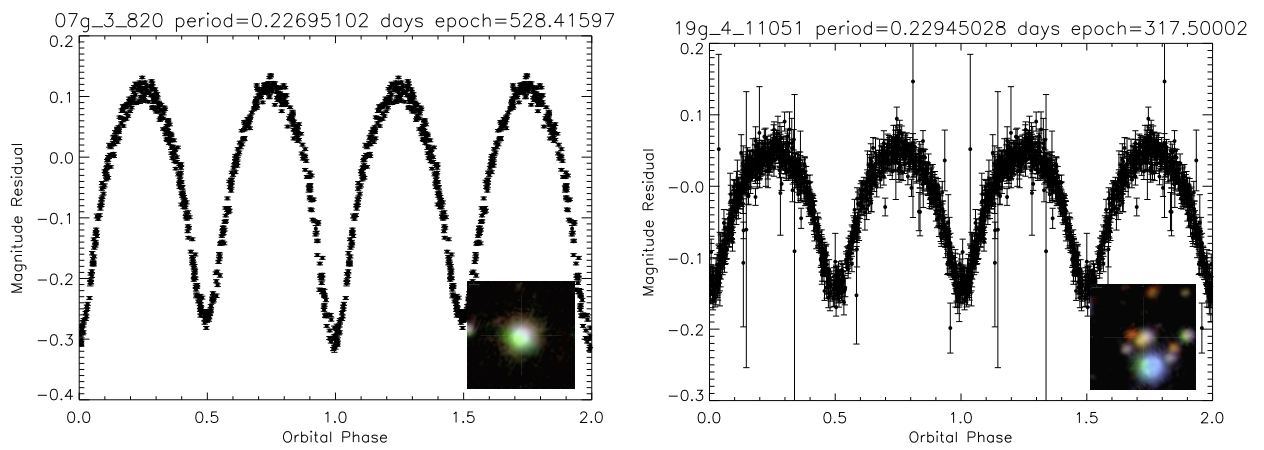


Figure 4.17 — Blue sample with  $P \leq 0.23$  days continued

Name	Period (days)	RA				DEC	
		<i>h</i>	<i>m</i>	<i>s</i>	<i>d</i>	<i>m</i>	<i>s</i>
19b-3-06008	0.1121579	19	33	49.3	36	54	01.8
07g-3-05744	0.1512067	07	07	47.6	12	59	42.1
17d-3-02440	0.1571555	17	17	28.7	04	07	30.7
19h-3-14922	0.1798301	19	38	44.1	36	30	14.7
19g-3-06701	0.2090313	19	37	04.0	36	36	24.8
07c-4-05645	0.2107227	07	05	25.9	13	23	14.3
19e-3-05704	0.2196803	19	32	32.8	36	32	11.8
19c-2-08140	0.2272810	19	37	11.3	36	22	39.0
19e-4-00861	0.2284277	19	31	04.5	36	30	01.3
19c-1-09997	0.2466007	19	34	45.7	36	22	47.4
03f-1-01082	0.2501641	03	36	29.1	38	58	10.6
03b-3-02411	0.2625199	03	38	26.0	39	38	16.3
19f-1-07389	0.2698691	19	31	34.6	36	08	37.9
07h-4-03156	0.2703216	07	06	05.8	13	04	10.1
19d-4-05861	0.2721970	19	36	36.6	36	48	12.3
07e-2-03887	0.2733565	07	03	23.5	12	34	39.1
19a-4-04542	0.2936766	19	30	29.7	36	48	35.7
07d-2-02291	0.2013071	07	08	43.1	12	51	50.3
07f-1-05360	0.2056109	07	02	34.0	12	42	25.9
07b-4-06173	0.2123376	07	02	31.3	13	22	60.0
07a-1-03517	0.2143045	07	01	56.1	12	45	21.0
07c-3-05395	0.2148488	07	07	40.8	13	09	25.4
07g-3-04935	0.2148496	07	07	40.8	13	09	25.5
03e-4-02972	0.2193154	03	34	38.5	39	22	22.1
03e-4-03812	0.2218956	03	34	30.8	39	24	48.5
19h-1-10160	0.2233888	19	35	53.7	36	08	47.8
19c-3-12555	0.2252182	19	37	30.9	36	46	55.7
19b-2-05229	0.2257090	19	33	41.2	36	24	31.7
19a-2-10658	0.2264576	19	33	17.5	36	17	17.5
07g-3-00820	0.2269510	07	07	03.1	12	59	58.4
19g-4-11051	0.2294503	19	34	55.9	36	39	56.5

**Table 4.3** — Table showing the sky coordinates for our WTS short-period eclipsing M-dwarf binaries: we list right ascension (RA) and declination (DEC) in the format *hms*(hours, minutes, seconds) and *dms*(degrees, minutes, seconds).

---

## Chapter 5

---

# A highly unequal-mass eclipsing M-dwarf binary in the WFCAM Transit Survey.

Star formation theory predicts that short-period M-dwarf binaries with highly unequal-mass components are rare. Firstly, the mass ratio of close binary systems is driven to unity due to the secondary preferentially accreting gas with high angular momentum. Secondly, both dynamical decay of multiple systems and interactions with tertiary stars that tighten the binary orbit would eject the lowest mass member. Generally, only the two most massive stars are paired after such interactions, and the frequency of tight unequal-mass binaries is expected to decrease steeply with primary mass. In this paper we present the discovery of a highly unequal-mass eclipsing M-dwarf binary, providing a unique constraint on binary star formation theory and on evolutionary models for low-mass binary stars. The binary was discovered using high-precision infra-red light curves from the WFCAM Transit Survey (WTS) and has an orbital period of 2.44 d. We find stellar masses of  $M_1 = 0.5294(\pm 0.0209)M_\odot$  and  $M_2 = 0.1428(\pm 0.0056)M_\odot$  (mass ratio 0.27), and radii of  $R_1 = 0.5141(\pm 0.0106)R_\odot$  and  $R_2 = 0.1736(\pm 0.0056)R_\odot$ . This puts the companion in a very sparsely sampled and important late M-dwarf mass-regime. Since both stars will share the same age and metallicity and straddle the theoretical boundary between fully and partially convective stellar interiors, a comparison can be made to model predictions over a large range of M-dwarf masses using the same model isochrone. Both stars appear to have a slightly inflated radius compared to 1 Gyr model predictions for their masses, but future work is needed to properly account for the effects of star spots on the light curve solution. A significant, sub-synchronous,  $\sim 2.56$  d signal with  $\sim 2\%$  peak-to-peak amplitude is detected in the WFCAM light curve, which we attribute to rotational modulation of cool star spots. We propose that the sub-synchronous rotation is either due to a stable star-spot complex at high latitude on the (magnetically active) primary (i.e. differential rotation), or to additional magnetic braking, or to interaction of the binary with a third body or circumbinary disk during its pre-main-sequence phase.

S.V.Nefs, J.L.B. Birkby, I.A.G. Snellen et al.  
*submitted to MNRAS*

## 5.1 Introduction

Stellar evolution models have found it difficult to accurately reproduce the fundamental properties of M-dwarf stars ( $M_* < 0.65M_\odot$ ), which are the most abundant population of stars in the Milky Way (over 70% in number; Henry et al. 1997). Furthermore, the formation process of binary M-dwarfs and their migration to close orbits are not well-understood (e.g. Goodwin & Whitworth 2007; Clarke 2012; Nefs et al. 2012). M-dwarfs are important to astrophysics because they help us understand a variety of problems, from the local star formation history, to the shape of the stellar (initial) mass function (e.g. Reid 1999; Gizis, Reid & Hawley 2002; Bochanski et al. 2007). Moreover, M-dwarfs are now being recognised as prime targets in the hunt for Earth-like exoplanets (e.g. Nutzman & Charbonneau 2008), as their small stellar size results in deeper transits and larger reflex motions induced by planetary companions. However, the current uncertainty in our understanding of M-dwarf formation and evolution means that the parameters of their planets, which scale with those of the host star, can not be determined to high accuracy, limiting a detailed characterisation of their compositions and atmospheres.

Hydrodynamical simulations (e.g. Bate, Bonnell & Bromm 2002) show that when a star-forming cloud collapses, it fragments into low-number multiple systems, which can be broken up by dynamical interactions (e.g. Goodwin et al. 2007). It is predicted that short-period M-dwarf binaries with significantly unequal-mass components should be very rare. The first reason is that simulations suggest that infalling gas with high angular momentum is preferentially accreted onto the lower-mass component during binary formation, driving the mass-ratio to unity (e.g. Bate & Bonnell 1997; Bate 2000). The momentum of the gas increases as accretion proceeds and is higher for closer binary systems. Gas with low angular momentum is mainly accreted by the primary because it essentially falls straight onto the centre of mass of an unequal-mass system, but high angular momentum gas falls in further away, closer to the orbital radius of the secondary, and need not to gain as much momentum to be captured by the companion (e.g. Bate & Bonnell 1997). The second reason for preference of equal mass ratios in low-mass binaries is that dynamical decay of multiple systems and exchange interactions with single stars in the collapsing cloud can increase the binary mass ratio, while at the same time tightening the binary orbit. In dynamical decay, typically the least massive component is ejected on a short time-scale, due to the instability of multiple star systems (e.g. Anosova 1986). In a dynamic exchange interaction the lowest mass star is also removed and replaced by the higher mass intruder. This means that only the two most massive stars survive an interaction, indicating that both the frequency of multiples and the frequency of systems with unequal-mass components steeply decrease with decreasing primary mass, and highly unequal, short-period, M-dwarf binary systems should thus be rare.

There is observational evidence for this hypothesis. Wisniewski et al. (2012) recently proposed a lack of unequal-mass stellar binaries at periods shorter than  $\sim 100$  d, combining current results from radial velocity, transit and imaging studies. Delfosse et al. (2004) find that M-dwarf binaries with orbital period  $P_{orb} < 50$  d possess a mass-ratio distribution which is peaked around 1 ('twins'), whereas wider binaries have a flat distribution. Clarke, Blake & Knapp (2012) find a frequency of close M-dwarf binary stars with a separation of less than 0.4 AU of only  $3.0^{+0.6}_{-0.9}\%$ , and argue that the frequency of  $< 0.4$  AU binaries is decreasing from 26% at  $10M_\odot$  to 1% at  $0.1M_\odot$  (see e.g. Lada (2006) and Raghavan et al. 2010). Bouchy et al. (2011) propose that G-type or lower mass stars have stronger disk braking than more massive stars, which would

cause any short-period low-mass companion to migrate inwards and become engulfed by the primary.

Detached, double-lined eclipsing binaries (EBs) provide a model-independent method for accurately calibrating the formation and evolution of stars (Andersen et al. 1991; Torres, Andersen & Giménez 2010). Dynamical measurements of the masses, radii, and temperatures of M-dwarf stars in eclipsing binary systems, suggest that current models under-predict the radii of M-dwarfs by 5 – 15%, and over-predict their effective temperatures by 3 – 5% (typically 100-200K; e.g. Lopez-Morales & Ribas 2005; Torres, Andersen & Giménez 2010). These discrepancies have been attributed to possible metallicity variations (e.g. Berger et al. 2006), but more likely they are due to strong magnetic fields and spots present on the stars of the observed tidally-locked, short-period M-dwarf binaries (e.g. Mullan & MacDonald 2001; Ribas 2006; Chabrier, Gallardo & Baraffe 2007). However, there is no current model that can accurately reproduce all of the observed dynamical measurements.

It is thought that stars with masses  $M < 0.35M_{\odot}$  converge towards agreement with the current models because they are likely to have fully-convective atmospheres, and thus would suffer less from the inflating effects of magnetic inhibition (Kraus et al. 2011). However, even the longest-period, non-synchronised M-dwarf EBs with secondary components in the fully-convective regime (Irwin et al. 2011; Doyle et al. 2011), still show significant radius inflation, despite much lower magnetic fields (see Birkby et al. 2012). For the lowest mass main-sequence M-dwarfs ( $0.08M_{\odot} < M < 0.2M_{\odot}$ ), there is even more uncertainty, due to a paucity of model-independent dynamical measurements. Only a few young objects in the Orion Nebula have data (see Irwin et al. 2007; Stassun, Mathieu & Valenti 2007). Constraints on M-dwarf evolution isochrones are further hindered by the apparent preference for equal mass MEBs. Low-mass ratio MEBs are valuable because their shared age and metallicity allow a more stringent assessment of the stellar model predictions over the wide span of M-dwarf masses.

In this paper we describe the discovery and characterisation of a main-sequence unequal mass, short-period, detached M-dwarf eclipsing binary system, whose components straddle the fully-convective boundary, and whose secondary star resides in the uncharted  $< 0.2M_{\odot}$  mass regime. The binary was discovered using high-precision infra-red light curves from the WFCAM Transit Survey (WTS). The WTS is an ongoing photometric monitoring campaign that operates as a back-up program running on the 3.8m United Kingdom Infrared Telescope (UKIRT) at Mauna Kea, Hawaii. By observing in the infra-red, the WTS is optimised for precision photometry of cool low-mass stars. Its primary objective is to hunt for planets orbiting M-dwarfs by regular monitoring of  $\sim 6000$  early- to mid M-dwarfs (for  $J < 16$ ), but also to characterise the host stars.

In Section 5.2 we present the observations and the data reduction of infra-red and optical time-series of the eclipses of our binary, WTS 19g-4-02069, and present low- to medium resolution spectroscopy in the optical and in the infra-red H-band. In Sections 5.3 and 5.4 we characterise the components of 19g-4-02069 using the available data, obtaining individual masses, radii, effective temperatures and activity indicators. In Section 5.5 we discuss the significance of the binary in the context of current low-mass stellar evolution models.

## 5.2 Observations & Data Reduction

### 5.2.1 WTS J-band time series photometry

The WTS, in operation since 2007 August, was awarded 200 nights of observing time on UKIRT. The survey uses the UKIRT Wide Field Camera (WFCAM), which has four  $2048 \times 2048$   $18 \mu\text{m}$  HgCdTe Rockwell Hawaii-II imaging arrays that each cover  $13.65 \times 13.65$  arcmin<sup>2</sup> on sky (with a pixel resolution of  $0.4$  arcsec pixel<sup>-1</sup>), and are separated by 94 per cent of a chip width (Casali et al. 2007). Observations for the WTS are obtained in the J-band ( $1.25 \mu\text{m}$ ), which maximises the sensitivity to M-dwarfs with effective temperatures  $T_{\text{eff}} < 4000\text{K}$ .

The survey targets four  $1.5$  deg<sup>2</sup> fields (the 03hr field, the 07hr field, the 17hr field and the 19hr field), selected to give both year-round visibility, an optimal number of dwarfs versus giants, relatively low reddening [E(B-V) between 0.057 and 0.234] and reduced contamination by blending stars, by observing close to but outside the galactic plane (galactic latitude  $b > 5^\circ$ ). The observing strategy, pipeline data reduction and WTS light curve generation has been extensively described in Kovacs et al. (submitted) and Birkby et al. (2012), and the interested reader is referred to these two publications. The infra-red light curves have an average cadence of 15 min. For each field, single deep exposures in the full WFCAM ZYJHK system were also obtained, to aid the photometric identification of M-dwarfs through fitting of the broad band spectral energy distributions (SEDs). The SED for 19g-4-02069, extending from Sloan Digitized Sky Survey (SDSS)  $u$  band to infra-red Wide Field Infrared Survey Explorer (WISE)  $4.6\mu\text{m}$ , is shown in Table 1.

The subject of this paper was selected from the list of 16 well-sampled detached M-dwarf eclipsing binaries with  $J \leq 16$  as presented in Birkby et al. (2012) in the 19hr field, the WTS target field which currently has the most extensive observational coverage ( $\sim 1100$  epochs). An initial source detection was performed using the Box-Least-Squares (BLS) algorithm, OCC-FIT (Aigrain & Irwin 2004; Miller et al. 2008). Fitting of the broad band SED of 19g-4-02069 yielded a system effective temperature of  $T_{\text{eff}} \sim 3050\text{K}$ , the lowest of the Birkby et al. (2012) sample, indicating a low-mass eclipsing M-dwarf binary system. The out-of-eclipse root mean square (rms) scatter of 19g-4-02069 is relatively high compared to other stars of similar magnitude ( $\sim 12.5$ mmag per datapoint), whereas  $\sim 6$ mmag is expected. We attribute this to stellar activity (see the discussion in Section 5.4.1). The WTS J band data for 19g-4-02069 are given in Table 2 and shown in Figure 5.1, folded on the binary orbital period.

### 5.2.2 INT i'-band follow-up photometry

We obtained follow-up photometric observations in the Sloan  $i$ -band on the 2.5m Isaac Newton Telescope (INT) on La Palma, using the Wide Field Camera (WFC), to refine our best-fitting light curve solution from the WFCAM J-band survey data. This imaging camera has a field of view of approximately  $34 \times 34$  arcmin<sup>2</sup> at prime focus, comprised of a mosaic of four  $2 \times 4\text{k}$  pixel CCDs, with a resolution of  $\sim 0.33$  arcsec/pixel. The observations were part of a wider WTS follow-up campaign to confirm planetary transit candidates, between July 18 and August 01 2010, leaving a few windows to observe binary eclipses. We used the WFC in fast readout mode (readout time 28 sec., for  $1 \times 1$  binning) to observe a full primary eclipse of 19g-4-02069 on the night of July 25 2010 and a full secondary eclipse on the night of July 31 2010. We

$\alpha_{J2000}$	19:35:03.55	
$\delta_{J2000}$	+36:31:16.49	
Broad-band SED	19g-4-02069	
<b>Band name</b>	<b>Central <math>\lambda</math> (<math>\mu\text{m}</math>)</b>	<b>magnitude</b>
u <sup>1</sup>	0.35	23.594( $\pm$ 3.0)
g	0.47	20.262( $\pm$ 0.02)
r	0.62	18.866( $\pm$ 0.01)
i	0.75	17.277( $\pm$ 0.01)
z	0.89	16.335( $\pm$ 0.01)
Z	0.89	15.928( $\pm$ 0.005)
Y	1.03	15.426( $\pm$ 0.007)
J	1.25	14.843( $\pm$ 0.004)
H	1.63	14.271( $\pm$ 0.004)
K	2.20	13.952( $\pm$ 0.004)
WISE1	3.4	13.842( $\pm$ 0.028)
WISE2	4.6	13.812( $\pm$ 0.044)

**Table 5.1** — Broad-band spectral energy distribution for the eclipsing M-dwarf binary 19g-4-02069. SDSS u,g,r,i and z magnitudes are quoted in the AB magnitude system, whereas the WFCAM Z,Y,J,H and K magnitudes are in the Vega system. <sup>1</sup>SDSS *u* is uncertain because of a red leak (Abazajian et al. 2004). The entries WISE1 and WISE2 refer to the first two wavelength channels of the WISE at 3.4 and 4.6  $\mu\text{m}$ . The source is too faint for detection at 12 and 22  $\mu\text{m}$ .

<b>WFCAM</b>	<b>HJD</b>	<b><math>J_{WTS}</math></b>	<b><math>\sigma_{J_{WTS}}</math></b>
J-band	-2454000	(mag)	(mag)
	317.808593	14.8003	0.0050
	....	....	....
<b>INT</b>	<b>HJD</b>	<b><math>\Delta m_{iINT}</math></b>	<b><math>\sigma_{m_{iINT}}</math></b>
i-band		(mag)	(mag)
Primary event			
	1403.904630	0.00146	0.00493
	....	....	....
Secondary event			
	1409.998380	-0.00071	0.00257
	....	....	....

**Table 5.2** — Photometry for binary 19g-4-02069 showing, from top to bottom, the WTS J-band photometry of 19g-4-02069, and the INT *i* band data. Quoted magnitudes in the WFCAM system (column 3) can be converted to other photometric systems as described in Hodgkin et al. (2009). The J-band errors  $\sigma_j$ , are estimated using a noise model including Poisson noise, sky noise, readout noise and errors in the background estimation. (This table is published in full in the online journal and is shown partially here for guidance regarding its form and content).

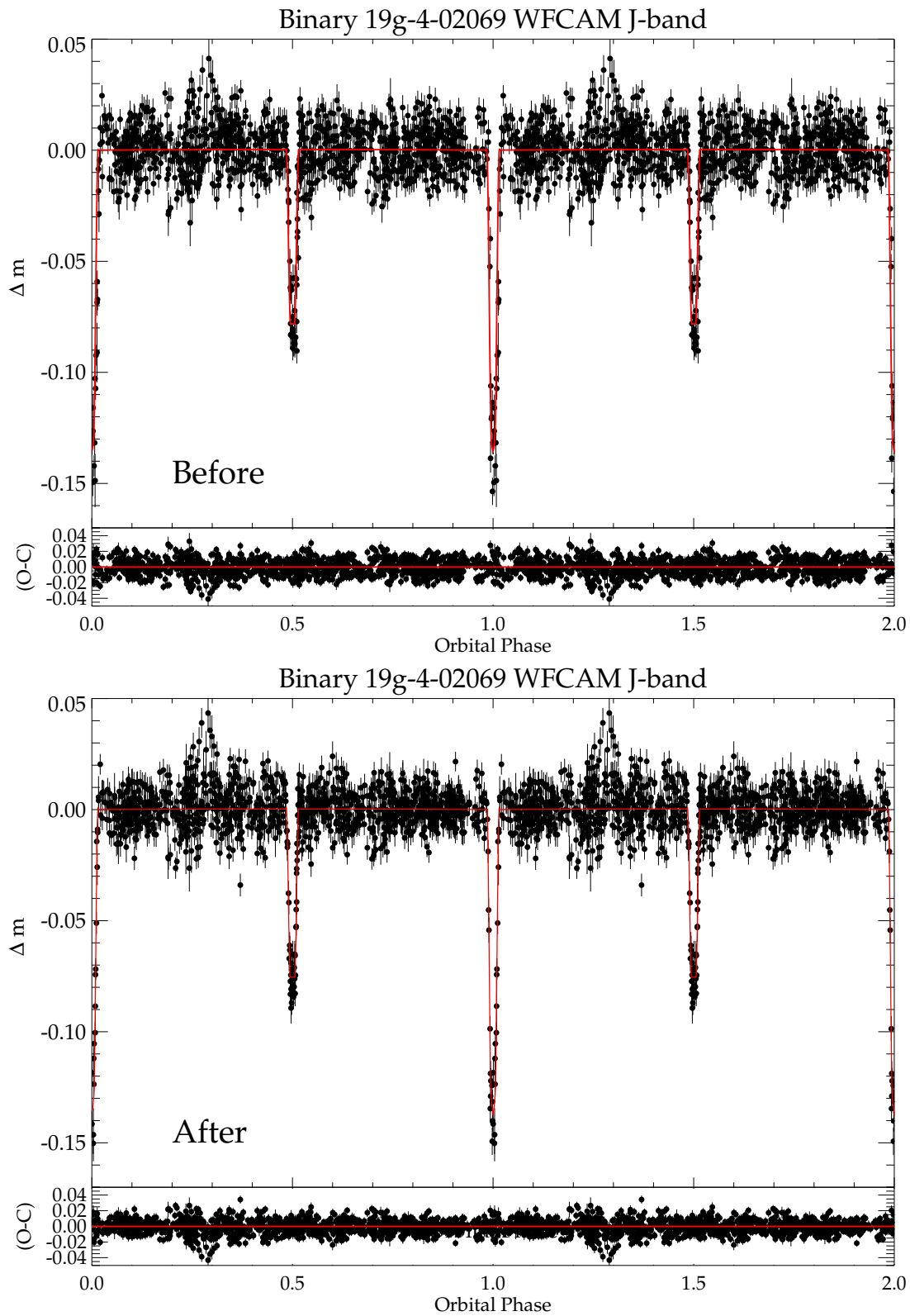


**Figure 5.1** — The WFCAM J-band discovery light curve of binary 19g-4-02069, before (upper panel) and after (lower panel) removal of the rotational signal, which reduces the total light curve rms by  $\sim 20\%$ , and corrects the shape of the eclipses. The data are shown in relative magnitudes  $\Delta m$ . The best-fit JKTEBOP models are overplotted with a solid red line.

centered the observations around the predicted times of eclipse (based on the J-band data), and allowed  $\sim 50$  min. of observations on either side of the predicted eclipses to acquire sufficient baseline. We obtained 82, 90 sec. exposures for the primary event and 52, 200 sec. exposures for the secondary, with out-of-eclipse rms of  $\sim 5.6$ mmag and  $\sim 2.2$ mmag. Error-bars on the data were obtained by assuming a  $\chi^2$  value of 1 for the out-of-eclipse parts using the models of Section 5.4.2.

We reduced the data using custom-built IDL routines to perform the standard 2-D image processing (i.e. bias subtraction and flat-field division). We remove low-level fringing by subtracting a scaled super sky-frame, which was obtained by median averaging dithered exposures of a blank field under dark sky conditions. To generate the light curves, we use variable aperture photometry and circular apertures with the IDL routine `APER`. We estimate the sky background using a  $3\sigma$  clipped median on  $30 \times 30$  pixel boxes. A master reference light curve is obtained from differential photometry on a set of  $\sim 10$  bright, nearby, non-saturated, non-blended reference stars, selecting for each reference star the aperture that minimises the out-of-eclipse rms. Airmass dependence is removed by fitting a second order polynomial to the out-of-eclipse data. The INT *i*-band data are presented in Table 2, and shown in Figure 5.2.

### 5.2.3 Low resolution spectroscopy

We obtained low-resolution spectroscopy using the William Herschel Telescope (WHT), to confirm the M-dwarf nature of the binary system 19g-4-02069 via measurement of the strengths of gravity sensitive atomic stellar absorption lines, and to estimate the system effective temperature and chromospheric activity. Observations were carried out on the night of July 16, 2010 using the Intermediate dispersion Spectrograph and Imaging System (ISIS). We used the R158R grating, which has a spectral resolution of  $R \sim 1200$  ( $1.81 \text{ \AA}/\text{pixel}$ ) at  $8500 \text{ \AA}$  and wavelength range of  $\sim 6000\text{-}9000 \text{ \AA}$ , for our  $1.0''$  wide slit, chosen to match the typical seeing conditions of the night. We opted to use ISIS red arm only with the red sensitive RED+ array and not use the dichroic because it can cause systematics and loss of efficiency up to  $\sim 10\%$ . A single 500 sec. spectrum was obtained using this setup at an airmass of  $\sim 1.35$ .

We reduced the data using a combination of custom-built IDL procedures and standard IRAF routines. In IDL we trim the spectrum, bias subtract and filter for cosmic rays, before we divide our data by a median averaged flatfield, which we first correct for dispersion effects using a pixel-integrated sensitivity function. We use IRAF's `APALL` routine to perform optimal 1-D spectral extraction. Wavelength calibration is obtained using arc spectra from the standard CuNe+CuAr lamps and flux-calibration is achieved with an early-type spectrophotometric standard. We did not remove telluric lines. The final spectrum is shown in Figure 5.3 as the black continuous line. In this figure, we also indicate a few important molecular absorption bands, and several atomic lines.

### 5.2.4 WHT ISIS optical spectroscopy

We obtained intermediate resolution spectra with ISIS on the WHT, in order to measure radial velocities. We used the red arm with the R1200R grating (spectral resolution  $R \sim 9300$ ,  $0.26 \text{ \AA}/\text{pixel}$ ) centred on  $8500 \text{ \AA}$ , giving a wavelength coverage of  $\sim 8100\text{-}8900 \text{ \AA}$ . This wavelength region (in particular the  $8700\text{-}8850 \text{ \AA}$  part) contains a number of relatively strong metallic

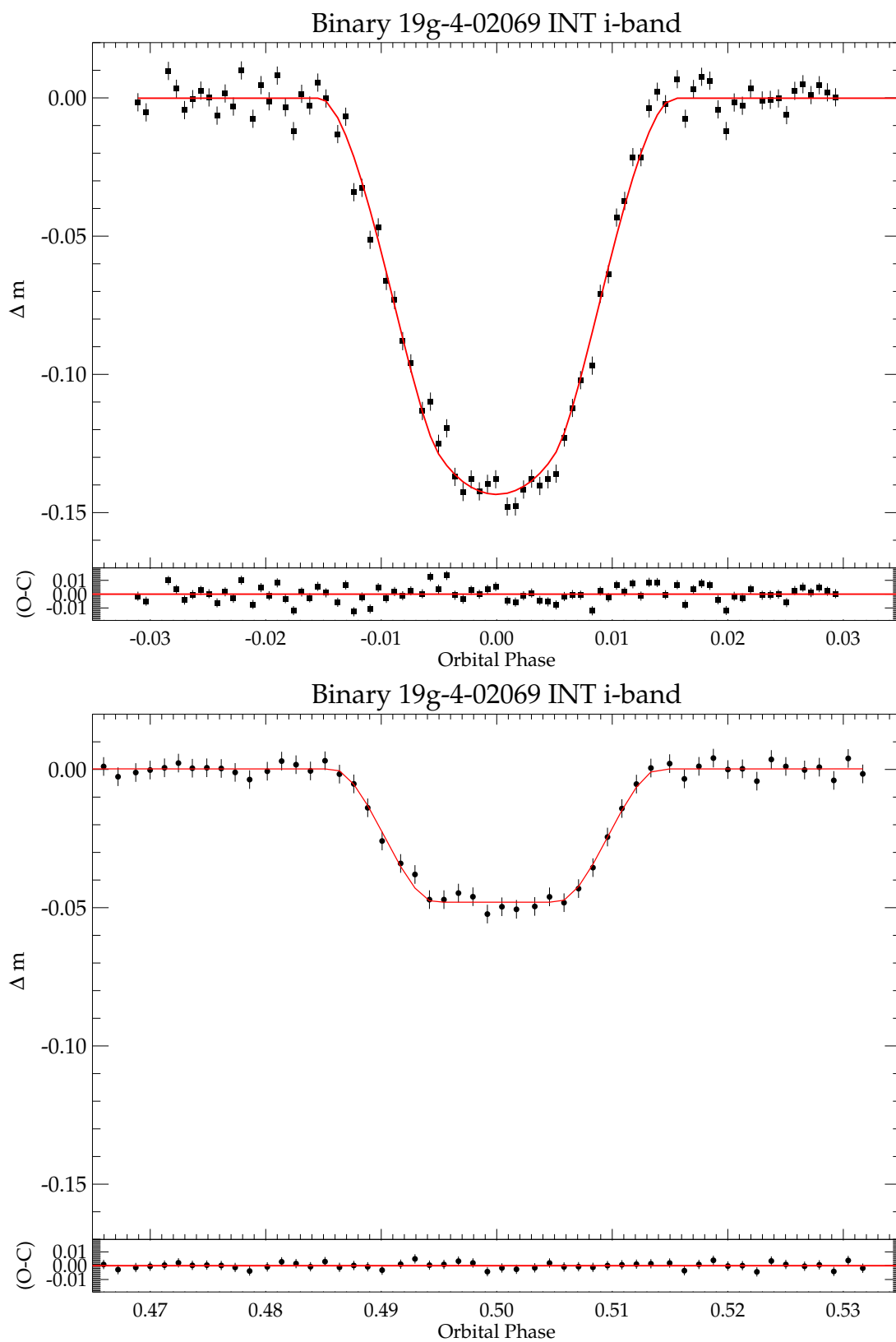


**Figure 5.2** — The follow-up INT *i'*-band light curves of the primary (upper panel) and the secondary eclipse (lower panel) of binary 19g-4-02069. Overplotted in red is the best-fit JKTEBOP model.

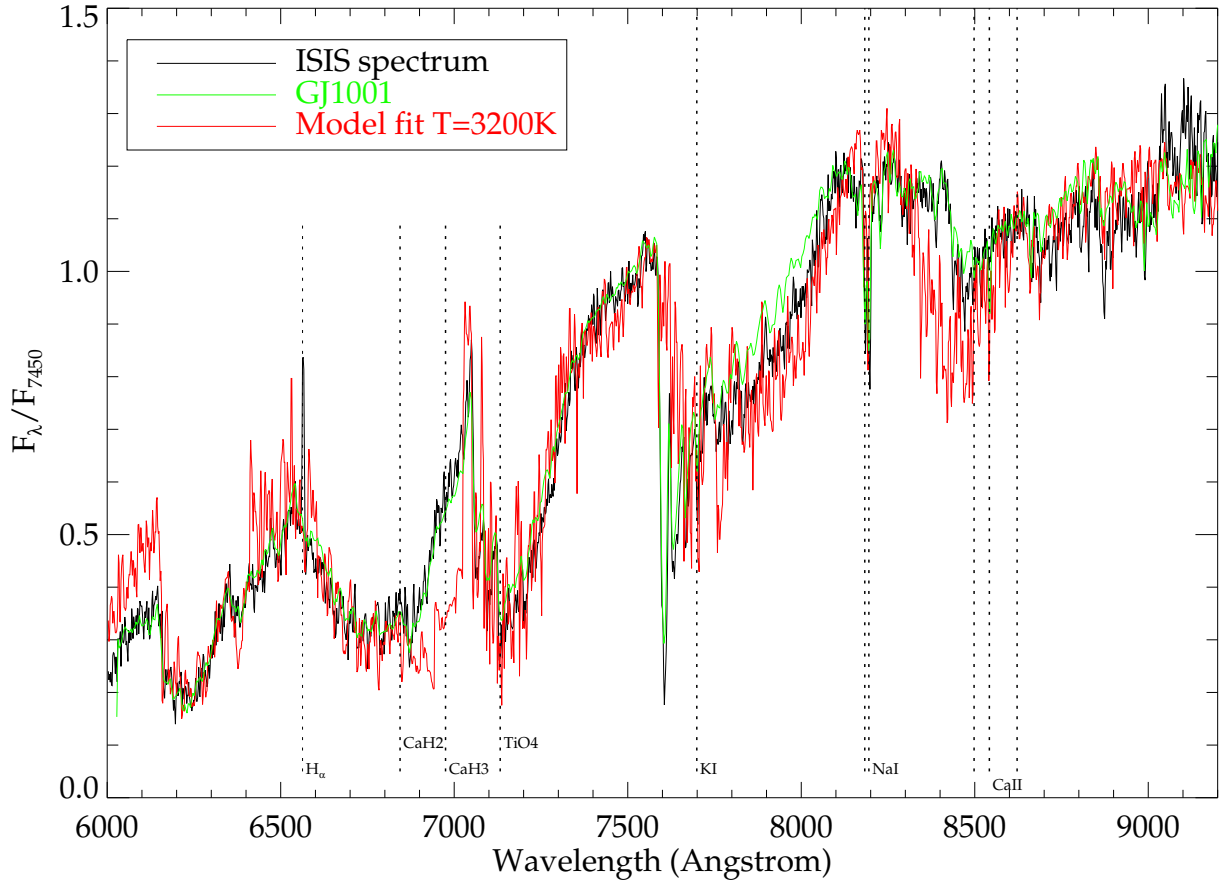


**Figure 5.3** — The observed low-resolution spectrum of binary 19g-4-02069 obtained with the WHT (solid black line), marking the main molecular and atomic features, with the best-fit NextGen model for  $T_{eff}=3200\text{K}$  (solid red line). The solid green line is an observed template spectrum for GJ1001, a single M4 star, archival data from the 6.5m Multiple Mirror Telescope (MMT, see Section 5.3.1). The left most vertical dotted line marks  $H_{\alpha}$  in emission for 19g-4-02069, suggesting active chromospheres.

absorption lines in M-dwarf atmospheres. Using this setup we obtained 5, 60 min ( $3 \times 20\text{min}$ ) exposures on the nights of July 17 and July 18, 2010. Exposures of 90 min ( $3 \times 30\text{ min}$ ) and 85 min ( $1 \times 1200 + 2 \times 1800$ ) were also acquired with the same grating, but centred on the H-alpha emission line ( $6563\text{ \AA}$ ), on the night of July 28, 2010. Data reduction was performed using standard IRAF procedures for instrumental signature removal (the CCDPROC package), with bias subtraction, flat fielding and correction for instrumental response. We then calibrate the observed wavelengths using CuNe+CuAr arc lamp spectra taken after each set of exposures. We flux calibrate the data using observations of a photometric standard. Our spectra have a relatively low signal-to-noise ratio of  $(S/N)=15$ , meaning that because of the low luminosity of the secondary star in the optical, its spectral lines are not detected. We use these observations to further constrain the radial velocity amplitude of the primary component as well as the orbital eccentricity in Sections 5.3 and 5.4.

### 5.2.5 GEMINI/GNIRS infra-red spectroscopy

We conducted observations with the GEMINI Near InfraRed Spectrograph (GNIRS) on the 8.1 m GEMINI-North Telescope, in queue-schedule mode in the H-band, to measure the secondary RVs. We moved observations into the infra-red, because the cooler companion is brighter at these wavelengths by 3-4 magnitudes. We opted to use an intermediate resolution setup, rather than a high resolution setup, to maximise the spectral throughput for the secondary star, which results in a compromise on the velocity resolution. We used the long slit (49") and the long-red camera configuration, in combination with the 110.5 lines/mm grating and a slit-width of 0.3", achieving a spectral resolving power of  $R \sim 5900$ . Our set-up is centred on  $\sim 1.555 \mu\text{m}$ , and has a wavelength range of 1.49-1.61  $\mu\text{m}$ . The corresponding velocity resolution is  $\sim 27.3 \text{ km/s/pixel}$ . In total, we obtained 86, 240 sec. exposures on five separate observing nights between March and July, 2011. Of these 86 exposures, 79 had sufficient signal-to-noise for radial velocity work. All observing runs are centered around the two quadrature points of the binary (phases  $\phi=0.25$  and 0.75), where the relative RVs are expected to be the largest. We observed our binary target using a standard *ABBA* on-source dither pattern, nodding along the slit.

We reduce the data using the GNIRS sub-package (version v1.11.1) of the Gemini IRAF package for spectral reduction and extraction, which is available online<sup>1</sup>, and which was adapted by us for optimal reduction of the current data set. Before running the IRAF script we apply the PYTHON script CLEANIR.PY to the raw data, to correct vertical striping (repetative every 8 columns), horizontal banding, and quadrant offsets, which represents a significant source of additional background noise in  $\sim 70\%$  of the 2-D spectra, the magnitude of which also varies between different data frames. In IRAF, we first correct the data for read out noise, the detector offset (which is measured from a dark area of the data), and non-linear response using NSPREPARE. Using NSREDUCE we then remove the instrumental signature by flatfielding and dark subtraction, followed by sky-subtraction by forming  $A - B$  and  $B - A$  pairs. On each sky-subtracted 2-D image we then measure the dispersion variations using NSSDIST, and rectify the images using NSTRANSFORM. With NSCOMBINE each  $A - B$  is then combined with the corresponding  $B - A$  by shifting the positive spectra on to each other, based on the header information. Because the raw data show frequent spikes from radioactive particle hits, caused by decaying thorium on the lenses used in GNIRS, we median combine all sky-subtracted ( $A - B, B - A$ ) pairs, which removes most of the hits. Our observations (especially the part taken at high airmass) also suffer from highly variable sky-lines from OH sky-glow, which causes line residuals even after sky-subtraction. Optimal 1-D spectral extraction was then performed using NSEXTRACT, which is based on the standard IRAF package APALL. Any remaining particle hits are identified by eye from the 1-D spectrum and clipped before further analysis. A summary of the spectral observations is shown in Table 3.

---

<sup>1</sup> Available at <http://www.gemini.edu/sciops/instruments/gnirs/data-format-and-reduction>

Setup	HJD -2455000	Slit(")	$\lambda_{cen}$ Å	$t_{int}$ (s)	Phase	RV <sub>1</sub> (km/s)	RV <sub>2</sub> (km/s)
ISIS-R158R	394.6889977	1.0	7250	500	0.400	–	–
ISIS-R1200R	395.4546658	1.2	8495	3×1200	0.713	+58.5(±1.6)	–
ISIS-R1200R	395.5849447	1.2	8495	3×1200	0.766	+58.4(±1.6)	–
ISIS-R1200R	395.6961503	1.2	8495	2×1200	0.812	+57.2(±1.8)	–
ISIS-R1200R	396.5676917	0.7	8495	3×1200	0.168	+3.7(±0.8)	–
ISIS-R1200R	396.6905442	1.0	8495	3×1200	0.219	-0.1(±1.0)	–
ISIS-R1200R	406.4130944	1.0	6562	1×1200 +2×1800	0.201	+0.2(±0.4)	–
ISIS-R1200R	406.5803028	1.0	6562	3×1800	0.269	0.5(±0.3)	–
GNIRS	713.9130117	0.3	15500	12×240	0.130	+5.8(±2.1)	–
GNIRS	736.0121099	0.3	15500	12×240	0.185	-1.9(±2.7)	–
GNIRS	711.3303809	0.3	15500	12×240	0.277	+1.8(±3.0)	+135.5(±3.0)
GNIRS	729.9526121	0.3	15500	21×240	0.680	+56.5(±4.0)	-79.6(±4.8)
GNIRS	730.0746367	0.3	15500	17×240	0.730	+60.1(±6.5)	-80.1(±4.2)
GNIRS	652.0859376	0.3	15500	6×240	0.820	+51.5(±3.0)	-68.7(±1.4)

**Table 5.3** — A summary of the spectral observations obtained with WHT ISIS and Gemini GNIRS. For the R1200R ISIS setup, the spectrograph was centered on 8495 Å, and around the H $\alpha$  emission line at central wavelength 6562 Å. The columns RV<sub>1</sub> and RV<sub>2</sub> indicate the radial velocity derived from the primary and secondary line shifts respectively, uncorrected for the systemic velocity of the binary system, but converted to the heliocentric system, as in Figure 5.4.

## 5.3 Spectroscopic analysis

### 5.3.1 Analysis of the low resolution ISIS spectrum

We determine the absorption indices in the red part of the optical spectrum of Sodium (Na<sub>8189</sub>) and Titanium Oxide (TiO<sub>7140</sub>) to constrain the luminosity class, and verify the main-sequence dwarf nature of 19g-4-02069. We follow the procedure as outlined in Figure 11 of Slesnick, Carpenter & Hillenbrand (2006), to distinguish low surface gravity giants from high gravity dwarfs. We find indices Na<sub>8189</sub>  $\sim$ 0.9 and TiO<sub>7140</sub>  $\sim$ 1.9, which are consistent with a main-sequence dwarf of spectral type  $\sim$ M3.5 (which is within the typical 1 $\sigma$  uncertainties of the Reid, Hawley & Gizis 1995 spectral type relation for TiO). We use the metallicity index  $\zeta_{TiO/CaH}$  (described by Reid et al. 1995, Lepine, Rich & Shara 2007 and Dhital et al. 2012), to find that the binary has solar metallicity within the uncertainties. Significant H $\alpha$  emission is seen (we estimate an equivalent width EW<sub>H $\alpha$</sub>  = -6 Å) which is probably caused by the magnetic activity of the binary, related to the chromospheres of the stars. The strong presence of the Na I doublet, the absence of deep infra-red Calcium triplet absorption (8498, 8542 and 8662 Å), and lack of significant lithium absorption (6708 Å), indicates that the primary is likely a mature M-dwarf, and not young and actively accreting nor a brown dwarf (e.g. Rebolo, Martin & Magazzu 1992).

We follow the procedure outlined in Nefs et al. (2012) and Birkby et al. (2012), to determine the system effective temperature, which can be used to derive individual component temperatures  $T_{1,2}$  when combined with the light curve parameters, by  $\chi^2$  fitting of a grid of NextGen atmosphere models (Allard et al. 1997) to the low resolution spectrum. This grid consists of

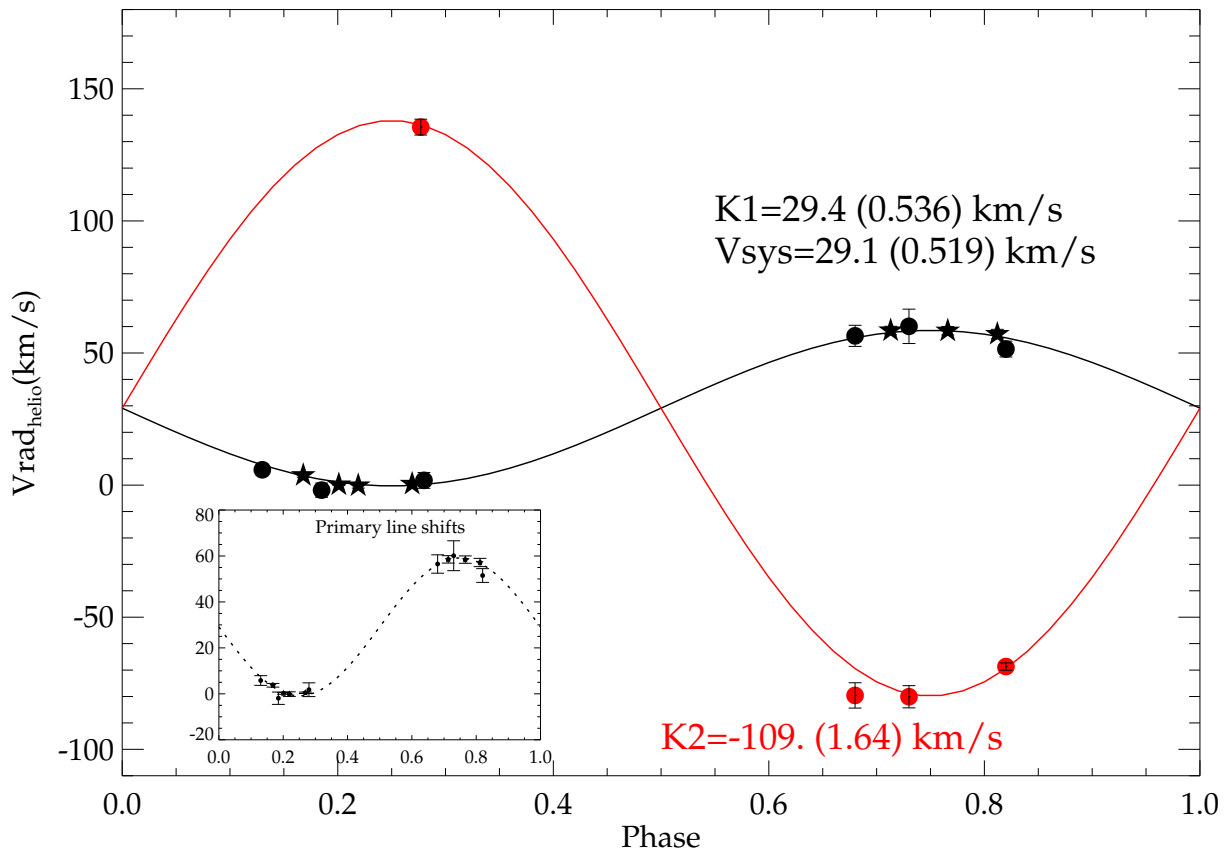


**Figure 5.4** — Radial velocity data for the primary (black filled symbols) and the secondary (red filled dots) stars of M-dwarf binary 19g-4-02069 using GNIRS. Black filled stars are data from WHT ISIS, dots are from GEMINI GNIRS. The black and red solid curves are the best-fit sine functions. We obtain a binary systemic velocity of  $29.1 (\pm 0.519)$  km/s. The data in the figure have been corrected to the heliocentric system.

models with  $\Delta T_{eff} = 100$  K, and assumes constant  $\log(g) = 5$  (typical for field M-dwarfs) and solar metallicity, spanning the  $\sim 6000$ - $9000$  Å region, which corresponds to the data-range least affected by instrumental effects. The model spectra are scaled to match the continuum of the observed spectrum. In the fitting procedure, we mask the strong telluric Oxygen bandhead around  $7600$  Å and the  $H_\alpha$  emission line. We use the formal errors as obtained from IRAF to derive the  $\chi^2$ , which we then optimise to determine the best-fitting model. To derive an error, we scale to  $\chi_{red}^2 = 1$ , yielding a final value of  $140$  K. Our best-fit model indicates  $T_{eff} = 3200$  K, which is consistent with a  $\sim$ M3-4 spectral type, following the  $T_{eff}$ , spectral type relation from Baraffe & Chabrier (1996). Assuming that the primary star dominates the emission of the system in the optical, this spectral type roughly corresponds to that of the hotter component. The spectrum of GJ100 (a  $\sim$ M4 single nearby M-dwarf<sup>2</sup>) is overplotted on Figure 5.3 as a green continuous line. It is a better match to the ISIS data in the spectral regions around  $6900$  Å than the NextGen model.

<sup>2</sup>Available at <http://spider.ipac.caltech.edu/staff/davy/ARCHIVE/index.shtml>

### 5.3.2 Radial velocities

#### WHT/ISIS

We used the IRAF routine FXCOR in conjunction with a grid of template synthetic stellar atmospheres of low-mass stars from the MARCS<sup>3</sup> spectral library (Gustafsson et al. 2008), degraded to match the resolution of the observed data, to obtain radial velocities from the R~9300 ISIS spectra through 1-D cross-correlation. In the cross-correlation procedure, we mask out the saturated near-infra-red Ca II triplet lines at 8498, 8542 and 8662 . The spectral templates had a plane-parallel atmospheric geometry, an  $T_{eff}$  range of 2800-4000 K (in steps of 100 K), solar metallicity,  $\log(g)=5$  and 2.0km/s microturbulence. For the final RVs we use the template model that maximises the strenght of the cross-correlation, which is the cool  $T_{eff}=3200$  K model. For the H $\alpha$  observations we simply fitted single Gaussians to the emission line. The data is listed in Table 3 and plotted in Figure 5.4 as black filled stars. From the primary RVs we can already set reasonable upper and lower limits on the mass ratio of the system, because there is only a limited range of  $(M_1, M_2)$  that can yield the observed  $K_1$ . We find an upper limit, assuming  $M_1 = 0.08M_{\odot}$  (corresponding to the hydrogen burning limit), of  $q < 0.55$ , and a lower limit, assuming an M0-dwarf primary with  $M_1 = 0.65M_{\odot}$ , of  $q > 0.25$ . This already indicates that 19g-4-02069 is in the interesting regime of short period low-mass-ratio M-dwarf binaries.

#### GEMINI/GNIRS

We used the spectral region 1.55-1.6 $\mu$ m, which is the least contaminated by telluric water vapor absorption, to extract RVs from the GNIRS data. With the IDL procedure *c\_crosscorrelate*, and a  $T_{eff}=3200$ K MARCS model as RV template, we obtained a cross-correlation function (CCF) for each spectrum, which were subsequently fit by a Lorentzian. To improve the contrast of the CCF, we first divide the spectrum by a second order polynomial. We report the detection of a clear secondary component in the CCF around the  $\phi = 0.75$  quadrature point, shifted by  $\sim 4.5$  spectral pixels. We show the CCF of the total added spectral data around  $\phi = 0.75$  in Figure 5.5 (black curve). The blue and red solid curves indicate best-fitting single Lorentzian profiles to the cross-correlation peaks of the secondary and primary binary components respectively. The data around the 0.25 quadrature suffers from higher noise due to highly variable sky and detector pattern noise, making it difficult to resolve the secondary lines. Only the datapoint at phase 0.28 has sufficient quality for radial velocity work on the secondary.

We fit the RVs as function of binary orbital phase  $\phi$  with a simple sine curve using IDL's MPFITFUN function, assuming a circular orbit. We first fit the primary RVs from ISIS and GNIRS, allowing only  $K_1$  and  $\gamma$  (the systemic velocity of the binary) to vary, fixing the phase using the well-determined orbital period from the light curve. For the secondary star we fix  $\gamma$  to the value derived from the primary and fit for  $K_2$ . To derive the RV errors we scale the errors from the Lorentzian/Gaussian CCF fit, such that the reduced  $\chi^2$  of the best-fitting RV model is unity. We show our results in Figure 5.4, where the black solid curve indicates the best-fitting sine function to the primary RVs, and the red solid curve the fit to the secondary RVs. We find radial velocity amplitudes of  $K_1=29.4(\pm 0.536)$  km/s and  $K_2=109.0(\pm 1.64)$  km/s, for a systemic velocity  $\gamma=29.1(\pm 0.519)$  km/s, indicating a binary mass-ratio  $q=0.27(\pm 0.015)$ .

<sup>3</sup>Available at <http://marcs.astro.uu.se/>

Parameter	i-band	J-band	J-band (spot-corrected)
<b>Lightcurve analysis</b>			
P (days)	2.44177678 ( $\pm 0.00003$ )		
$T_0$ (MJD)	2454319.8327011 ( $\pm 0.00002$ )		
$(R_1 + R_2)/a$	0.10284( $\pm 0.00182$ )	0.10365( $\pm 0.00195$ )	0.09837( $\pm 0.00355$ )
$R_2/R_1$	0.33768( $\pm 0.00327$ )	0.34272( $\pm 0.00289$ )	0.33897( $\pm 0.00462$ )
$J$	0.40002( $\pm 0.01178$ )	0.64637( $\pm 0.01223$ )	0.63662( $\pm 0.02077$ )
$i(^{\circ})$	87.74875( $\pm 0.14625$ )	87.73833( $\pm 0.15028$ )	88.23382( $\pm 0.33917$ )
$R_1/a$	0.076883( $\pm 0.00137$ )	0.07719( $\pm 0.00146$ )	0.07347( $\pm 0.00266$ )
$R_2/a$	0.02596( $\pm 0.00137$ )	0.02646( $\pm 0.00146$ )	0.02490( $\pm 0.00266$ )
$L_2/L_1$	0.04199( $\pm 0.0041$ )	0.07444( $\pm 0.0044$ )	0.07173( $\pm 0.0073$ )
$T_2/T_1$	0.77899( $\pm 0.0083$ )	0.89224( $\pm 0.0072$ )	0.88889( $\pm 0.0123$ )
$\chi_{red}^2$	1.093	4.057	1.004
<b>Estimated temperatures</b>			
$T_{eff}(K)$	3200( $\pm 140$ )		
$T_1(K)$	3300( $\pm 140$ )		
$T_2(K)$	2950( $\pm 140$ )		
<b>Radial velocity analysis</b>			
$K_1$ (km/s)	29.4( $\pm 0.536$ )		
$K_2$ (km/s)	109.0( $\pm 1.64$ )		
$\gamma$ (km/s)	29.1( $\pm 0.519$ )		
$q$	0.270( $\pm 0.0151$ )		
$a(R_{\odot})$	6.687( $\pm 0.183$ )		
<b>Derived masses and radii</b> <b>ADOPTED</b>			
$M_1 (M_{\odot})$	<b>0.5294(<math>\pm 0.0209</math>)</b>	0.5294( $\pm 0.0209$ )	0.5289( $\pm 0.0209$ )
$R_1 (R_{\odot})$	<b>0.5141(<math>\pm 0.0106</math>)</b>	0.5162( $\pm 0.0111$ )	0.4911( $\pm 0.0185$ )
$M_2 (M_{\odot})$	<b>0.1428(<math>\pm 0.0056</math>)</b>	0.1428( $\pm 0.0056$ )	0.1427( $\pm 0.0056$ )
$R_2 (R_{\odot})$	<b>0.1736(<math>\pm 0.0056</math>)</b>	0.1769( $\pm 0.0058$ )	0.1665( $\pm 0.0092$ )

**Table 5.4** — Best-fit parameters and derived quantities for the M-dwarf binary system 19g-4-02069. Note that we adopted the masses and radii derived from the INT i-band light curve parameters (see the discussion in Section 5.4.3).

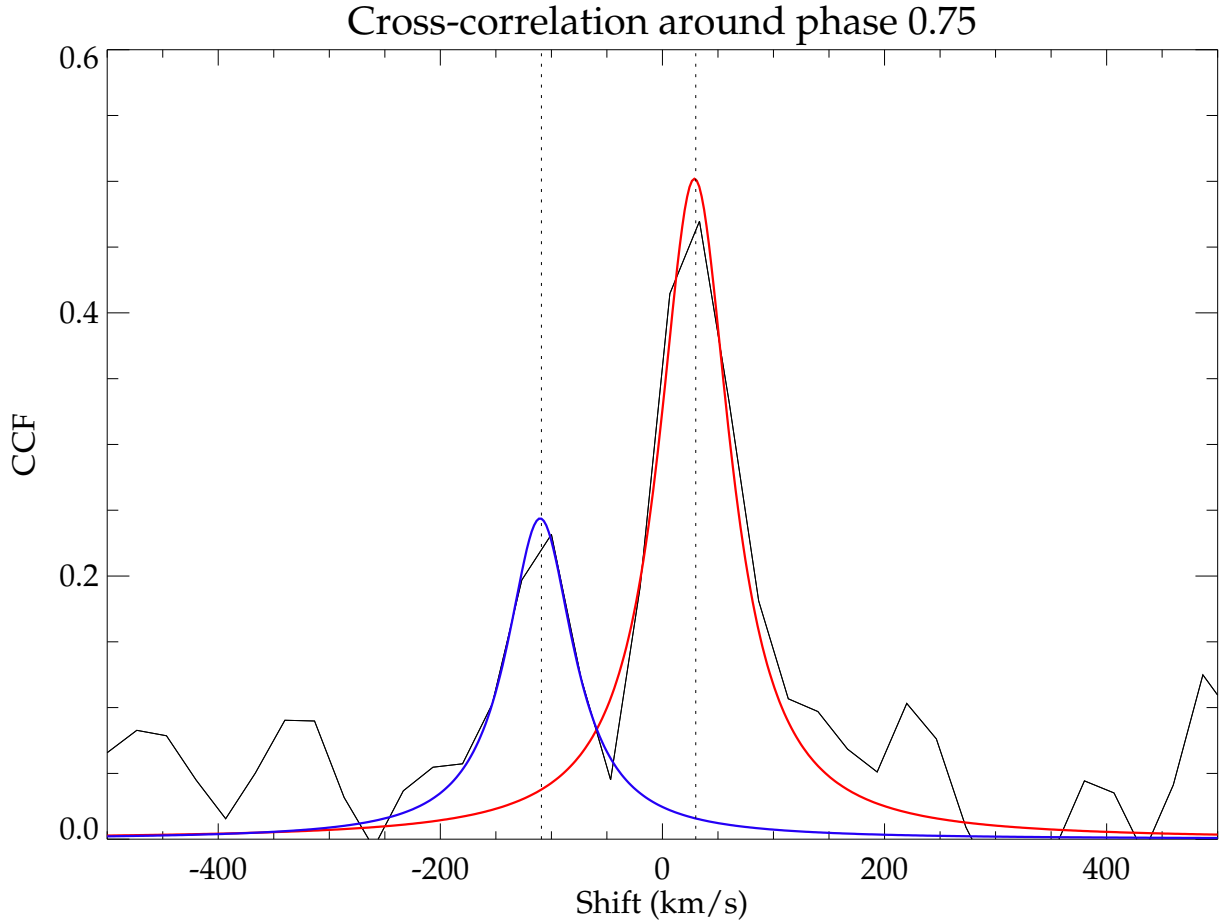


**Figure 5.5** — The cross-correlation function for the summed spectral data around the 0.75 quadrature point using a template spectrum with  $T_{eff}=3200\text{K}$ , corrected for the Solar motion and the systemic velocity of the binary. The red and the blue solid curves indicate the best-fit single Lorentzian profiles for the primary and secondary lines.

## 5.4 Lightcurve modelling

### 5.4.1 WFCAM J-band photometry

#### Spot correction

There is significant out-of-eclipse scatter in the J-band light curve ( $\sim 2\%$  peak-to-peak), which is not in phase with the binary orbit. To investigate the possible periodicity of this variation, we clip the primary and secondary eclipses from the light curve, and perform a frequency analysis using the IDL implementation `FASPER.PRO` of the Lomb-Scargle periodogram (Lomb 1976; Scargle 1982). The upper panel of Figure 5.6 shows this frequency spectrum for binary 19g-4-02069. Using the IDL routine, we determine a false-alarm probability (FAP) to filter out peaks that are likely caused by spurious detections on light curve systematics (horizontal dashed line). Significant power is apparent around  $\sim 2.44$  d binary period, yet the actual peak is  $\sim 0.14$  d away at  $\sim 2.56$  d. We indicate various integer and half-integer aliases of the binary orbital period in Figure 5.6 using vertical dotted lines. From previous binary studies, similar deviations are

seen in systems that are either young and not fully synchronised (e.g. the pre-main sequence eclipsing binary Paranal 1802; Cargile et al. 2008) or not fully circularised due to their relatively long orbital period (e.g. Irwin et al. 2011). We discuss possible causes for this apparent discrepancy in Section 5.5.

When folded onto the non-synchronous 2.56 d period determined from the Lomb-Scargle analysis, we find a clear nearly-sinusoidal modulation of the data, which we attribute to star spots on a rotating stellar surface. We also performed an independent check of these results using the IDL implementation EPFOLD of the Analysis of Variance (AoV; Schwarzenberg-Czerny 1989) algorithm and plot the results in the lower panel of Figure 5.6. We confirm a best-fit period which is very close to the  $\sim 2.563$  d period suggested by the Lomb-Scargle algorithm. No significant signal is obtained at the orbital period. The second highest peak in the lower panel is at  $\sim 2.432$  d, but at relatively low significance. In Figure 5.7 we show the clipped light curve folded on the best-fit periodicity for spot modulation. We attempt to correct the J-band light curve using a single sine with 8.1 mmag amplitude, which appears to minimise the out-of-eclipse rms. In the upper panel of Figure 5.1 we show the phase-folded but uncorrected light curve (black filled dots), while in the lower panel we show the J-band data, corrected for the  $\sim 8.1$  mmag rotation signal. We do not claim that this method is the best method for removing rotational signal from a lightcurve, because if spots are occulted during the eclipse the light variation may strongly deviate from the sinusoid. However, we find that with our correction the out-of-eclipse rms decreases from  $\sim 10.6$  to 9.1 mmag ( $\sim 15\%$  reduction), and in eclipse it decreases from  $\sim 11.2$  to 8.9 mmag ( $\sim 20\%$  reduction). This means that the rms in and out of eclipse are approximately the same after the correction (in fact the difference between the rms values in and out of eclipse decreases from  $\sim 5\%$  to  $\sim 2\%$  after correction), indicating that our correction likely does not introduce large systematics. Zoom-ins around the eclipses of the corrected and uncorrected data are shown in Figure 5.11 of the Appendix.

#### JKTEBOP PARAMETERS

We used the binary light curve modelling program JKTEBOP<sup>4</sup> (Southworth et al. 2004), which is based on the Eclipsing Binaries Orbit Program (EBOP; Popper & Etzel 1981; Etzel 1981) for the fitting of the uncorrected and corrected J-band data. For binary 19g-4-02069, with orbital period 2.44 d and mass ratio 0.27, Equation 6 of Morris (1985) predicts ellipsoidal light variations of just  $\sim 0.4$  mmag in the J-band, indicating that the binary stars are likely only very slightly deformed by mutual tidal interactions. This, together with the low derived values of the stellar oblateness in our subsequent fitting with JKTEBOP, justifies the application of this model (which is only suitable for detached systems) to the 19g-4-02069 binary system (see also Popper & Etzel 1981).

For the light curve modelling we allowed the following six parameters to vary: i) the binary orbital period  $P_0$ , ii) the mid-eclipse epoch  $T_0$  of the primary eclipse, iii) the sum of the stellar radii in units of the binary semi-major axis,  $(R_1 + R_2)/a$ , iv) the ratio of the radii  $k = R_2/R_1$ , v) the orbital inclination  $i$  and vi) the ratio of central surface brightness  $J = J_2/J_1$ , which in the infra-red is approximately proportional to the ratio of eclipse depths. We used as input the initial estimate of the binary ephemeris obtained from the automated OCCFIT BLS algorithm.

<sup>4</sup>Available at <http://www.astro.keele.ac.uk/jkt/>

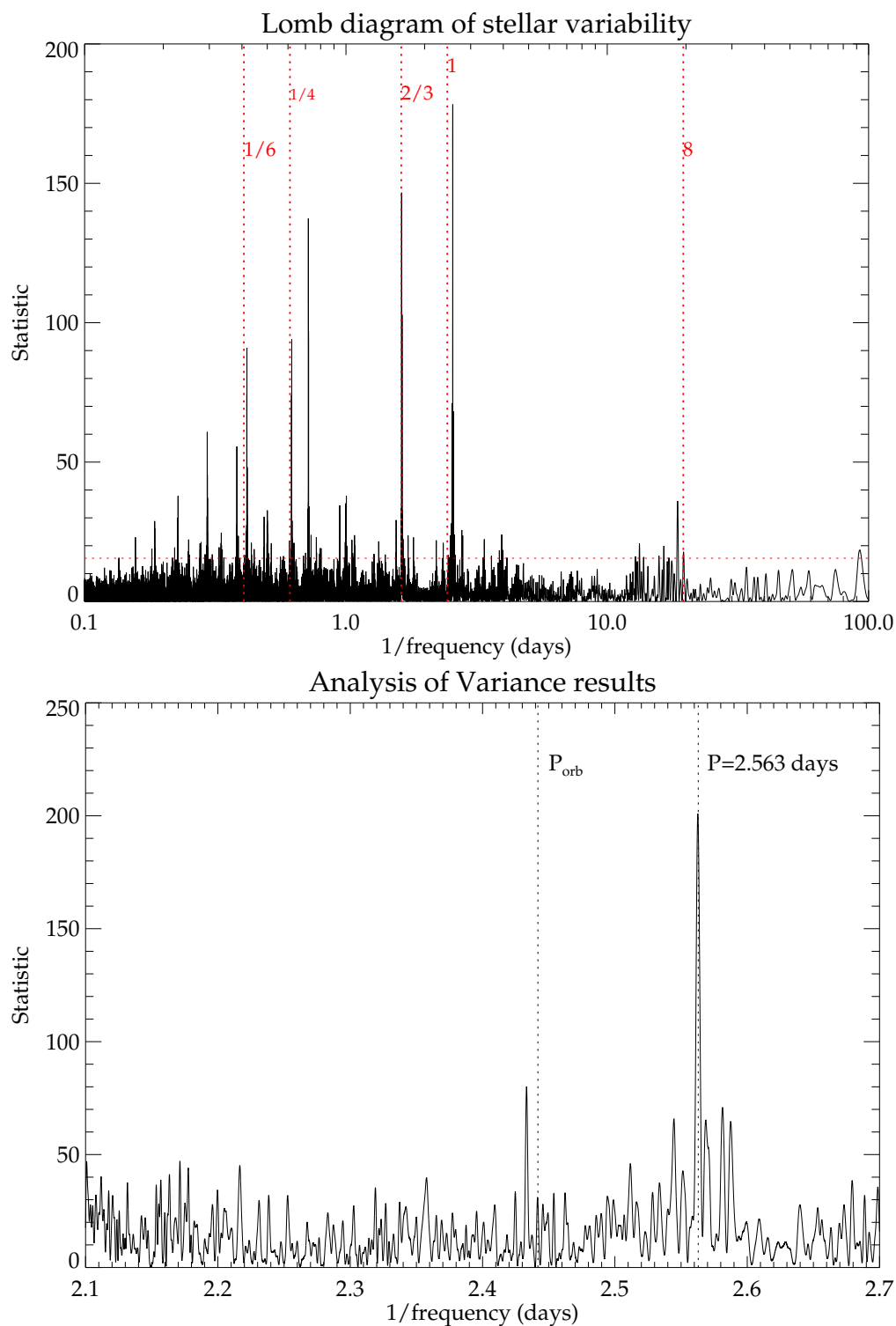


**Figure 5.6** — Upper panel: Lomb-Scargle diagram of the dominant frequencies in the WFCAM J-band light curve after removing the eclipses. A significant peak is at  $\sim 2.563$  days. We indicate several period aliases with the red dashed lines. The red horizontal line indicates the 99% confidence level for peak rejection. Lower panel: Analysis of Variance results for binary 19g-4-02069. We show the frequency spectrum between 2.1 and 2.7 d and note that we confirm a strong signal at the period determined by the Lomb-Scargle method, and no significant signal at the orbital period  $P_{orb} \sim 2.44$  d. The second most significant peak is at  $\sim 2.432$  d, but with low significance.

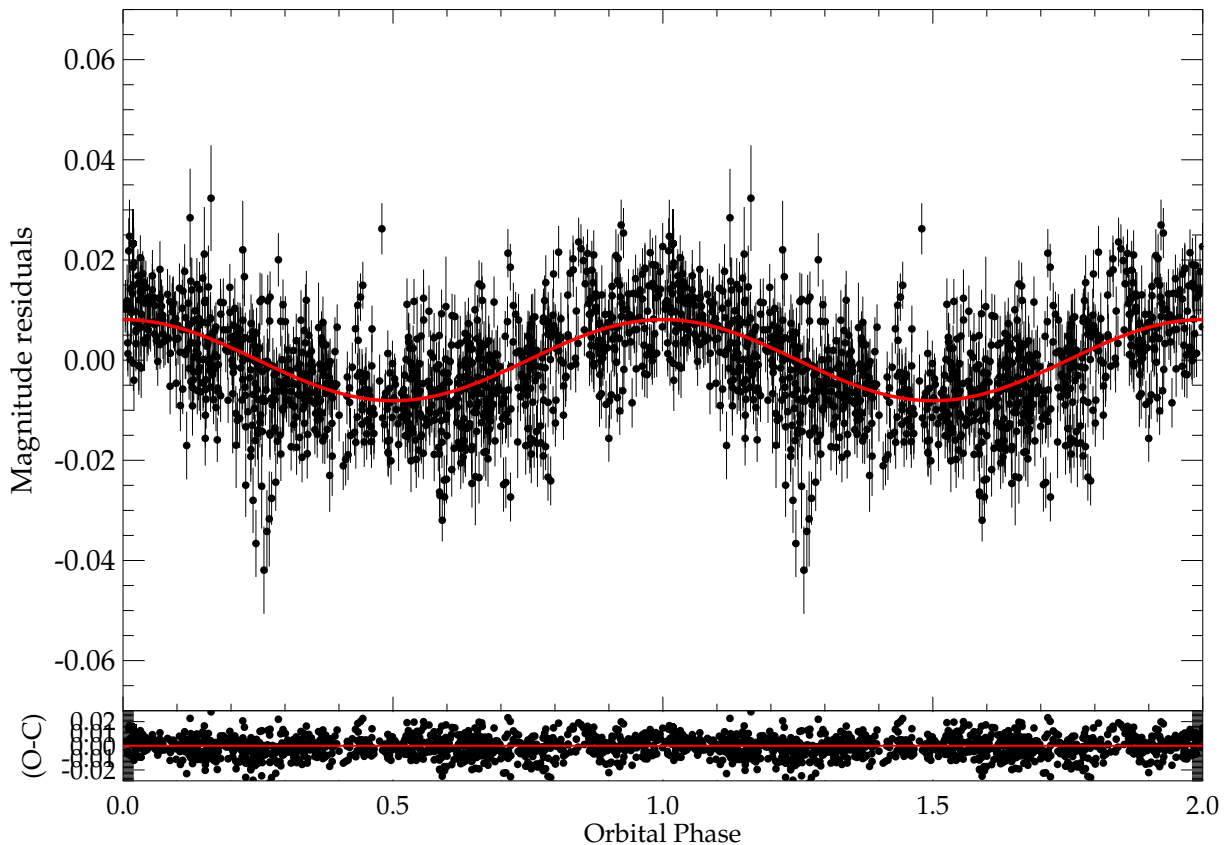


**Figure 5.7** — The clipped WFCAM J-band light curve folded on the  $\sim 2.563$  day frequency peak. A significant rotational modulation can be seen. The solid red curve is the best fit sinusoid to the data with amplitude  $\sim 8.1$  mmag.

We kept the mass-ratio of the system,  $q$ , fixed at the value determined by the spectroscopic analysis. We did not fit the reflection coefficients, but calculated them from the system geometry. We also assumed a gravity darkening coefficient, which was fixed at a value typical for stars with convective envelopes ( $\beta=0.32$ ; Lucy 1967). We found that treating additional third light as an extra fitting parameter did not significantly improve the quality of our fit, so we fixed it to zero. We adopted linear limb-darkening coefficients from Claret et al. (2000) in the J-band (see Table 5.5), which were calculated from PHOENIX model atmospheres (Allard et al. 1997), for a surface gravity  $\log(g) = 5$ , solar metallicity and 2 km/s micro-turbulence and stellar effective temperatures  $T_{1,2}$ , such as derived in Section 5.4.2. We did not fit for the limb-darkening coefficients, because the S/N is too poor, and kept  $T_{1,2}$  (see Section 5.4.2) fixed. The orbital eccentricity  $e$  and the argument of periape  $\omega$  were also kept fixed, because our initial runs indicated that the data were firmly consistent with a circular binary orbit ( $|e \cdot \cos(\omega)| < 0.000079$ ). This is expected from tidal dissipation theory given the relatively short circularisation timescale  $\sim 200$  Myr (Zahn 1977).

To assess the  $1\sigma$  parameter uncertainties we used the Monte Carlo routine from JKTEBOP (Southworth et al. 2005). In this procedure, Gaussian random noise is repeatedly (10000 times) added to the model light curve before a new fit is made to the data, which yields a distribution for each parameter. With JKTEBOP we also performed a prayer-bead error analysis, which

		<i>i</i> -band	J-band
Linear	Primary	0.69	0.41
	Secondary	0.78	0.46
Quadr.	Primary	[0.22;0.58]	
	Secondary	[0.37;0.49]	

**Table 5.5** — Limb-darkening coefficients used as input to the EBOP models for the WFCAM J-band and the INT *i*-band light curves. For the optical red data we indicate both linear and quadratic coefficients.

can be useful in the presence of correlated noise (Southworth 2008), and found that parameter values derived from both methods were consistent within the  $1\sigma$  uncertainties, and that the uncertainties were not significantly different from the prayer-bead analysis. We therefore adopted the MCMC method from hereon. Numerical results of the light curve fitting are given in Table 4.

The derived parameters for the uncorrected and the spot-corrected data are inconsistent within the quoted  $1\sigma$  uncertainties,  $(R_1 + R_2)/a$ ,  $R_2/R_1$ , and  $J$  are smaller after correction, whereas  $i$  is higher. In Figure 5.11 of the Appendix it is apparent that the correction removes outlying data points in eclipse, which bias the measured depths of the eclipses and the duration of ingress/egress. Note that the errors of the corrected light curve data points are scaled to obtain  $X_{red}^2=1$ . The derived ratio of radii ( $R_2/R_1=0.339\pm0.005$ ) in the corrected data indicates that the companion is significantly smaller than the primary. An impact parameter  $b = (a/R_1) * \cos(i)=0.43$  suggests that the eclipses are full and the system is non-grazing, which lifts the degeneracy between  $R_2/R_1$  and  $i$ . The ratio of secondary to primary luminosity is  $L_2/L_1=0.072(\pm0.0073)$ , which indicates that only  $\sim 7\%$  of the system light in the infra-red is due to the secondary star. From  $L_2/L_1$  and  $R_2/R_1$  we derive, using Stefan-Boltzmann’s law, a wavelength specific temperature ratio  $T_2/T_1=0.89(\pm0.012)$ . Assuming that all of the light in the system comes from the primary, and the stars radiate as blackbodies, this indicates  $T_2 \sim 2850\text{K}$  for the secondary, which would be consistent with a M5 type star according to the  $T_{eff}$ -spectral type relation presented in Stephens et al. (2009), M5 according to the 1 Gyr model from Baraffe & Chabrier (1996), and M6 according to Reyle et al. (2011).

## 5.4.2 INT *i*’-band photometry

The lack of out-of-eclipse baseline for the optical data means that we can not accurately determine the amplitude of any spot modulation, so we opted to fit the light curve without making any spot corrections. The INT eclipses have a flat bottom, which confirms that the secondary star is fully superimposed on the primary during eclipse. To model with JKTEBOP, we adopted the linear coefficients from Claret et al. (2004) for the Sloan *i*’-band. The derived parameters  $(R_1 + R_2)/a$  and  $R_2/R_1$  are consistent with the spot-corrected infra-red results, within the quoted  $1\sigma$  uncertainties of the J-band data. The orbital inclination  $i$  is slightly lower in the optical, but only by  $\sim 1.4\sigma$ . The optical data reveal a surface brightness ratio  $J=0.400(\pm0.012)$  and a wavelength specific luminosity ratio  $L_2/L_1=0.044(\pm0.004)$ . This result shows that the secondary is significantly dimmer at optical wavelengths. Also, a ratio  $T_2/T_1=0.779(\pm0.008)$  is derived in the optical ( $\sim 11\%$  lower than in the infra-red), not surprising since the stars are not perfect blackbody radiators. To derive component temperatures  $T_{1,2}$  we used MARCS model

spectra to derive model surface brightness ratios  $J_\lambda$ , which were compared to the optical and infra-red observations. We reproduced the observations, within the estimated  $1\sigma$  uncertainties, for  $T_1=3300\text{K}$  and  $T_2=2950\text{K}$ . We adopt these values of  $T_1$  and  $T_2$  in our subsequent discussion.

### 5.4.3 Stellar Masses and Radii

We derived the component masses and radii from the combined RV analysis (incorporating both the ISIS and the GNIRS measurements), the i-band light curve fitting parameters, and Keplers law according to the following two equations (see e.g. Hilditch 2001):

$$M_1 = \frac{K_2 P (K_1 + K_2)^2}{2\pi G \sin(i)^3} \quad (5.1)$$

$$R_1 = x_1 a = x_1 \left[ \frac{P^2 G M_1 (1 + K_1/K_2)}{4\pi^2} \right]^{1/3}, \quad (5.2)$$

where  $x_1$  denotes the best-fit scaled binary orbital separation,  $R_1/a$ , from JKTEBOP. We propagate the errors from the light curve and radial velocity analysis. The main motivation for using the i-band results is that for the infra-red data, many spot cycles are folded into the light curve, and although our single sine correction removes part of the scatter, tracing the stellar activity cycle over such a long observational baseline ( $\sim 5$  years) is difficult because the spot configuration may have evolved significantly. Moreover, the J-band data has significant gaps and generally only few observations per night, making it difficult to accurately model the precise behaviour of the spots. Because the optical data for the primary and the secondary event have been obtained within 6 d of observations, they likely trace the same spot configuration. Moreover, both the photometric quality and the number of in-transit datapoints of the optical data can rival the J-band photometry. One problem in the current work is the limited coverage of the parts out of eclipse. Work by Goulding et al. (2012) shows that the light curve amplitude of a spot in the J-band is generally 55% of that in the I-band, indicating that  $\sim 3\%$  peak-to-peak variations would be expected for INT observations of the full binary orbit. This could introduce an additional error to our light curve fitting results. Future work should address this issue by obtaining multiband photometric observations of concurrent binary eclipses and sufficient baseline, to catch a single spot cycle. With  $x_1=0.0768$ ,  $K_1=29.4\text{km/s}$ , and  $K_2=109.0\text{ km/s}$ , we find radii of  $R_1=0.5141(\pm 0.0106)R_\odot$ ,  $R_2=0.1736(\pm 0.0056)R_\odot$ , and masses  $M_1=0.5294(\pm 0.0209)M_\odot$ ,  $M_2=0.1428(\pm 0.0056)M_\odot$ . This translates to 2.1-3.2% errors on the radii and  $\sim 4\%$  errors on the masses, although we caution that these errors do not include possible uncertainties from star spots. Note that these masses and radii are consistent with main-sequence model predictions (see Section 5.5.2), rather than pre-main sequence, providing further support for the mature nature of the system.

## 5.5 Discussion

In this paper we have presented the discovery of a highly unequal-mass eclipsing M-dwarf stellar binary, using the high-precision infra-red light curves of the WFCAM Transit Survey,

and follow-up characterisation with optical photometry and optical and IR spectroscopy on 2.5-8 m class telescopes. With two components straddling the fully convective boundary, and with shared ages and metallicities, our binary provides a rare and more stringent comparison to model atmosphere predictions of fundamental M-dwarf properties over a wide span of stellar masses. The cool M5V secondary of the binary is in an important mass-regime for studies of Earth-like exoplanets. In this section we will discuss our binary in the context of current theories for low-mass binary formation, which predict such close unequal systems to be rare.

### 5.5.1 The mass-ratio distribution

The distributions of binary orbital separation and mass-ratio, as function of primary mass, provide important constraints on star formation simulations (e.g. Burgasser et al. 2007, Bate et al. 2012, Clarke 2012). These simulations suggest that accreting gas with high angular momentum and dynamical interactions tend to drive up the mass-ratio of close binary systems towards unity. Dynamical interactions are frequent in the binary birth environment, and interactions with more massive stars will generally bias binary primaries towards higher masses. This indicates that it is unlikely that close, unequal binary systems with low-mass primaries can be maintained for very long. For example, a  $0.5+0.1M_{\odot}$  M-dwarf binary that is formed in a cluster with stellar density  $n_* \sim 2000\text{pc}^{-3}$  has a life-expectancy against disruption from solar type stars of order  $\sim 10$  Myr (Goodwin & Withworth 2007). Furthermore, low-mass binary systems and unequal-mass systems are more easily perturbed due to their lower binding energy.

In Figure 5.8 we show the mass-ratio distribution of close binary systems ( $P_{orb} < 10$  d) with M-dwarf primaries. This figure was compiled from Table 6, which holds the currently available sample of M-dwarfs discovered as eclipsing and non-eclipsing, double-lined, spectroscopic binaries. This is an updated version of Figure 9 in Wisniewski et al. (2012), who included only a few M-dwarf systems in the eclipsing binary period range. The left panel of our Figure 5.8 shows mass-ratio as function of binary orbital period for 55 sources, of which 20 are spectroscopic binaries, whereas the right panel shows a histogram of the mass-ratio distribution in bins of 0.05. We separate the M-dwarfs depending on whether their primaries are more or less massive than the fully convective boundary at  $\sim 0.35M_{\odot}$  (black and red filled squares). With a mass-ratio of 0.27, it is clear that 19g-4-02069 occupies an interesting position in these diagrams, because over 80% of the stellar binaries have  $q > 0.8$ . There may be an observational bias towards more equal-mass binaries because of the steep relation of mass and luminosity for M-dwarfs, causing the spectral lines of low-luminosity companions to remain unresolved. Three binaries are observed in the range  $q=[0.4-0.5]$ , but none at lower  $q$ . Of these three, two are very short-period ( $\sim 0.4$  d) and young, 20 Myr T-Tauri stars (NSVS-06507557; Cakirh & Ibanoglu 2010) and 150 Myr young cluster members (2MASSJ04463285; Hebb et al. 2006). Theory shows that significant dynamical processing can occur prior to the main-sequence, indicating that low mass-ratio systems should be more abundant while young. For example, a significant difference in the binary fraction between young clusters and field solar type stars has been observed (e.g. Duchene et al. 2007).

A possible explanation for the existence of 19g-4-02069 is that the physics of gas accretion onto (close) binary systems is different than suggested by smoothed particle hydrodynamic (SPH) and ballistic particle simulations (from e.g. Artymowicz 1983; Bate & Bonnell 1997; Bate 2002). Two-dimensional warm grid-based simulations from Ochi et al. (2005) and de

Val-Borro et al. (2011) confirm that gas preferentially enters the secondary Roche lobe, but flows around the secondary and is then channeled onto the primary star, which grows a more massive accretion disk, which means that  $q$  can decrease during the accretion phase. Very recent numerical work from Zhao & Li (2012) suggests that adding magnetic fields to binary formation simulations can have a similar effect. Such a magnetic field could apply a brake on the material that flows onto the binary, decreasing its angular momentum and significantly shrinking the protobinary separation, meaning that  $q$  could be low for short binary orbits. If these simulations are correct, low- $q$  pairs are expected to be abundant around a wide range of primary masses on the main-sequence, which would be consistent with our observations of 19g-4-02069. However, disrupting third-body interactions can still remove low- $q$  components from binaries. Another explanation for the low mass-ratio of 19g-4-02069 could be that the binary was isolated from the birth environment early on, for example through ejection from the cloud due to binary-single star or binary-binary interactions, or because the natal cluster became unbound due to rapid gas removal.

### 5.5.2 The mass-radius relation for M-dwarfs

Highly unequal-mass M-dwarf binaries provide important test cases of low-mass stellar evolution theory because they cover a large range of M-dwarf masses, which encompass significant changes in stellar atmospheric structure. Furthermore, since the binary components have the same age and metallicity, stellar evolution models can be tested using two less free parameters. Also, Earth-like planets in the habitable zones around late-type M-dwarfs are prime targets for new transit surveys and ELTs, and require accurate calibration of their small host stars. For example, for the Neptune-sized planet orbiting the M5V host star GJ1214b (Charbonneau et al. 2009, de Mooij et al. 2012), a 15% uncertainty in stellar radius could translate to the difference between an ocean planet and a gaseous H- or He-type atmosphere.

Theory predicts that stars in the fully convective mass regime ( $<0.35M_{\odot}$ ) respond differently to rapid rotation and strong magnetic fields (which can reduce convective efficiency) than their partially-convective cousins (e.g. Chabrier et al. 2007). Most importantly, because in fully convective atmospheres heat flow is nearly adiabatic, model stellar radii and temperatures are expected to better match the observations. It has been argued that strong magnetic fields can shift the fully convective mass boundary to masses as low as  $0.1M_{\odot}$  (Mullan & MacDonald 2001). Such predictions can be tested with a sample of mass-radius-temperature measurements. However, in the stellar-mass regime  $<0.2M_{\odot}$  there is a lack of model-independent data.

In Figures 5.9 and 5.10 we present the current sample of mass-radius-temperature measurements for M-dwarfs. In these figures, filled black and red dots indicate dynamically derived model-independent masses and radii for the primaries and secondaries of eclipsing double-lined M+M-dwarf binary systems. Green triangles represent measurements of M-dwarfs in other kinds of systems. In the inset of Figure 5.9 we show the available measurements in the regime  $<0.2M_{\odot}$ , further detailing their origin. There is significant scatter in these data. Four of the data-points are from M-dwarfs orbiting F- or G-type stars, i.e. single line systems, and rely on model-dependent constraints on the properties of the primary and/or assume spin-orbit alignment (Pont et al. 2005, 2006; Beatty 2007). Three of the M-dwarf systems have either a white dwarf primary, which may have had a phase of common envelope evolution or significant mass-transfer and are likely to be tidally interacting, or B-type subdwarf (Parsons et al.

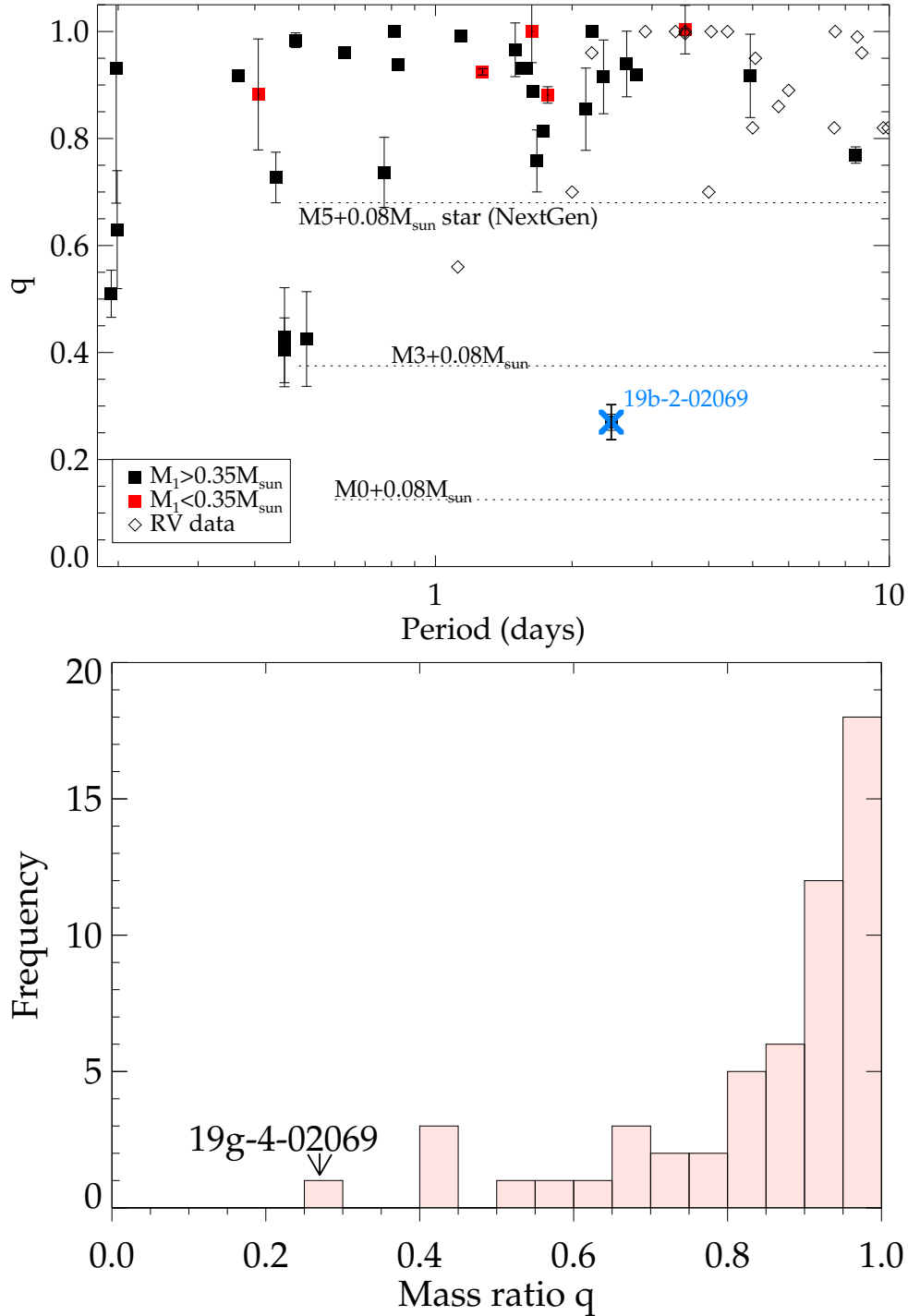


**Figure 5.8** — The mass-ratio distribution of short period ( $P < 10$  d) M-dwarfs reported in literature. **Upper panel:** binary orbital period (in d) versus mass-ratio. Black filled squares indicate eclipsing M-dwarf binaries with  $M_1 > 0.35M_{\odot}$ , red squares indicate eclipsing binaries with  $M_1 < 0.35M_{\odot}$ , whereas open diamonds show M-dwarf binaries reported in radial velocity surveys. The large blue cross is our measured mass-ratio for M-dwarf binary 19g-4-02069. The three black dashed lines show the respective mass-ratios for M-dwarf binary systems with a secondary at the hydrogen burning limit, assuming primaries of  $0.6M_{\odot}$  (M0 spectral type; Baraffe & Chabrier 1996),  $0.2M_{\odot}$  (M3), and  $0.11M_{\odot}$  (M5). These lines indicate the lower limits in  $q$  to which M-dwarf primaries with stellar secondaries are confined. **Lower panel:** histogram of mass-ratio.

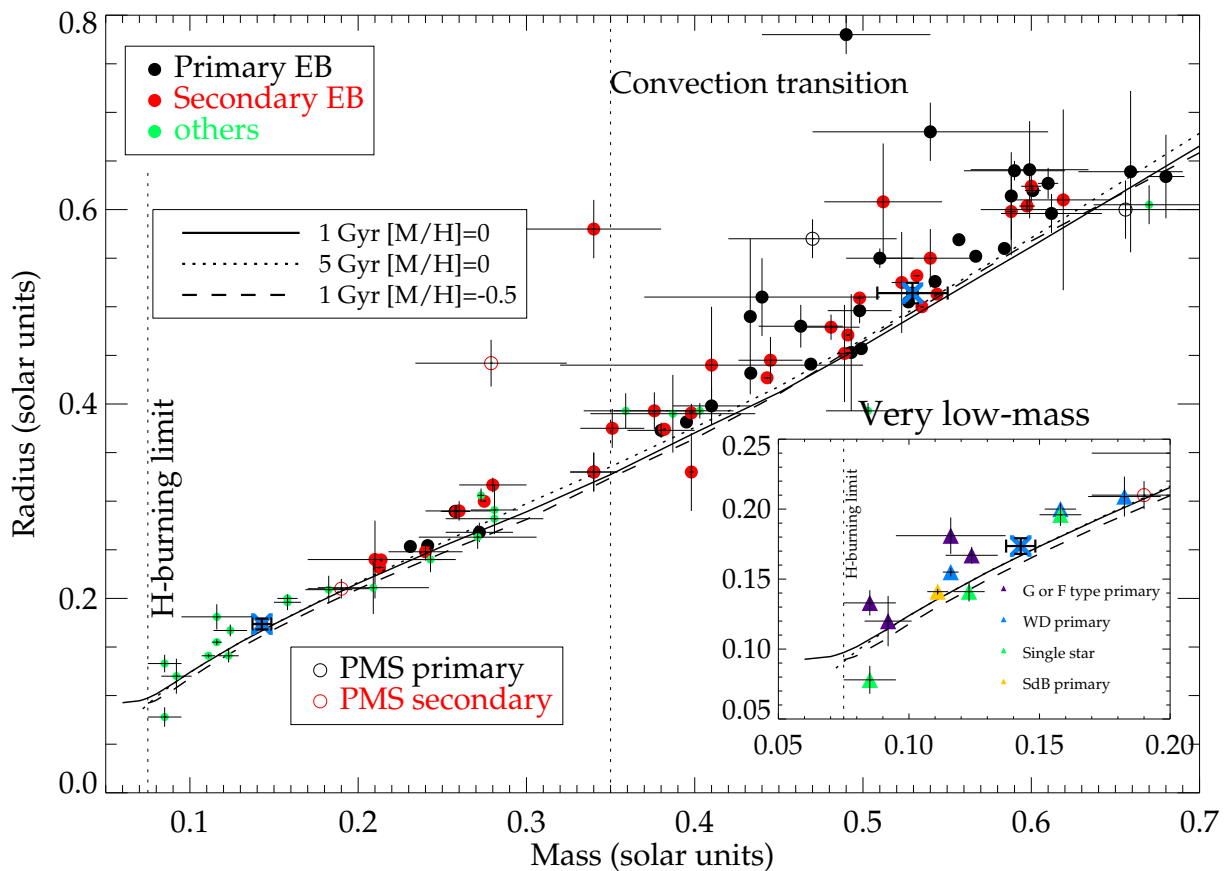


**Figure 5.9** — The mass-radius diagram for low-mass stars with mass less than  $0.7M_{\odot}$ . The vertical dashed line at  $0.075M_{\odot}$  indicates the hydrogen burning limit, whereas the line at  $\sim 0.35M_{\odot}$  represents the proposed transition to fully convective stellar atmospheres (Chabrier & Baraffe 1997). Black filled dots are the primary stars in double-lined eclipsing M+M-dwarf binaries, whereas red filled dots are the secondaries. The small filled green dots indicate M-dwarfs with masses and radii determined through other methods, which we further examine in the inset for very low mass M-dwarfs ( $M < 0.2M_{\odot}$ ). The purple, blue, and yellow triangles indicate measurements of M-dwarfs in eclipsing systems with higher mass G or F type primaries, white dwarf (WD) primaries, or subdwarf B-type (SdB) primaries respectively. The green filled triangles are single star measurements using radius measurements from interferometry.

2012;Pyrazas 2012). Three other systems are from interferometric data with directly measured radii, but with estimated masses from a model mass-luminosity relation (e.g. Demory et al. 2009). Finally two data-points are pre-main sequence M-dwarf binaries which have secondaries in the  $< 0.2M_{\odot}$  regime (JW380, Irwin et al. 2007; 2MASSJ04463285, Hebb et al. 2006). The cool companion of 19g-4-02069A is in a special position as it provides a model-independent anchoring point of mass and radius for fully convective low-mass main-sequence M-dwarfs.

The companion is  $0.0067R_{\odot}$  (4.0%) larger in radius than the 1Gyr solar metallicity Baraffe model, whereas the primary is larger by  $0.025R_{\odot}$  (5.0%). The radius of the companion can be constrained to  $0.0056R_{\odot}$  (3.2%) at the  $1\sigma$  level, its mass is uncertain by  $0.0056M_{\odot}$  (4.0%), indicating that it is currently outside the  $< 3\%$  range advocated by e.g. Torres (2012) as a stringent constraint on models. We illustrate this by showing three Baraffe (1998) models for: i) 1 Gyr solar metallicity (solid black curve); ii) 5 Gyr solar metallicity (dotted curve) and iii) 1 Gyr

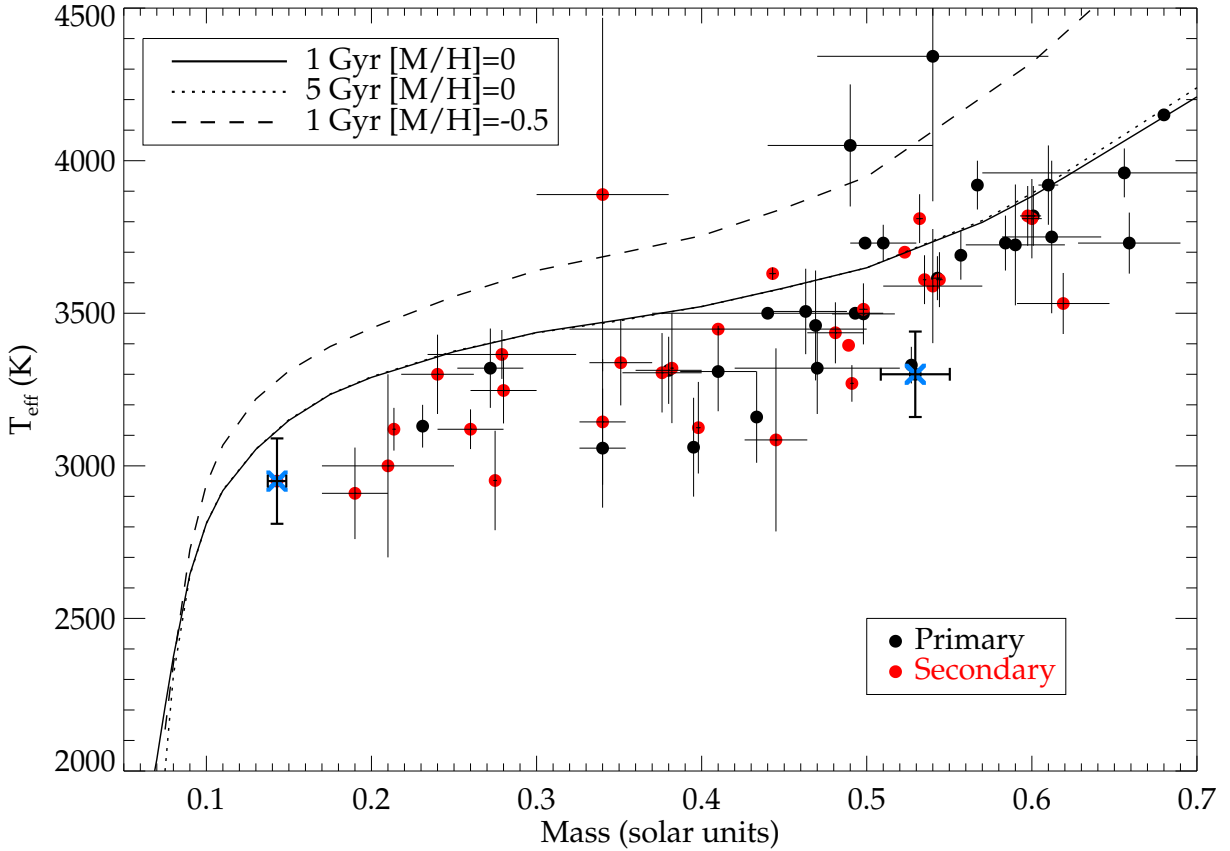


**Figure 5.10** — Current census of mass, effective temperature measurements for stars with mass less than  $0.7M_{\odot}$ . Similar to Figure 5.9, filled dots indicate primary (black) and secondary (red) components of double-lined eclipsing binaries. The blue crosses indicate the position of the components of binary 19g-4-02069. The solid black, dotted and dashed curves are Baraffe model predictions for different ages and metallicities. The data for this figure are tabulated in the Appendix.

metal poor,  $[M/H]=-0.5$  (dashed curve) in Figure 5.9. A 3% accuracy range on the companion mass could be reached if the uncertainty on  $K_2$  is pushed down to the  $\sim 1$  km/s level. It is interesting to note that the effective temperature for the fully-convective secondary is consistent with the 1 Gyr model within the 140 K measurement error, but the partially-convective primary has a  $T_{eff}$  lower by  $\sim 350$  K. Although there is significant scatter in the mass- $T_{eff}$  diagram around  $0.5M_{\odot}$ , potentially due to the inhomogeneous set of methods by which temperature has been determined, such a difference could be explained by magnetic inhibition theory (e.g. Chabrier et al. 2007) if the primary is an active star and has a significant magnetic field, whereas the secondary may not. Five of the seven literature eclipsing binaries with  $q < 0.6$  are fast rotators ( $P < 1$  d), and three of these seven are still on pre-main sequence tracks. The primary of main-sequence M-dwarf binary V405 And (Vida et al. 2009;  $q \sim 0.429$ ,  $P \sim 0.465$  d) is inflated with respect to the Baraffe model by 73%, whereas the secondary is not significantly inflated. This system is much more active than 19g-4-02069, with frequent flaring events. In NSVS-65550671 (Dimitrov & Kjurkcieva 2010,  $q \sim 0.510$ ,  $P \sim 0.193$  d), both components are inflated ( $\sim 17\%$  for the primary,  $\sim 12\%$  for the secondary). Hebb et al. (2006) present a  $q \sim 0.404$ ,  $P \sim 0.465$  d system in the young open cluster NGC 1647, which has an inflated  $0.47M_{\odot}$  primary and a non-

inflated  $0.19M_{\odot}$  secondary. According to Figure 1 from Irwin 2007,  $0.5M_{\odot}$  M-dwarfs reach the main sequence by  $\sim 150$  Myr, and by  $\sim 300$  Myr for  $0.2M_{\odot}$ , indicating that one or both components of the Hebb et al. binary may be pre-main-sequence. In the pre-main-sequence binary NSVS-06507557 (Cakirh & Ibanoglu 2010;  $q \sim 0.425$ ,  $P \sim 0.520$  d) the contrary is true when comparing with the models: the secondary is inflated by 35%, whereas the primary is consistent with the models. One explanation is that in such a young system, the size contraction through gravitational collapse of the secondary may not have progressed as much as that of the higher mass primary, because lower mass stars reach the Zero Age Main Sequence (ZAMS) at later times. Binary 19g-4-02069 has a  $>5$  times lower rotation rate than these four systems, suggesting that inhibition by stellar rotation is the main reason for the observed difference in radius inflation.

### 5.5.3 Non-synchronous rotation?

In Section 5.4.1 we determined that the WFCAM J-band data exhibit a  $\sim 2\%$  peak-to-peak near-sinusoidal periodicity. The variability was not in phase with the binary eclipses, therefore we attributed it to a rotational modulation in brightness caused by star spots. The  $H_{\alpha}$  profile, as observed with ISIS (Section 5.3.2), suggests that the primary star is the main contributor to both the emission of this line and the J-band variability, because the observed radial velocity shift is consistent with the primary. Furthermore, the secondary star contributes only  $\sim 7\%$  of the total J-band emission, therefore requiring spot modulations of order  $\sim 0.0162/0.07 \sim 0.23$  mag, to account for the variability, which would require a very high spot coverage on the secondary and a magnetically quiet primary. The best-fit period of  $\sim 2.563$  d,  $\sim 0.14$  d ( $\sim 5\%$ ) longer than the binary orbital period of  $\sim 2.44$  d, would suggest that the primary star rotates at a subsynchronous rate. This finding is in contrast with current predictions from tidal theory (e.g. Zahn 1977), that suggest orbital synchronisation on timescales of the order  $10^{4-6}$  yr and *supersynchronous* rotation for young stars. We discuss two possible scenarios that could explain the observations.

In the first scenario, high latitude spots have a longer rotation period than spots near the M-dwarf equator due to significant differential rotation over the stellar surface. This causes the observed rotation rate  $\Omega_{obs} = 2\pi/P_{obs}$  to be lower than the true equatorial rate  $\Omega_{eq}$ . On the Sun for example, a spot at  $60^{\circ}$  latitude has a rotation period  $\sim 25\%$  longer than on the equator, and the intermediate latitude  $\theta$  is given by the equation  $\Omega(\theta) = \Omega_{eq} - d\Omega \sin^2(\theta)$ , where  $d\Omega$  is the difference in rotation between the equator and the poles. Donati et al. (2008) presented a spectropolarimetric survey of a small number of single early-type M-dwarfs (ranging from M0 to M3), and detect significant differential rotation in four objects of their sample. For example, OT Ser (M1.5 dwarf;  $\sim 3.38$  d -  $d\Omega/\Omega_{eq} \sim 0.06$ ) and DS Leo (M0 dwarf;  $\sim 14$  d -  $d\Omega/\Omega_{eq} \sim 0.16$ ) show surface rotation variations which are consistent with, although somewhat higher than our observations. It has been argued by Barnes et al. (2005) that for low-mass stars the surface differential rotation vanishes with increasing convective depth, such that fully convective stars rotate mostly as solid bodies. This is supported by observations from e.g. Donati et al. (2006a) and Morin et al. (2008a,b) who show little to no differential rotation in late-type M-dwarfs. We therefore argue that the variability of 19g-4-02069 could be caused by a large high-contrast stable cool spot complex located near to the rotation pole(s) of the  $0.5M_{\odot}$  primary, where the rotational shear is relatively low. A dichotomy in magnetic field geometry has been pointed out by Morin et al. (2010) for stars above and below  $0.5M_{\odot}$ , suggesting

that the dynamo mechanism for  $0.5M_{\odot}$  stars is rather like that of solar-type stars, where the Coriolis force induced by fast stellar rotation (19g-4-02069 rotates at  $\sim 10\times$  the solar rotation value) tends to drive up star spots to polar latitudes. The photometric signal in Figure 5.7 has a relatively high scatter compared to the sine amplitude ( $\sim 10.4$  mmag scatter for a  $\sim 16.2$  mmag signal), which may suggest that the size of the region could have fluctuated over the timescale ( $\sim 5$  years) of our observations.

In the second scenario, the binary could have gone through an extra phase of spin-down besides tidal dissipation. In the sample of Strassmeier et al. (2012) 74% of the rapidly-rotating active binary stars are synchronized and in circular orbits, but 26% (61 systems) are rotating asynchronously of which half have  $P_{rot} > P_{orb}$ , mostly giant stars. It is suggested that a magnetic wind could have applied a braking torque on the stars on the main-sequence, the magnitude of which may depend on stellar mass, interior structure, and activity. This could indicate that the primary and (fully convective) secondary star of 19g-4-02069 may have been braked with different rates, which could be tested by comparing the rotation periods of both stars. Alternatively, the subsynchronous rotation may have been established during the pre-main sequence phase of the binary, through magnetic interaction with a circumbinary disk with a central hole (e.g. Casey et al. 1993). Here, the magnetic field of the primary could have coupled to the (slower) disk motion, slowing down rotation due to angular momentum transfer to the disk. Arguably, this would require 19g-4-02069 to be young, because any asynchronous rotation could be rapidly dissipated through tidal interaction on the main-sequence, however we currently have no observational evidence to suggest a young system.

## 5.6 Conclusion

In this work we have presented the discovery of a highly unequal-mass eclipsing M-dwarf binary ( $q=0.27$ ) with  $P=2.44$  d, using the high-precision near-infra-red time-series of the WFCAM Transit Survey. We find stellar masses  $M_1=0.5294 (\pm 0.0209)M_{\odot}$  and  $M_2=0.1428 (\pm 0.0056)M_{\odot}$ , and radii of  $R_1=0.5141 (\pm 0.0106)R_{\odot}$  and  $R_2=0.1736 (\pm 0.0056)R_{\odot}$ . The companion star is therefore in a sparsely sampled and important M-dwarf mass-regime for studies of Earth-like exoplanets which require accurate calibration of their host star radius and mass. We suggest that the low mass-ratio of our binary may be explained by the different accretion physics such as recently proposed by 2-D warm grid-based (Ochi et al. 2005, de Val-Borro et al. 2011) or magnetic field braking simulations (Zhao & Li 2012), which suggest that short period low- $q$  pairs may be abundant around primaries within a large mass range. Alternatively, the binary may have been isolated from the birth environment early on through ejection or rapid gas removal. Since both stars share the same metallicity and age and straddle the theoretical dividing line between fully and partially convective atmospheres, a comparison can be made to model stellar atmospheres with the same isochrone over a wide span of masses. We find that both stars have slightly inflated radii compared to 1 Gyr model predictions for their mass, but we argue that future work will be required to quantify the effects of star spots on the light curve solution. The effective temperature of the secondary is consistent with theoretical models, but for the primary it is lower by  $\sim 350$  K, which could be explained by magnetic inhibition theory (e.g. Chabrier et al. 2007) if the primary is an active star and has a significant magnetic field, whereas the secondary may not. The detection of a 2.56 d  $\sim 2\%$  signal in the WFCAM light

curve is attributed to subsynchronous rotation of a relatively stable star-spot complex at high latitude on the magnetically active primary, suggesting that its dynamo is more like solar-type stars, with the Coriolis force driving up star spots to polar latitudes.

## 5.7 Acknowledgements

SVN, JLB, IAGS, SH and DJP have received support from RoPACS during this research, and BS and GK are supported by RoPACS, a Marie Curie Initial Training Network funded by the European Commissions Seventh Framework Programme. The United Kingdom Infrared Telescope is operated by the Joint Astronomy Centre on behalf of the Science and Technology Facilities Council of the U.K. This research has benefitted from the M, L, and T dwarf compendium housed at DwarfArchives.org and maintained by Chris Gelino, Davy Kirkpatrick, and Adam Burgasser. This research uses products from SDSS DR7. Funding for the SDSS and SDSS-II has been provided by the Alfred P. Sloan Foundation, the U.S. Department of Energy, the National Aeronautics and Space Administration, the Japanese Monbukagakusho, the Max Planck Society, and the Higher Education Funding Council for England. This publication also makes use of data products from the Two Micron All Sky Survey, which is a joint project of the University of Massachusetts and the Infrared Processing and Analysis Center/California Institute of Technology, funded by the National Aeronautics and Space Administration and the National Science Foundation.

## Bibliography

- Aigrain, S., & Irwin, M. 2004, *MNRAS*, 350, 331  
 Allard, F., Hauschildt, P. H., Alexander, D. R., & Starrfield, S. 1997, *ARA&A*, 35, 137  
 Andersen, J. 1991, *A&ARv*, 3, 91  
 Anosova, J. P. 1986, *Ap&SS*, 124, 217  
 Artymowicz, P. 1983, *Acta Astron.*, 33, 223  
 Baraffe, I., Chabrier, G., Allard, F., & Hauschildt, P. H. 1998, *A&A*, 337, 403  
 Baraffe, I., & Chabrier, G. 1996, *ApJ*, 461, L51  
 Barnes, J. R., Collier Cameron, A., Donati, J.-F., et al. 2005, *MNRAS*, 357, L1  
 Bate, M. R. 2000, *MNRAS*, 314, 33  
 Bate, M. R., Bonnell, I. A., & Bromm, V. 2002, *MNRAS*, 336, 705  
 Bate, M. R. 2012, *MNRAS*, 419, 3115  
 Bate, M. R., & Bonnell, I. A. 1997, *MNRAS*, 285, 33  
 Beatty, T. G., Fernández, J. M., Latham, D. W., et al. 2007, *ApJ*, 663, 573  
 Becker, A. C., Agol, E., Silvestri, N. M., et al. 2008, *MNRAS*, 386, 416  
 Berger, D. H., Gies, D. R., McAlister, H. A., et al. 2006, *ApJ*, 644, 475  
 Birkby, J., Nefs, B., Hodgkin, S., et al. 2012, *MNRAS*, 426, 1507  
 Blake, C. H., Torres, G., Bloom, J. S., & Gaudi, B. S. 2008, *ApJ*, 684, 635  
 Bochanski, J. J., Munn, J. A., Hawley, S. L., et al. 2007, *AJ*, 134, 2418  
 Bouchy, F., Pont, F., Melo, C., Santos, N. C., Mayor, M., Queloz, D., Udry, S. 2005, *A&A*, 431, 1105  
 Bouchy, F., Bonomo, A. S., Santerne, A., et al. 2011, *A&A*, 533, A83

- Çakırlı, Ö., & Ibanoglu, C. 2010, *MNRAS*, 401, 1141
- Casali, M., Adamson, A., Alves de Oliveira, C., et al. 2007, *A&A*, 467, 777
- Casey, B. W., Mathieu, R. D., Suntzeff, N. B., Lee, C.-W., & Cardelli, J. A. 1993, *AJ*, 105, 2276
- Carter, J. A., Fabrycky, D. C., Ragozzine, D., et al. 2011, *Science*, 331, 562
- Chabrier, G., Gallardo, J., & Baraffe, I. 2007, *A&A*, 472, L17
- Charbonneau, D., Berta, Z. K., Irwin, J., et al. 2009, *Nature*, 462, 891
- Claret, A. 2000, *A&A*, 363, 1081
- Claret, A. 2004, *A&A*, 428, 1001
- Clark, B. M., Blake, C. H., & Knapp, G. R. 2012, *ApJ*, 744, 119
- Clarke, C. J. 2012, *IAU Symposium*, 282, 409
- Creevey, O. L., Benedict, G. F., Brown, T. M., et al. 2005, *ApJ*, 625, L127
- de Mooij, E. J. W., Brogi, M., de Kok, R. J., et al. 2012, *A&A*, 538, A46
- de Val-Borro, M., Gahm, G. F., Stempels, H. C., & Pepliński, A. 2011, *MNRAS*, 413, 2679
- Davenport, J.R.A., Becker, A.C., West, A.A. et al. 2012, arXiv:1206.6056.
- Delfosse, X., Forveille, T., Mayor, M., Burnet, M., & Perrier, C. 1999, *A&A*, 341, L63
- Delfosse, X., Beuzit, J.-L., Marchal, L., Bonfils, X.; Perrier, C.; SÁI'gransan, D.; Udry, S.; Mayor, M. 2004, *Spectroscopically and Spatially Resolving the Components of the Close Binary Stars*, 318, 166
- Demory, B.-O., Ségransan, D., Forveille, T., et al. 2009, *A&A*, 505, 205
- Devor, J., Charbonneau, D., Torres, G., et al. 2008, *ApJ*, 687, 1253
- Dimitrov, D. P., & Kjurkchieva, D. P. 2010, *MNRAS*, 406, 2559
- Dhital, S., West, A. A., Stassun, K. G., et al. 2012, *AJ*, 143, 67
- Donati, J.-F., Forveille, T., Collier Cameron, A., et al. 2006, *Science*, 311, 633
- Donati, J.-F., Morin, J., Petit, P., et al. 2008, *MNRAS*, 390, 545
- Doyle, L. R., Carter, J. A., Fabrycky, D. C., et al. 2011, *Science*, 333, 1602
- Duchêne, G., Bontemps, S., Bouvier, J., et al. 2007, *A&A*, 476, 229
- Etzel, P. B. 1981, *Photometric and Spectroscopic Binary Systems*, 111
- Gizis, J. E., Reid, I. N., & Hawley, S. L. 2002, *AJ*, 123, 3356
- Goodwin, S. P., Kroupa, P., Goodman, A., & Burkert, A. 2007, *Protostars and Planets V*, 133
- Goodwin, S. P., & Whitworth, A. 2007, *A&A*, 466, 943
- Goulding, N. T., Barnes, J. R., Pinfield, D. J., et al. 2012, arXiv:1211.5288
- Gustafsson, B., Edvardsson, B., Eriksson, K., et al. 2008, *A&A*, 486, 951
- Hartman, J. D., Bakos, G. Á., Noyes, R. W., Sipőcz, B., Kovács, G., Mazeh, T. , Shporer, A., Pál, A., 2011, *AJ*, 141, 166
- Hebb, L., Wyse, R. F. G., Gilmore, G., & Holtzman, J. 2006, *AJ*, 131, 555
- Hełminiak, K. G., Konacki, M., RóŻyczka, M., et al. 2012, *MNRAS*, 425, 1245
- Henry, T. J., Ianna, P. A., Kirkpatrick, J. D., & Jahreiss, H. 1997, *AJ*, 114, 388
- Hilditch, R. W. 2001, *An Introduction to Close Binary Stars*, by R. W. Hilditch, pp. 392. ISBN 0521241065. Cambridge, UK: Cambridge University Press, March 2001.
- Hodgkin, S. T., Irwin, M. J., Hewett, P. C., & Warren, S. J. 2009, *MNRAS*, 394, 675
- Huélamo, N., Vaz, L. P. R., Torres, C. A. O., et al. 2009, *A&A*, 503, 873
- Irwin, J., Aigrain, S., Hodgkin, S., et al. 2007, *MNRAS*, 380, 541
- Irwin, J., Charbonneau, D., Berta, Z. K., et al. 2009, *ApJ*, 701, 1436
- Irwin, J. M., Quinn, S. N., Berta, Z. K., et al. 2011, *ApJ*, 742, 123
- Kraus, A. L., Tucker, R. A., Thompson, M. I., Craine, E. R., & Hillenbrand, L. A. 2011, *ApJ*,

- 728, 48
- Lada, C. J. 2006, *ApJ*, 640, L63
- Lépine, S., Rich, R. M., & Shara, M. M. 2007, *ApJ*, 669, 1235
- Lomb, N. R. 1976, *Ap&SS*, 39, 447
- López-Morales, M., & Ribas, I. 2005, *ApJ*, 631, 1120
- Lopez-Morales, M., Orosz, J. A., Shaw, J. S., et al. 2006, arXiv:astro-ph/0610225
- Maceroni, C., & Montalbán, J. 2004, *A&A*, 426, 577
- Maxted, P. F. L., O'Donoghue, D., Morales-Rueda, L., Napiwotzki, R., & Smalley, B. 2007, *MNRAS*, 376, 919
- Miller, A. A., Irwin, J., Aigrain, S., Hodgkin, S., & Hebb, L. 2008, *MNRAS*, 387, 349
- Morales, J. C., Ribas, I., Jordi, C., et al. 2009, *ApJ*, 691, 1400
- Morin, J., Donati, J.-F., Forveille, T., et al. 2008, *MNRAS*, 384, 77
- Morin, J., Donati, J.-F., Petit, P., et al. 2008, *MNRAS*, 390, 567
- Morin, J., Donati, J.-F., Petit, P., et al. 2010, *MNRAS*, 407, 2269
- Morris, S. L. 1985, *ApJ*, 295, 143
- Mullan, D. J., & MacDonald, J. 2001, *ApJ*, 559, 353
- Nefs, S. V., Birkby, J. L., Snellen, I. A. G., et al. 2012, *MNRAS*, 425, 950
- Nutzman, P., & Charbonneau, D. 2008, *PASP*, 120, 317
- Ochi, Y., Sugimoto, K., & Hanawa, T. 2005, *ApJ*, 623, 922
- Parsons, S. G., Marsh, T. R., Copperwheat, C. M., Dhillon, V. S., Littlefair, S. P., Gänsicke, B. T., Hickman, R. 2010, *MNRAS*, 402, 2591
- Parsons, S. G., Gänsicke, B. T., Marsh, T. R., et al. 2012, *MNRAS*, 426, 1950
- Pont, F., Melo, C. H. F., Bouchy, F., Udry, S., Queloz, D., Mayor, M., Santos, N. C. 2005, *A&A*, 433, L21
- Pont, F., Moutou, C., Bouchy, F., et al. 2006, *A&A*, 447, 1035
- Popper, D. M., & Etzel, P. B. 1981, *AJ*, 86, 102
- Pyrzas, S., Gänsicke, B. T., Brady, S., et al. 2012, *MNRAS*, 419, 817
- Raghavan, D., McAlister, H. A., Henry, T. J., et al. 2010, *ApJS*, 190, 1
- Rebolo, R., Martin, E. L., & Magazzu, A. 1992, *ApJ*, 389, L83
- Reid, I. N., Hawley, S. L., & Gizis, J. E. 1995, *AJ*, 110, 1838
- Reid, I. N. 1999, *Star Formation 1999*, 327
- Reylé, C., Rajpurohit, A. S., Schultheis, M., & Allard, F. 2011, 16th Cambridge Workshop on Cool Stars, Stellar Systems, and the Sun, 448, 929
- Ribas, I. 2003, *A&A*, 398, 239
- Ribas, I. 2006, *Ap&SS*, 304, 89
- Scargle, J. D. 1982, *ApJ*, 263, 835
- Schwarzenberg-Czerny, A. 1989, *MNRAS*, 241, 153
- Seager, S., & Mallén-Ornelas, G. 2003, *Scientific Frontiers in Research on Extrasolar Planets*, 294, 419
- Ségransan, D., Kervella, P., Forveille, T., & Queloz, D. 2003, *A&A*, 397, L5
- Shkolnik, E. L., Hebb, L., Liu, M. C., Reid, I. N., & Collier Cameron, A. 2010, *ApJ*, 716, 1522
- Slesnick, C. L., Carpenter, J. M., & Hillenbrand, L. A. 2006, *AJ*, 131, 3016
- Southworth, J., Smalley, B., Maxted, P. F. L., & Etzel, P. B. 2004, *The A-Star Puzzle*, 224, 54
- Southworth, J., Smalley, B., Maxted, P. F. L., Claret, A., & Etzel, P. B. 2005, *MNRAS*, 363, 529

- Southworth, J. 2008, MNRAS, 386, 1644
- Stassun, K. G., Mathieu, R. D., & Valenti, J. A. 2007, ApJ, 664, 1154
- Strassmeier, K. G., Weber, M., Granzer, T., & Irvén, S. 2012, Astronomische Nachrichten, 333, 663
- Torres, G., Andersen, J., & Giménez, A. 2010, A&ARv, 18, 67
- Torres, G. 2012, arXiv:1209.1279
- Torres, G., & Ribas, I. 2002, ApJ, 567, 1140
- Vaccaro, T. R., Rudkin, M., Kawka, A., Vennes, S., Oswalt, T. D., Silver, I., Wood, M., Smith, J. A. 2007, ApJ, 661, 1112
- Vida, K., Oláh, K., Kővári, Z., Korhonen, H., Bartus, J., Hurta, Z., Posztobányi, K. 2009, A&A, 504, 1021
- Wisniewski, J. P., Ge, J., Crepp, J. R., et al. 2012, AJ, 143, 107
- Young, T. B., Hidas, M. G., Webb, J. K., Ashley, M. C. B., Christiansen, J. L., Derekas, A. and Nutto, C. 2006, MNRAS, 370, 1529
- Zahn, J.-P. 1977, A&A, 57, 383
- Zhao, B., & Li, Z.-Y. 2012, arXiv:1210.2308

## **Appendix**

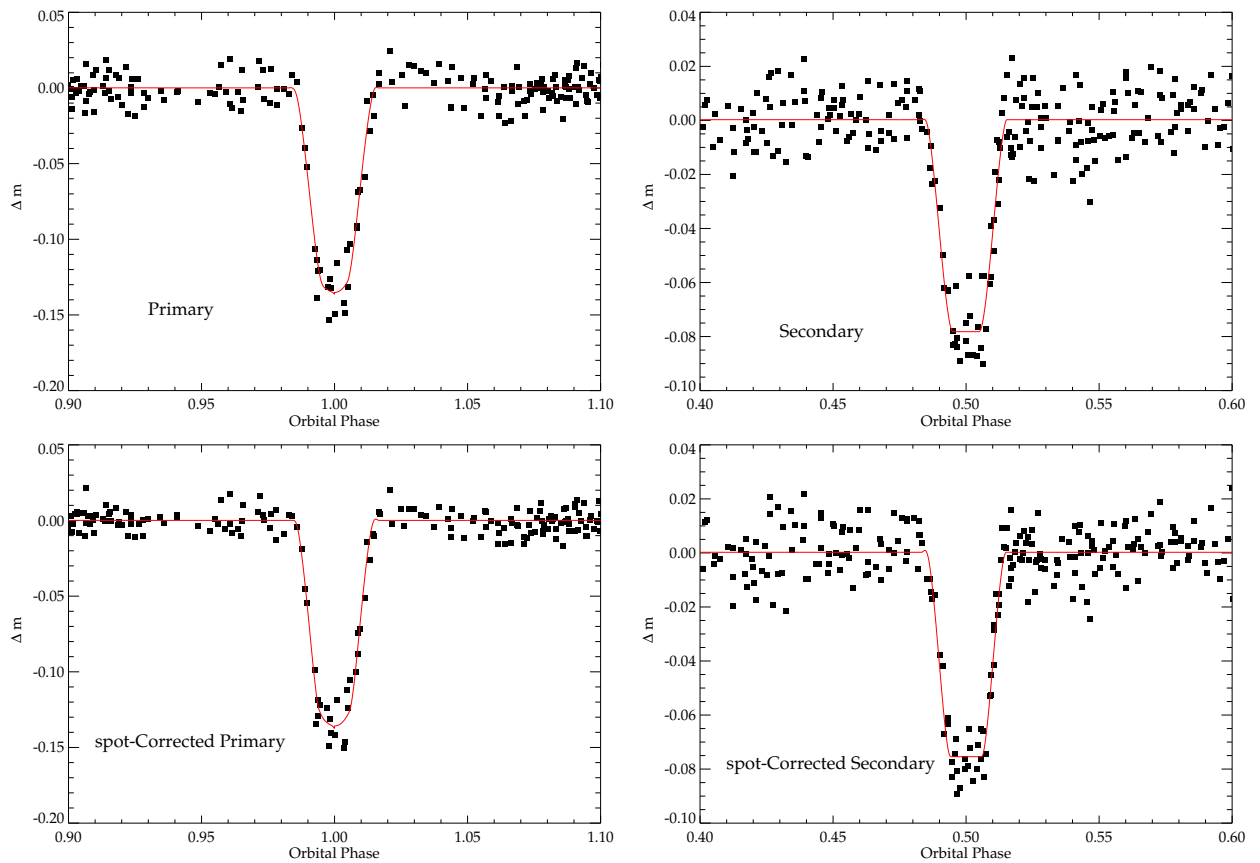


**Figure 5.11** — *The WFCAM J-band discovery light curve, before (left panels) and after (right panels) removal of the rotational signal using a single sine with amplitude 8.1 mmag, which improves the light curve rms by  $\sim 20\%$ . Note that this procedure effectively removes several outliers in the secondary event. The best-fit JKTEBOP model is overplotted as a solid red curve.*

Name	Ref.	$M_1$ ( $M_\odot$ )	$M_2$ ( $M_\odot$ )	$R_1$ ( $R_\odot$ )	$R_2$ ( $R_\odot$ )	$T_1$ (K)	$T_2$ (K)	P d	type	$(\frac{T_2}{T_1})$	q
OGLEBW3V38	(1)	0.44(0.07)	0.41(0.09)	0.51(0.04)	0.44(0.06)	3500	3448(11)	0.198	SB2	0.985	0.950
2MASSJ0154	(2)	0.659(0.031)	0.619(0.028)	0.639(0.083)	0.610(0.093)	3730(100)	3532(100)	2.639	SB2	0.947	0.939
NSVS-6550671	(3)	0.510(0.02)	0.260(0.02)	0.550(0.01)	0.290(0.01)	3730(60)	3120(65)	0.193	SB2	0.836	0.510
2MASSJ04463285	(4)	0.470(0.05)	0.190(0.02)	0.570(0.02)	0.210(0.01)	3320(150)	2910(150)	0.630	SB2	0.877	0.404
NSVS-06507557	(5)	0.656(0.086)	0.279(0.045)	0.600(0.03)	0.442(0.024)	3960(80)	3365(80)	0.520	SB2	0.850	0.425
NSVS-01031772	(6)	0.5428(0.0027)	0.498(0.0025)	0.526(0.0028)	0.509(0.003)	3615(72)	3513(31)	0.368	SB2	0.972	0.917
GJ2069	(7)	0.433(0.0018)	0.398(0.0015)	0.490(0.08)	0.330(0.04)	–	–	2.771	SB2	–	0.920
GJ3236	(8)	0.38(0.02)	0.28(0.02)	0.3729(0.0078)	0.3167(0.0075)	3313(110)	3247(108)	0.771	SB2	0.98	0.737
CUCnc	(7)	0.4333(0.0017)	0.398(0.0014)	0.4317(0.0052)	0.3908(0.0094)	3160(150)	3125(150)	2.77	SB2	0.989	0.919
SDSS-MEB-1	(9)	0.272(0.02)	0.24(0.022)	0.268(0.01)	0.248(0.009)	3320(130)	3300(130)	0.407	SB2	0.99	0.880
V405And	(10)	0.49(0.05)	0.21(0.04)	0.78(0.02)	0.24(0.04)	4050(200)	3000(300)	0.465	SB2	0.741	0.429
ASAJ011328-3821.1	(11)	0.612(0.03)	0.445(0.019)	0.596(0.02)	0.445(0.024)	3750(250)	3085(300)	0.445	SB2	0.822	0.727
LP-133-373	(12)	0.34(0.014)	0.34(0.014)	0.33(0.02)	0.33(0.02)	3058(195)	3144(206)	1.63	SB2	0.973	1.000
T-Lyr1-17236	(13)	0.680(0.011)	0.523(0.006)	0.634(0.043)	0.525(0.052)	4150	3700	8.43	SB2	0.892	0.769
CMDra	(14)	0.231(0.001)	0.2136(0.001)	0.2534(0.0019)	0.2396(0.002)	3130(70)	3120(70)	1.27	SB2	0.997	0.925
LSPMJ1112+7626	(15)	0.3951(0.0022)	0.2749(0.0011)	0.3860(0.005)	0.2978(0.005)	3061(162)	2952(163)	41.03	SB2	0.964	0.696
IRXSJ154727	(16)	0.2576(0.0085)	0.2585(0.008)	0.2895(0.0068)	0.2895(0.0068)	–	–	3.55	SB2	–	0.997
WTS19b-2-01387	(17)	0.498(0.019)	0.481(0.017)	0.496(0.013)	0.479(0.013)	3498(100)	3436(100)	1.499	SB2	0.982	0.966
WTS19c-3-01405	(17)	0.410(0.023)	0.376(0.024)	0.398(0.019)	0.393(0.019)	3309(130)	3305(130)	4.939	SB2	0.999	0.917
WTS19e-3-08413	(17)	0.463(0.025)	0.351(0.019)	0.480(0.022)	0.375(0.02)	3506(140)	3338(140)	1.673	SB2	0.952	0.758
JW380	(18)	0.26(0.02)	0.15(0.01)	1.19(0.11)	0.90(0.10)	–	–	5.3	SB2	–	0.58
KOI126BC	(19)	0.2413(0.003)	0.2127(0.0026)	0.2543(0.0014)	0.2318(0.0013)	–	–	1.767	SB2	–	0.881
MG1-646680	(20)	0.499(0.002)	0.443(0.002)	0.457(0.005)	0.427(0.004)	3730(20)	3630(20)	1.638	SB2	0.973	0.888
MG1-78457	(20)	0.527(0.002)	0.491(0.001)	0.505(0.0075)	0.471(0.008)	3330(60)	3270(60)	1.586	SB2	0.982	0.932
MG1-116309	(20)	0.567(0.002)	0.532(0.002)	0.552(0.0085)	0.532(0.006)	3920(80)	3810(80)	0.827	SB2	0.972	0.938
MG1-1819499	(20)	0.557(0.001)	0.535(0.001)	0.569(0.0022)	0.500(0.0085)	3690(80)	3610(80)	0.630	SB2	0.978	0.961
MG1-506664	(20)	0.584(0.002)	0.544(0.002)	0.560(0.0025)	0.513(0.0055)	3730(90)	3610(90)	1.548	SB2	0.968	0.932
MG1-2056316	(20)	0.469(0.002)	0.382(0.001)	0.441(0.002)	0.374(0.002)	3460(180)	3320(180)	1.723	SB2	0.960	0.814
SDSSJ001641-000925	(21)	0.54(0.07)	0.34(0.04)	0.68(0.03)	0.58(0.03)	4342(475)	3889(579)	0.199	SB2	0.896	0.630
TrES-Her0-07621	(22)	0.493(0.003)	0.489(0.003)	0.453(0.06)	0.452(0.05)	3500	3395	1.137	SB2	0.97	0.992
BD-225866Aa	(23)	0.5881(0.0029)	0.5881(0.0029)	0.614(0.045)	0.598(0.045)	–	–	2.211	SB2	–	1.000
UNSW2A	(24)	0.599(0.035)	0.512(0.035)	0.641(0.05)	0.608(0.06)	–	–	2.144	SB2	–	0.855
HIP96515Aa	(25)	0.59(0.03)	0.54(0.03)	0.64(0.01)	0.55(0.03)	3724(198)	3589(187)	2.346	SB2	0.964	0.915
YYGem	(26)	0.6009(0.0047)	0.5975(0.0047)	0.6196(0.0057)	0.6036(0.0057)	3819(98)	3819(98)	0.814	SB2	1.000	0.994
GUBoo	(27)	0.610(0.006)	0.600(0.006)	0.627(0.016)	0.624(0.016)	3920(130)	3810(130)	0.492	SB2	0.972	0.984
HAT-TR-205-013	(28)		0.124(0.01)		0.167(0.006)				SB1		
OGLE-TR-5B	(29)		0.271(0.035)		0.263(0.012)				SB1		
OGLE-TR-6B	(29)		0.359(0.025)		0.393(0.018)				SB1		
OGLE-TR-7B	(29)		0.281(0.029)		0.282(0.013)				SB1		
OGLE-TR-123B	(30)		0.085(0.01)		0.133(0.009)				SB1		
OGLE-TR-122B	(31)		0.092(0.009)		0.120(0.018)				SB1		
OGLE-TR-106B	(31)		0.116(0.021)		0.181(0.013)				SB1		
OGLE-TR-125B	(31)		0.209(0.033)		0.211(0.027)				SB1		
OGLE-TR-78B	(31)		0.243(0.015)		0.24(0.013)				SB1		
OGLE-TR-18B	(32)		0.387(0.049)		0.390(0.040)				SB1		
GJ191	(33)	0.281(0.014)	single	0.291(0.025)	single	3570(156)			single		
GJ699	(33)	0.158(0.008)	single	0.196(0.008)	single	3163(65)			single		
GJ551	(33)	0.123(0.006)	single	0.141(0.007)	single	3042(117)			single		
GJ887	(33)	0.503(0.025)	single	0.393(0.008)	single				single		
GJ411	(33)	0.403(0.02)	single	0.393(0.008)	single	3570(42)			single		
GJ380	(33)	0.670(0.033)	single	0.605(0.02)	single				single		
RRCae-B	(34)	WD	0.1825(0.0139)	WD	0.209(0.0143)		3100(100)		WD		
NNSer-B	(35)	SdB	0.111(0.004)	SdB	0.141(0.002)				SdB		
GKVir	(36)	WD	0.116(0.003)	WD	0.155(0.003)				WD		
SDSSJ1212 0123	(37)	WD	0.273(0.002)	WD	0.306(0.007)				WD		
SDSSJ1210+3347	(37)	WD	0.158(0.006)	WD	0.200(0.003)				WD		

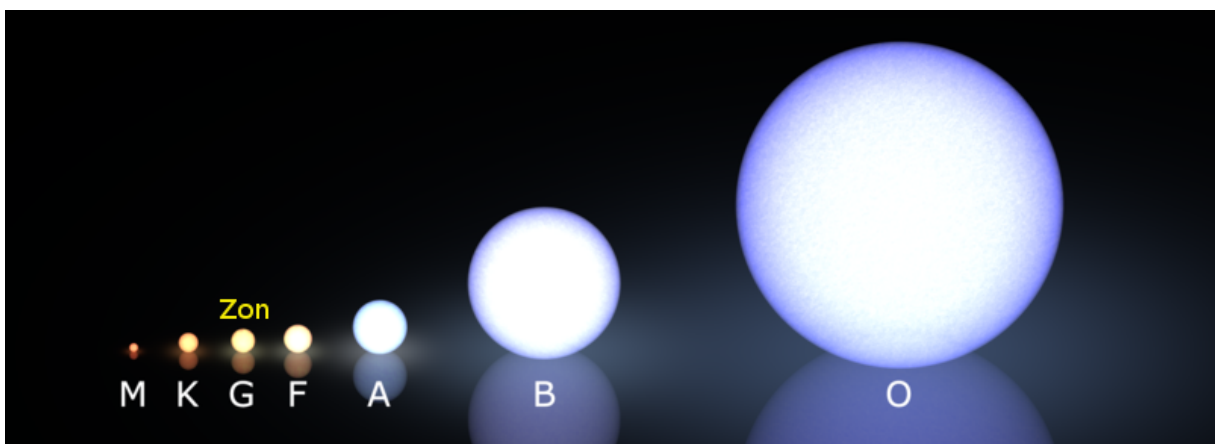
**Table 5.6** — Literature values for the M-dwarf systems used in Figure 5.8, 5.9 and 5.10. References: (1) Maceroni & Montalban (2004), (2) Becker et al. (2008), (3) Dimitrov & Kjurkchieva (2010), (4) Hebb et al. (2006), (5) Cakirh & Ibanoglu (2010), (6) Lopez-Morales et al. (2006), (7) Ribas (2003), (8) Irwin et al. (2009), (9) Blake et al. (2008), (10) Vida et al. (2009), (11) Helminiak et al. (2012), (12) Vaccaro et al. (2007), (13) Devor et al. (2008), (14) Morales et al. (2009), (15) Irwin et al. (2011), (16) Hartman et al. (2011), (17) Birkby et al. (2012), (18) Irwin et al. (2007), (19) Carter et al. (2011), (20) Kraus et al. (2011), (21) Davenport et al. (2012), (22) Creevey et al. (2005), (23) Shkolnik et al. (2010), (24) Young et al. (2006), (25) Huelamo et al. (2009), (26) Torres & Ribas (2002), (27) López-Morales & Ribas (2005), (28) Beatty (2007), (29) Bouchy et al. (2005), (30) Pont et al. (2006), (31) Pont et al. (2005), (32) Bouchy et al. (2005), (33) Segransan et al. (2002), (34) Maxted et al. (2007), (35) Parsons et al. (2010), (36) Parsons et al. (2012), (37) Pyrzas et al. (2012).

# Nederlandse samenvatting

Eenmaal tijdens de vele uren waarnemen voor dit proefschrift heb ik kunnen genieten van een echt donkere sterrenhemel, zonder heldere maan en wolken. De sensatie van hoog in de Andes in Chili geen hand voor ogen kunnen zien, duizenden sterren, schaduwen van de Melkweg en alle bekende sterrenbeelden op hun kop, was een ervaring die me zeker lang zal bijblijven. De aanblik van zo veel sterren roept bij ieder meteen een aantal belangrijke vragen op.

## Hoe stralen sterren?

De vraag hoe de sterren aan onze nachthemel stralen is pas in de loop van de vorige eeuw beantwoord toen geleerden ontdekten dat sterren hete bollen van gas zijn, zo heet dat in hun kern waterstof (het lichtste element in ons heelal) kan samensmelten tot helium (het op één na lichtste element). Dit proces geeft energie aan de meeste sterren die we kennen tijdens een groot deel van hun leven en zorgt ervoor dat ze niet snel ineenstorten onder hun eigen gewicht. Een belangrijke ontdekking is ook dat niet iedere ster even zuinig met zijn brandstof omspringt en dat dit afhangt van de massa van de ster. Zware sterren verzwelgen hun waterstof en veranderen al snel in grote rode reuzesterren, terwijl normale sterren zoals onze zon wel 10 miljard jaar onafgebroken en constant kunnen stralen. Deze constante levensfase van sterren wordt de *Hoofdreeks* genoemd. Het is een fascinerend gegeven dat sterren variëren in grootte met een factor van  $\sim 100$  op de Hoofdreeks, van 10 maal kleiner dan onze eigen Zon, tot  $\sim 10$  maal groter. De lichtkracht van sterren varieert zelfs met een factor  $\sim 300$  miljoen. In Figuur 1 worden een aantal hoofdreekssterren onderling vergeleken in grootte. Elk van deze sterren heeft een bijbehorende temperatuur die loopt van  $\sim 3000^\circ\text{C}$  tot  $\sim 40000^\circ\text{C}$ , en wordt geclassificeerd



**Figuur 6.1** — Sterren die waterstof fuseren op de Hoofdreeks, onderling vergeleken in grootte. De reeks loopt van links naar rechts met koele rode dwergsterren aan de linkerkant en hete witte O-sterren aan de rechterkant. Onze Zon is een gelige ster van klasse G. Credits: Jeff Bryant.

als een van de reeks O B A F G K M (O sterren zijn heet, M sterren koel). Onze Zon is van klasse G.

## Hoe ontstaan sterren?

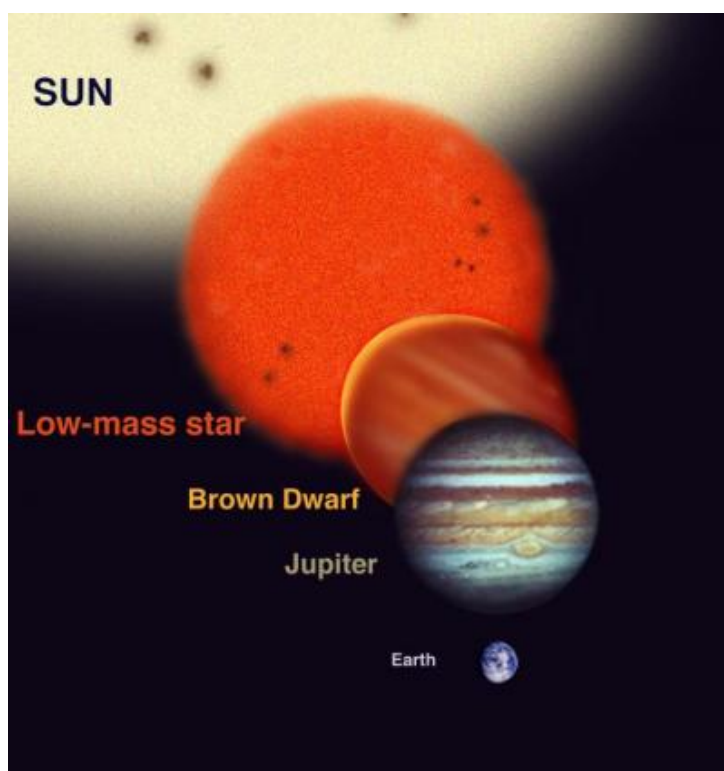
Het huidige idee is dat sterren ontstaan in grote, ijle en erg koude wolken van gas en stof, die genoeg materiaal in zich hebben voor de vorming van honderden tot zelfs duizenden sterren. Op enig moment kunnen in deze wolken gebieden instabiel worden en onder invloed van de zwaartekracht samen gaan trekken. Uiteindelijk wordt de dichtheid van het instortende gas zo hoog dat er een ster in het centrum van het gebiedje ontstaat (wat typisch 10000 jaar duurt). Omdat de wolk altijd een beetje draait, kan niet al het materiaal recht op de ster vallen, maar komt ook terecht in een draaiende platte schijf rond de ster (een zogenaamde *circumstellaire schijf*). Het idee is dat in deze schijven kleine stofdeeltjes kunnen samenklonteren, om uiteindelijk planeten te vormen.

## Rode dwergen, bruine dwergen en planeten

Dit proefschrift gaat voornamelijk over de allerkleinste sterren die de Natuur kan maken - de *rode dwergen* (ook wel M-dwergen genoemd door astronomen). Ze zijn de kleinste normale sterren die waterstof kunnen fuseren en zijn  $\sim 8\%$  tot  $60\%$  de grootte van onze Zon. Rode dwergen vormen de grootste populatie ( $> 70\%$ ) van alle sterren in onze Melkweg. Echter, tussen de  $\sim 6000$  sterren die waarneembaar zijn met het blote oog op een heldere avond zit geen enkele M-dwerg. Dit komt omdat M-dwergen hun waterstof zo langzaam fuseren dat ze maar weinig licht kunnen uitstralen - slechts  $0.015\%$  tot  $7\%$  van de Zon. We hoeven geen medelijden te hebben want rode dwergen hebben de langste adem van alle sterren en zijn amper veranderd sinds hun ontstaan. Objecten lichter dan  $\sim 0.08$  zonsmassa's hebben geen waterstofverbranding in de kern en worden daarom niet als echte sterren aangemerkt; ze worden *bruine dwergen* genoemd. Nog kleiner dan de bruine dwergen zijn de planeten, die koud en donker zijn vergeleken met de sterren. In Figuur 2 worden de afmetingen van sterren en planeten onderling vergeleken. Wat meteen opvalt is dat de grootte van rode dwergen, bruine dwergen en reuzeplaneten die bestaan uit gas, zoals Jupiter, vergelijkbaar zijn. Hun massa verschilt echter met een factor  $\sim 600$ . Onze aarde is echt een dreumes op deze schaal,  $\sim 10$  maal kleiner dan Jupiter en  $\sim 100$  maal kleiner dan onze Zon.

## Dubbelsterren

Het lijkt er op dat onze Zon eenzaam door het leven gaat zonder stellair maatje. Recent onderzoek laat echter zien dat ruim  $50\%$  van alle sterren die lijken op onze Zon een *dubbelster* of een *meervoudig systeem* is. In zo'n stelsel draaien de sterren hun banen rond een gemeenschappelijk zwaartepunt. De zwaarste van het duo wordt de *primaire* ster genoemd en de lichtere de *secundaire* ster of *begeleider*. De huidige waarnemingen van dubbelsterren suggereren dat zwaardere primaire sterren vaker een begeleider hebben dan lichtere. Zwarte hete sterren van het type B en O (zie ook Figuur 1) hebben zelfs bijna altijd een begeleider. Voor rode dwergen is dit waarschijnlijk nog slechts  $30\text{-}40\%$ , terwijl  $10\text{-}30\%$  van alle bruine dwergen een maatje



**Figuur 6.2** — De grootte van sterren, bruine dwergen en planeten onderling vergeleken. Terwijl rode dwergen significant kleiner zijn dan onze Zon, zijn ze in grootte vergelijkbaar met bruine dwergen en gasvormige planeten zoals Jupiter. Credit: Gemini Observatory/Artwork by Jon Lomberg.

heeft. Een ander interessante observatie is dat de verhouding tussen de massa van de primaire ster en zijn begeleider mogelijk afhangt van zowel de omlooperperiode van de sterren in een dubbel-systeem als van de massa van de primaire ster. Met andere woorden, hoe lichter de primaire ster is, hoe groter de kans is dat hij deel uitmaakt van een tweeling-systeem, waar de twee sterren bijna gelijke massa en grootte hebben. Ook is het vermoeden dat dubbelsterren in nauwe banen veel vaker voorkomen als tweeling. Op grond van deze bevindingen zou geconcludeerd kunnen worden dat dubbelsterren van rode dwergen, in nauwe banen, met ongelijke massa heel zeldzaam zouden moeten zijn. In Hoofdstuk 5 komen we terug op deze interessante kwestie, waar we de ontdekking presenteren van een dubbelster van M-dwergen met duidelijk ongelijke massa's.

Er zijn echter nog veel onzekerheden over hoe de vorming van dubbelsterren precies in zijn werk gaat. Het lijkt wel waarschijnlijk dat de vorming van dubbelsterren plaatsvindt in dezelfde geboortewolken van gas en stof van waaruit eenzame sterren ontstaan. Wat ook duidelijk lijkt, is dat hun vormingsproces complexer is dan dat van eenzame sterren. Dit komt omdat de sterren in een dubbelsysteem met elkaar concurreren om het omliggende gas en stof van hun geboortewolken. Dit maakt het noodzakelijk om de precieze fysische processen te doorgronden die de evolutie van dubbelsterren bepalen, en die uiteindelijk de nu waargenomen eigenschappen van dubbelsterren kunnen verklaren. Het is echter lastig om de vroegste beginstadia van dubbelsterren direct en grondig waar te nemen, omdat de sterren dan nog omhuld worden door de dichte lagen van het gas en stof waaruit ze gevormd werden. Het is dus belangrijk om de eigen-

schappen van de huidige populatie dubbelsterren te bestuderen en hun vorming na te bootsen in computer simulaties en de uitkomsten hiervan onderling te vergelijken. In de Hoofdstukken 3,4 en 5 van dit proefschrift worden de eigenschappen van dubbelsterren van rode dwergen nader onder de loep genomen en vergeleken met de voorspellingen van de huidige theoriën over ontstaan en evolutie van deze belangrijke groep sterren.

## Waarom M-dwergen bestuderen?

Vroeger werden M-dwergen gezien als de nogal rustige, saaie broertjes van sterren als onze Zon, maar niets blijkt minder waar te zijn:

- Ze kunnen een nogal temperamentvol gedrag vertonen als gevolg van hun zeer sterke magnetische velden. Kortsluitingen van dit magneetveld in de atmosfeer van een rode dwerg zorgen voor intense uitbarstingen van heet gas en sterke variaties in de helderheid van de ster. Ook ontstaan er door de magnetische activiteit soms grote koele gebieden op het oppervlak van de ster, die 'stervlekken' worden genoemd. Soortgelijke fenomenen spelen zich ook af op onze Zon, maar op een veel kleinere schaal.
- M-dwergen vormen de ontbrekende puzzelstukjes in computer simulaties die proberen te beschrijven hoe sterren en dubbelsterren vormen. Dit komt omdat zij het schemergebied vertegenwoordigen tussen sterren als onze Zon (of zwaarder) en de veel lichtere bruine dwergen. Het doorgronden van M-dwergen en M-dwerg dubbels leert ons daarom veel over de processen die de eigenschappen bepalen van objecten met sterk uiteenlopende massa's. We beschrijven hoe onze eigen waarnemingen hierbij een rol spelen in Hoofdstuk 5 van dit proefschrift.
- Rode dwergen hebben een fundamenteel andere structuur dan sterren die lijken op onze Zon. Dit komt omdat ze de energie die vrijkomt bij het fuseren van waterstof in hun kern op een andere manier vervoeren naar het oppervlak. Het lijkt erop dat hoe lichter een M-dwerg is, hoe meer hij zijn energie vervoert door middel van *convectie*, een proces dat je kunt vergelijken met het opstijgen van warme lucht van een verwarmingsinstallatie. Het precies doorgronden van deze processen is mogelijk door modellen van sterstructuur te vergelijken met precieze metingen in dubbelstersystemen. Dit wordt beschreven in Hoofdstukken 3 en 5 van dit proefschrift.
- M-dwergen bieden nieuwe mogelijkheden voor de zoektocht naar planeten rond andere sterren (*exoplaneten*) die lijken op onze Aarde. Er zijn wetenschappers die geloven dat een mogelijke aardachtige planeet rond een M-dwerg stabiel leven kan voortbrengen ondanks de furie van de moederster.
- Ondanks hun veelvuldig voorkomen in ons Heelal zijn de fundamentele eigenschappen van eenzame M-dwergen (b.v. hun grootte en temperatuur bij een gegeven massa) tot nu toe nog onvolledig bekend en beschreven. In het bijzonder is dit het geval voor de kleinste M-dwergen (met een massa kleiner dan  $\sim 20\%$  van onze Zon), mogelijke doelen voor zoektochten naar een 'Tweeling-Aarde'. In dit proefschrift probeer ik meer uitsluitsel te geven over deze eigenschappen door middel van een zoektocht naar en directe metingen aan M-dwerg dubbelsterren.

## Open vragen

Er zijn vele open vragen gerelateerd aan M-dwergen, waar dit proefschrift volledig of gedeeltelijk aan raakt:

**Kunnen theoretische modellen voor de structuur van M-dwergen de waargenomen eigenschappen verklaren?** Deze vraag wordt behandeld in Hoofdstuk 3 en 5, waar ik vervolgwarnemingen presenteer aan nieuwe nauwe dubbelsterren en direct hun grootte, massa en temperatuur meet.

**Waarom vormen sommige sterren als dubbelsystemen en blijven andere in eenzaamheid achter?** Gedeeltelijk besproken in Hoofdstuk 3,4 en 5.

**Wanneer tijdens de stervorming wordt een dubbelster gevormd en hoe hangen hun eigenschappen af van de vormingsomgeving?** Gedeeltelijk besproken in Hoofdstuk 3,4 en 5.

**Hoe verzamelen de sterren materie in een dubbelster?** Er is een huidig debat over de vraag of de primaire ster van een dubbelster bij voorkeur het omliggende gas en stof steelt en de begeleider klein blijft (ongelijke dubbelsterren mogelijk) of dat de begeleider deze materie steelt voordat het op de primaire ster kan vallen (Tweelingen waarschijnlijk). In dit proefschrift (zie Hoofdstuk 5) zoek ik actief naar ongelijke dubbelsterren van M-dwergen om te bepalen welk scenario waarschijnlijk is voor deze sterren.

**Hoe komen dubbelsterren in nauwe banen terecht?** Deze vraag wordt besproken in Hoofdstuk 4 van dit proefschrift, waar we argumenteren hoe waarschijnlijk het is dat nauwe dubbelsterren ter plekke gevormd kunnen worden of kunnen evolueren tijdens hun leven op de Hoofdreeks.

**Hoe vaak kunnen M-dwergen voorkomen als dubbelsterren in nauwe banen?** Deze vraag wordt besproken in Hoofdstuk 3 van dit proefschrift.

**Is er een minimum mogelijke baan voor M-dwerg systemen?** Aangezien de huidige waarnemingen en modellen suggereren dat dubbelsterren met periodes korter dan ongeveer 5 uur zeldzaam zijn, confronteren we deze ideeën met onze nieuwe bevindingen in Hoofdstuk 4.

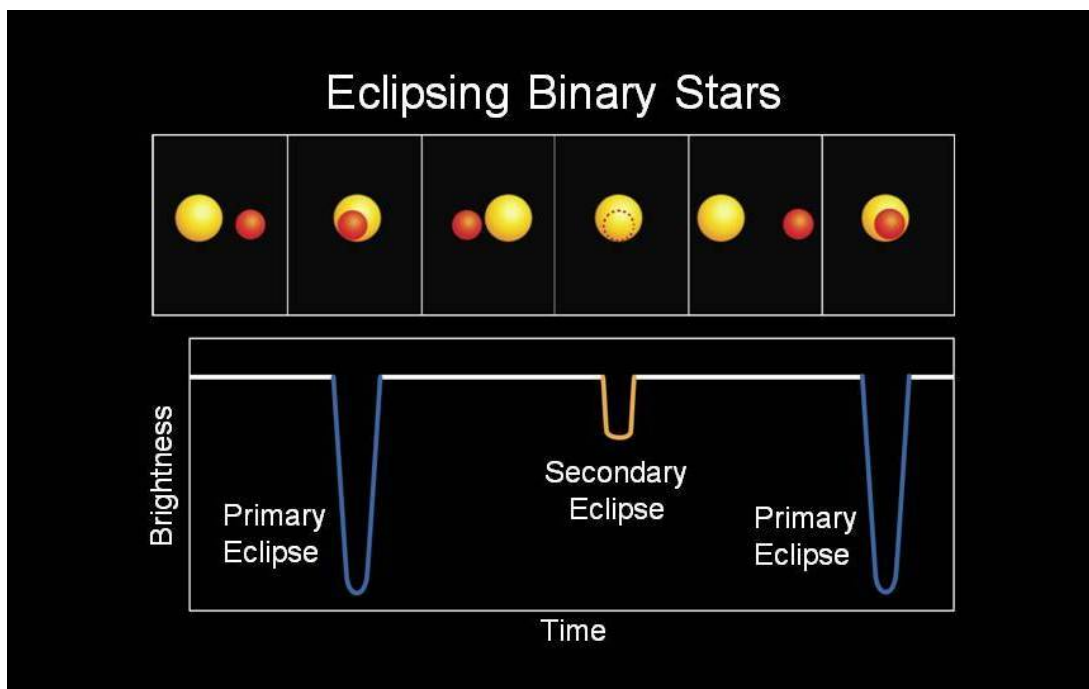
**Hoeveel van deze nauwe systemen zijn Tweeling en hoeveel ongelijk?** Zie Hoofdstuk 5.

**Kunnen wisselwerkingen tussen sterren de vorming van M-dwerg dubbelsterren beïnvloeden?** Ik bespreek de mogelijke verstoringen van M-dwerg dubbelsterren door andere sterren in Hoofdstuk 5.

**Hoe ziet het magneetveld van M-dwergen er uit en hoe ontwikkelt dit zich in een dubbelster?** Ik argumenteer in Hoofdstuk 4 dat de vorm en de sterkte van het magneetveld in (lichte) M-dwergen erg belangrijk is voor hun evolutie in dubbelsterren en dat deze invloed tot nu toe onderschat is.

**Hoeveel en wat voor soort planeten kunnen we vinden rond M-dwergen?** Hoewel niet de primaire motivatie van dit proefschrift, bespreek ik kort wat onze waarnemingen kunnen bijdragen aan het mogelijk bevestigen van de huidige modellen voor het vormen van planeten rond M-dwergen en het nauwkeurig bepalen door het precies meten van de eigenschappen van M-dwergen in dubbelsterren.

Historisch gezien is het moeilijk geweest M-dwergen in voldoende aantallen langdurig waar te nemen, aangezien voorafgaande zoektochten voornamelijk bestonden uit gegevens in het zichtbare licht, waar M-dwergen maar zwak stralen.



**Figuur 6.3** — De helderheids-variaties van een dubbelster systeem met een baan waar we precies tegen de zijkant aankijken, waardoor de beide sterren elkaar periodiek gedeeltelijk uitdoven. De diepte van de eclipsen hangt af van de verhouding tussen de grootte van de primaire ster en zijn begeleider. Een kleinere begeleider (b.v. een planeet) geeft kleinere dipjes in de helderheid (typisch 1%). Credits: Nasa.

### Methode: jacht op eclipsen.

In dit proefschrift proberen we de open vragen die bestaan over M-dwergen zo goed mogelijk te beantwoorden met een nieuwe unieke set gegevens, verkregen door waarnemingen op Mauna Kea, Hawaii. In de loop van 5 jaar heeft de 3.8m United Kingdom Infrared Telescope (UKIRT) opnames gemaakt van 4 gebieden aan de nachthemel en zodoende duizenden metingen verricht aan de helderheid van meer dan 250000 sterren, waaronder ruim 10000 M-dwergen. Een belangrijke truc die we hebben gebruikt voor de totstandkoming van deze dataset, is onze waarnemingen te verrichten met een detector (vergelijkbaar met die in moderne fotocamera's maar dan veel groter) die gevoelig is voor infrarood licht. Infrarode straling (ook wel warmtestraling genoemd) is roder dan met het menselijk oog waarneembaar is. We hebben ons hierbij gericht op licht met een golflengte van 1.2 micrometer (1 micrometer is een miljoenste meter), omdat hier de invloed van onze eigen Aardatmosfeer klein is. Hoewel M-dwergen zwak zijn in het zichtbare licht zijn ze aanmerkelijk helderder (typisch  $\sim 40$  maal) in het infrarood, wat er voor zorgt dat we significant meer M-dwergen in één keer kunnen bestuderen. Onze zoektocht is de eerste gepubliceerde zoektocht naar M-dwerg dubbelsterren op deze schaal.

Een belangrijke methode van dit proefschrift is het zoeken naar de periodieke veranderingen in helderheid als twee sterren hun baan zodanig hebben dat ze voor een Aardse waarnemer elkaars licht periodiek gedeeltelijk verduisteren (vergelijkbaar met een Zonsverduistering door de Maan). Dit worden *eclipsen* genoemd of, in het geval van een exoplaneet rond een ster, *transits* (zie ook Figuur 6.3). Uiteraard geven niet alle dubbelster-banen een waarneembare eclips, maar aangezien we een grote hoeveelheid sterren bestuderen is de kans op het vinden van zulke eclipsen

sen toch behoorlijk. Het bestuderen van eclipsen helpt enorm in het onderzoek naar M-dwergen omdat: i) de periode van een dubbelster eenvoudig en nauwkeurig gemeten kan worden, ii) de helling van de baan direct bepaald kan worden en iii) de verhouding tussen de grootte van de primaire ster en zijn begeleider kan gemeten worden. Dit helpt om, samen met vervolgwaarnemingen, de grootte en de massa van beide sterren nauwkeurig te meten, zonder tussenkomst van modelvoorspellingen. De methode van eclipsen levert dus een unieke en accurate manier om de fundamentele eigenschappen van sterren te kunnen bepalen en theorieën te verifiëren. Omdat M-dwergen significant kleiner zijn dan zonsachtige sterren geeft een grotere begeleider relatief gezien een diepere dip in de helderheid van de moederster. Dit betekent dat planeten ter grootte van onze Aarde gevonden kunnen worden d.m.v. hun transits over M-dwergen. Ik zal mijn gegevens, die in samenwerking met onderzoeksgroepen uit Engeland, Spanje, Duitsland en Rusland verkregen zijn, presenteren in Hoofdstukken 3,4 en 5 van dit proefschrift.

## Dit proefschrift

In **Hoofdstuk 2** laat ik zien dat niet ieder waargenomen transit signaal daadwerkelijk afkomstig is van een echte planeet. Belangrijke zogenoemde *vals-positieven* zijn gevallen waarbij de diepe dips van de eclipsen in een dubbelstersysteem worden gemengd met het signaal van een derde ster (de zogenaamde *blends*). In Hoofdstuk 2 presenteer ik een nieuwe methode die mogelijkveel tijd kan besparen op opvolgstudies naar deze valse planeetkandidaten, door blends uit te sluiten, alleen gebruikmakend van de beschikbare fotometrische data.

In **Hoofdstuk 3** beschrijf ik hoe onze zoektocht naar eclipsen van M-dwerg dubbelsterren is opgezet op Hawaï. Tevens presenteren we onze eerste vervolgwaarnemingen aan M-dwerg dubbelstersystemen, waarbij we nauwkeurig de grootte, massa, temperatuur en magnetische activiteit bepalen van deze sterren. We vinden dat onze sterren 3-12% groter zijn dan voorspeld door modellen. We combineren onze gegevens ook met bestaande waarnemingen uit de literatuur en vinden dat deze afwijkingen in grootte van M-dwergen niet significant afhangen van de omlooptijd van de dubbelster, in tegenstelling tot eerdere publicaties.

Het onderwerp van **Hoofdstuk 4** is een uitgebreide zoektocht in de lichtkrommen van zo'n 260000 sterren, waargenomen met de UKIRT telescoop, naar dubbelster systemen met ultrakorte omlooptijden. In deze bijzondere gegevens bevinden zich meer dan 10000 M-dwergen. In tegenstelling tot wat voorspeld wordt door de huidige theorieën voor evolutie van M-dwerg dubbelsterren vinden we 4 systemen (8 M-dwergen) met tot voorheen ongekend snelle omlooptijden korter dan 4 uur. Ons innigste duo is een bijna-Tweeling van kleine koele M-dwergen in een 2.5 uur durende baan. Omdat we 5 jaar lang op gezette tijden deze rode dwergen hebben waargenomen, weten we met grote nauwkeurigheid hun periodes en is de vorm van hun lichtkrommen goed bekend, wat aanmerkelijk helpt om deze objecten te kunnen classificeren als mogelijke dubbelstersystemen. We vermoeden dat de afstand tussen de sterren sneller is afgenomen dan verwacht door modellen, mogelijk omdat de invloed van de sterke magneetvelden van M-dwergen in een dubbelsysteem tot nu toe onderschat zijn. Een andere mogelijkheid is dat tijdens hun vorming de zwaartekrachtverstoring van een derde ster hun baan snel heeft verkleind.

In **Hoofdstuk 5** beschrijf ik de ontdekking van een interessant dubbelstersysteem van kleine M-dwergen die een opvallend ongelijke massa hebben: de zwaarste ster van dit duo heeft 4 maal meer massa dan de lichte ster. De beide sterren draaien ook rond elkaar in een korte

periode van 2.44 dagen, wat overeen komt met een afstand  $\sim 13$  keer kleiner (!) dan de afstand tussen onze Zon en haar dichtstbijzijnde planeet Mercurius. Dit is belangrijk aangezien huidige simulaties van de vorming van sterren voorspellen dat dubbelsterren met een lage massa in korte omloopbanen voornamelijk voorkomen als bijna-Tweeling. Ik stel voor in dit hoofdstuk dat onze vondst erop wijst dat de accretie van materie in M-dwerg dubbelsterren wellicht op vergelijkbare wijze kan verlopen als bij zwaardere dubbelsterren, in ieder geval voor M-dwergen met een massa rond 50% die van onze Zon. De lichte begeleider heeft slechts 14% van de massa van onze Zon. Onze gegevens zijn uniek omdat we voor de eerste keer zo'n lage massa direct kunnen meten zonder gebruik te hoeven maken van model voorspellingen en we zodoende onbevooroordeeld kunnen testen in hoeverre deze modellen kloppen. Opvallend is verder aan dit tweetal dat de zwaarste M-dwerg langzamer rond zijn eigen as draait dan hij rond zijn partner draait.

# Curriculum Vitae

I was born in the middle of Spring 1983 May 5th (a Dutch public Holliday) in Halsteren, a small village in the southern part of Holland, close to the Belgian border. There I attended Dutch high school (the Mollerlyceum). Living in a rural area gave me the fantastic oppurtunity of observing under dark night sky conditions with a small (and later bigger) telescope. I think around that time my passion for stargazing quickly developed into a crazy fever (I can remember watching the Moon eclipse Saturn at  $-12^{\circ}\text{C}$ ). Ignoring the advice of my former physics teacher, who thought I was anything but made for exact science, I decided to study Astronomy in Leiden to become a professional astronomer. Leiden, with its friendly village feeling, is a fantastic place to live for a young student. In Leiden I finished my Bachelor's working on a small project related to the dusty tori around the active nuclei of galaxies, under the supervision of Huub Rottgering. During my three years as a Master Student (I took more classes than I was supposed to) I worked under the supervision of Bernhard Brandl and Brent Groves on a project studying the physics and application of Neon and Sulphur emission lines in a variety of astronomical environments. This succesfull project made it into a published paper (written together with Brent), my first small contribution to science. For my large research project I had the privilage to work in the famous Starformation Group here in Leiden, under the supervision of Ewine van Dishoek and Tim van Kempen, working on submillimeter data of two interesting starforming regions. During my undergraduate I was so fortunate to observe a week on La Palma with the Isaac Newton Telescope, as part of student training (supervised by Ignas Snellen).

Around the time of my graduation I was very much in doubt what I wanted to do next and whether becoming a professional astronomer really was my true calling. I was then very lucky to receive an email from Ignas whether I was interested in applying for a PhD in Leiden to study planets transiting red dwarf stars using new data from the United Kingdom Infrared Telescope Transit Survey (WTS). After what I think was the shortest PhD job interview ever I accepted the position and the opportunity of working in Ignas' by then small group of students. During my PhD I collaborated with many reasearchers of the RoPaCs community. My 4 years as a PhD allowed me to travel to the Observatories of La Palma (using the William Herschel Telescope and the Isaac Newton Telescope many times), Siding Springs Australia and La Silla, Chili. I have presented my work at scientific conferences in Munich, Cambridge, Tenerife, Madrid and Leiden, and at the NOVA Fall School in Dwingeloo, the Netherlands. During my PhD, I was a teaching assistent for the undergraduate Physics course on Classical Mechanics, the Astronomy course on Stars and the Bachelor Student Projects. I also had the opportunity to assist two talented young Dutch high school students to work on a project in Leiden, which was later awarded with an excellence prize. I gave several talks on exoplanets to Dutch highschool students. Although we did not find any planets transiting M-dwarfs, I made the right decision during the PhD to focus instead on their host stars. This yielded an interesting MNRAS paper and a UK press release on the exciting and unexpected discovery of four ultra-short period eclipsing M-dwarf binaries. If nothing else, I hope my contribution to science would be the recognition of red dwarfs as fascinating targets of study, both with current and future facilities.



# Acknowledgements

No doubt in my mind that this thesis would not have been written up without the love and support of a very special woman that I hold close to my hart. Nicole, you are the sweetest, funniest and most caring girl that I have ever met, we prove that internet dating can work out well. I think we have a bright future ahead of us, whatever will come our way. I am grateful to both my parents and their families for continuous love and encouragements. Mom, you can be proud guiding your two children through life on to their PhD and beyond! Dad, many thanks for your support and welcoming me to your new family. Sister, you are the best, I wish you luck with whatever you will do next, and hope you will enjoy your graduation next May!

Science is never a solitary endeavour, so I owe a lot of gratitude to many people around the Sterrewacht here in Leiden and other colleagues who have made this thesis possible. First of all, I would like to thank my supervisor Ignas, for his ability to reduce difficult matters into simple concepts, carefully reading my many sometimes hopeless paper drafts, and his patience when this PhD student took an unexpected turn. Your red pen will be missed. Thank you Jayne for being my main collaborator on red dwarf binaries and planets here in Leiden and to our many interesting scientific discussions. I have learnt a lot from you and hope you will do well in life as a PostDoc and continue to spread round the importance of M-dwarfs. Thanks also goes out to the other members of the Leiden exoplanet group (Simon, Ernst, Matteo, Gilles, Henriette and others), for making this challenging and ever-changing field clear to me in our regular meetings, for maintaining the high level of research, that I found sometimes difficult to keep up with. Emanuelle, I hope I was able to make a meaningful contribution to your first thesis chapter, by observing at La Silla, Chili. I wish you good luck with your thesis work, mastering the black arts of infrared transit photometry and beyond.

I would also like to thank our collaborators from the Rocky Planets Around Cool Stars group, Simon, David, Roberto, Eduardo, Johannes, Patricia, Joana, Jezus, Brigitta, Gabor and many others for their good company during our conferences, their ideas and help with my papers and press-release, and letting me ravage their lightcurves with IDL in search of tiny close red dwarf duos.

